Influencing River Morphodynamics by Means of a Bubble Screen: Application to Open-Channel Bends

THÈSE N^{O} 5676 (2013)

PRÉSENTÉE LE 5 AVRIL 2013

À LA FACULTÉ DE L'ENVIRONNEMENT NATUREL, ARCHITECTURAL ET CONSTRUIT
LABORATOIRE DE CONSTRUCTIONS HYDRAULIQUES
PROGRAMME DOCTORAL EN ENVIRONNEMENT

ÉCOLE POLYTECHNIQUE FÉDÉRALE DE LAUSANNE

POUR L'OBTENTION DU GRADE DE DOCTEUR ÈS SCIENCES

PAR

Violaine DUGUÉ

acceptée sur proposition du jury:

Prof. I. Smith, président du jury
Prof. A. Schleiss, Dr K. Blanckaert, directeurs de thèse
Prof. Ph. Belleudy, rapporteur
Prof. S. N. Lane, rapporteur
Prof. A. J. Wüest, rapporteur

ÉCOLE POLYTECHNIQUE
FÉDÉRALE DE LAUSANNE

Suisse
2013

A ma famille

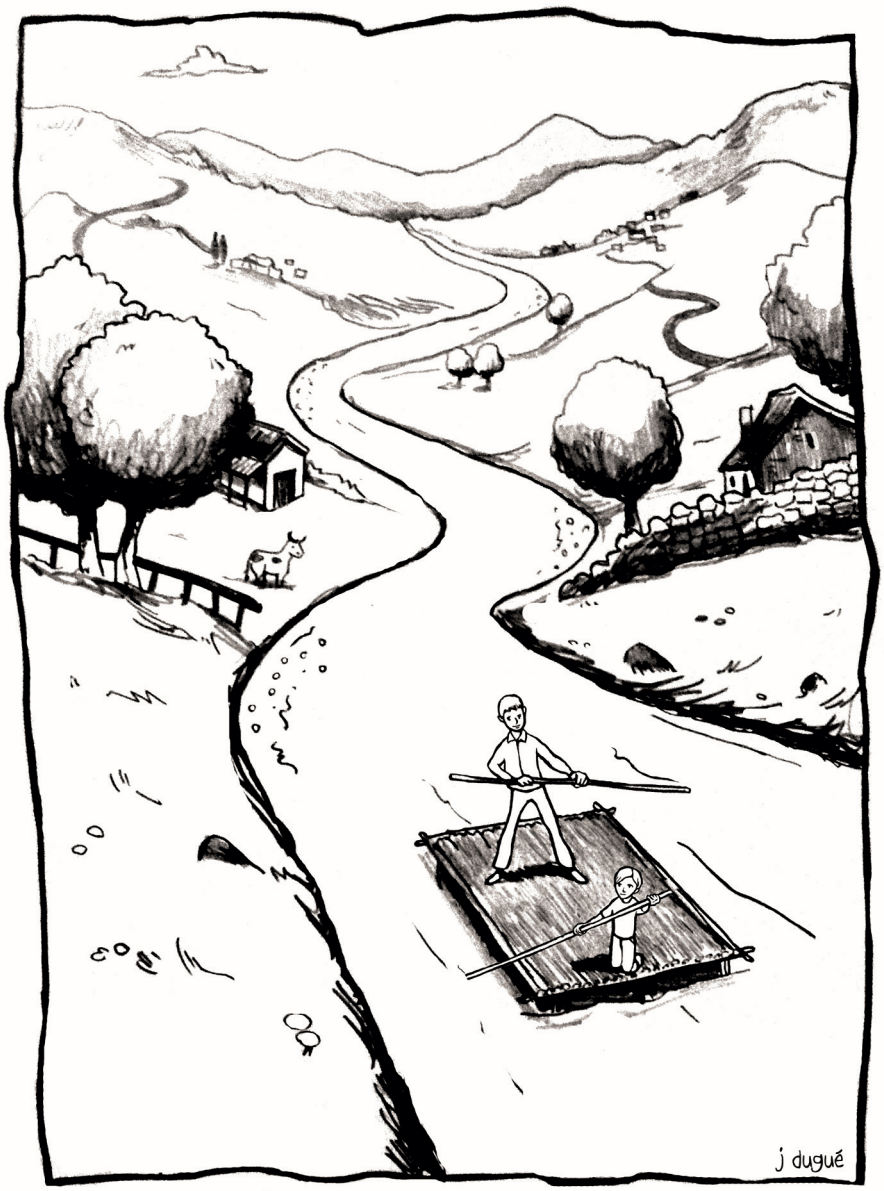

Abstract

Influencing river morphodynamics by means of a bubble screen
Application to open-channel bends

In the past decades, river engineering projects have shown a tendency towards more sustainable techniques. Preserving river ecomorphology while maintaining its principal economical functions calls for engineering techniques that intelligibly influence the fluvial system rather than forcing it.

In this research project, an innovative technique that consists in indirectly manipulating the river morphology by provoking changes in the secondary flow patterns is investigated. A bubble screen, originating from a porous tube located on the river bed, can generate a secondary flow, called bubble-induced secondary flow, which is able to redistribute velocity patterns and consequently modify the bed morphology. The main advantage of this technique, contrary to "hard" engineering techniques such as groynes, riprap, or bottom vanes, is that it does not imply a fixed construction on the river bed that can represent a threat for shipping. The bubble-screen technique has no visual impact, and can be used in a non-permanent way.

The objectives of the present research project are to investigate how river morphodynamics can be influenced by means of the bubble-screen technique. Special attention is given to the feasibility of the bubble-screen technique on inbank flow in a sharply curved laboratory flume with fixed banks with the aim of reducing local erosion near the outer bank and attenuating the morphological gradients resulting from the complex interactions between streamwise flow, curvature-induced secondary flow and bed morphology. Several laboratory experiments are performed following a stepwise approach with increasing degree of complexity.

Straight flow experiments show that the bubble-induced secondary flow redistributes the streamwise velocity, which modifies also bed morphology. The strength and size of the bubble-induced secondary flow are found to be independent of the base flow velocity and to increase with the water depth. The size of the secondary flow cell ranges from 3 (immobile bed) to 7 (mobile bed) times the water depth. Similar sizes of bubble-induced secondary flow cells have been reported in literature for water depths ranging from 0.1 to 5 m, indicating that laboratory experiments are relevant for an application in natural rivers and open-channels. On a mobile bed, a positive interplay occurs between the bubble screen, the bubble-induced secondary flow and the morphology. This coupled hydraulic-morphologic behaviour explains the larger size and strength of the secondary flow over a mobile bed than over an immobile bed.

Experiments performed in a sharply curved open-channel bend under clear-water scour conditions show that the bubble-induced secondary flow shifts the curvature-induced secondary flow in inwards direction and reduces its strength. The bubble screen considerably reduces morphological gradients. Maximum bend scour is reduced by about 50% and occurs

further away from the outer bank where it does not endanger the bank stability. The location of maximum scour coincides with the junction of curvature-induced and bubble-induced secondary flows. At this location, the maximum streamwise velocities and maximum vertical velocities impinging on the bed also occur, which indicates their importance with respect to the formation of bend scour. The bubble screen also substantially reduces deposition at the inner bank.

Experiments performed in the curved channel under live-bed conditions, i.e. with a constant sediment feeding at the flume entry, show that the bubble-screen efficiency is not uniform on the whole length of the flume. In the upstream part of the bend, the strength of the curvature-induced secondary flow is too strong to be influenced by the bubble-induced secondary flow. However, in the downstream part of the bend, as the curvature-induced secondary flow is weaker, the bubble-induced secondary flow is able to modify the flow patterns and to shift the scour location in the middle of the flume. Experiments performed with several transverse positions of the porous tube respective to the outer bank, indicate that the bubble screen is more efficient when located the nearest from the outer bank.

Finally, the dependency of the efficiency of the bubble-screen technique on the different bed and sediment conditions is investigated. Based on this new insight, a straightforward method to evaluate the efficiency of a bubble screen to redistribute the flow patterns and the morphology is proposed, and applied on two natural bends on the Nishnabotna East and Ledra rivers. The minimum air discharge required to counteract the maximal transverse velocities induced by the curvature are relatively low as compared to other types of environmental applications of the bubble screens.

The reported laboratory experiments demonstrate the potential of the bubble-screen technique to modify the morphology in a variety of applications in shallow rivers and open-channels.

Keywords : Bubble screen, bubble-induced secondary flow, experimental investigation, deposition, local scour, morphodynamics, open-channel bend, secondary flow.

Résumé

Influencer la morphodynamique des rivières à l'aide d'un écran de bulles Application aux canaux courbes

Depuis quelques décennies, les projets d'aménagement des cours d'eau s'orientent vers des techniques plus écologiques. Sauvegarder l'aspect éco-morphologique d'une rivière tout en conservant ses fonctions économiques nécessite d'utiliser des outils qui permettent d'influencer le système fluvial plutôt que de le contraindre.

Ce projet de recherche a pour objectif de décrire une technique innovante qui consiste à manipuler indirectement la morphologie d'une rivière en modifiant les courants secondaires. Un écran de bulles, provenant d'un tuyau poreux placé au fond de la rivière, peut générer un courant secondaire additionnel capable de redistribuer le champ de vitesse et par conséquent de modifier la morphologie du lit. L' avantage majeur de cette technique, au contraire des techniques constructives comme les épis, les enrochements ou les vannes de fond, est qu'elle n'est pas une construction fixe dans la rivière qui pourrait représenter un danger pour la navigation. L'écran de bulles n'a pas d'impact visuel négatif et peut être utilisé de manière temporaire.

L'objectif de ce projet de recherche est d'étudier comment la morphodynamique d'une rivière peut être influencée par un écran de bulles. Une attention particulière est accordée à son application sur les écoulements dans les canaux courbes avec berges fixes avec l'objectif de réduire l'érosion locale près de la rive extérieure et d'atténuer les gradients morphologiques résultant de l'interaction complexe entre l'écoulement longitudinal, le courant secondaire induit par la courbure et la morphologie du lit. Plusieurs expériences en laboratoire sont réalisées en augmentant progressivement le degré de complexité.

Les expériences dans un canal droit montrent que le courant secondaire induit par les bulles modifie la distribution du champ de vitesses longitudinales, provoquant des modifications morphologiques. La force et la taille de ce courant secondaire sont indépendants de la vitesse de l'écoulement principal et augmentent avec la hauteur d'eau. La taille du courant secondaire est comprise entre 3 (fond fixe) et 7 (fond mobile) fois la hauteur d'eau. Des tailles similaires ont été reportées dans la littérature pour des hauteurs d'eau comprises entre 0.1 et 5 m, indiquant que les expériences en laboratoire sont pertinentes pour une application dans les rivières naturelles et les canaux à surface libre. Une interaction positive est également observée entre l'écran de bulles, le courant secondaire induit par les bulles et la morphologie. Ce comportement hydro-morphologique explique que la longueur et la force du courant secondaire soient plus importantes sur un fond mobile que sur un fond fixe.

Les expériences réalisées dans un canal courbe sans apport sédimentaire, montrent que le courant secondaire induit par les bulles repousse le courant secondaire induit par la courbure vers la rive intérieure et réduit sa force. L'écran de bulles réduit fortement les gradients morphologiques. L'érosion maximale est réduite de 50% et est éloignée de la rive

extérieure où elle n'affecte plus la stabilité de la rive. L'érosion maximale est observée à la jonction des deux courants secondaires induits par les bulles et par la courbure. Les vitesses longitudinales et verticales maximales sont observées au même endroit, démontrant leur importance quant à la formation de l'érosion locale. L'écran de bulles réduit également de manière significative la sédimentation près de la rive intérieure.

Les expériences réalisées dans le canal courbe avec transport sédimentaire et une alimentation constante en sédiments montrent que l'efficacité de l'écran de bulles à modifier l'écoulement et la morphologie n'est pas uniforme sur l'ensemble du canal. Dans la partie amont de la courbe, le courant secondaire induit par la courbure est trop puissant pour être influencé par le courant secondaire induit par les bulles. Cependant, dans la partie aval de la courbe, le courant secondaire induit par la courbure étant plus faible, le courant secondaire induit par les bulles est capable de modifier l'écoulement et de déplacer l'érosion vers le milieu du canal. Plusieurs expériences réalisées avec différentes positions transversales du tube poreux montrent que l'écran de bulles est plus efficace si il est placé au plus près de la rive extérieure.

Enfin, l'impact des différentes conditions de lit et de transport sédimentaire sur l'efficacité de l'écran de bulles est étudié. Basée sur ces résultats, une méthode simple pour évaluer l'efficacité de l'écran de bulles à redistribuer l'écoulement et la morphologie est proposée et appliquée sur des méandres de l'East Nishnabotna et de la Ledra. Le débit d'air minimal requis pour contrer le courant secondaire induit par la courbure est relativement faible par rapport à d'autres types d'application environnementale des écrans de bulles.

Les expériences en laboratoire reportées démontrent le potentiel de l'écran de bulles à être utilisé comme technique pour influencer la morphologie dans les rivières et les canaux à surface libre peu profonds.

Mots-clés : Ecran de bulles, étude expérimentale, courant secondaire induit par les bulles, déposition, érosion locale, morphodynamique, canal courbe, courants secondaires.

Acknowledgements

Ce rapport est le résultat de trois années, riches en "expériences", passées au sein du Laboratoire de Constructions Hydrauliques à l'Ecole Polytechnique Fédérale de Lausanne. Ce document fait également office de compte-rendu pour le projet de recherche n° 200021-125095 financé par le Fond National Suisse pour la recherche.

Je tiens, dans un premier temps, à remercier le Prof. Anton Schleiss, directeur du laboratoire et de ma thèse, pour m'avoir accueillie dans son équipe. L'atmosphère qu'il a su créer au LCH m'a donné des conditions idéales pour mener à bien mes recherches.

Je ne remercierai jamais assez mon co-directeur de thèse le Dr. Koen Blanckaert pour m'avoir fait confiance avant même le début de ce projet. J'ai eu une chance extrême d'avoir pu travailler avec lui malgré la distance et d'avoir pu profiter de son expérience. C'est lui également qui a initié ce projet et il est certain que le présent rapport n'aurait pu être commencé ni terminé sans ses conseils et ses commentaires.

J'aimerai également remercier les Prof. Philippe Belleudy, Stuart Lane et Alfred Wüest pour avoir accepté de participer à mon jury de thèse et pour avoir lu et évalué ce rapport. Je remercie également le Prof. Christophe Ancey pour avoir accepté de présider ce jury ainsi que le Prof. Ian Smith pour l'avoir remplacé au pied levé.

Une thèse expérimentale ne serait rien sans un bon support technique. Je remercie les membres de l'atelier, Michel, Panpam, Laurent, Shawna, Gregory, Virgile, Stéphane et David pour leur aide sur le canal courbe et sur le modèle de Gage. Un merci également à Cédric et Mike pour leur aide avec l'instrumentation et l'informatique. Je n'oublie bien sûr pas les nombreux "esclaves" de la halle qui ont balayé patiemment le sable répandu autour de mon canal.

Un grand merci également à nos secrétaires Scarlett et Caroline pour avoir supporté toutes mes questions administratives. Je remercie également les Dr. Jean-Louis Boillat, Giovanni de Cesare, Michael Pfister et Mário Franca pour avoir partagé leurs connaissances en hydraulique avec moi. Un merci très chaleureux à mon professeur invité Colin Rennie pour m'avoir conseillé et participé aux expériences.

Je voudrai remercier tous les collègues et amis du LCH avec qui j'ai eu le plaisir de travailler et de vivre ces trois années. A ceux qui m'ont accueillie et qui sont partis vers d'autres horizons: Mathias, Jolanda, Marcelo, Javier, Fadi, Matteo, Jean-Marc, Walter, Martin et Michael. Et à ceux qui à leur tour me verront partir: Milad, Théodora, Tamara, Ana Margarida, José Pedro, Rafael, Stéphane, Mona, Sebastián, Raphaël, Mohammad Javad, Félix, Elena, David, Fränz et Alexandre. J'ai passé de chouettes moments avec eux et je ne suis pas prête de les oublier !

Merci aussi aux étudiants que j'ai eu la chance d'assister dans le cadre des projets de master et de mini-centrale et spécialement à Sylvain Rigaud pour avoir participé à cette thèse en testant les bulles autour des piles de pont.

Un remerciement spécial pour les nombreuses "permanences Internet" qui ont été d'un grand support moral en toute circonstances: Koen, Benoît, Sylvain, Claire, Julien auteur de l'illustration deux pages plus haut, Benjamin, Sébastien, Elise et Olivier bien sûr.

Je remercie également mes amis français, pour m'avoir offert leur soutien précieux. Un grand merci spécialement adressé à la team 2009 de Lyon qui verra naître de nombreux docteurs !

Ce travail est dédié à ma famille: ma grand-mère Renée, mes parents Dominique et David, mes frères et sœur Sébastien, Aurélie et Benjamin, sans oublier Bruno et Charlotte. Vivre et travailler loin d'eux n'a pas été une expérience facile. Je les remercie pour cela de leur soutien constant. Une pensée toute particulière pour les petits bouts de la famille qui ont grandis ou sont nés pendant cette thèse.

Finalement, le plus grand merci s'adresse évidemment à Olivier. Sans son soutien inconditionnel, ses aller-retour hebdomadaires entre Grenoble et Lausanne et ses encouragements à continuer malgré les difficultés rencontrées, cette thèse n'existerait tout simplement pas.

Contents

Notation

Roman lower cases

b	Distance between the air line-source and the inner/*right* bank	[m]
d	Distance between the air line-source and the outer/*left* bank	[m]
d_m	Sediment mean diameter	[m]
$f_{n,0}$	Function from the linear model that represents the form of the vertical profiles of v_n* (de Vriend, 1977)	[-]
f_n	Function from the non-linear model without neglecting inertia effect according to Blanckaert and de Vriend (2010) that represents the form of the vertical profiles of v_n*	[-]
g	Gravitational acceleration	[m s^{-2}]
n / y	Transverse reference coordinate, positive in outward direction, 0 at the centreline	[m]
n_b	Transverse position of the porous tube	[m]
q_a	Air discharge per unit length of air line-source	[dm^3 s^{-1} m^{-1}]
$q_{a,min}$	Minimum air discharge per unit length of air line-source required to counteract the curvature-induced secondary flow	[dm^3 s^{-1} m^{-1}]
q_f	Water discharge per unit width	[m^3 s^{-1} m^{-1}]
q_s	Sediment discharge per unit width	[kg m^{-1} s^{-1}]
tke	Turbulent kinetic energy	[m^2 s^{-2}]
s / x	Streamwise reference coordinate, positive in downstream direction	[m]
v_i *(i=s, n, z)* *(i=x, y, z)*	Time-averaged local velocity component along *i*-direction	[m s^{-1}]
v_i^* *(i=s, n)*	Deviation from the depth-averaged velocity component in *i*-direction	[m s^{-1}]
$v_{n,surf}$	Transverse velocity at the water surface	[m s^{-1}]
$v_{n,surf,bub}$	Transverse velocity at the water surface induced by the bubble screen	[m s^{-1}]
$v_{n,surf,bub,max}$	Maximal value of the transverse velocity at the water surface induced by the bubble screen	[m s^{-1}]
$v_{n,surf,ref}$	Transverse velocity at the water surface induced by the curvature	[m s^{-1}]

$v_{n,surf,ref,max}$	Maximal value of the transverse velocity at the water surface induced by the curvature	[m s^{-1}]
$v_{y,max}$	Maximal transverse velocity induced by the bubble screen	[m s^{-1}]
$v_{z,bubble,0}$	Final rising velocity of a single air bubble	[m s^{-1}]
$v_{z,bubble}$	Final rising velocity of the air bubbles in the bubble screen	[m s^{-1}]
$v_{z,flow}$	Vertical flow velocity observed in the bubble screen	[m s^{-1}]
$v_{z,flow,max}$	Maximal upward velocity observed in the bubble screen	[m s^{-1}]
y_{min}, y_{max}	Transverse limit of the ADVP measurements	[m]
z	Vertical reference coordinate, positive in upward direction	[m]
z_b	Bed level	[m]

Roman capital

A_b	Buoyancy of the bubble screen	[m s^{-1}]
A/R	Scour factor	[-]
B	Flume width	[m]
C	Chézy friction coefficient	[m$^{1/2}$ s^{-1}]
C_f	Dimensionless Chézy friction coefficient all around the flume	[-]
C_{f0}	Dimensionless Chézy friction coefficient in the upstream straight reach	[-]
Fr	Water flow Froude number	[-]
H	Flume-averaged flow depth	[m]
H_a	Atmospheric pressure head	[m]
H_w	Cross-sectional averaged water depth	[m]
K	Factor of proportionality from Odgaard's theory (1981)	[-]
L	Length of the air line-source	[m]
P_a	Air-pressure in the porous tube	[Pa]
Q	Water discharge	[m^3 s^{-1}]
Q_a	Air discharge	[m^3 s^{-1}]
R	Flume centreline radius of curvature	[m]
R_w	Inertial force of the river flow	[m s^{-1}]
S_s	Flume-averaged water slope	[-]

U	Flume-averaged velocity	[m s^{-1}]
U_w	Cross-sectional averaged velocity	[m s^{-1}]
U_n	Depth-averaged velocity in transverse direction	[m s^{-1}]

Greek symbols

α_s	Normalized transverse velocity gradient	[-]
η	Water entrainment efficiency	[-]
θ	Cross-section angle	[°]
ψ	Streamfunction	[m^2 s^{-1}]
ψ_y, ψ_z	Transverse and vertical streamfunctions	[m^2 s^{-1}]
ψ_m	Maximal intensity of the streamfunction	[m^2 s^{-1}]
ψ_p	Pseudostreamfunction	[m^2 s^{-1}]

Subscripts

s, n ,z	Streamwise, transverse and vertical directions
x, y ,z	

Operator

$\langle\ \rangle$	Depth-averaged value

Acronyms

ADVP	Acoustic Doppler Velocity Profiler
EPFL	Ecole Polytechnique Fédérale de Lausanne
IGB	Leibniz-Institute of Freshwater Ecology and Inland Fisheries
LCH	Laboratory of Hydraulic Constructions
LES	Large-Eddy Simulation
RANS	Reynolds-Averaged Numerical Simulations
TUD	Delft University of Technology

Chapter 1

Introduction

Water is an essential resource for every life forms on Earth and especially for Humans. In addition to its drinking potential, it is also used for agriculture, transportation, recreation or for producing energy. It is then not surprising to see how civilisations settled around rivers. However, river morphologies are continuously evolving in time with eventual consequences for dwellers. For example, in open-channel bends, deposition continues to occur at the inner side of the meander affecting for instance the navigable width of the river, and erosion that occurs near the outer bank can endanger constructions located by this side of the river.

Several techniques to counteract the natural morphological development of a river already exist but imply generally fixed constructions and, consequently, a possible threat for navigation. Moreover, they are not always well integrated in the landscape as they do not always respect eco-morphological aspects of the river. New techniques to control morphological evolution of meanders are thus required to satisfy both human safety and river ecology conservation.

In this context, this research project investigates an innovative technique that consists in indirectly manipulating the river morphology by provoking changes in the secondary flow patterns. The rising air bubbles of a bubble screen are used as an advective source that is expected to redistribute the base flow patterns in the river, and consequently influence its morphological development. This technique could be applied for example to counteract downward velocities that impinge on the channel bed and results in local scour, such as bridge or bend scour.

Further, this chapter contextualizes the research project, formulates the main objectives and describes the structure of the report.

1.1 CONTEXT

This research aims at generating generic knowledge with a wide range of validity. Attention is mainly focussed on the application of the bubble screen in open-channel bends for the following reasons:

- This research is part of an ongoing joint research programme on open-channel bends that exploits synergies between laboratory experiments at Ecole Polytechnique Fédérale de Lausanne (EPFL), field experiments at the Leibniz-Institute of Freshwater Ecology and Inland Fisheries (IGB, Germany) and numerical modeling at Delft University of Technology (TUD, The Netherlands). Consequently, experimental facilities, research methodology and experimental data are already available.
- The idea of using bubble screen to influence bend morphodynamics comes from a collaboration between Ecole Polytechnique Fédérale de Lausanne (K. Blanckaert), $HKV_{consultants}$ (H. Wijbenga) and Rijkswaterstraat (RIZA department of the Dutch Ministry of Transport, Public Works and Water Management, R. Schielen). Preliminary experimental and numerical research on the application of bubble screen in open-channel bends were triggered in order to demonstrate the feasibility of the bubble-screen technique to influence open-channel bends hydrodynamics. The experimental part was performed at Ecole Polytechnique Fédérale de Lausanne (Blanckaert et al., 2008) and the numerical part was performed at Deltares (van Balen, 2007). This preliminary research demonstrated that a bubble screen is able to generate a secondary flow in straight and curved flows, which can redistribute the flow pattern and the bed shear stresses. Consequently, application of a bubble screen in a mobile-bed configuration is supposed to influence also the bed morphology.

1.2 OBJECTIVES

Bubble screen, curtains or plumes have been already widely investigated and used in environmental hydraulics, for example for lake destratification or as barriers against salt water intrusion in harbour locks. However, the application of an air-bubble screen in river morphodynamics has not yet been systematically investigated or applied. Consequently, knowledge concerning the application of bubble screen in shallow free-surface flow configurations as well as the interaction between the bubble-induced flow structures with sediment transport and river morphological development, is missing.

The present research project is performed in the continuity of the preliminary studies (see Section 2.3) by extending the parameter range already investigated. Application of the bubble-screen technique is investigated in straight and curved open-channel flows over a mobile bed by means of laboratory experiments performed in a flume at EPFL, which consists of a straight reach and a sharply curved bend. The investigation is limited to inbank flow in open-channel bends with fixed banks due to the experimental design of the flume.

The main objectives of the present research are:

- to understand the processes induced by a bubble screen in shallow flow configurations, regarding the base flow depth and velocity;
- to gain insight in the interaction between the bubble screen, bubble-induced flow structure, base flow, sediment transport and morphology;
- to provide detailed data on the three-dimensional flow field and morphology in a sharply curved open-channel bend that is essential for numerical model validation;
- to determine a range of applicability of the bubble-screen technique at the prototype scale.

1.3 STRUCTURE OF THE REPORT

The present document is divided into eight chapters. Chapter 4 to Chapter 7 are written as scientific papers. Those chapters are thus self-contained and are framed by this *Introduction* (Chapter 1), the *Literature review* (Chapter 2), the *Design of experiments* (Chapter 3) and the *Conclusions* (Chapter 8).

The bubble-screen technique has been investigated in several configurations, following a stepwise approach with increasing degree of complexity, as schematically shown in Figure 1.1. Chapter 4 deals with the application of a longitudinal bubble screen in straight flow. In Chapters 5 and 6, the bubble screen is applied to open-channel bends under clear-water scour and live-bed conditions, respectively. Finally, Chapter 7 deals with the impact of sediment transport on the efficiency of the bubble-screen technique and concludes with the applicability of the bubble screen at the prototype scale. In the following, a short outline of the four main chapters is provided.

Chapter 4: *Influencing flow patterns and bed morphology in straight open-channels by means of a bubble screen*

The ability of a longitudinal bubble screen to redistribute the flow field and bed morphology in straight shallow rivers and open-channels is tested with laboratory experiments. Effects of flow shallowness, base flow velocity and bed morphology are investigated under still-water and straight-flow conditions. Finally, the interplay between the air-bubble screen, the bubble-induced secondary flow, the patterns of longitudinal flow and the morphology is explained.

Chapter 5: *Reduction of bend scour under clear-water scour conditions with a bubble screen*

Experiments are performed in a laboratory sharply curved flume on a mobile bed under clear-water scour conditions with and without the bubble screen. Morphological and hydrodynamical comparisons are provided in order to determine the efficiency of the bubble screen to influence the development of the typical morphology.

(by *V. Dugué, K. Blanckaert, Q. Chen and A. J. Schleiss*, accepted for publication in *International Journal of Sediment Research*)

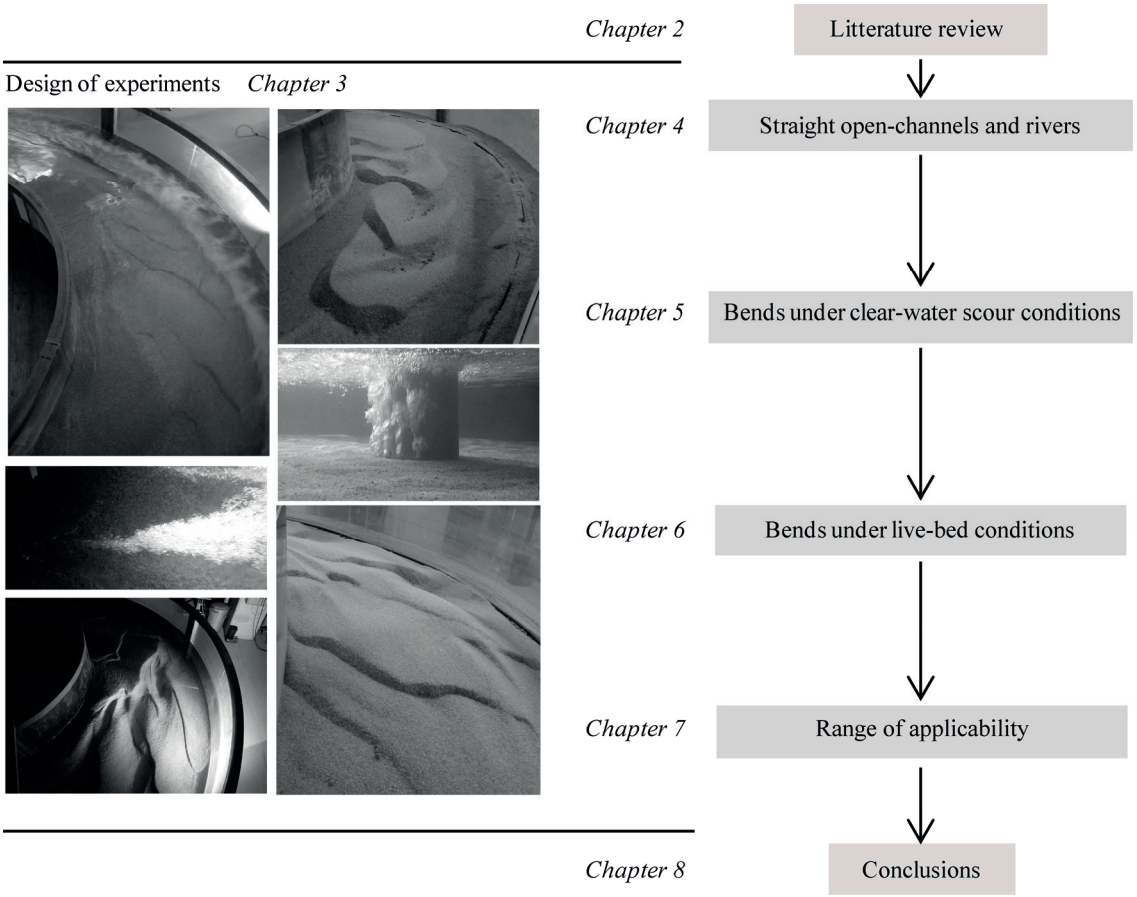

Figure 1.1: Methodology of the research project. The bubble screen is investigated in several configurations with increasing degree of complexity by means of laboratory experiments. The structure of the report follows this approach.

Chapter 6: *Influence of a bubble screen on bend morphodynamics under live-bed conditions*

This chapter investigates the influence of a bubble screen on a sharply curved bend morphodynamics under live-bed conditions with the aim of gaining insight in the interaction between the base flow, the bubble-induced flow structure, the bed morphology and the sediment transport. Morphological and hydrodynamical comparisons of a reference experiment without the bubble screen and an experiment that involves the bubble-screen technique are provided. A first condition on the efficiency of the bubble screen is given.

Chapter 7: *Application range of a bubble screen for reducing scour in open-channel bends*

Based on the new insights given in Chapters 4 to 6, the influence of sediment transport and bed characteristics on the efficiency of the bubble-screen technique is estimated. The condition on the efficiency of the bubble-screen technique, already mentioned in Chapter 6, is validated. A range of applicability of the bubble-screen technique in open-channel bend is then given and applied to two sharply curved rivers.

Finally, Chapter 8 gives general conclusions and an outlook on further research. The appendixes provide additional experimental results (Appendixes A to D), as well as preliminary experimental results on the application of the bubble-screen technique on local scour around bridge piers (Appendix E).

Chapter 2

Literature review

This chapter outlines relevant scientific background on open-channel bend morphodynamics, bubble plumes and screens and on the preliminary experimental and numerical investigations regarding applications of bubble screens in open-channel bend hydrodynamics. The content shall allow general understanding of the concerned fields. More references related to the study are included in Chapters 4 to 7.

Abundant research has been performed on morphodynamics and on open-channel bends, by means of experiments, numerical simulations and analytical developments. Proceedings of the specialized congress "River Coastal and Estuarine Morphodynamics" (1999-2011) summarize well the state of the art in the field of morphodynamics, suggesting that many engineering techniques are available to modify the bed topography in rivers.

Bubble plumes, curtains or screens are used in many fields of engineering and have been abundantly investigated. In water management, bubble plumes and screens have been used as barriers to contain density intrusions or oil spills, as breakwaters, for destratification purposes in lakes, to stop turbidity currents or even the spread of invasive species. However, bubble screens have not yet been investigated or applied in river morphodynamics.

Preliminary research has been performed on the influence of a bubble screen on an open-channel bend hydrodynamic by means of experiments and numerical simulations. This demonstrated the efficiency of a bubble screen to redistribute flow and bed shear stress patterns in a sharply curved open-channel bend.

2.1 RIVER MORPHODYNAMICS

River morphodynamics define the complex interplay between flow patterns, bed morphology and sediment transport that occurs in a river. Flow patterns induce sediment transport that build bed morphology, which will modify the flow field in return.

River morphodynamics have a broad range of time and spatial scales, spanning from few seconds to several centuries (Figure 2.1) (Church, 2007; Nikora, 2007). At the century scale, the general shapes of rivers, meanders, straight channels, braided rivers, are formed. At the time scale of years, macroscale features of the river, such as point bars and scour holes are created. Finally, at the time scale of days, mesoscale bedforms, such as dunes and ripples, migrate along the river.

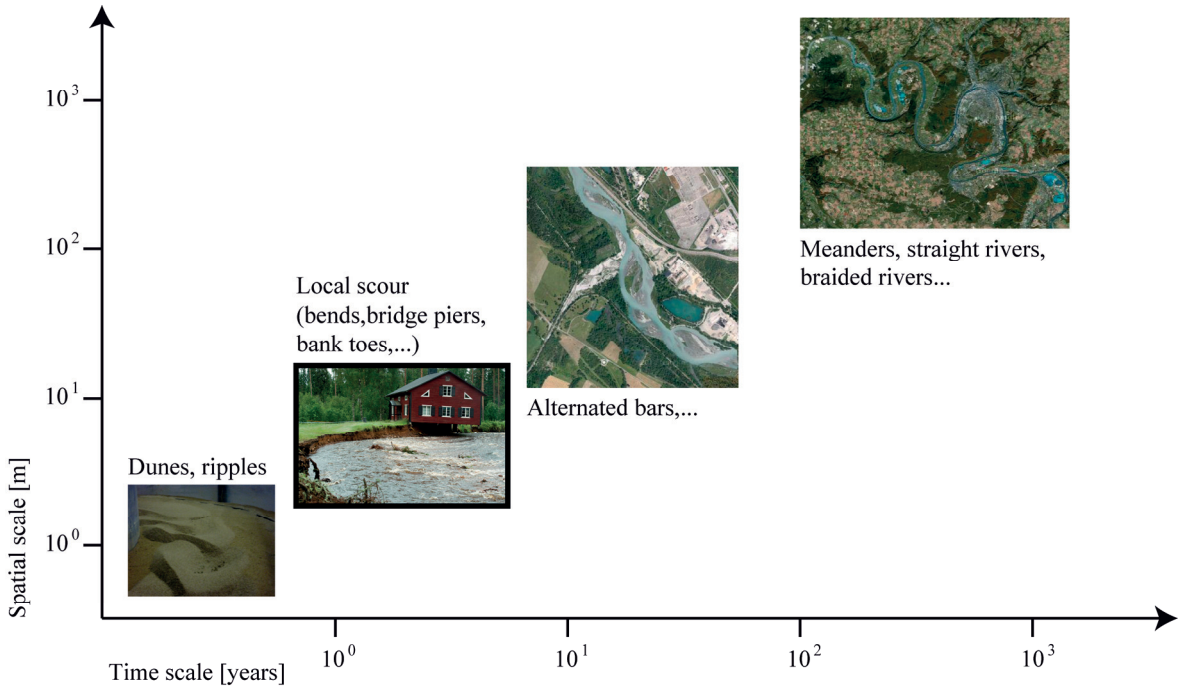

Figure 2.1: Examples of different rivers morphodynamic features considering different time and spatial scales. This research project focus on the morphodynamic features resulting in local erosion at bends, bridge piers and bank toes (highlighted with black frame).

In the present study, the scale considered is highlighted with a black frame in Figure 2.1. This scale focuses on the shape and morphological development of river cross-sections. Moreover, it includes the development of local scour (bend scour, bridge scour, bank toes scour) and deposition zones (point bar). Erosion occurs as part of the natural evolution of the river or as a result of river training works and infrastructures. Herein are reported some examples where scour is observed:

- The presence of a bridge pier in a river generates a three-dimensional turbulent flow, characterized by downward velocities that impinge on the bed. These downward velocities generate a local scour at the upstream toe of the pier which can endanger the stability of the structure foundations.

- Structures such as groynes or bridge abutments are often required to protect river banks or infrastructures. However, such kind of structures induce flow separation, reduce the river width and can therefore induce local scour.
- In open-channel bends, the change in curvature generates a curvature-induced secondary flow that redistributes the bed morphology in a cross-section. The typical bar-pool bed morphology develops with a local bend scour near the outer bank and sedimentation near the inner bank.

The last feature is of particular interest in the present study and is developed in the following sections.

2.1.1 Open-channel bends morphodynamics

Open-channel bends are characterized by a particular morphological profile related to the existence of a secondary flow, induced by the curvature of the channel and perpendicular to the streamwise axis (Figure 2.2). The presence of this so-called "curvature-induced secondary flow" has been investigated in many laboratory experiments (Rozovskii, 1957; Blanckaert and Graf, 2001; Abad and Garcia, 2009b), field experiments (Frothingham and Rhoads, 2003; Blanckaert et al., 2009; Nanson, 2010; Engel and Rhoads, 2012; Sukhodolov, 2012) and theoretical studies (Engelund, 1974; Odgaard and Bergs, 1988; Johannesson and Parker, 1989). The curvature-induced secondary flow redistributes the velocities and the boundary shear stresses, and hence also the sediment transport and morphology (Rozovskii, 1957; Blanckaert and de Vriend, 2003; 2004; Blanckaert and Graf, 2004). Under its action, the streamwise velocity and erosive capacity increase/decrease in the outer/inner part of the cross-section. In addition the inward directed sediment transport due to inward transverse velocity of the curvature-induced secondary flow enhance sediment transport. Consequently, a typical bed morphology, called bar-pool bed topography, develops characterized by a transverse bed slope, scouring near the outer bank and deposition near the inner bank (Engelund, 1974; Bathurst et al., 1979; Odgaard, 1981; Blanckaert, 2010).

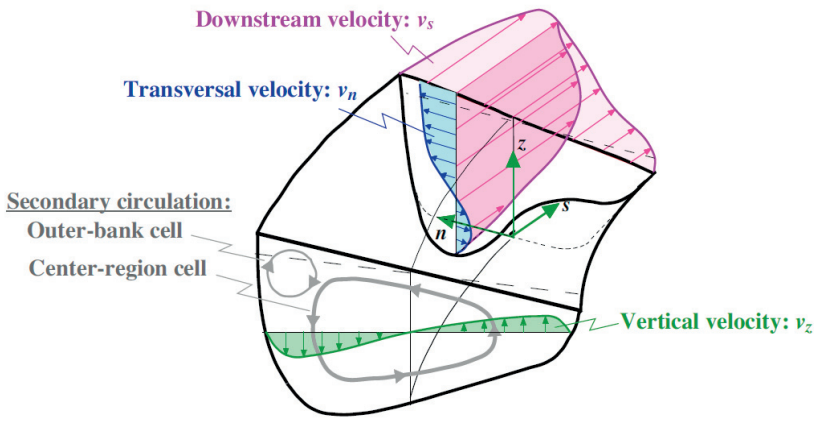

Figure 2.2: Definition sketch of curved open-channel flow (Blanckaert, 2002).

Abundant literature on hydrodynamics and morphodynamics aspects of open-channel bends is available, resultant from laboratory and field experiments, numerical simulations and analytical development. Results of experimental studies in laboratory curved channels

investigate either hydrodynamics on a fixed horizontal bed or morphodynamics on a mobile bed (Rozovskii, 1957; Odgaard and Bergs, 1988; Whiting and Dietrich, 1993a; Blanckaert and Graf, 2001; Abad and Garcia, 2009b; a; Blanckaert, 2010). Concerning numerical simulations, modeling of flow field in curved channels have been performed by means of depth-integrated models (Blanckaert and de Vriend, 2003; 2010). Also, 3D modeling have been performed with either the use of large-eddy simulation (LES) (van Balen et al., 2009; van Balen et al., 2010a; van Balen et al., 2010b) or Reynolds averaged numerical simulations (RANS) (Zeng et al., 2008; van Balen et al., 2010a).

2.1.2 Solutions to counteract erosion and deposition in open-channel bends

The formation of the typical bar-pool bed morphology in open-channel bends leads to adverse impacts, such as increased risk of erosion at the outer bank or reduced navigable width. Therefore, the study of solutions to counteract erosion and deposition in open-channels has been a subject of great interest for the river research community. Several techniques have already been studied to reduce these adverse impacts and are reported in literature. There are two ways for influencing bend morphodynamics: influencing the flow patterns or acting directly on the bed morphology. Some of the existing countermeasures are summarized below.

Riprap is one of the most extensively used countermeasures against local scour at the toe of the outer bank (Figure 2.3a). First, riprap shifts the thalweg from the outer bank then it paves the slope between the thalweg and the outer bank, protecting it from erosion (Martin-Vide et al., 2010). An undulated bank riprap protection was found to be effective in reducing bend scour and creating refuges for aquatic species (Chèvre and Schleiss, 2005).

Construction of bottom (or submerged) vanes (Figure 2.3d) can prevent the development of the secondary flow by generating a secondary circulation that counteracts the curvature-induced secondary flow (Odgaard and Spoljaric, 1986; Odgaard and Wang, 1991; Voisin and Townsend, 2002). Consequently, the pronounced curvature-induced bend topography is reduced. However, bottom vanes represent fixed structures at river bed and consequently a possible threat for shipping.

Fixing the bed by a concrete lining at the outer bend prevents it from erosion and avoids sediment deposition at the inner bank by modifying the flow field (Figure 2.3b). The formation of point bars is hindered. Outer bend layers are already applied in bends on the river Waal near St-Andries in the Netherlands and in the bend upstream of Nijmegen (Sloff et al., 2006). This countermeasure is especially relevant in urban environments where vertical banks are imposed by space limitations or preferred for their visual aspect (Roca et al., 2007).

Groynes or spur dikes with a limited height (bed groynes or submerged groynes) can be built near the outer bank (Przedwojski, 1995; Sukhodolov et al., 2002). They redirect the flow toward the center of the channel and promote sedimentation near the bank (Figure 2.3e). However, their maintenance is difficult and they can be destroyed during floods.

Application of macro-roughness elements at vertical outer banks can shift the core of high downstream velocities away from the bank, decrease the flow velocity adjacent to the

bank, hence reducing bend scour and the potential failure of bank protection walls (Figure 2.3c) (Hersberger, 2002).

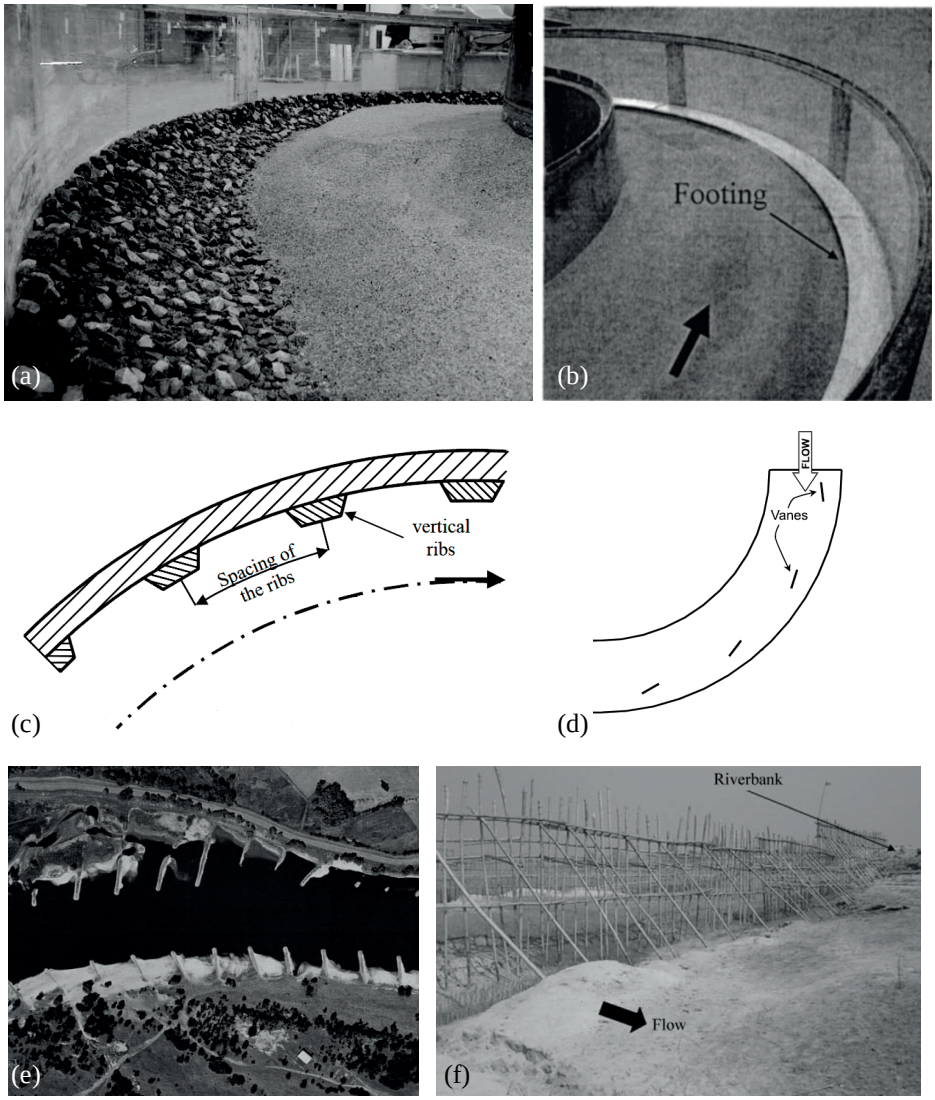

Figure 2.3: Countermeasures: (a) Riprap (Martin-Vide et al., 2010), (b) outer bend layer (Roca et al., 2007), (c) macro-roughness elements (Hersberger, 2002), (d) bottom vanes (Voisin and Townsend, 2002), (e) groynes (Sukhodolov et al., 2002) and (f) bandal-like structures (Teraguchi et al., 2011).

Bandal-like structures consist of a framework of naturally available bamboo driven into the riverbed and supported by struts where bamboo matting is fixed at the water level (Teraguchi et al., 2011). The structure has an upper half part blocked to divert the high velocity flow near the water surface into the main channel direction and the lower half part with an opening to allow passage of flow (Figure 2.3f). The reduced velocity of flow passing through the lower opening cannot enhance the sediment transport, resulting in deposition near the bank. In addition, the flow diverted towards the main channel can develop a deeper navigation channel. They are cheaper than the construction of groynes.

Finally, the navigable width of the river can be increased by dredging the deposited sediment. The sediment balance is not disturbed if the extracted material is dumped near the dredge location into the scoured holes.

2.2 AIR-BUBBLE PLUMES AND SCREENS

2.2.1 Description of a bubble plume

A bubble plume results from the injection of air in a water body. It can be either two-dimensional (bubble screen or curtain) or three-dimensional (bubble plume or column). Schematically, a bubble plume has a similar behavior than a vertical turbulent buoyant jet and can be decomposed in three different zones (Figure 2.4).

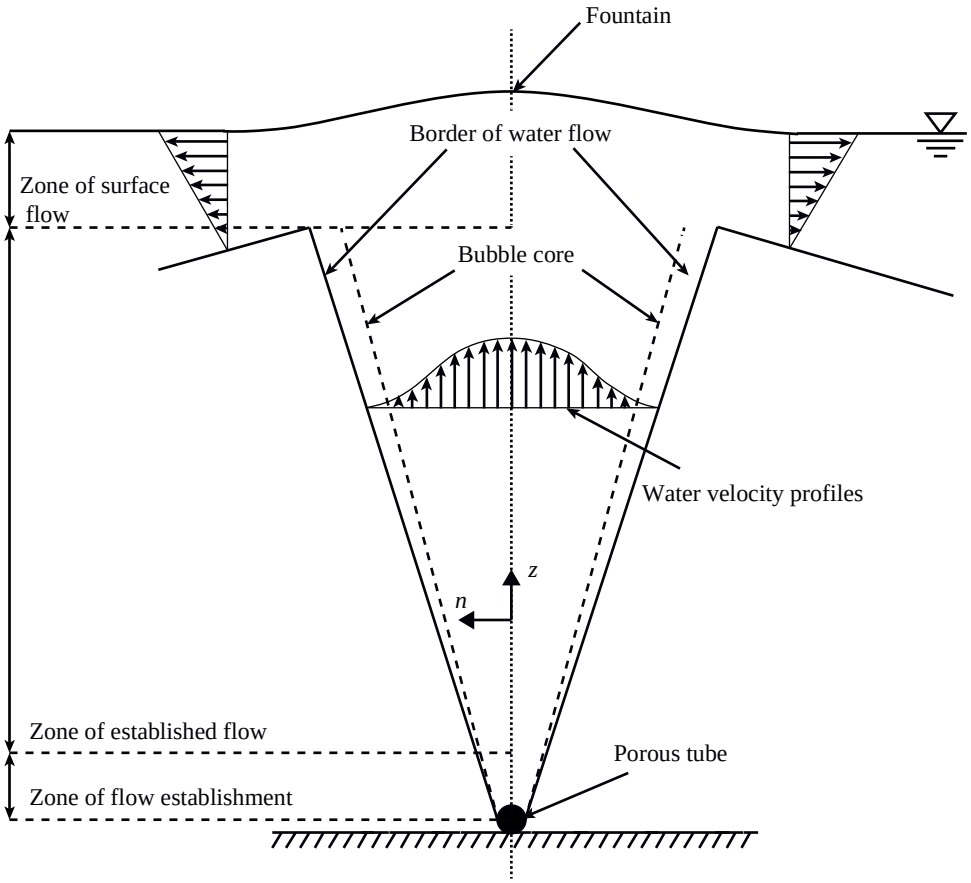

Figure 2.4: 2D schematic diagram of a bubble plume (Fanneløp et al., 1991; Kubasch, 2001).

A zone of flow establishment (ZFE) is located close to the air injector (Milgram, 1983). At the injector exit, the gas enters the ambient fluid in the form of a jet with the shape of large individual bubbles or jets. In this zone, the flow goes from jet-like to plume-like and is mostly dominated by the initial momentum of the gas, the gas expansion and the breakup of the gas into bubbles (Friedl and Fanneløp, 2000). The main controlling flow parameters are the air discharge, the injector diameter and design. ZFE is very small comparing with the water depth and consequently its impact on the plume is less important on a large scale than on a laboratory scale.

Above ZFE, the zone of established flow (ZEF) is driven only by buoyancy effects. The initial momentum of the injected air plays no significant role. It is composed of an inner bubble core where most of the bubbles are found and a surrounding entrained water flow with upward movement. Due to water entrainment, the bubble plume expands while it is rising. The expansion of the entrained water flow is wider than that of the bubble core. As the

bubbles rise in the entrained water flow, their upward velocity is considerably higher than that of individual bubbles in stagnant water. According to Leifer et al. (2000), the rising velocity of a single air bubble is approximately constant at $v_{z,bubble,0} = 0.24$ m s^{-1}. In the ZEF, Gaussian curves are most commonly used to represent the void fraction and the water velocity profiles in the bubble plume, with a width linearly increasing with the water depth (Kobus, 1968). The main controlling parameter of ZEF is the air discharge.

Finally, beneath the water surface, the zone of surface flow (ZSF) extends to a depth about equal to the plume diameter. In this zone, the influence of the water surface is significant and the rising water is deflected outwards into a radial/transverse direction for air-bubble plume/screen respectively and bubbles are released into the atmosphere. Above the bubble plume, a local elevation of the water surface (the fountain) can be observed.

The steady-state bubble plume can be described by conventional integral models that consider water entrainment, relative phase flow velocity, rates of expansion of the entrained water flow and rates of expansion of the bubble core (Ditmars and Cederwall, 1974; McDougall, 1978; Milgram, 1983; Wüest et al., 1992).

2.2.2 Bubble-induced secondary flow

According to Fanneløp et al. (1991), two regions of recirculating flow, called primary cells, are found on both sides of a line-source air-bubble plume in still-water conditions. Their size varies from 2.5 to 7 times the water depth independently of depth and air discharge. However, at very low air discharge, the cell size is found to increase with increasing air discharge (Wen and Torrest, 1987; Riess and Fanneløp, 1998).

The differences in size of secondary flow are mostly related to the different definitions of the bubble-induced secondary flow size. Jirka and Harleman (1979), for instance, defined the end of the recirculation zone as the location where the depth of the surface current reached half the water depth. Fanneløp et al. (1991) results were based on observations at the free surface: the appearance of the surface is rough (due to turbulence) in the recirculation zone but very smooth in the flow outside.

The cores of the two cells, also called rotor cores, are located close to the plume, independently of the air discharge but their transverse distance from the porous tube is found to be dependant of the ratio L/H (Figure 2.5) (Riess and Fanneløp, 1998).

The different geometries of experimental setups can also explain the large range of bubble-induced secondary flow size. In a tank of limited width, the bubble-induced secondary flow size will be affected by boundary conditions. Wen and Torrest (1987) found a secondary flow cell size of $4H$ for water depths between 0.25 m and 0.9 m (parameters defined in Figure 2.5). Goossens (1979) performed experiments at small and large scales and found a range of influence of about 4 times the water depth, for water depths between 2 and 5 m. These results indicate that similar secondary flow cell sizes are found independently of the water depth.

Only few studies have examined the effect of the channel geometrical parameters b, L, and H, defined in Figure 2.5, on the characteristics of the bubble-induced secondary flow. Riess and Fanneløp (1998) determined that the length-to-depth ratio L/H is a characteristic

parameter for the secondary flow in still-water conditions. The largest cell was found with a L/H ratio equal to 1. If L/H is lower or higher than unity, the cell was smaller. Experiments with different air discharges and water depths, but with the same L/H ratio, showed similar behaviour. The effect of boundary conditions in still-water conditions was also investigated by Neto et al. (2008) on a circular bubble plume, generated by a single-source nozzle. A large recirculating cell was generated in both square and rectangular tanks but strong 3D effects appeared in the latter due to the asymmetric configuration of the tank. In his confined setup, two secondary flows were observed in the vertical plane.

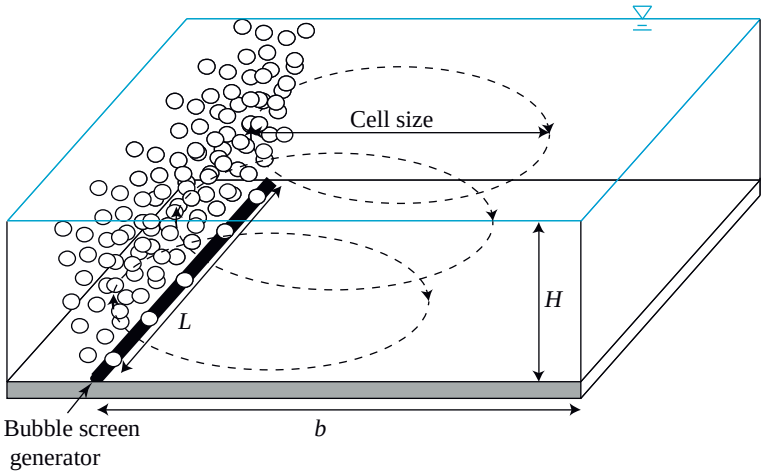

Figure 2.5: Definition sketch of relevant geometric parameters of the bubble screen (b: transverse distance between the air-line source and the opposite bank, L: length of the air-line source, H: water depth).

Nakai and Arita (2002) studied the application of an air curtain perpendicular to the base flow in rivers in order to prevent saline wedge intrusion. They observed that the characteristics of the bubble-induced flow patterns depend on the relative importance of the air curtain buoyancy A_b and the inertial force of the river flow R_w defined as below:

$$A_b = \left(q_a g\right)^{1/3} \tag{2.1}$$

$$R_w = \frac{q_f}{H} \tag{2.2}$$

where q_a is the air discharge per unit length of line-source and q_f is the water discharge per unit width. If $A_b >> R_w$, convection by the base flow is weak and the bubble-induced vertical jet spreads to both sides of the air curtain near the water surface. If $A_b << R_w$, convection by the base flow is so strong that the bubble-induced vertical jet only spreads to the downstream side of the air curtain. In this second case, the efficiency of the bubble screen to prevent saline wedge intrusion is reduced.

2.2.3 Application of bubble plumes and screens

Bubble plumes and screens have already been proposed and applied in several fields at large and small scales. For example, they can be used:

- in lakes, reservoirs or wastewater treatment systems for the destratification and the aeration of stagnant water in order to improve water quality or to prevent growth of

algae (Schladow, 1992; Wüest et al., 1992; Lemckert and Imberger, 1993; DeMoyer et al., 2003; Sahoo and Luketina, 2006);

- as "pneumatic oil barriers" in order to produce barriers against crude oil spreading across a water surface and to protect coastal habitats against damage from oil (Fanneløp, 1994);
- as inhibitors of ice formation in lakes and harbour basin (Eidnes, 2004);
- as breakwaters for the protection of coastal or offshore structures from an occasional storm or against high amplitude waves (Taylor, 1955; Bulson, 1963; 1968);
- to deflect large drifting objects (icebergs, ships out of control) away from vulnerable structures, such as oil and gas production platform (Riess and Fanneløp, 1995);
- to vent steam, non-condensable gases, and aerosol mixtures into water pools in nuclear power plants and chemical reactors (Smith, 1998);
- in harbour entrances to prevent salt water intrusion (Nakai and Arita, 2002);
- as fish barriers to stop the spread of invasive species in estuaries (Sager et al., 1987; Welton et al., 2002);
- as an artificial aeration in ice-covered rivers (Neto et al., 2007);
- to influence hydrodynamics in open-channel bends (Blanckaert et al., 2008). Preliminary experiments and numerical modeling have been performed and are presented in Section 2.3.

2.3 PRELIMINARY EXPERIMENTAL AND NUMERICAL RESEARCH

2.3.1 Preliminary experimental research

The potential of a bubble screen to modify bend flow patterns has been previously investigated by Blanckaert et al. (2008). Laboratory experiments were performed in a sharply curved flume (Figure 2.6) with a fixed horizontal bed, with and without a bubble screen, that originates from a porous tube located on the bed near the outer bank.

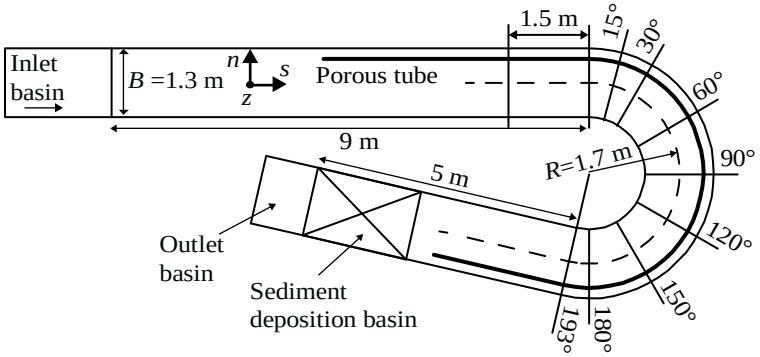

Figure 2.6: Experimental setup and reference system of the preliminary experiments

Table 2.1 summarizes the hydraulic and geometric conditions of the two experiments. The bed and the outer bank were composed of glued quasi-uniform sediments with a mean diameter d_m = 0.002 m. A streamwise bed slope of 0.22% was installed in the upstream straight flow reach, and the bed was horizontal in the rest of the flume. In the experiment performed with the bubble screen, the porous tube was placed at 0.2 m from the outer bank from the bend entry to the bend exit.

A curvilinear reference system (*s*, *n*, *z*) is adopted where the streamwise *s*-axis coincides with the flume's centerline, the transverse *n*-axis points in the outward direction and the vertical *z*-axis in the upward direction. Mean velocity vector on an entire profile, with its three components (v_s, v_n, v_z), was measured by means of an Acoustic Doppler Velocity Profiler (more details in Section 3.2.1) in the upstream straight reach (s = 1.5 m before the bend entry) and in the cross-sections at θ = [15, 30, 60, 90, 120, 150, 180]° in the bend (Figure 2.6).

Table 2.1: Experimental conditions of the fixed horizontal bed experiments

Label*	Q [$m^3\ s^{-1}$]	H [m]	U [$m\ s^{-1}$]	Fr [-]	q_a [$dm^3\ s^{-1}\ m^{-1}$]	R/B [-]	R/H [-]	B/H [-]
CF89_FH_NB	0.089	0.16	0.43	0.35	-	1.31	10.7	8.2
CF89_FH_B	0.089	0.16	0.43	0.35	0.16	1.31	10.7	8.2

Q is the water discharge, H is the flume-averaged water depth, $U = Q/(BH)$ is the flume-averaged velocity, Fr is the Froude number and q_a is the air discharge per unit length of porous tube. *The first part of the experiments' labels refers to Curved Flow (CF) with the water discharge in [l s^{-1}], the second part experiments performed on Fixed Horizontal bed (FH), and the last part experiments without (NB) or with (B) the bubble screen.

Figure 2.7 illustrates the bubble-induced secondary flow generated by the bubble screen in a straight flow over fixed horizontal bed. This bubble-induced secondary flow occupies the entire water depth H, and has a width of about 4H. The streamwise velocity distribution is influenced by this additional secondary flow. Without the bubble screen, the streamwise velocity is uniformly distributed on the entire cross-section (Figure 2.7a). With the bubble screen, low velocities from near the bottom are advected by the rising velocities near the water surface and then shifted away by the surface current. As a result, the core of maximum streamwise velocities between n = 0 m and n = 0.45 m is not found near the water surface but at about mid-depth. As a result, the velocity gradients, shear stresses and turbulent kinetic energy are enhanced in the lower half of the water column. In an experiment with a mobile bed, this new velocity distribution is supposed to enhance the sediment transport and to modify the flat bed morphology.

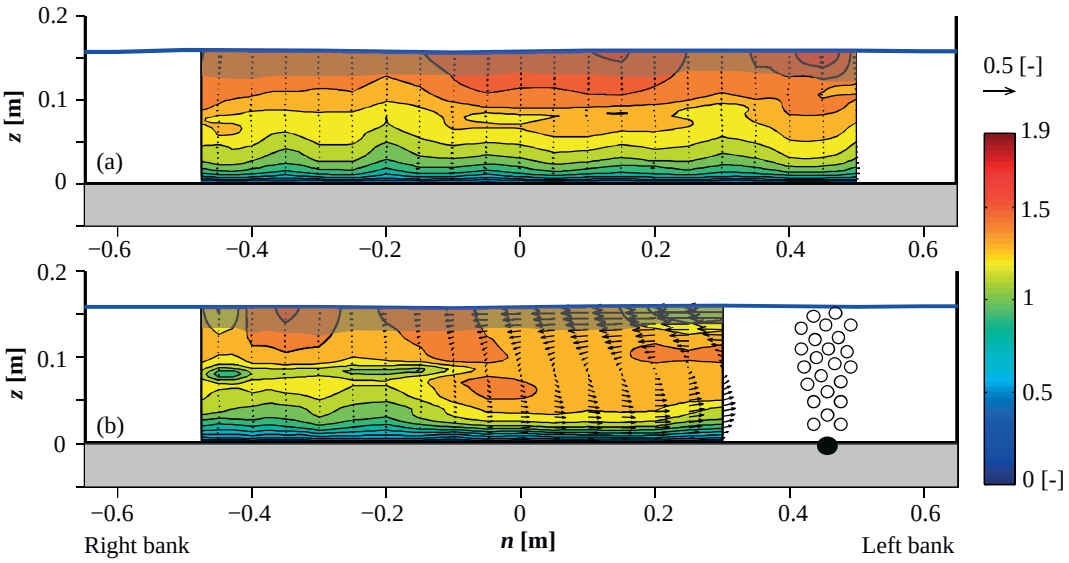

Figure 2.7: Mean normalized streamwise velocities v_s/U (contours) and normalized cross-sectional velocities $(v_n, v_z)/U$ (vectors) in a straight channel on a fixed horizontal bed for (a) a reference experiment without the bubble screen and (b) an experiment with the bubble screen. The shaded area near the water surface indicates extrapolated values. Experiments and analysis are reported by Blanckaert et al. (2008).

Figure 2.8 illustrates the velocity patterns in the cross-section at 90° in the bend for the reference experiment without the bubble screen (Figure 2.8a) and in an experiment with the bubble screen placed at 0.2 m from the outer bank (Figure 2.8b). Without the bubble screen, the curvature-induced secondary flow covers the entire width of the cross-section. In the presence of the bubble screen, the curvature-induced secondary flow is shifted in inward direction by the counter-rotating bubble-induced secondary flow which extends from n = 0 m to n = 0.45 m. The latter has comparable intensity and is only slightly smaller in size than in the straight uniform flow experiments under similar hydraulic conditions. The streamwise velocity distribution is also influenced by the presence of the bubble screen. Lower magnitude are observed in the region covered by the bubble-induced secondary flow. In a mobile-bed experiment, this redistribution should shift the scour zone from the outer bank to the center of the channel.

In both straight and curved open-channel flows, the bubble screen can generate a bubble-induced secondary flow that is able to redistribute the streamwise velocity patterns and to counteract the curvature-induced secondary flow in the case of a curved open-channel. Consequently, the bed shear stress patterns are also redistributed and would consequently modify bed morphology.

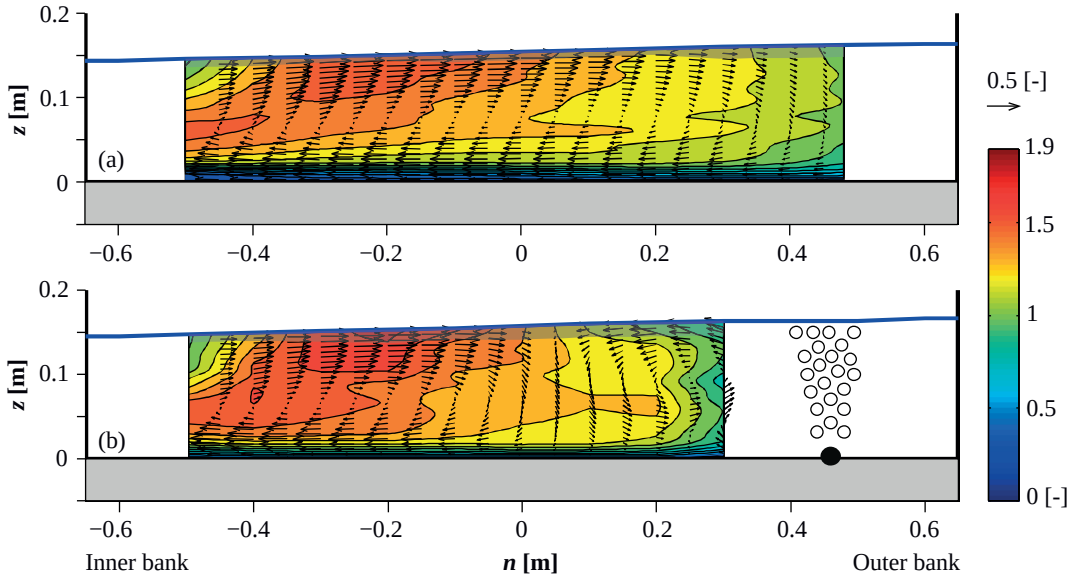

Figure 2.8: Mean normalized streamwise velocities v_s/U (contours) and normalized cross-sectional velocities $(v_n, v_z)/U$ (vectors) in a sharply curved channel on a fixed horizontal bed for (a) a reference experiment without bubble screen and (b) an experiment with the bubble screen. The shaded area near the water surface indicates extrapolated values. Experiments and analysis are reported by Blanckaert et al. (2008).

2.3.2 Preliminary numerical modeling

A numerical modeling of an air-bubble screen in flowing water has been performed with a Computational Fluid Dynamics (CFD) calculation using the commercial CFD-package ANSYS CFX (van Balen, 2007).

Simulations in straight and curved flows have been performed using the same geometries than in the preliminary experimental research. The numerical results were compared with data available from the experiments described in the above section 2.3.1. The bubble screen was introduced by means of a special continuous inlet strip of 4 mm width with volume fractions 0.2 (air) and 0.8 (water). From these standard values, several initial air conditions were tested and are summarized in Table 2.2.

Table 2.2: Boundary conditions at the air inlet, for several cases tested in the numerical modeling.

Case	Initial velocity	Air discharge	Distance from the outer bank
	[m s^{-1}]	*[dm^3 s^{-1}]*	*[m]*
CD-2a	0.3	3.48	0.2
CD-2b	0.6	6.95	0.2
CD-3b	0.3	3.62	0.1

A schematic comparison of the secondary flows obtained in the cross-section at 90° in the bend for the several investigated tests is drawn in Figure 2.9. Secondary flows measured in the experiment with the bubble screen are represented on the top. Secondary flows' strengths are represented by the ratio between the tangential velocity at the water surface and the flume-averaged longitudinal velocity U = 0.43 m s^{-1}.

Numerical results are in good agreement with experimental ones (Figure 2.9). Two recirculating cells can be observed with the bubble screen. Position and air flow rate are the most significant actors on the cell's range of influence. In the experiments as well as in the simulations, the two secondary flows (curvature and bubble-induced) have a comparable strength (40%). The simulation that most closely resembles experimental results is the simulation CD-2b where the sizes are the closest from those measured in the experiment. The size of the bubble-induced secondary flow varies from *H* for small air discharges to 2.3*H* for higher air discharges.

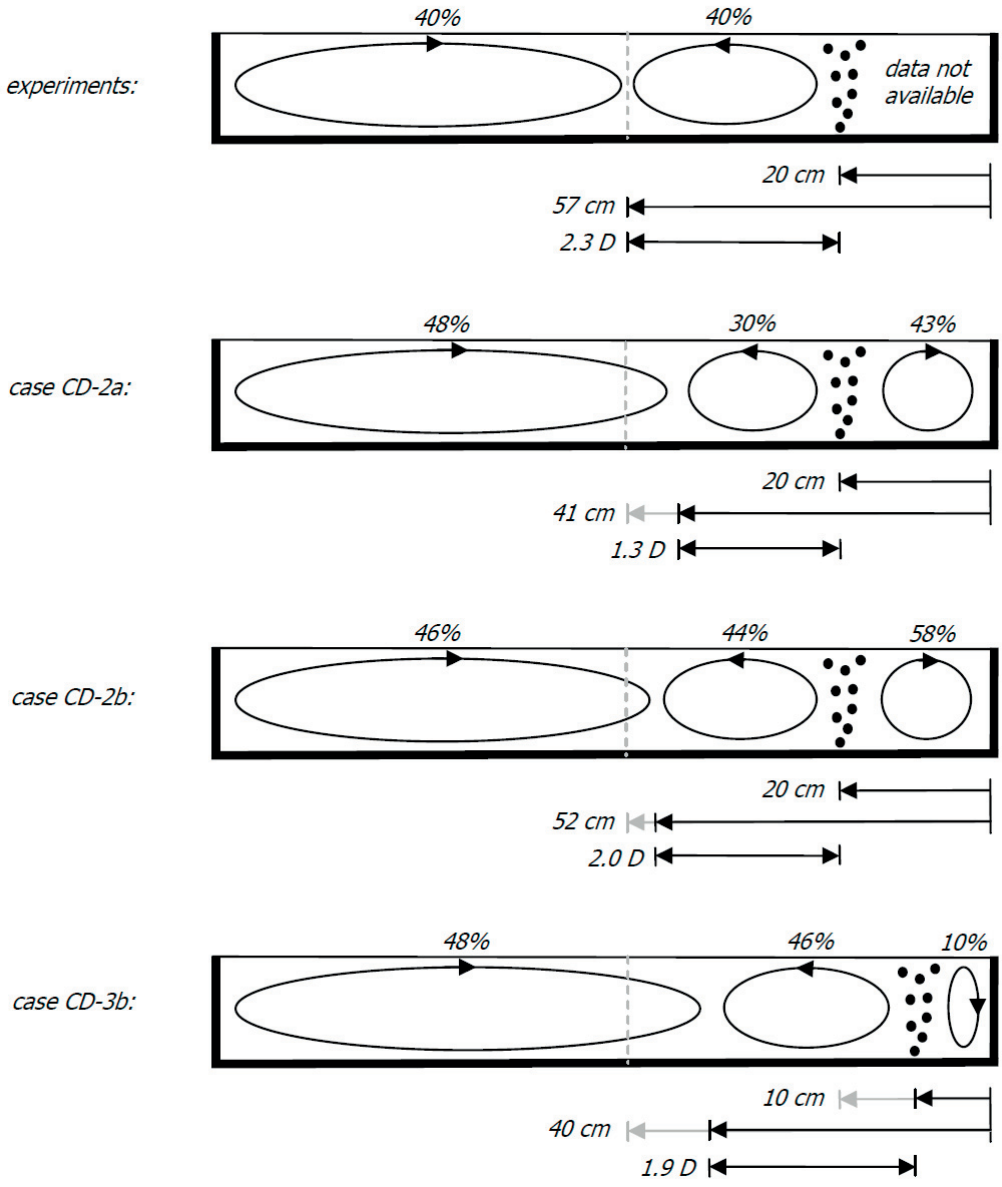

Figure 2.9: Schematisation of the numerical simulation results for several cases, in the cross-section at 90° in the bend. The percentages give the maximum fraction of the tangential velocity to the averaged streamwise velocity (van Balen, 2007).

Additional simulations were performed using several air-bubble screens and have shown that many lateral secondary flow cells developed: 4 and 6 secondary flows with 2 and 3 bubble

screens, respectively. These additional flow cells are expected to have negative effects on the bed morphology and to enhance erosion.

These preliminary simulations have shown the feasibility of the bubble-screen technique to redistribute bend flow patterns and the reproducibility of experimental results by means of numerical simulations. The latter represents a useful tool for testing different bubble-screen conditions before implementation in the field.

2.4 CONCLUDING REMARKS

From the review of the existing literature on the application of bubble plumes and screens, the following conclusions can be drawn:

- Several techniques to counteract the development of the bar-pool bed morphology in open-channel bends have been investigated and applied. All of these techniques are fixed constructions on the river bed which can represents a possible threat for shipping.
- Bubble plumes and screens have been extensively studied for large-scale environmental applications. Only few literature exists on their application in free-surface shallow flows. The remaining open discussion mainly concerns:
  - the effect of flow shallowness on the bubble-induced secondary flow;
  - the interaction between the river base flow, the bubble screen and the bubble-induced secondary flow.
- Finally, bubble screens have not yet been investigated nor applied in river morphodynamics. In order to estimate the potential of the bubble screen to be applied in rivers, better insight should be gained into:
  - the interaction between the bubble-induced flow structures and a mobile bed in straight and curved flow configurations;
  - the morphological development of open-channel bends with the bubble screen under both low-mobility and high-mobility conditions.

Chapter 3

Design of experiments

This chapter introduces experiments performed at the Laboratory of Hydraulic Constructions at the Ecole Polytechnique Fédérale de Lausanne (EPFL), Switzerland, in a sharply curved flume.

The experimental setup, already used in the frame of the research projects of Blanckaert (2002), and Duarte (2008), as well as in the preliminary experimental research on the application of bubble screen in open-channel bend (Blanckaert et al., 2008), is herein described. Sediment characteristics were uniform in all experiments, contrary to the bed and sediment transport conditions. The bubble screen was generated by means of a porous rubber tube, composed of lines of fine holes, placed on the channel bed and linked to an air compressor.

Several experiments were performed following a stepwise approach with an increasing degree of complexity. First, the bubble screen was tested under still water and straight flow conditions on a fixed horizontal bed. Then, interplay between the bubble screen, the base flow pattern and the bed morphology in straight flow under live-bed conditions was investigated. Finally, curved flow experiments were performed on a mobile bed under both clear-water scour and live-bed conditions.

In this chapter, the instrumentation and measurements are described. The principal measuring device was an Acoustic Doppler Velocity Profiler (ADVP), developed at EPFL, which measures simultaneously the three-dimensional velocity profile along an entire water column with high spatial and temporal resolution.

Detailed data on the 3D flow field and bed topography were collected, which can be used for the validation of numerical models. Major results are described in Chapters 4 to 7 and all results of ADVP measurements are provided in the Appendixes.

3.1 EXPERIMENTAL SET-UP

3.1.1 Straight and curved laboratory open-channel

Experiments were performed in a sharply curved laboratory flume at the Ecole Polytechnique Fédérale de Lausanne (EPFL) in Switzerland (Figure 3.1). This flume had vertical PVC sidewalls and a constant width B = 1.3 m. From upstream to downstream, the flume was composed of a 2 m long inlet basin, followed by a 9 m long straight inflow reach, a 193° bend with a centerline radius of curvature R = 1.7 m (R/B = 1.31), and a 5 m long straight outflow reach which included a 2 m long sediment deposition basin, before the outlet basin. The overall length of the flume is 22.7 m along the centerline.

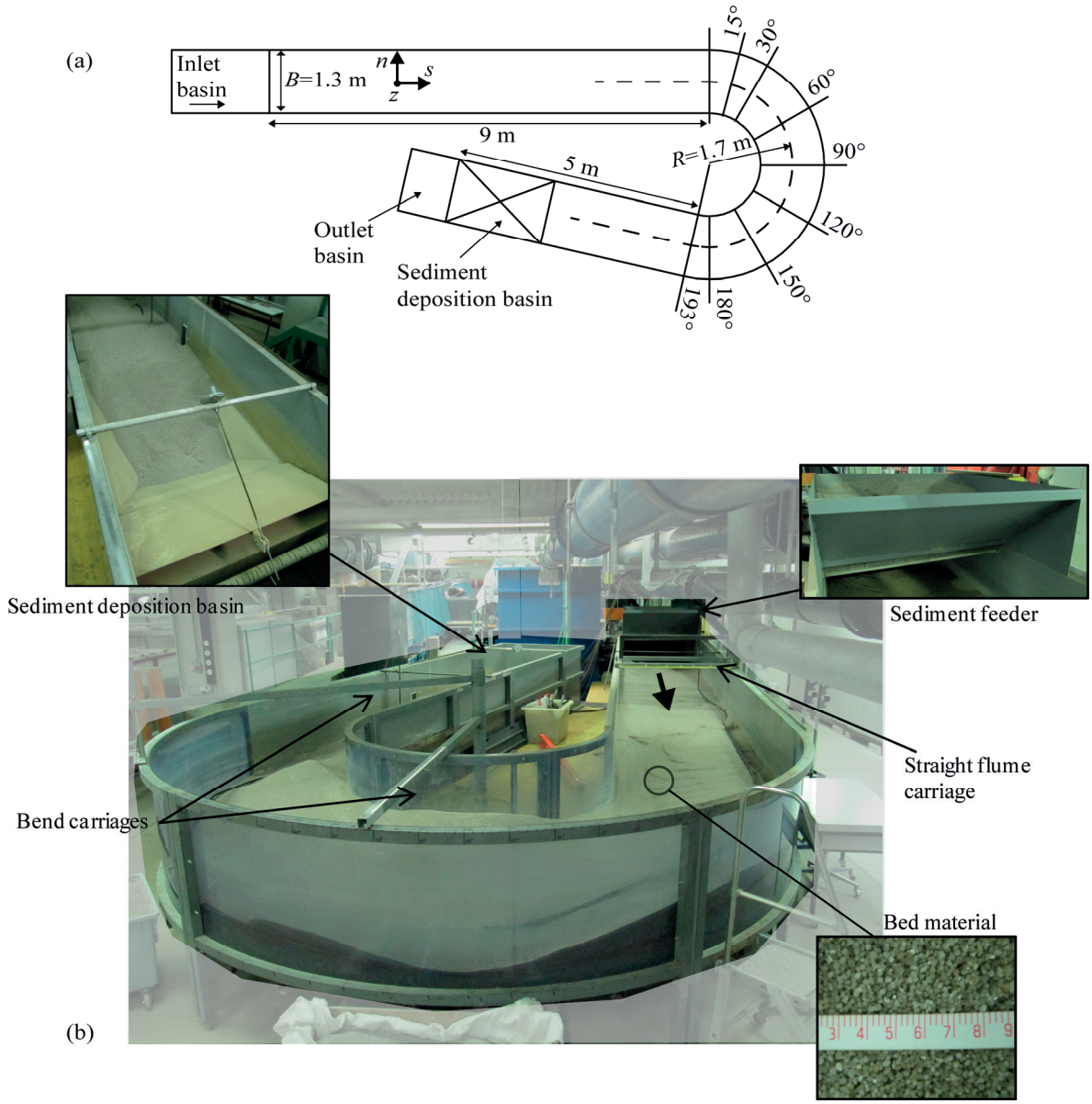

Figure 3.1: (a) Plan view of the curved laboratory flume, (b) pictures of the main components of the experimental setup.

The dimensions of the flume were chosen in order to optimize the measurements performed with the Acoustic Doppler Velocity Profiler (Section 3.2.1) as well as to amplify the

generated flow structures. The flume has already been used for the PhD research projects of Blanckaert (2002) on secondary flows in sharp open-channel bends and Duarte (2008) on the influence of the bank geometry and roughness on the outer bank cell. The preliminary experiments with the bubble screen, introduced in Section 2.3.1, have been also performed in this flume on a fixed horizontal bed (Blanckaert et al., 2008).

A curvilinear reference system (s, n, z) was adopted where the s-axis represents the streamwise direction, the transverse n-axis points in the outward direction and the vertical z-axis in the upward direction (Figure 3.1a).

Water discharge in the flow recirculation system was controlled by an automatically operated pump and valve. Water level in the channel was regulated with a gate, located after the sediment deposition basin.

Quartz sand of nearly uniform diameter 0.0016 m < d_m < 0.0022 m with a mean diameter of 0.002 m was used as bed material. When conducting experiments with a mobile bottom, sediment was continuously fed into the flume near the entrance. Sediment fell from a funnel on a plate, and was moved into the flume by means of a back-and-forth moving scraper. The frequency of the scraper regulated the sediment discharge. Emptying of the deposition basin and filling of the feeder had to be done manually.

Measuring instruments can be mounted on three carriages. The carriage for the straight flow reaches was guided by a rail. The two bend carriages pivoted around a pile placed in the center of curvature of the bend (Figure 3.1b).

The still water and straight flow conditions (Sections 3.3.1, 3.3.2 and 3.3.3) were investigated in the upstream straight reach of the flume whereas the curved flow experiments (Sections 3.3.4 and 3.3.5) were performed in the whole flume.

3.1.2 Bubble-screen implementation

The bubble screen was generated by means of a porous rubber tube, with an inner diameter of 0.01 m (high-pressure tube of porous rubber, Multivis Waterbehandeling B.V.), placed on the bed of the flume. It was ballasted with a chain submerged in the sand to impede its movements (Figure 3.2a), and connected at both ends to a pressurized air system to guarantee nearly the same air pressure over the entire length of the tube (Figure 3.2b). The porous tube was composed of aligned microscopic holes located on both sides of the diameter with a longitudinal spacing of 0.003 m.

The air pressure was regulated with a manometer (Figure 3.2c) and the air discharge measured with a rotameter (Figure 3.2d).

3.2 INSTRUMENTATION

3.2.1 Acoustic Doppler Velocity Profiler (ADVP)

Flow measurements in the curved open-channel were performed by means of an Acoustic Doppler Velocity Profiler (ADVP), developed at Ecole Polytechnique Fédérale de Lausanne (Figure 3.3a). The system consists of a central emitter, which periodically sends an acoustic

signal with a frequency of 1 MHz in the vertical downward direction. From the returning signal of four receivers surrounding the emitter, the mean velocity vector with its three components (v_s, v_n, v_z) can be obtained on an entire vertical profile at one go. Moreover, the ADVP provides a measurement of the bed elevation by means of the sonar-backscattered response. The working principle of the ADVP and its experimental uncertainty are reported in detail by Lemmin and Rolland (1997), Hurther and Lemmin (1998), Blanckaert and Lemmin (2006) and Blanckaert (2010).

The ADVP was placed in a box filled with water that touches the water surface by means of an acoustically transparent mylar film, allowing quasi non-intrusive measurements (Figure 3.3b). However, the housing involved flow perturbations near the water surface which can be bridged by means of extrapolations (Blanckaert, 2010).

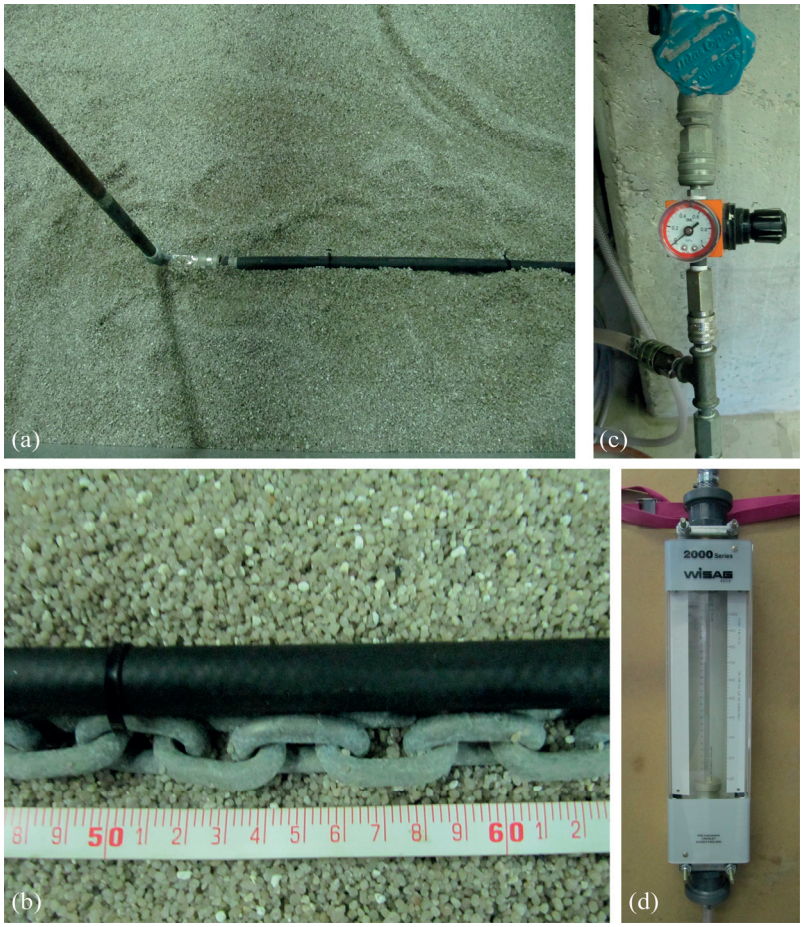

Figure 3.2: (a) Connection of the porous tube to the alimentation system, (b) porous tube ballasted with the chain, (c) manometer, and (d) rotameter.

The uncertainty in the streamwise velocity component v_x has been estimated at 4%, at 10% in the cross-stream velocities (v_y, v_z) and at less than 10% in depth-averaged mean velocities (Blanckaert, 2010).

The configuration used for the reported experiments was symmetrical (central emitter surrounded by the 4 receivers at an angle of 45° with respect to flow direction) (Blanckaert and Lemmin, 2006). This configuration allowed measurements only in the central part of the channel (n = –0.45 m to n = 0.45 m). Consequently, vertical profiles were measured in the

investigated cross-sections every 0.05 m in the range n = –0.45 m to n = 0.45 m in the reference experiments without bubble screen and in the range n = –0.45 m to n = 0.35 m when using the bubble screen (Figure 3.3b). Velocity measurements were not possible with the ADVP near the bubble screen because of interferences between air-bubbles and the ADVP's acoustic signal. Measurements were recorded with a sampling frequency of 31.25 Hz with a sampling period of 100 s.

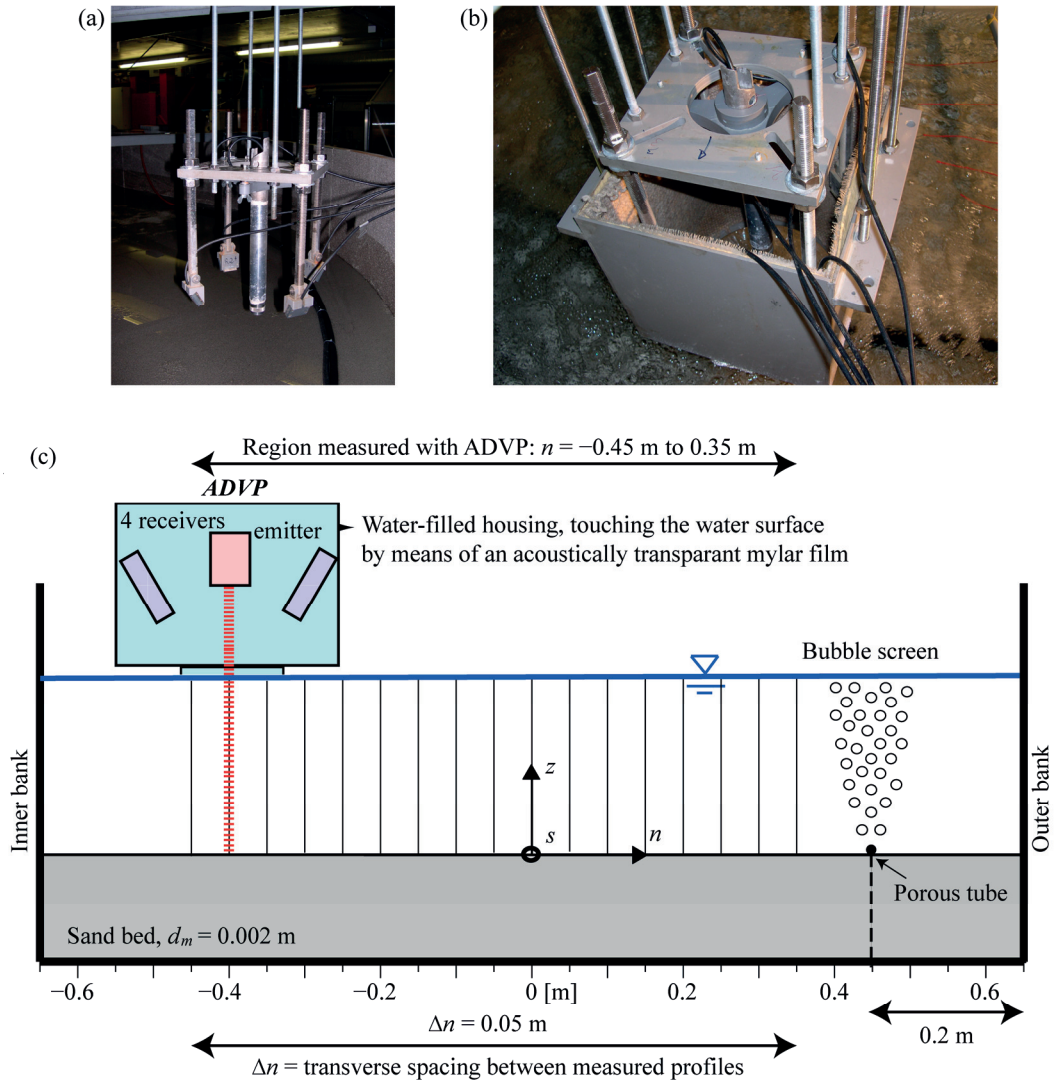

Figure 3.3: Acoustic Doppler Velocity Profiler (ADVP). (a) Central emitter and surrounding receivers, (b) ADVP in the water filled box and (c) measurement grid in one cross-section.

3.2.2 Water surface and bathymetry measurements

Bottom elevation was measured by laser altimetry (Distometer Leica) with a transverse spacing of 0.05 m. Additional values of the bed topography were obtained from the ADVP measurements. The water surface elevation was measured by means of a point gauge in the transverse positions n = [–0.6, –0.5, –0.3, –0.1, 0.1, 0.3, 0.5, 0.6] m. Both instruments were installed on a movable carriage that covered the width of the flume, along the flume.

Streamlines at the water surface were visualized with floating wool threads and photographs. Dune positions were documented by means of photographs.

3.3 TESTS PARAMETERS AND PROCEDURE

Experiments were performed using a stepwise approach with increasing degree of complexity. They can be classified in five different categories:

- Still water experiments;
- Straight flow experiments on an immobile bed;
- Straight flow experiments under live-bed conditions;
- Curved flow experiments under clear-water scour conditions;
- Curved flow experiments under live-bed conditions;
- Additional curved flow experiments on the optimal location of the bubble screen under live-bed conditions.

Experimental procedures involved, in most of cases, reference experiments without bubble screen and bubble-screen experiments performed with the bubble screen.

3.3.1 Still water experiments

The still water experiments were carried out in the upstream straight part of the curved open-channel. The flume was filled with water and closed at both ends and was used as a reservoir. The porous tube was located on the initially flat bed at 0.2 m from the left bank.

The ADVP requires a water depth larger than 0.1 m for high-quality measurements. In order to obtain results that are representative for shallow rivers, the experiments were designed to avoid interaction between the bubble-induced secondary flow and the opposite vertical sidewall. Since Blanckaert et al.'s (2008) experiments indicated that the transverse size of the bubble-induced secondary flow cell is about 4H, this defined the maximum allowable water depth in the experiments as (1.3 m − 0.2 m / 4) = 0.275 m. Based on these constraints, experiments were performed for three different water depths in the range H_w = 0.11 m to H_w = 0.21 m. For each water depth, two different air pressure conditions were investigated (Table 3.1). Velocity patterns were measured in the cross-section at −2 m before the bend entry.

Table 3.1: Experimental conditions for the still water experiments.

Label*	Q $[m^3 s^{-1}]$	H_w $[m]$	U_w $[m s^{-1}]$	Fr $[-]$	q_a $[dm^3 s^{-1} m^{-1}]$	B/H $[-]$
SW_11	0	0.11	0	0	0.18; 0.24	12.1
SW_16	0	0.16	0	0	0.18; 0.24	8.3
SW_21	0	0.21	0	0	0.18; 0.24	6.1

H_w is the cross-sectional averaged water depth and $U_w = Q/(BH_w)$ the cross-sectional averaged velocity. *The first part of the experiment's label refers to Still Water (SW) and the second number corresponds to the water depth [cm].

Results of still water experiments for an air discharge q_a = 0.24 dm^3 s^{-1} m^{-1} are described and analyzed in Chapter 4. Results of experiments performed with both q_a = 0.18 dm^3 s^{-1} m^{-1} and q_a = 0.24 dm^3 s^{-1} m^{-1} are presented in Appendix A.

3.3.2 Straight flow experiments on an immobile bed

Straight flow experiments were performed in the upstream straight part of the flume, on a mobile bed. The water depth was controlled with the downstream flap gate. According to Shields condition, streamwise velocities were not sufficient to initiate bed-load transport. Three different flow depths, similar to those chosen for the still water experiments (Section 3.3.1), were investigated and the air pressure applied to the porous tube has been kept constant at P_a = 600 kPa. Consequently, the air discharge is constant for all experiments. Hydraulic parameters are summarized in Table 3.2.

Table 3.2: Experimental parameters for the straight flow experiments on an immobile bed.

Label*	Q [m^3 s^{-1}]	H_w [m]	U_w [m s^{-1}]	Fr [-]	q_a [dm^3 s^{-1} m^{-1}]	B/H [-]
SF_11_1	0.013	0.11	0.09	0.09	0.24	12.1
SF_11_2	0.026	0.11	0.19	0.18	0.24	12.1
SF_11_3	0.039	0.11	0.28	0.27	0.24	12.1
SF_16_1	0.019	0.16	0.09	0.08	0.24	8.2
SF_16_2	0.039	0.16	0.19	0.15	0.24	8.2
SF_16_3	0.058	0.16	0.28	0.23	0.24	8.2
SF_21_1	0.026	0.21	0.10	0.07	0.24	6.3
SF_21_2	0.052	0.21	0.19	0.13	0.24	6.3
SF_21_3	0.078	0.21	0.29	0.20	0.24	6.3

*The first part of the experiment's label refers to Straight Flow (SF); the second part indicates the water depth [cm] and the third part is an index pertaining to the mean flow velocity.

Results of straight water experiments on an immobile bed are described and analyzed in Chapter 4. Results of all straight flow experiments performed on an immobile bed are presented in Appendix B.

3.3.3 Straight flow experiments under live-bed conditions

An experiment was performed with the bubble screen in the upstream straight reach of the flume with a mobile bed under live-bed conditions. A constant sediment feeding of q_s = 0.025 kg m^{-1} s^{-1} was supplied at the flume entry and a streamwise velocity sufficient to transport the sediment as bed load was chosen. First, an experiment without bubble screen was run in order to obtain the initial reference bed level. Then, the bubble screen was installed at 0.2 m from the left bank from 5 m upstream of the bend entry to 2.5 m downstream of the bend exit. The experiment was performed using similar hydraulic and sediment conditions until the new morphological equilibrium was reached. Experimental parameters are summarized in Table 3.3.

Table 3.3: Experimental parameters for the straight flow experiments under live-bed conditions.

Label*	Q $[m^3 s^{-1}]$	H $[m]$	U $[m s^{-1}]$	Fr $[-]$	q_a $[dm^3 s^{-1} m^{-1}]$	B/H $[-]$
SF_LB_B	0.075	0.12	0.47	0.42	0.24	10.5

*The first part of the experiment's label refers to Straight Flow (SF), the second part Live Bed conditions (LB) and the last part indicates that a bubble screen was applied.

Results of straight flow experiments under live-bed conditions are described and analyzed in Chapter 4. Velocity profiles measured in all investigated cross-sections are presented in Appendix C.

3.3.4 Curved flow experiments under clear-water scour conditions

Two experiments under similar hydraulic and clear-water scour conditions were performed in the open-channel bend. Experimental parameters are summarized in Table 3.4.

For the experiment with the bubble screen, the porous tube was placed at 0.2 m from the outer bank. The bubble screen extended from 5 m upstream of the bend entry to 2.5 m downstream of the bend exit.

Table 3.4: Experimental parameters for the curved flow experiments under clear-water scour conditions.

Label*	Q $[m^3 s^{-1}]$	H $[m]$	U $[m s^{-1}]$	Fr $[-]$	q_a $[dm^3 s^{-1} m^{-1}]$	R/B $[-]$	R/H $[-]$	B/H $[-]$
CF57_CW_NB	0.057	0.142	0.31	0.26	-	1.31	11.9	9.1
CF55_CW_B	0.055	0.139	0.31	0.26	0.21	1.31	12.2	9.3

*The first part of the experiments' labels refers to Curved Flow (CF) with the water discharge in [l s^{-1}], the second part experiments performed under clear-water scour (CW) conditions, and the last part experiments without (NB) or with (B) the bubble screen.

Experiments were continued until morphological equilibrium was reached. It is well known that the temporal development of the bed morphology is asymptotic, with a fast initial development that subsequently continuously slows down, to become ultimately infinitesimally slow. The experiments were performed until all sediment transport vanished and the remaining evolution became infinitesimally slow, which occurs after about three weeks of continuous run.

Results of clear-water scour experiments are described and analyzed in Chapter 5 and compared with the other curved flow experiments in Chapter 7.

3.3.5 Curved flow experiments under live-bed conditions

Three experiments were performed under live-bed conditions in the whole flume. Two reference experiments were carried out without the bubble screen using two different water discharges. The last experiment was done under similar hydraulic and sediment conditions than the second reference experiment but with the presence of the bubble screen. Experimental parameters are summarized in Table 3.5.

Table 3.5: Experimental parameters for the curved flow experiments under live-bed conditions

Label*	Q $[m^3 s^{-1}]$	q_s $[kg\ m^{-1}s^{-1}]$	H $[m]$	U $[m\ s^{-1}]$	q_a $[dm^3 s^{-1} m^{-1}]$	R/B [-]	R/H [-]	B/H [-]
CF63_LB_NB	0.063	0.023	0.10	0.49	-	1.31	17.2	13.2
CF75_LB_NB	0.075	0.025	0.14	0.41	-	1.31	12.1	9.2
CF75_LB_B	0.075	0.025	0.14	0.41	0.24	1.31	12.1	9.2

*The first part of the experiments' labels refers to Curved Flow (CF) with the water discharge in [l s^{-1}], the second part experiments performed under live-bed (LB) conditions, and the last part experiments without (NB) or with (B) the bubble screen.

Experiments were continued until morphological equilibrium was reached when: (i) the rate of sediment fed to the flume was equal to the rate of sediment deposited in the downstream basin, (ii) the bed morphology remained stable, with the exception of migrating mesoscale bedforms (dunes).

Results of live-bed experiments are described and analyzed in Chapter 5 for CF63_LB_NB experiment and in Chapters 6 and 7 for CF75_LB_NB and CF75_LB_B experiments. Velocity patterns measured in the investigated cross-sections in CF75_LB_NB and CF75_LB_B experiments are presented in Appendix D for comparison.

3.3.6 Additional experiments on the optimal location of the bubble screen

Four experiments were performed under similar hydraulic, sediment and air conditions in order to determine the optimized position of the porous tube with the aim of maximizing the bubble-induced flow and morphology structures. Three different transverse positions of the porous tube from the outer bank were investigated and compared with a reference experiment without bubble screen CF63_LB_NB_{00}. The transverses distance between the outer bank and the porous tube are given in Table 3.6. Each test was performed under live-bed conditions with a constant sediment feeding (q_s = 0.025 kg s^{-1} m^{-1}). The bed was initially horizontal and all experiments were stopped after 7 hours of run. Experimental parameters are summarized in Table 3.6.

Table 3.6: Experimental parameters for the short-term experiments.

Label*	Q $[m^3 s^{-1}]$	H $[m]$	U $[m\ s^{-1}]$	Fr [-]	q_a $[dm^3 s^{-1} m^{-1}]$	d $[m]$	R/B [-]	R/H [-]	B/H [-]
CF63_LB_NB_{00}	0.063	0.11	0.46	0.45	-	-	1.31	16.2	12.3
CF63_LB_B_{10}	0.063	0.11	0.46	0.45	0.24	0.1	1.31	16.2	12.3
CF63_LB_B_{20}	0.063	0.11	0.46	0.45	0.24	0.2	1.31	16.2	12.3
CF63_LB_B_{30}	0.063	0.11	0.46	0.45	0.24	0.3	1.31	16.2	12.3

*The first part of the experiments' label refers to Curved Flow (CF) with the water discharge [l s^{-1}], the second part experiments performed under Live-Bed (LB) conditions, and the last part experiments without (NB) or with (B) the bubble screen. The subscript in the last four experiment gives the transverse distance between the porous tube and the outer bank [cm].

After 7h of run, the final bed morphology was measured on a refined grid using a laser distometer. Results of the short-term experiments are described and compared in Chapter 6.

Chapter 4

Influencing flow patterns and bed morphology in straight open-channels by means of a bubble screen

The ability of a bubble screen to redistribute the flow field and bed morphology in shallow rivers and open-channels has been investigated in laboratory experiments. Rising air bubbles generated by a pressurized porous tube situated on the bed induced secondary flow perpendicular to the porous tube. The secondary flow redistributed the longitudinal velocity, which caused also morphological redistribution under mobile-bed conditions. The strength and size of the bubble-induced secondary flow were independent of the base flow velocity and increased with water depth. The size of the secondary flow cell ranged from 3 (immobile bed) to 7 (mobile bed) times the water depth. Similar sizes of bubble-induced secondary flow cells have been reported in literature for water depths ranging from 0.1 m to 5 m, indicating that the laboratory experiments are relevant for natural rivers and open-channels. A mutually strengthening interplay occurred between the bubble screen, the bubble-induced secondary flow, and the morphology. The bubble-induced secondary flow considerably increased the rising velocity of the air bubbles, which on its turn strengthened the secondary flow. The morphological redistribution increased on one hand the flow depth in the region covered by the secondary flow cell, which increased on the other hand the size and strength of the secondary flow cell, and its effect on the morphological redistribution. This coupled hydraulic-morphologic behaviour explains the larger size and strength of the secondary flow over a mobile bed than over a flat immobile bed. The results demonstrate the potential of the bubble screen as a technique to modify the morphology in a variety of applications in shallow rivers and open channels.

4.1 INTRODUCTION

Line plumes, curtains or screens of air bubbles are encountered in the management and engineering of water resources at different spatial scales. They have been widely used for promoting destratification and aeration in lakes (Schladow, 1992; Wüest et al., 1992), reservoirs (Sahoo and Luketina, 2006) or wastewater treatment systems (DeMoyer et al., 2003; Bombardelli et al., 2007) with the aim to improve water quality or to prevent growth of algae. Bubble curtains have been installed perpendicular to the base flow in harbour entrances to prevent salt water intrusion (Nakai and Arita, 2002), as fish barriers to stop the spread of invasive species in estuaries (Sager et al., 1987; Welton et al., 2002) or as an artificial aeration in ice-covered rivers (Neto et al., 2007).

Knowledge of the surrounding flow induced by the air bubbles is important for most applications, and has been largely studied (Figure 4.1b). According to Fanneløp et al. (1991), two regions of recirculating flow, called primary cells, are found on both sides of a line-source air-bubble plume in still-water conditions. Their size varies from 2.5 to 7 times the water depth independent of depth and air discharge, except at very low air discharges (Wen and Torrest, 1987; Riess and Fanneløp, 1998). The cores of the two cells, also called rotor cores, are located close to the plume, independently of the air discharge.

Only few studies have examined the effect of the channel geometrical parameters b, L, H (defined in Figure 4.1) on the characteristics of the bubble-induced secondary flow. Riess and Fanneløp (1998) determined that the length-to-depth ratio L/H is a characteristic parameter for the secondary flow in still-water conditions. If L/H is lower or higher than unity, the cell is rather small. The largest cell was found with a L/H ratio of unity. Experiments with different air discharges and water depths, but with the same L/H ratio, showed similar behaviour. The effect of boundary conditions in still-water conditions was also investigated by Neto et al. (2008) on a circular bubble plume, generated by a single-source nozzle. A large recirculating cell was generated in both square and rectangular tanks but strong 3D effects appeared in the latter due to the asymmetric configuration of the tank. In his confined setup, two secondary flows were observed in the vertical plane.

Nakai and Arita (2002) studied the application of an air curtain perpendicular to the base flow in rivers in order to prevent saline wedge intrusion. They observed that the characteristics of the bubble-induced flow patterns depend on the relative importance of the buoyancy of the air curtain A_b and the inertial force of the water flow R_w defined as below:

$$A_b = \left(q_a g\right)^{1/3} \tag{4.1}$$

$$R_w = \frac{q_f}{H} \tag{4.2}$$

where q_a is the air discharge per unit length of air-line source and q_f is the water discharge per unit width. If $A_b >> R_w$, convection by the base flow is weak and the bubble-induced vertical jet spreads to both sides of the air curtain near the water surface. If $A_b << R_w$, convection by the base flow is so strong that the bubble-induced vertical jet only spreads to the downstream side of the air curtain.

(a)

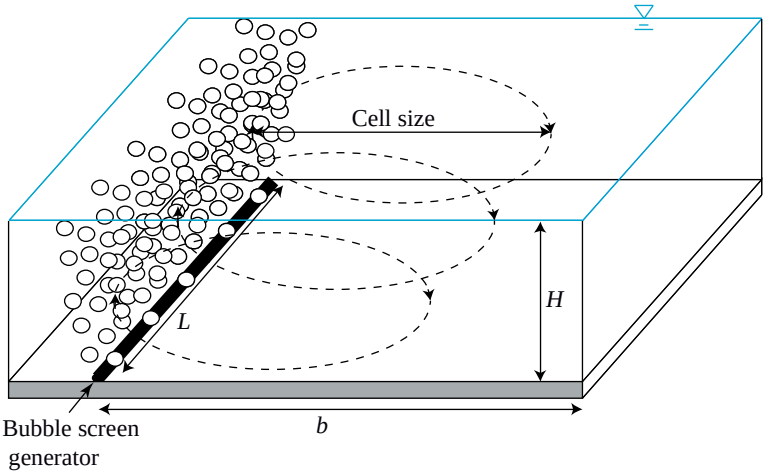

(b)

Reference	*b* [m]	*L* [m]	*H* [m]	*L/H* [-]	*b/H* [-]	Air source	q_a [$dm^3 s^{-1} m^{-1}$]	Flow conditions
[Wen and Torrest 1987]	2.4	0.3	0.6, 1.2	0.25, 0.5	4, 2	Perforated pipe and porous tube	0.68 - 11.52	Still water
[Fanneløp et al. 1991]	20	1	1	1	20	Steel perforated pipe	0.87 - 4.8	Still water
[Riess and Fanneløp 1998] Setup 1	20	1	0.5, 1	1, 2	20, 40	Steel perforated pipe	1 - 4.5	Still water
[Riess and Fanneløp 1998] Setup 2	20	0.5	0.5, 1	0.5, 1	20, 40	Steel perforated pipe	1 - 4.5	Still water
[Riess and Fanneløp 1998] Setup 3	20	0.25	0.5, 1	0.25, 0.5	20, 40	Steel perforated pipe	0 - 0.417	Still water
[Nakai and Arita 2002]	10.4	0.05	0.2	0.25	52	Perforated circular cylinder	0.028 - 0.042	Perpendicular flow
[Blanckaert et al. 2008]	1.1	6.5	0.159	40.88	6.92	Porous tube	0.059 - 0.277	Longitudinal flow

Figure 4.1: (a) Definition sketch of relevant parameters: *b* is the transverse distance between the air line-source and the opposite bank, *L* the length of the air line-source, *H* the water depth and q_a the air discharge per unit length of air line-source; (b) line-source bubble plume experiments listed in chronological order

Some recent investigations (Blanckaert et al., 2008; Dugué et al., 2011) aimed at extending the application range of bubble screens to shallow open-channels and rivers, in order to influence the flow field and to modify the morphology. Local scour, for example near bridge piers and abutments or in channel bends, is often caused by vertical velocities impinging on the channel bed. The rising air bubbles could counteract these downwards vertical velocities. Moreover, they induce secondary flow cells that are known to redistribute the patterns of velocity and boundary shear stress (Blanckaert and Graf, 2004).

Results from the previous investigations on bubble screens cannot straightforwardly be extended to their application parallel to the base flow direction in shallow rivers. The characteristics of the bubble-induced flow patterns can be expected to depend on the flow shallowness and on the velocity of the base flow. Moreover, in relatively narrow rivers, they can be expected to be influenced by the riverbanks. Recently, experiments performed in straight and curved shallow open-channel flumes on a fixed horizontal bed have shown that a longitudinal bubble screen, parallel to the flow direction, can generate a bubble-induced

secondary flow perpendicular to the bubble screen with a size of about 4 times the water depth, which causes a redistribution of the longitudinal velocity and of the boundary shear stress (Blanckaert et al., 2008). This size is in agreement with previous studies under still-water conditions (Wen and Torrest, 1987; Fanneløp et al., 1991). Similar experiments performed on a mobile bed under clear-water scour conditions have shown that this bubble-induced redistribution of the longitudinal velocity causes morphological changes (Dugué et al., 2011). These results suggest that bubble screens could represent a useful tool for influencing morphodynamics in shallow rivers. The advantages of this technique would be the reversibility and possible non-permanent use of the bubble screen in contrast to existing engineering techniques.

The objectives of the present paper is to extend the parameter space studied by Blanckaert et al. (2008) and to gain insight in the effect of bubble screens on the hydrodynamics and morphodynamics in shallow river configurations, by investigating:

- the effects of flow shallowness under still-water and flow conditions,
- the effects of the base flow velocity,
- the effects of mobile-bed conditions,
- the interplay between the air-bubble screen, the bubble-induced secondary flow, the patterns of longitudinal flow and the morphology.

It should be noted that the present investigation is limited to configurations with fixed sidewalls.

4.2 EXPERIMENTS AND MEASUREMENTS

4.2.1 Experimental set-up

Laboratory experiments were performed in a 9 m long straight open-channel at Ecole Polytechnique Fédérale de Lausanne (EPFL). The flume had a rectangular cross-section of constant width B = 1.3 m with smooth PVC vertical walls (Figure 4.2a). The bed was horizontal and covered with a quasi-uniform quartz sand with a mean diameter d_m = 0.002 m. An orthogonal Cartesian reference system (x, y, z) was adopted where the longitudinal x-axis coincides with the centreline of the flume, starts at the upstream extremity of the bubble screen and points in the downstream direction, the transversal y-axis points in the left-direction and the vertical z-axis upwards. This representation has been adopted in order to facilitate comparison with preliminary experiments performed in the same channel (Blanckaert et al., 2008; Blanckaert et al., 2010).

The bubble screen was generated by means of a porous tube of inner diameter 0.01 m (high-pressure tube of porous rubber, Multivis Waterbehandeling B. V.), installed on the bed at 0.2 m from the left bank parallel to the longitudinal direction of the flume. It was composed of fine holes located on both sides of the diameter, approximately 3 mm apart in longitudinal direction. The porous tube was installed from 4 m downstream of the flume entrance onto the

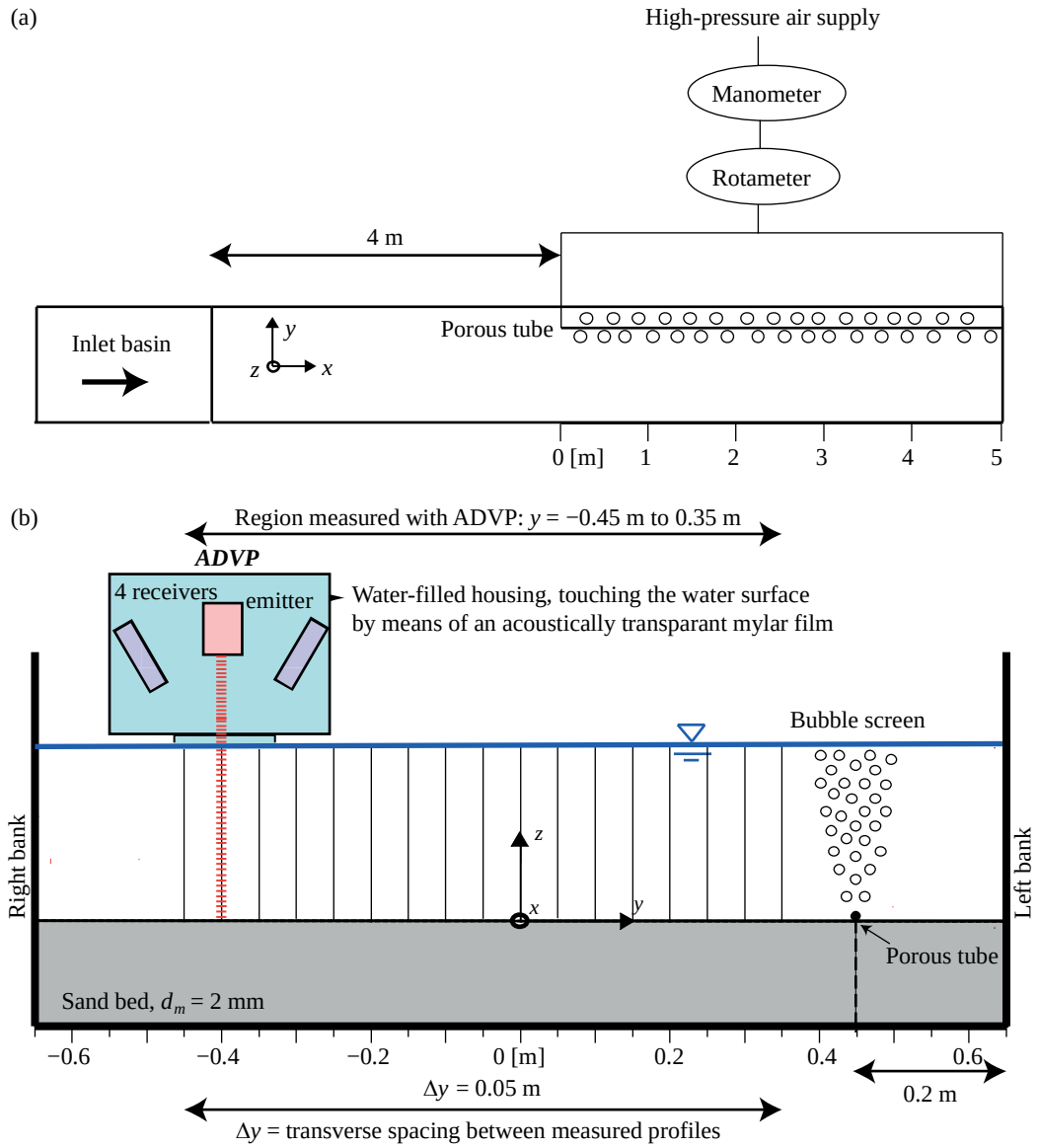

Figure 4.2: (a) Plan view of the channel with the porous tube installed on the bed, (b) Scheme of the velocity measurements performed in a cross-section with the Acoustic Doppler Velocity Profiler (ADVP).

flume exit and was ballasted on its whole length with a chain to avoid its movement. Air from the laboratory's high-pressure network was supplied at both ends of the porous tube to guarantee a quasi-constant pressure along its entire length. The pressure and air discharges were measured in the supply line with a manometer and a rotameter, respectively. The maximal air pressure tested by Blanckaert et al. (2008), P_a = 600 kPa, has been chosen and kept constant for all experiments, resulting in an air discharge per unit meter of porous tube length of about 0.24 $dm^3\ s^{-1}\ m^{-1}$.

4.2.2 Velocity measurements

Non-intrusive velocity measurements were performed with an Acoustic Doppler Velocity Profiler (ADVP), developed at EPFL (Lemmin and Rolland, 1997; Hurther and Lemmin, 1998; Blanckaert and Lemmin, 2006). The ADVP consists of a central emitter surrounded by four receivers, placed in a housing that touches the water surface. It measures the quasi-

instantaneous velocity vector simultaneously along the entire water column (Figure 4.2b). From these measurements, the time-averaged velocities in the three directions (v_x, v_y and v_z) are derived. The housing induces flow perturbations near the water surface, which can be bridged by means of extrapolations (Blanckaert, 2010). The uncertainty in the longitudinal velocity component v_x is estimated at about 4%, and in the secondary flow velocities (v_y, v_z), at about 10% (Blanckaert, 2010). Earlier experiments with bubble plumes (Milgram, 1983; Fanneløp et al., 1991) have shown that only long-time-averaged measurements give repeatable results. Therefore, the results presented herein represent 100 s averages.

4.2.3 Experimental conditions

The experiments were performed under three different conditions: (i) still water, (ii) flow on an immobile flat sand bed, (iii) flow on a mobile sand bed with active sediment transport. Table 4.1 shows the experimental parameters for all investigated conditions.

The ADVP velocimeter requires a water depth larger than 0.1 m for high-quality measurements. In order to obtain results that are representative for shallow natural rivers, the experiments were designed to avoid interaction between the bubble-induced secondary flow and the opposite vertical sidewall. Because Blanckaert et al.'s (2008) experiments indicated that the transverse size of the bubble-induced secondary flow cell is about 4*H*, this defined the maximum allowable water depth in the experiments as (1.3 m – 0.2 m) / 4 = 0.275 m. Based on these constraints, experiments were performed for water depths in the range between H = 0.11 m and H = 0.21 m.

Table 4.1: Experimental conditions.

Label*	Q $[m^3\ s^{-1}]$	H $[m]$	U $[m\ s^{-1}]$	Fr $[-]$	B/H $[-]$
SW_11	0.000	0.11	0.00	0.00	12.1
SW_16	0.000	0.16	0.00	0.00	8.3
SW_21	0.000	0.21	0.00	0.00	6.1
SF_11_1	0.013	0.11	0.09	0.09	12.1
SF_11_2	0.026	0.11	0.19	0.18	12.1
SF_11_3	0.039	0.11	0.28	0.27	12.1
SF_16_1	0.019	0.16	0.09	0.08	8.2
SF_16_2	0.039	0.16	0.19	0.15	8.2
SF_16_3	0.058	0.16	0.28	0.23	8.2
SF_21_1	0.026	0.21	0.10	0.07	6.3
SF_21_2	0.052	0.21	0.19	0.13	6.3
SF_21_3	0.078	0.21	0.29	0.20	6.3
SF_LB_B	0.075	0.12	0.47	0.42	10.5

Q is the water discharge, H is the cross-sectional averaged water depth, $U = Q/(BH)$ is the cross-sectional averaged velocity, and Fr is the Froude number. *The first part of the experiment's label refers to Still Water (SW) or Straight Flow (SF), LB is added for the Live-Bed experiment; the second part indicates the water depth [cm] and the third part an index pertaining to the mean flow velocity for straight flow experiments. The last part in the Live-Bed experiment indicates that a bubble screen was applied.

In the still-water experiments, the flume was filled with water and closed at both ends. In the straight flow experiments, the flow depth was controlled with a flap gate at the end of the channel. The base flow longitudinal velocities were chosen in order to avoid bed-load sediment transport. Velocity profiles were measured in the cross-section at x = 3 m downstream from the origin of the porous tube, on a grid with a transverse spacing of 0.05 m in the range y = –0.45 m to y = 0.45 m (Figure 4.2b). However, the presence of bubbles caused disturbances in the acoustic signal, leading to non-reliable measurements in the region y > 0.35 m. Water surface and bed elevations in the investigated cross-section were measured by means of a point gauge.

In the mobile-bed experiment, a constant sediment feeding of q_s = 0.025 kg m^{-1} s^{-1} was supplied at the flume entrance and a velocity was chosen that is sufficient to transport the sediment as bed load. First, an experiment without bubble screen was run in order to obtain the initial reference bed level. Then, the bubble screen was installed and the experiment was performed using similar hydraulic and sediment conditions until the new morphological equilibrium was reached. For this experiment, ADVP measurements were performed in six cross-sections at x = [2, 2.5, 3.0, 3.5, 4.0, 4.5] m downstream from the origin of the porous tube, on the same cross-sectional grid as in the immobile-bed experiments. The bed elevation was measured by means of a laser distometer on a grid with a longitudinal spacing of 0.1 m between x = 1 m and x = 5 m and a transverse spacing of 0.05 m. Water surface elevations were measured with a manual point gauge.

4.2.4 Method of analysis

In order to facilitate comparisons, the bubble-induced secondary flow will be visualized by means of the streamfunction ψ (Batchelor, 1967), defined as:

$$\psi = \frac{1}{2}\left(\psi_y + \psi_z\right) \tag{4.3}$$

$$\psi_y = -\int_{z_b}^{z} v_y dz \tag{4.4}$$

$$\psi_z = \int_{y_{\min}}^{y_{\max}} v_z dy + cste \tag{4.5}$$

in which z_b represents the bed elevation and the integration constant is chosen such that the cross-sectional averaged values of ψ_y and ψ_z are equal. y_{max} and y_{min} represent the transverse limits of the measuring grid in the considered cross-section. Similar to Blanckaert et al. (2008), the value ψ = –1 10^{-3} m^2 s^{-1} was adopted as a criterion to delimit the size of the bubble-induced secondary flow.

4.3 EXPERIMENTAL RESULTS

4.3.1 Effects of flow shallowness and base flow velocity on the bubble-induced secondary flow

These experiments aimed at analyzing the effects of the flow shallowness and the base flow velocity on the strength and size of the bubble-induced secondary flow. Furthermore, they aimed at providing reference data for comparison with the mobile-bed experiment. Experiments were conducted under both still-water and straight-flow conditions with three different water depths: H = 0.11 m, H = 0.16 m and H = 0.21 m (Table 4.1). For each water depth, experiments were performed with four different base flow velocities: U = 0 m s^{-1} (still-water condition), U = 0.09 m s^{-1}, U = 0.19 m s^{-1} and U = 0.28 m s^{-1} (Table 4.1). Figure 4.3 illustrates the bubble-induced secondary flow by means of the streamfunction ψ and the vector patterns of secondary flow (v_y, v_z) for experiments performed with the same base flow velocity U = 0.28 m s^{-1} at three different water depths.

The measured patterns show convincingly that the water depth controls the size and strength of the bubble-induced secondary flow, which increase with higher water depths. The bubble-induced secondary flow covers the region y = 0.13 m to y = 0.45 m (~ 3.0H), for H = 0.11 m (Figure 4.3a), the region y = –0.06 m to y = 0.45 m (~ 3.2H), for H = 0.16 m (Figure 4.3b), and it extends from y = –0.25 m to y = 0.45 m (~ 3.4H), for H = 0.21 m (Figure 4.3c).

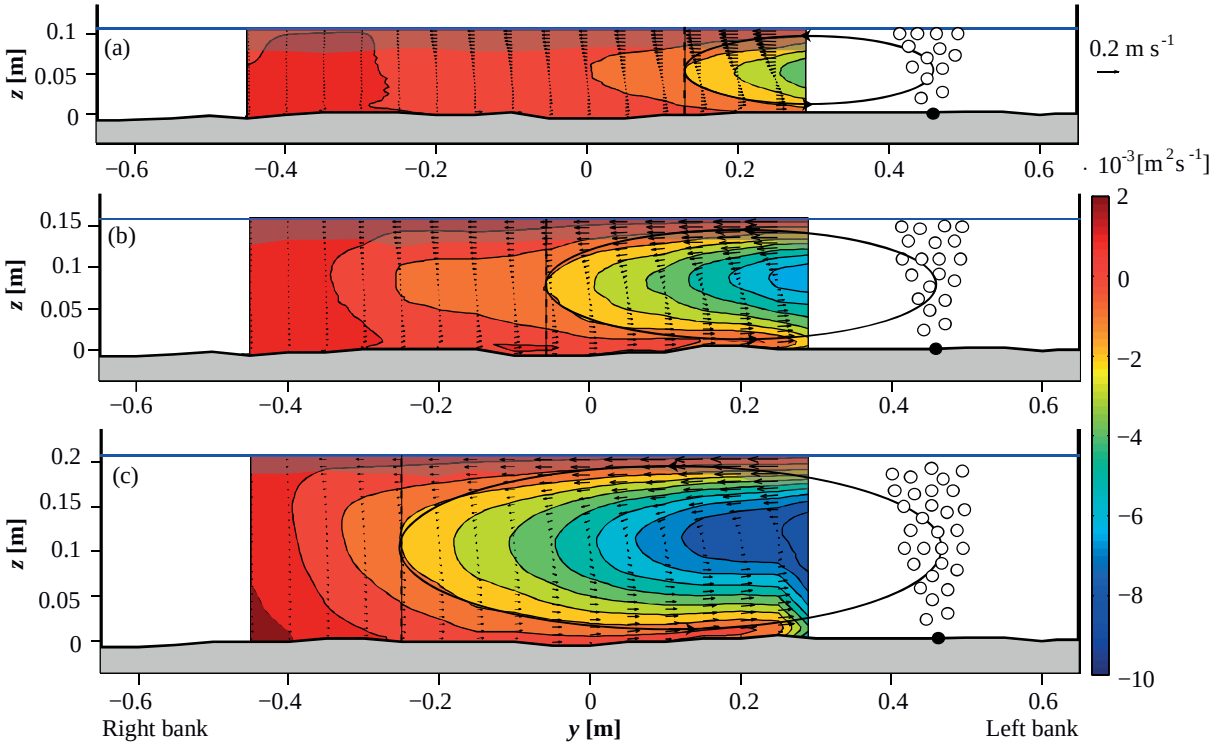

Figure 4.3: Cross-sectional patterns of bubble-induced secondary flow in the straight-flow experiments (Table 4.1): (a) SF_11_3, (b) SF_16_3, (c) SF_21_3. Streamfunction ψ 10^3 [m^2 s^{-1}] (colour isolines) and bubble-induced secondary flow (v_y, v_z) (vector representation). The shaded area near the water surface indicates extrapolated values. The dashed lines indicate the value ψ = –1 10^{-3} m^2 s^{-1} which is chosen as criterion to delimit the secondary flow cell.

These results are in line with previous studies performed under still-water conditions (Wen and Torrest, 1987; Fanneløp et al., 1991; Riess and Fanneløp, 1998) where the bubble-induced secondary flow size was found to be proportional to the water depth, and to have a size of 2.5H to 7H. In the three experiments, the core of the bubble-induced secondary flow is found near the bubble screen and amplifies with increasing water depth. The maximal intensity is found in the core of the bubble-induced secondary flow and increases with the water depth, with a value of ψ_m = –4.1 10^{-3} m^2 s^{-1} for H = 0.11 m (Figure 4.3a), ψ_m = –6.7 10^{-3} m^2 s^{-1} for H = 0.16 m (Figure 4.3b) and ψ_m = –8.8 10^{-3} m^2 s^{-1} for H = 0.21 m (Figure 4.3c).

Similar streamfunction patterns were obtained for all 12 experiments covering three flow depths, and four base flow conditions (Table 4.1) and the main results of all cases are summarized in Figure 4.4. For each of the investigated water depths, the secondary flow patterns are about identical for the four investigated base flow velocities, and the size of the bubble-induced secondary flow cell is not significantly influenced by the base flow velocity, and is consistently about 3.3 ± 0.04 times the water depth (Figure 4.4a). This means that the base flow parallel to the bubble screen is mainly advecting the bubble-induced secondary flow pattern in downstream direction without significantly modifying it. The increase of ψ with increasing water depth (Figure 4.3) was to be expected, because the definition of ψ includes integration with respect to the water depth (Equations (4.3), (4.4), (4.5)). The normalized streamfunction ψ/H provides a measure for the magnitude of the secondary flow vectors (v_y, v_z) in the bubble-induced secondary flow cell. Figure 4.4b shows that ψ_m/H is in all 12 experiments within the range –0.035 ± 0.010 m s^{-1}. The results suggest a slight increase in the amplitude of ψ_m/H with increasing water depth.

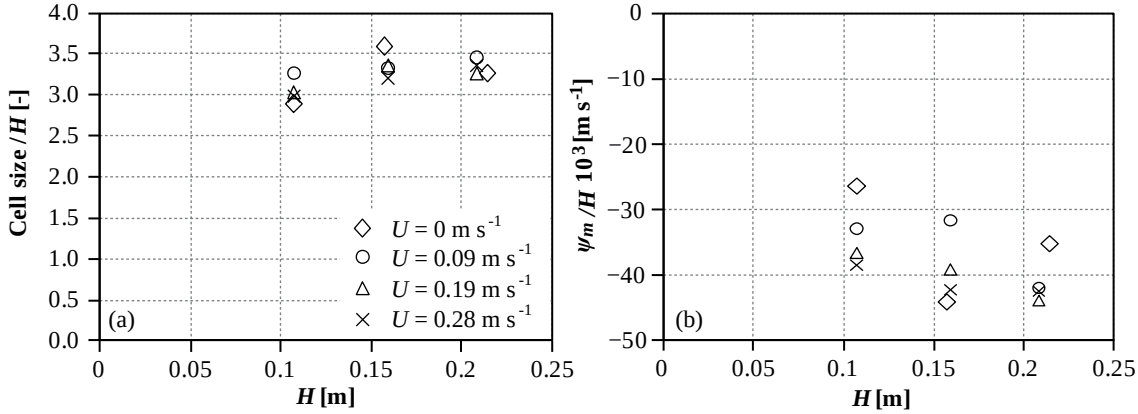

Figure 4.4: Dependence of characteristics of the bubble-induced secondary flow on the water depth H for the four different base flow velocity conditions. (a) Normalized size and (b) normalized maximal intensity ψ_m/H.

4.3.2 Interplay between the patterns of longitudinal flow and the bubble-induced secondary flow

The bubble-induced secondary flow advects momentum and thereby causes a redistribution of the pattern of longitudinal velocities. Figure 4.5 shows the patterns of the normalized longitudinal velocity v_x/U and the vector pattern of secondary flow (v_y, v_z) at three different

water depths with a base flow of U = 0.28 m s^{-1}. The corresponding patterns of the secondary flow streamfunctions are shown in Figure 4.3.

In all experiments, upwards velocities induced by the bubble screen are advecting low momentum fluid originating from the near-bottom zone towards the water surface. The high momentum fluid originating from near the water surface is advected by the bubble-induced secondary flow away from the bubble screen near the water surface leading to a core of maximum longitudinal velocities near the water surface at the outer edge of the bubble-induced secondary flow cell.

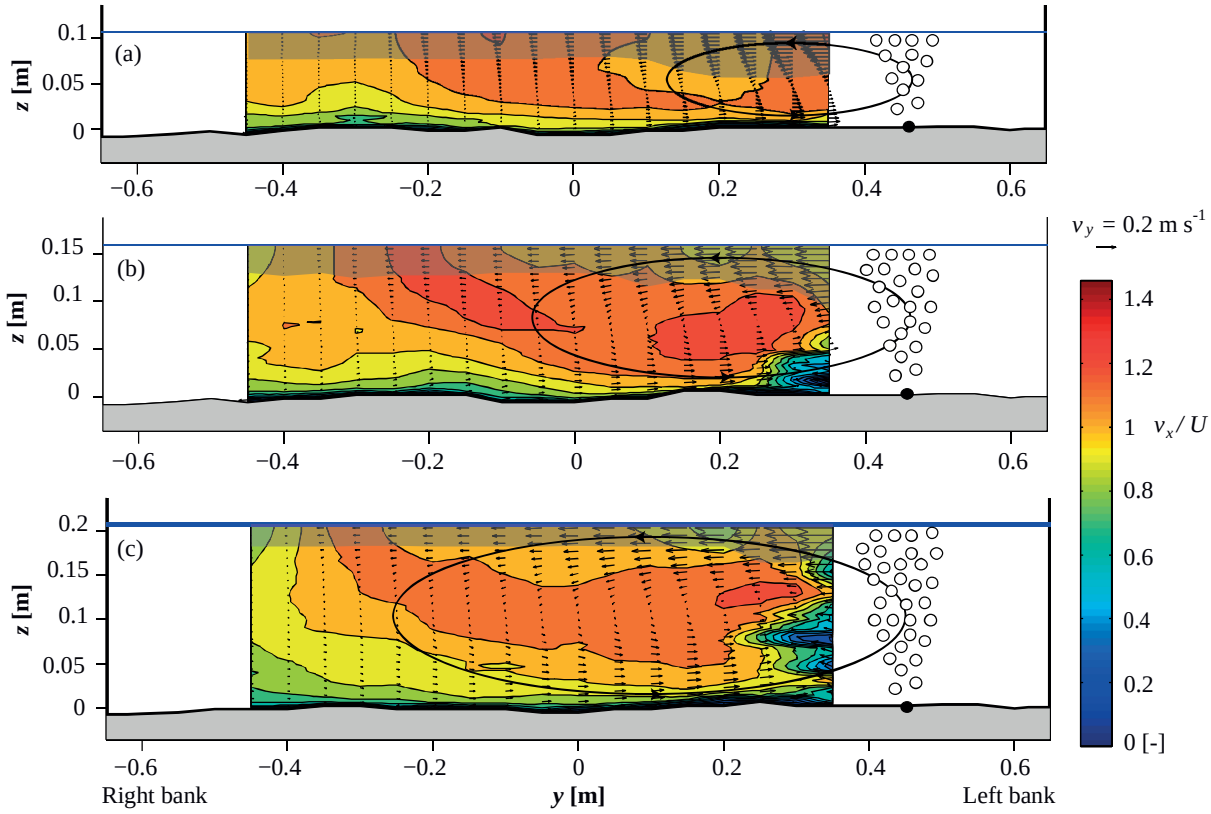

Figure 4.5: Influence of the bubble-induced secondary flow (v_y, v_z) (vector representation) on the normalized longitudinal velocity v_x/U (colour isolines) in the straight-flow experiments (Table 4.1): (a) SF_11_3, (b) SF_16_3 and (c) SF_21_3. The shaded area near the water surface indicates extrapolated values.

Advection by the secondary flow velocities extends the core of highest velocities towards the bubble screen at some distance under the water surface. Due to the combined effect of advection by secondary flow and bottom friction, the core of highest velocities is not found in the lower part of the water column, but at about mid-depth.

The results above (Section 4.3.1) have shown that the base flow velocity has no significant effect on the characteristics of the bubble-induced secondary flow. It can be expected, however, that the advective redistribution of the longitudinal velocities by the secondary flow depends on the base flow velocity. Figure 4.6 indicates qualitatively similar patterns for the three investigated base flows in the experiments with water depth of H = 0.11 m. Quantitatively, however, the resulting velocity gradients seem to be attenuated with increasing base flow. This can tentatively be attributed to an increase of the diffusive character of the flow with increasing base flow.

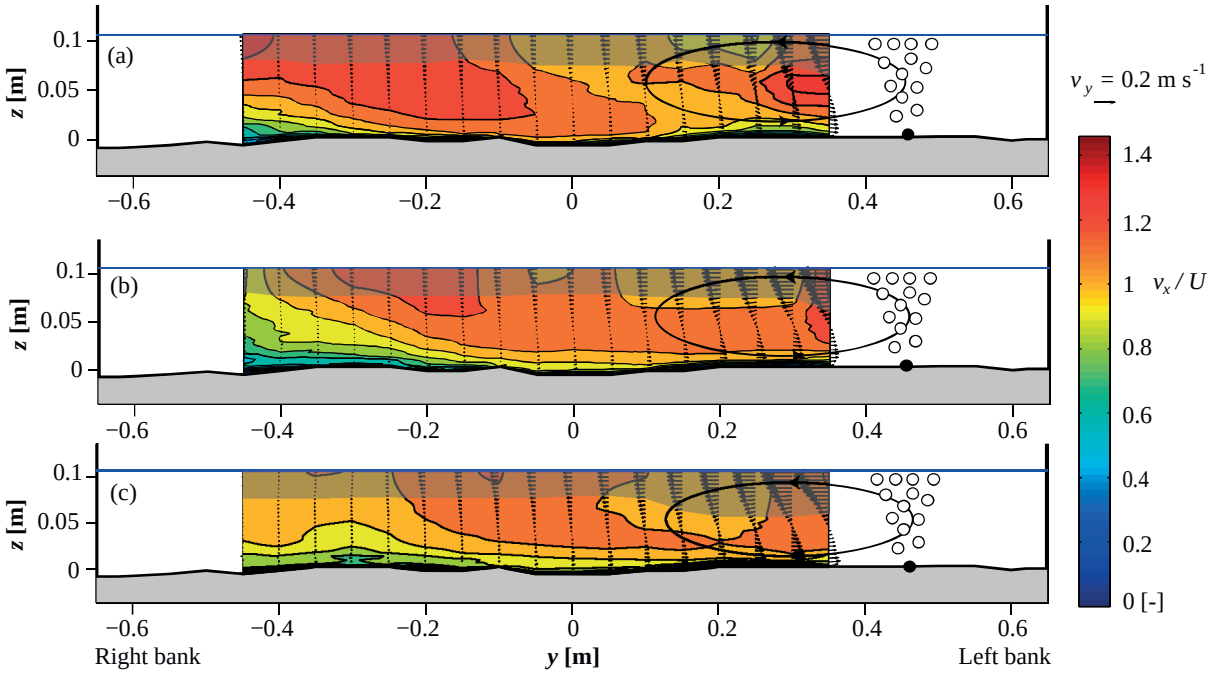

Figure 4.6: Influence of the bubble-induced secondary flow (v_y, v_z) (vector representation) on the normalized longitudinal velocity v_x/U (colour isolines) in the straight-flow experiments (Table 4.1): (a) SF_11_1, (b) SF_11_2 and (c) SF_11_3. The shaded area near the water surface indicates extrapolated values.

4.3.3 Interaction of the bubble-induced flow structures with the bed morphology, the base flow and the sediment transport

The bubble-induced secondary flow redistributes the velocities, and can therefore be expected to redistribute the sediment transport and modify the resulting bed morphology under mobile-bed conditions. Figure 4.7 illustrates the equilibrium morphology in the mobile-bed SF_LB_B experiment with bubble screen. The final channel-averaged bed level defines the reference level (z = 0 m). In the initial zone (x = 1 m to about x = 2.5 m), two scour holes form at each side of the bubble screen: one is situated at the toe of the bank adjacent to the bubble screen, and the other is located about 0.3 m away from the bubble screen. From about x = 2.5 m on, the right scour hole widens in downstream direction and moves away from the bubble screen, and it attains the right bank at the channel exit. Sediment scoured in both scour holes is transported towards the bubble screen by the bubble-induced secondary flow and leads to the development of a deposition bar centred on the porous tube.

This morphological development suggests that an interaction exists between the bubble-induced secondary flow, the base flow and the morphology, which seems to lead to a strengthening of the processes. Moreover, it suggests that a longer longitudinal distance is required under mobile-bed conditions than under immobile-bed conditions to attain equilibrium between the base flow, the bubble-induced secondary flow and the morphology.

In order to explain the influence of the bubble-induced secondary flow on the equilibrium morphology in the initial part of the channel, the streamfunction patterns measured in the SF_16_2 and SF_LB_B experiments are drawn in the same cross-section at x=3 m in Figure 4.8a and Figure 4.8b, respectively. In addition, Figure 4.8c shows the pattern

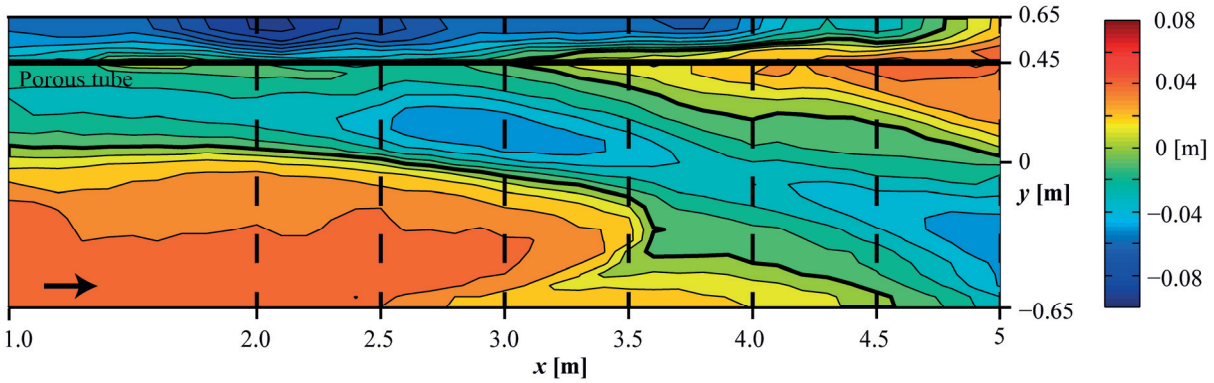

Figure 4.7: Isolines of the equilibrium bed level with an interval of 0.01 m derived from laser distometer measurements for the SF_LB_B experiment. The bold line represents the z = 0 m contour and delimits scour and deposition zones. The dashed lines indicate cross-sections where velocity measurements have been performed.

of longitudinal velocities in the SF_LB_B experiment in the same cross-section. The sizes of the secondary flow in the SF_16_2 and SF_LB_B experiments are similar, which indicates that the immobile-bed experiment may be representative for the initial conditions in the mobile-bed experiment when the morphological adjustment starts. However, the location of the maximal amplitude of the streamfunction is found farther from the bubble screen under mobile-bed conditions than under immobile bed which reveals a positive interaction with the bed morphology. Vertical downward velocities are about zero in the core of the bubble-induced secondary flow cell, and increase to their maximum value near the outer edge of the cell, where they impinge on the bed. As explained above, advective momentum transport by

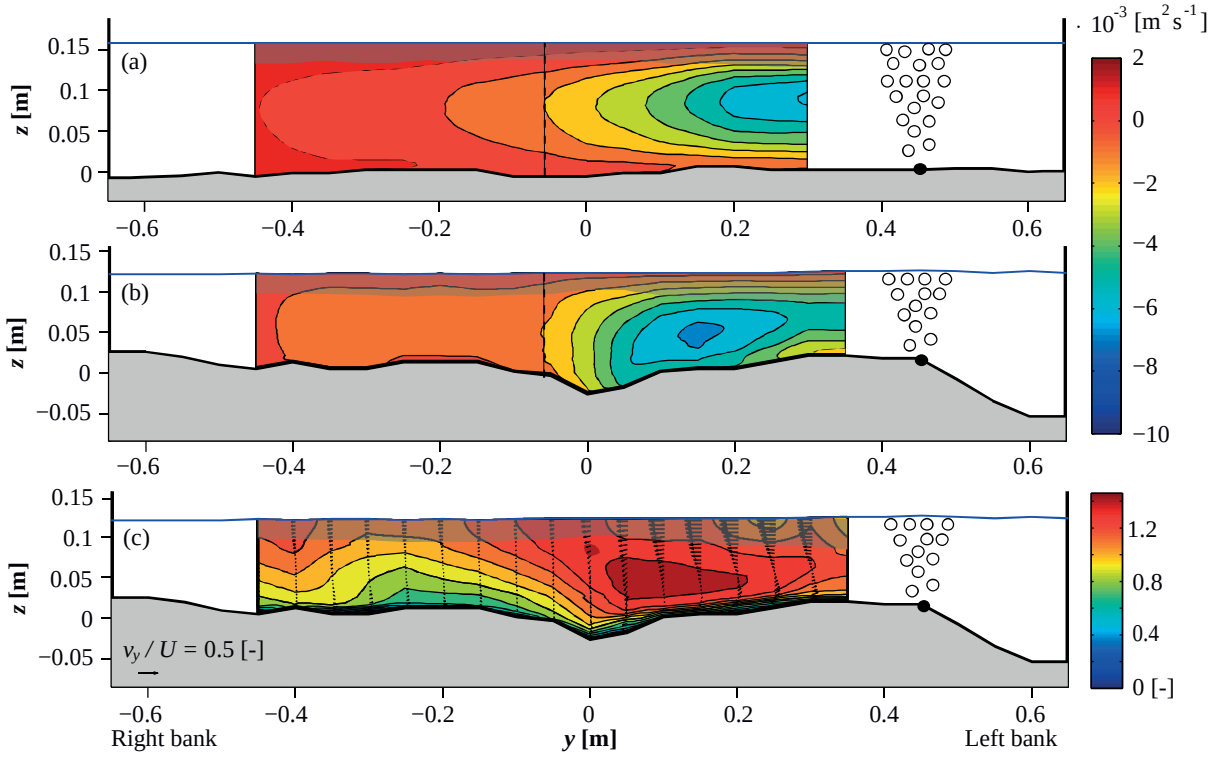

Figure 4.8: Bubble-induced secondary flow in the cross-section at x = 3 m for (a) the straight-flow experiment SF_16_2 and (b) the mobile-bed experiment SF_LB_B: Streamfunction ψ 10^{-3}[m^2 s^{-1}]. (c) Mean normalized longitudinal velocities v_x (contours) and cross-sectional velocities (v_y, v_z) (vectors) in the same cross-section for the SF_LB_B experiment. The shaded area near the water surface indicates extrapolated values.

the secondary flow redistributes the longitudinal velocity, and causes the core of maximum longitudinal velocities to be situated in the lower part of the water column in the region covered by the outer half of the secondary flow cell. This enhances the bed shear stress and the turbulence, and hence the sediment transport capacity. The vertical velocities impinging on the bed, and the redistribution of the longitudinal velocities explain the development of bed scour in the region covered by the outer half of the secondary flow cell. The transverse component of the secondary flow is directed away from the bubble screen over the entire flow depth, which concurs with the outwards shift of the scour hole farther downstream (Figure 4.7).

Figure 4.9 shows the patterns of the normalized longitudinal velocity and the bubble-induced secondary flow measured in three different cross-sections at x = 2.5, 3.5 and 4.5 m downstream from the beginning of the bubble screen. In each cross-section, scour occurs in the region covered by the outer half of the bubble-induced secondary flow cell, and the maximum scour occurs near the outer edge of the cell where vertical velocities impinge on the bed. In the three cross-sections, the transverse component of the secondary flow is directed away from the bubble screen over the entire flow depth, which concurs with the outwards shift of the scour hole farther downstream (Figure 4.7). At x = 2.5 m, the maximal scour is found at y = 0.15 m (Figure 4.9a), whereas it extends from y = 0 m to y = 0.2 m at x = 3.5 m (Figure 4.9b) to finally covers half of the cross-section from y = –0.4 m to y = 0.15 m at x = 4.5 m (Figure 4.9c).

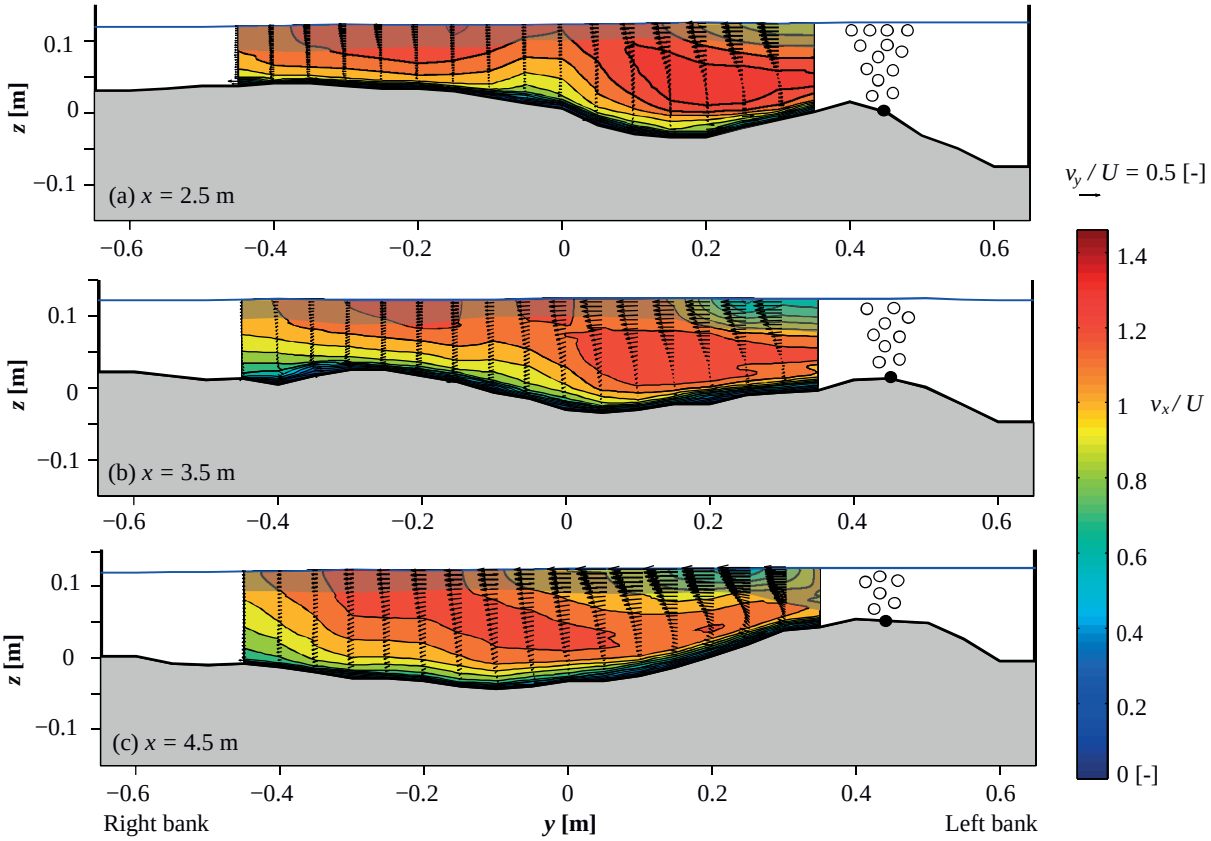

Figure 4.9: Mean normalized longitudinal velocities v_x (contours) and cross-sectional velocities (v_y, v_z) (vectors) at three measured cross-sections in SF_LB_B experiment. The shaded areas near the water surface indicates extrapolated values.

These results show a strengthening of processes. Scour extent as well as the bubble-induced secondary flow size widen with increasing x. Figure 4.10 summarized the longitudinal growth of the size and the strength of the bubble-induced secondary flow cell, both normalized with the flume-averaged flow depth. The secondary flow cell grows about linearly in longitudinal direction (Figure 4.10a) and almost reaches the right bank at the flume exit, where its size reached a maximum value of about 6.5H. At x = 3.5 m, topographic steering by a dune front in the right half of the cross-section causes some additional flow redistribution away from the bubble screen that contributes to the widening of the cell, and explains the maximum value of the cell size recorded in that cross-section. The strength of the bubble-induced secondary flow does not show a clear longitudinal evolution, and is characterized by values in the range $\psi_m/H = -0.075 \pm 0.025$ m s^{-1}. This is about twice the strength that was observed in the immobile-bed experiments.

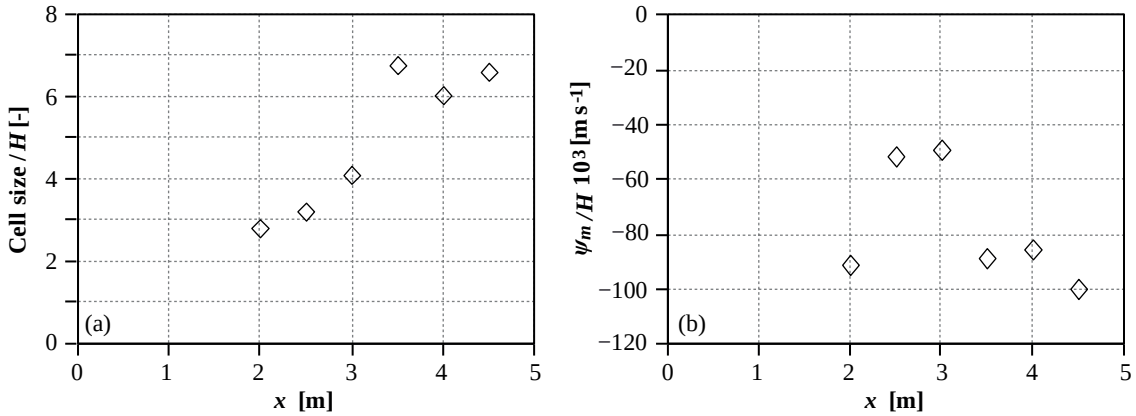

Figure 4.10: Longitudinal evolution of the bubble-induced secondary flow characteristics in the SF_LB_B mobile-bed experiment: (a) Normalized cell size and (b) normalized maximal intensity ψ_m/H. To be compared to Figure 4.4 for the immobile-bed experiments.

4.4 DISCUSSION

4.4.1 Interaction between the air-bubble screen, the bubble-induced secondary flow, and the morphology

The experimental observations indicate a mutually strengthening interaction between the air-bubble screen, the bubble-induced secondary flow, and the morphology.

A first mutually strengthening interplay exists between the rising air bubbles and the bubble-induced secondary flow cell. According to Leifer et al. (2000), the rising velocity of a single air bubble is approximately constant at $v_{z,bubble,0}$ = 0.24 m s^{-1} in the range of applied bubble sizes, independent of the flow depth. A bubble screen, however, entrains surrounding water and induces a secondary flow cell with maximum vertical flow velocities $v_{z,flow}$ situated in the vertical profile above the porous tube. These vertical flow velocities advect the rising air bubbles, and thereby increase the rising velocity of the air bubbles to:

$$v_{z,bubble} = v_{z,bubble,0} + v_{z,flow} \tag{4.6}$$

This increased rising speed can be expected to increase the quantity and the velocity of water entrained by the rising air bubbles, and hence to amplify the secondary flow cell. In first approximation, this mutually strengthening interaction can be quantified by expressing the efficiency of the rising air bubbles to entrain water as:

$$\eta = \frac{v_{z,\,flow}}{v_{z,bubble}} = \frac{v_{z,\,flow}}{v_{z,bubble,0} + v_{z,\,flow}} = 1 - \frac{v_{z,bubble,0}}{v_{z,bubble,0} + v_{z,\,flow}} \tag{4.7}$$

Equations (4.6) and (4.7) straightforwardly lead to:

$$v_{z,bubble} = \frac{v_{z,bubble,0}}{1-\eta} \tag{4.8}$$

Although no velocity measurements could be made in the region covered by the air-bubble screen, the final rising velocity of the air bubbles, $v_{z,bubble}$, and the water entrainment efficiency, η, can be estimated from the measured patterns of the transverse velocity v_y as follows. According to Wen and Torrest (1987), the vertical flow velocities above the porous tube are zero at the bed and the water surface, and reach a maximum value, $v_{z,flow,max}$, at about mid depth (Figure 4.11). Assuming then a parabolic velocity distribution over the depth, the depth-averaged vertical velocity, $v_{z,flow}$ equals two thirds of the maximum vertical velocity, $v_{z,flow,max}$. Mass conservation in the secondary flow cell relates $v_{z,flow,max}$ to the maximum transverse velocity near the water surface directed away from the bubble screen, $v_{y,max}$, which occurs at a distance of about *1H* away from the bubble screen (Figure 4.5, Figure 4.6, Figure 4.8, Figure 4.9), as schematically represented in Figure 4.11:

$$v_{y,\max}\frac{H}{2} = v_{z,\,flow,\max}H = \frac{3}{2}v_{z,\,flow}H \quad \text{or} \quad v_{z,\,flow} = \frac{1}{3}v_{y,\max} \tag{4.9}$$

leading to:

$$v_{z,bubble} = v_{z,bubble,0} + \frac{1}{3}v_{y,\max} \tag{4.10}$$

$$\eta = 1 - \frac{v_{z,bubble,0}}{v_{z,bubble,0} + (1/3)v_{y,\max}} \tag{4.11}$$

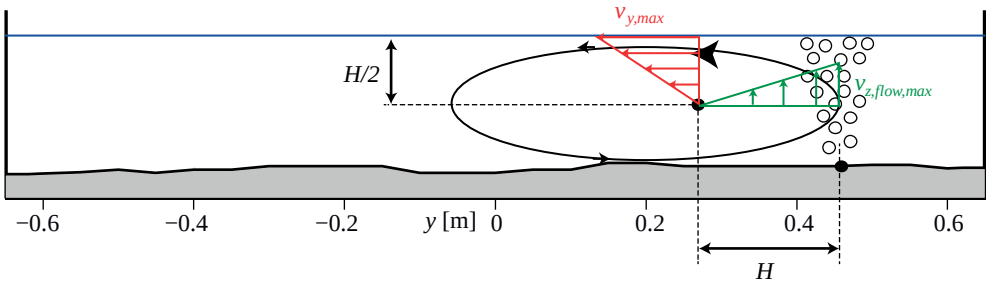

Figure 4.11: Schematical representation of the asymmetrical bubble-induced secondary flow cell, and the application of the principle of mass conservation to the secondary flow cell.

Based on the measured patterns of the transverse velocity v_y (Figure 4.5, Figure 4.6, Figure 4.8, Figure 4.9), both quantities have been estimated in the range $v_{z,bubble} = 0.33 \pm 0.04$ m s^{-1}, and $\eta = 0.25 \pm 0.08$ for all experiments (Figure 4.12). According to Equation (4.8), this means that the mutually strengthening interaction between the rising air bubbles and the bubble-induced secondary flow cell increased the rising speed of the bubbles by about 33%. The water depth and the base flow velocity did not considerably influence the water entrainment efficiency in the range of investigated depths. As expected, the water entrainment efficiency of the air bubbles was similar in the immobile-bed and mobile-bed experiments. The water entrainment efficiency can, however, be expected to depend on the air discharge, which was identical in all reported experiments.

A second mutually strengthening interplay exists between the bubble-induced secondary flow cell and the morphological redistribution. The morphological redistribution increases the flow depth in the region covered by the secondary flow cell, which increases the size and strength of the latter, because both were found to scale with the flow depth. This in turn, enhances the redistribution of the velocity and the bed shear stress, and hence the morphological redistribution. The larger normalized size and strength of the bubble-induced secondary flow cell in the mobile-bed configuration than in the immobile-bed configuration further confirms and illustrates this mutually strengthening interaction, which is favourable for the application of the bubble-screen technique with morphodynamic purposes in shallow rivers and open channels.

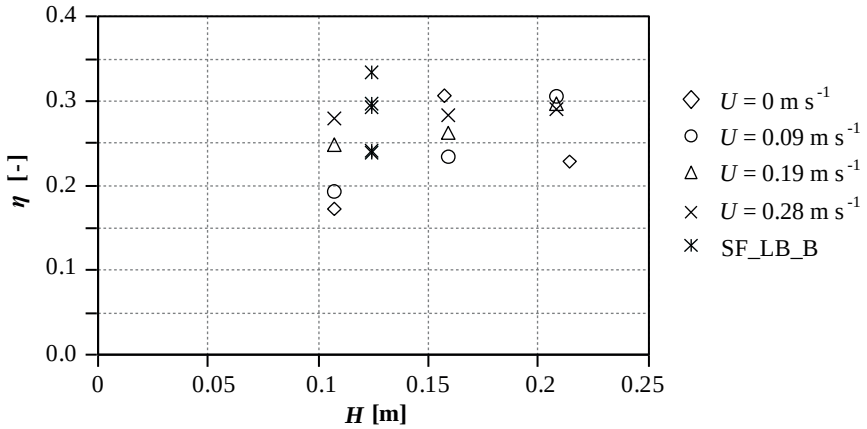

Figure 4.12: Dependence of the water entrainment efficiency η on the flow depth H for all investigated experimental conditions.

4.4.2 Relevance for application in natural rivers and open-channels

The reported experimental results convincingly demonstrate that the bubble screen can modify the flow patterns and the bed morphology in shallow laboratory open-channels. Hereafter, some further issues are discussed that need to be addressed before applications of the bubble-screen technique in shallow rivers or open-channels:

The reported experiments performed in a shallow flume with a maximal investigated water depth $H = 0.21$ m resulted in secondary flow cells with a size of 3 (immobile bed) to 7 (mobile bed) times the flow depth, independent of the base flow velocity and flow depth. The applicability of these experimental investigations to higher water depths typically encountered

in natural rivers or open-channels is of primary concern. Experiments performed under still-water conditions reported in literature (Figure 4.1b) have shown that the bubble-induced secondary flow size varies from 2.5 to 7 time the water depth, independent of the water depth (Riess and Fanneløp, 1998), whereby differences between results are mostly related to the different definitions of the bubble-induced secondary flow size or to the different geometries of experimental setups. Wen and Torrest (1987), for example, found a secondary flow cell size of 4*H* for water depths between 0.25 m and 0.9 m. Goossens (1979) performed experiments at small and large scales and found a range of influence of about 4 times the water depth, for water depths between 2 and 5 m. These results indicate that similar secondary flow cell sizes are found independently of the water depth and base flow velocity, and that the results obtained in the here reported laboratory experiments are relevant for natural rivers and open-channels.

Typical natural rivers at bankful flow have a width-to-depth ratio of the order of 20 (Blanckaert, 2011). With a size of 3 to 7 times the flow depth, the bubble-induced secondary flow is not constrained by the channel width, but can induce morphological changes in a substantial part of the channel cross-section.

In the mobile-bed experiment SF_LB_B (Figure 4.7), considerable scour occurred between the bubble screen and the adjacent bank. More research is required to investigate the flow field and its interaction with the morphology in this region, and possibly to optimize the position of the bubble screen relative to the bank. At present, application of the bubble-screen technique should be limited to configurations with fixed banks.

The bubble-screen technique has already shown promising results for an application in open-channel bends (Blanckaert et al., 2008; Dugué et al., 2011). However, the ability of the bubble screen to redistribute the bed morphology suggests that this technique has an application potential in a variety of configurations. For example, it could be used at the toe of bridge piers of abutments in order to counteract downwards velocities impinging on the bed and shift the scour location away from the structure. A fixed layer may be required in the narrow region between the bubble screen and the structure to avoid scour. A bubble screen could also be applied to avoid deposition in a determined zone of the riverbed, or to create preferential corridors for sediment transport. As an example, they could be used to prevent silting in harbours by "guiding" the mean longitudinal velocities and consequently the sediment-laden flows.

4.5 CONCLUSIONS

In the reported shallow-flow laboratory experiments, rising air bubbles generated by a pressurized porous tube situated on the bed entrained the surrounding water and induced secondary flow perpendicular to the porous tube. In the investigated range of conditions, the vertical velocity of the entrained water was about 25% of the rising velocity of the air bubbles, which defines the water entrainment efficiency. The bubble-induced secondary flow redistributed the pattern of the longitudinal velocity, which caused morphological redistribution under mobile-bed conditions.

The strength and size of the bubble-induced secondary flow were independent of the base flow velocity, which mainly advected the bubble-induced secondary flow downstream without modifying its characteristics. The size of the bubble-induced secondary flow cell ranged from 3 (immobile bed) to 7 (mobile bed) times the water depth, and also the strength primarily scaled with the water depth. Similar sizes of bubble-induced secondary flow cells have been reported in literature for water depths ranging from about 0.1 m to about 5 m. This indicates that the processes are not primarily scale dependent, and that the findings of the laboratory investigation are therefore relevant for natural rivers and open-channels.

A mutually strengthening interplay occurred between the bubble screen, the bubble-induced secondary flow and the morphology. Advection by the bubble-induced secondary flow considerably increased the rising velocity of the air bubbles (as compared to the rising velocity of a single air bubble), and hence also the rising velocity of the entrained water, which on its turn strengthened the bubble-induced secondary flow. The morphological redistribution increased the flow depth in the region covered by the bubble-induced secondary flow, which caused an increase in size and strength of the secondary flow cell. This in turn, enhanced the morphological redistribution. When scaled with the water depth, the size and strength of the bubble-induced secondary flow cell were larger in the mobile-bed configuration than in the immobile-bed configuration, which confirms and illustrates this coupled hydraulic-morphologic behaviour.

The results demonstrate the potential of the bubble-screen technique to modify the morphology in a variety of applications in shallow rivers and open channels.

Chapter 5

Reduction of bend scour under clear-water scour conditions with a bubble screen*

The interplay between streamwise flow, curvature-induced secondary flow, sediment transport and bed morphology leads to the formation of a typical bar-pool bed morphology in open-channel bends. The associated scour at the outer bank and deposition at the inner bank may endanger the outer bank's stability or reduce the navigable width of the channel. Previous preliminary laboratory experiments in a sharply curved flume with a fixed horizontal bed have shown that a bubble screen located near the outer bank can generate an additional secondary flow located between the outer bank and the curvature-induced secondary flow and with a sense of rotation opposite to the latter. This bubble-induced secondary flow redistributes velocities and bed shear stresses. The reported study investigates the implications of a bubble screen on the flow and the morphology in configurations with mobile bed. Velocity measurements show that the bubble-induced secondary flow shifts the curvature-induced secondary flow in inwards direction and reduces its strength. The bubble screen considerably reduces morphological gradients. Maximum bend scour is reduced by about 50% and occurs further away from the outer bank where it does not endanger the bank stability anymore. The location of maximum scour coincides with the junction of the curvature-induced and bubble-induced secondary flows. At this same location, the maximum streamwise velocities and maximum vertical velocities impinging on the bed also occur, which indicates their importance with respect to the formation of bend scour. The bubble screen also substantially reduced deposition at the inner bank. These preliminary experiments show the potential of a bubble screen to influence and modify the bed morphology.

* This chapter has been accepted for publication in *International Journal of Sediment Research*

5.1 INTRODUCTION

Low-gradient rivers often develop a meandering morphology, whereby each individual bend of the meander is characterized by a particular morphological profile. Outer banks are vulnerable to scouring, whereas deposition occurs near the inner bank. This so-called bar-pool morphology is related to the existence of a curvature-induced secondary flow, where secondary flow is defined as flow perpendicular to the streamwise axis. This secondary flow redistributes the velocities and the boundary shear stresses, and hence also the sediment transport and the morphology (Rozovskii, 1957; Blanckaert and de Vriend, 2003; 2004; Blanckaert and Graf, 2004; Blanckaert and de Vriend, 2010).

The formation of the typical bar-pool morphology in open-channel bends leads to adverse impacts, such as increased risk of erosion at the outer bank or reduced navigable width. Several techniques exist to reduce these adverse impacts, but they generally imply substantial constructive works. Techniques reported in literature include bottom vanes (Odgaard and Spoljaric, 1986; Odgaard and Wang, 1991), fixed layers (Roca et al., 2007), submerged groynes (Przedwojski, 1995; Fazli et al., 2008) and bandal-like structures (Teraguchi et al., 2011). However, these techniques have the disadvantage of being fixed constructions on the bed that represent a possible threat for navigation. This paper describes an innovative technique that consists in indirectly manipulating the morphology by provoking changes in the flow pattern.

Previous preliminary laboratory experiments in a sharply curved flume with a fixed horizontal bed have shown that a bubble screen, which originates from a porous tube located on the bed near the outer bank, can generate an additional secondary flow located between the outer bank and the curvature-induced secondary flow and with a sense of rotation opposite to the latter (Blanckaert et al., 2008). In these previous preliminary experiments, the additional bubble-induced secondary flow was efficient in redistributing velocities and boundary shear stresses. The cores of maximum descending vertical velocities and of maximum streamwise velocities, which are assumed to play an important role with respect to the development of the bend scour, were shifted away from the outer bank and situated at the junction of both secondary flows.

Contrary to "hard" engineering techniques, bubble screens have the advantage of being controllable, ecological (oxygenation), reversible and non-permanent. Bubble plumes and screens have already been applied in a wide range of applications, such as aeration and destratification of lakes and reservoirs (Schladow, 1992; Wüest et al., 1992), or venting of aerosol mixtures into water pools in nuclear power plants (Smith, 1998). However, bubble screens have not yet been investigated or applied in shallow river morphodynamics.

Following the promising results of the previous preliminary study over a fixed horizontal bed (Blanckaert et al., 2008), similar experiments with mobile bed have been performed with and without the bubble screen in order to understand its influence on the interplay between the morphology and the flow field. Morphologic and hydrodynamic comparisons are provided in this paper with the aim to answer the following questions:

- Can the bubble-screen technique be applied to manipulate the morphology in open-channel bends ?
- How does the bubble-induced secondary flow redistribute the velocities and the morphology ?

This paper briefly describes the laboratory flume and the experimental conditions, presents the results for the reference and bubble-screen experiments and discusses the impact of the bubble screen on the morphology and hydrodynamics of the bend.

5.2 EXPERIMENTS AND MEASUREMENTS

5.2.1 Experimental set-up

Experiments were performed in a sharply curved laboratory flume (Figure 5.1a) at the Ecole Polytechnique Fédérale de Lausanne (EPFL) in Switzerland. This flume has vertical PVC sidewalls and a width that is constant at B = 1.3 m. From upstream to downstream, the flume consists of a 9 m long straight inflow reach, a 193° bend with centerline radius of curvature R = 1.7 m, and a 5 m long straight outflow reach which includes a sediment deposition basin. The same flume was used in the previous preliminary experiments by Blanckaert et al. (2008) to investigate the influence of the bubble screen on the flow in a configuration with fixed horizontal bed.

Measurements will be reported in an orthogonal curvilinear (s, n, z) reference system, with downstream s-axis along the flume's centerline, transverse n-axis pointing outward, and upward vertical z-axis. Quartz sand of nearly uniform diameter 0.0016 m < d_m < 0.0022 m with a mean diameter of 0.002 m was used as bed material. When conducting experiments with sediment feeding, the same sand was continuously introduced near the flume entrance.

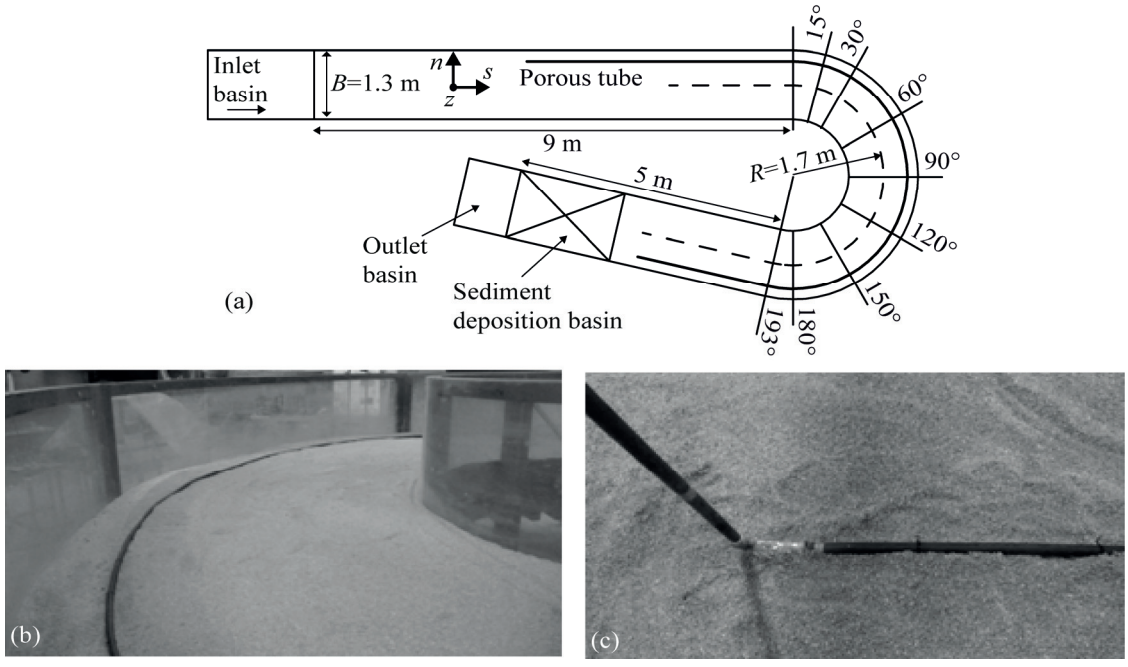

Figure 5.1: (a) Plan view of the curved flume with the porous tube. (b) and (c) Porous tube with the connection to the pressurized air system existing at the two sides of the tube.

A porous tube, with an inner diameter of 0.01 m (high-pressure tube of porous rubber, Multivis Waterbehandeling B.V.), placed on the bed of the flume generated the air-bubble screen. It was ballasted with a chain submerged in the sand to impede its movements, and connected at both ends to a pressurized air system to guarantee the same air pressure over the entire length of the tube (Figure 5.1b and Figure 5.1c). Microscopic holes in the tube were located on opposite sides of the diameter with a longitudinal spacing of 0.003 m. The size of the bubbles was estimate to vary between 0.002 m to 0.015 m, with an average diameter of about 0.005 m. The air pressure was regulated with a manometer and the air discharge measured with a rotameter. An air discharge of 0.21 $dm^3 s^{-1}$ per unit length of porous tube was applied. For experiments with a bubble screen, the porous tube was placed at 0.2 m from the outer bank. The bubble screen extended from 5 m upstream of the bend entry to 2.5 m downstream of the bend exit.

5.2.2 Velocity, water surface, and bathymetry measurements

Flow was measured with an Acoustic Doppler Velocity Profiler (ADVP) developed at EPFL. This non-intrusive instrument measures the quasi-instantaneous velocity vector simultaneously along an entire water column. From this measurement, the mean velocity vector with its three components (v_s, v_n, v_z) can be obtained. Moreover, the ADVP provides a measurement of the bed elevation. The working principle of the ADVP and its experimental uncertainty are reported in detail by Lemmin and Rolland (1997), Hurther and Lemmin (1998), Blanckaert and Lemmin (2006), and Blanckaert (2010). Detailed velocity measurements were only performed in the cross-section at 70° in the bend, where the bar-pool morphology is most pronounced (Figure 5.2). Because of interference of the air bubbles with the ADVP's acoustic signal, velocity measurements were not possible near the bubble screen. As a consequence, no velocities were measured between the porous tube and the outer bank.

The water surface was measured with a point gauge in the transverse positions n = [−0.62, −0.6, −0.5, −0.3, −0.1, 0.1, 0.3, 0.5, 0.6, 0.62] in 77 cross-sections situated between 5 m upstream of the bend in the straight inflow reach and 1.35 m downstream of the bend in the straight outflow reach. The bed morphology was measured with a laser distometer on a refined grid with a transverse spacing of 0.05 m, from 4 m upstream of the bend to 2 m downstream of the bend, and a longitudinal spacing of 5° in the bend.

5.2.3 Experimental conditions

Three experiments were performed under different conditions of sediment supply and bubble generation, but with similar hydraulic conditions in order to facilitate comparison. Experimental conditions are listed in Table 5.1. The CF63_LB_NB experiment was performed under live-bed conditions with a constant rate of sediment feeding at the entrance of the flume, but without bubble screen; the CF57_CW_NB experiment was performed under clear-water scour conditions without bubble screen and the CF55_CW_B experiment was performed under clear-water scour conditions with bubble screen. In the labels, CF stands for curved flow, LB for live-bed, CW for clear-water scour, NB for no bubble screen, and B for bubble screen. In all experiments, the initial condition was a flat bed.

Table 5.1: Experimental conditions.

Label*	Q $[m^3\ s^{-1}]$	q_s $[kg\ m^{-1}s^{-1}]$	P_a [kPa]	H [m]	U $[m\ s^{-1}]$	S_s $[10^{-4}]$	R/B [-]	R/H [-]	B/H [-]
CF63_LB_NB	0.063	0.023	-	0.10	0.49	28	1.31	17.2	13.2
CF57_CW_NB	0.057	-	-	0.14	0.31	7.36	1.31	11.9	9.1
CF55_CW_B	0.055	-	500	0.14	0.31	1.61	1.31	12.2	9.3

Q is the water discharge, q_s is the sediment discharge, P_a is the chosen air-pressure, H is the final flume-averaged flow depth, $U = Q/BH$ is the flume-averaged velocity, S_s is the flume-averaged water slope. *The first part of the experiments' labels signifies curved flow (CF) with the water discharge in [l s^{-1}], the second part live-bed (LB) or clear-water scour (CW) conditions, and the last part experiments without (NB) or with (B) the bubble screen.

All experiments were performed until morphological equilibrium was reached. Under live-bed conditions, equilibrium was reached when: (i) the rate of sediment fed to the flume equaled the rate of sediment deposited in the downstream basin, (ii) the bed morphology remained stable, with the exception of migrating mesoscale bedforms. Under clear-water scour conditions, it is well known that the temporal development of the bed morphology is asymptotic, with a fast initial development that subsequently continuously slows down, to become ultimately infinitesimally slow. Roca et al. (2007) illustrated this for bend scour, and Masjedi et al. (2010) for bridge pier scour. The clear-water scour experiments were performed until all sediment transport vanished and the remaining evolution became infinitesimally slow.

The migration of mesoscale bedforms at equilibrium in the live-bed experiment complicated the velocity measurements: bedforms migrated over a substantial distance during the time required to measure one cross-section, resulting in significant modifications in the flow patterns. In order to circumvent this problem and to allow for detailed ADVP measurements, the bed morphology was frozen by spraying paint on it, and the sediment feeding was stopped. In the clear-water scour experiment, sediment transport had vanished at equilibrium and the mesoscale bedforms remained stationary. Therefore, no freezing of the bed was required to allow for detailed ADVP velocity measurements. This comparable easy in execution was the primary motivation for performing the experiment with bubble screen under clear-water scour conditions. The CF63_LB_NB and CF57_CW_NB experiments without bubble screen were first performed in order to verify that similar dominant features of the morphology and flow field develop under live-bed and clear-water scour conditions.

5.3 RESULTS

5.3.1 Influence of the bubble screen on the bed morphology

Figure 5.2 illustrates the morphology in the three experiments. The flume-averaged bed level defines the reference level, z = 0 m. The live-bed (CF63_LB_NB) and clear-water scour (CF57_CW_NB) experiments without bubble screen are characterized by similar morphological features that are typical for sharply curved open-channel bends (Roca et al., 2007; Blanckaert, 2010): a bar-pool morphology with two deep scour holes located near the entry and exit of the bend, respectively, and a depositional bar at the inner bank between the cross-sections located at 30° and 150° in the bend. The maximum scour depth in both experiments is similar and about 0.25 m under the flume-averaged bed level. These similar morphological features lend credit to the experiments performed under clear-water scour conditions.

The bubble screen in the CF55_CW_B experiment considerably attenuates morphological gradients: the bed level is in general much flatter than in the experiments without bubble screen due to reduced scour and deposition. The maximum scour depth is reduced by about 50% to 0.12 m and its location is shifted away from the outer bank towards the center of the flume, where it does not endanger bank stability anymore. The depositional bar at the inner bank has almost vanished, and does not noticeably reduce the navigable width anymore.

Figure 5.3a reports the streamwise evolution of the transverse bed slope (determined by linear fitting) in the three experiments. In both experiments without bubble screen, the transverse bed slope shows pronounced streamwise variations and reaches considerable maximum values in both scour holes. The bubble screen considerably attenuates the maximum transverse bed slope and its streamwise variations. Figure 5.3b further substantiates the pronounced morphological modification induced by the bubble screen in the cross-section at 70° in the bend for the three experiments.

In the clear-water scour experiment with bubble screen (CF55_CW_B), no sediment transport is observed in the outer-part of the cross-section and the bed remains nearly flat at its initial level. Without bubble screen, bend effects cause a substantial increase of the velocities and bed shear stress in this zone that leads to the formation of the maximum bend scour. These results indicate the efficiency of the bubble screen to counteract the curvature-induced increase in velocities and bed shear stresses in this zone.

Mesoscale bedforms occur in all experiments (see photos inserted in Figure 5.2). In the clear-water scour experiment without bubble screen (CF57_CW_NB), large amplitude dunes can be discerned in the downstream part of the bend. In the clear-water scour experiment with bubble screen (CF55_CW_B), dunes have smaller wavelength and amplitude. The inwards shift of the location of the dunes is reminiscent of the inwards shift of the location of the core of maximum streamwise velocities.

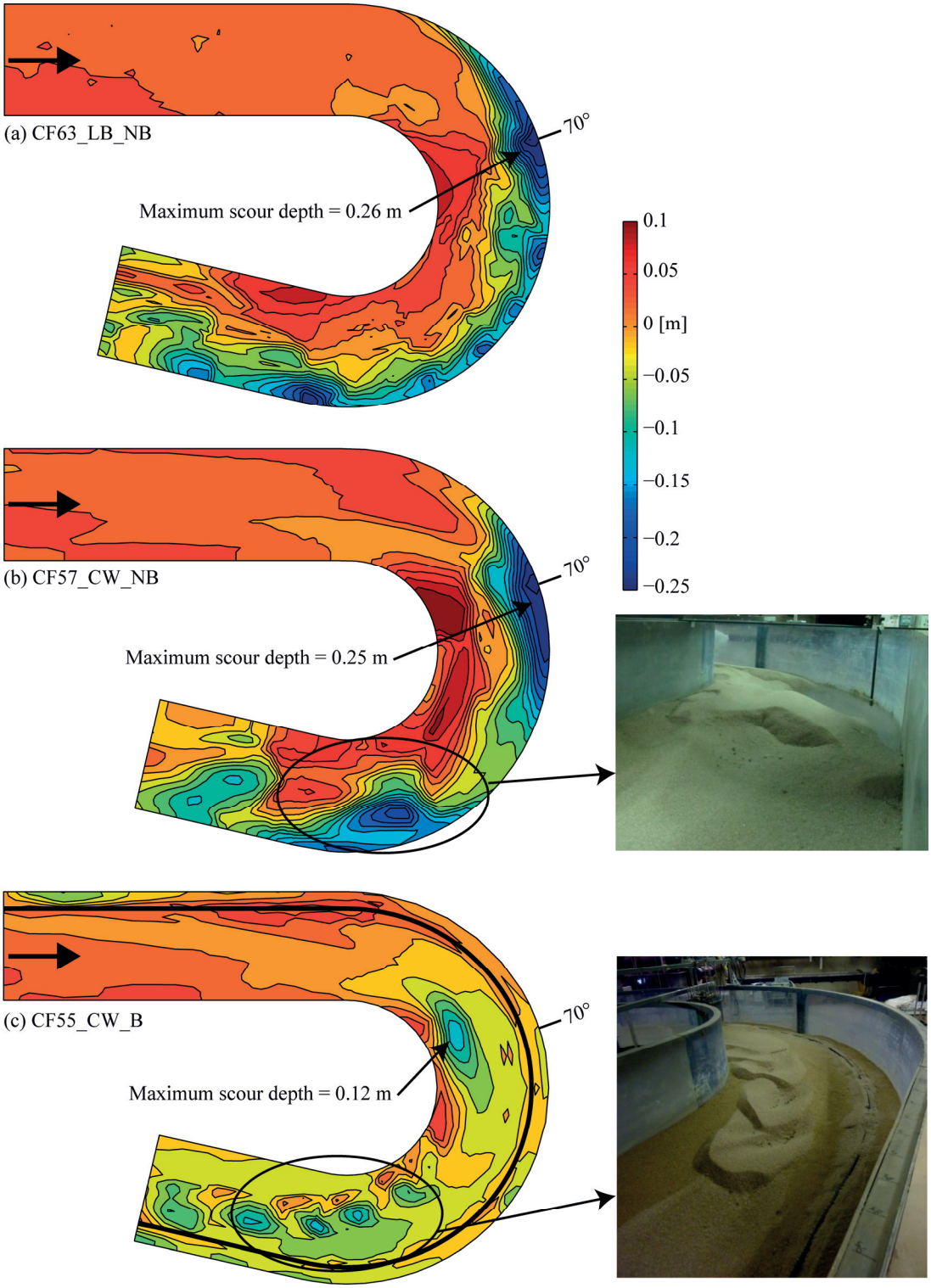

Figure 5.2: Isolines of the bed level with an interval of 0.02 m derived from laser distometer measurements for (a) CF63_LB_NB, (b) CF57_CW_NB and (c) CF55_CW_B experiments. The same color scale has been used to facilitate comparison. The inserted pictures on the right provide visualization of the mesoscopic bedform features in the downstream part of the bend.

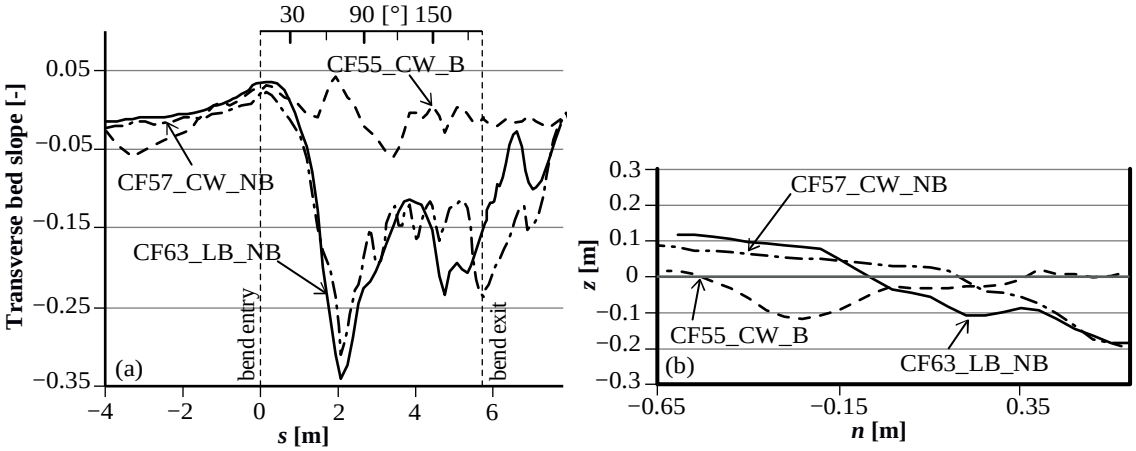

Figure 5.3: (a) Streamwise evolution of the transverse bed slope and (b) bed elevations in the cross-section at 70° in the bend (b). Comparison of the live-bed experiment without bubble screen (CF63_LB_NB), the clear-water scour experiment without bubble screen (CF57_CW_NB) and the clear-water scour experiment with bubble screen (CF55_CW_B). The streamwise distance from the bend entry is indicated by *s*, the transverse distance from the centerline by *n*, and the elevation over the flume-averaged bed level by *z*.

5.3.2 Influence of the bubble screen on the velocity redistribution

In order to explain how the bubble screen redistributes the morphology, the present section investigates its influence on the flow field. Figure 5.4, Figure 5.5 and Figure 5.6 report patterns of the three velocity components (streamwise, transverse and vertical), as well as the profiles of the water surface and bed elevations, in the cross-section at 70° in the bend for the CF63_LB_NB and CF55_CW_B experiments. Flow patterns in the CF57_CW_NB experiment (not shown) are similar to those in the CF63_LB_NB experiment, which further lends credit to the experiments performed under clear-water scour conditions. In the CF63_LB_NB experiment, the depth near the inner bank was too shallow to measure with the ADVP. In the CF55_CW_B experiment, the velocities in the vicinity of the bubble screen could not be measured because of interference between the bubbles and the ADVP signal.

In the reference CF63_LB_NB experiment without bubble screen, the flow patterns typical of open-channel bends are observed (Blanckaert, 2011): curvature-induced secondary flow is constrained to the deepest part of the cross-section with transverse velocities toward the outer bank at the surface and toward the inner bank at the bed, and vertical velocities impinging on the bed close to the outer bank (Figure 5.4a and Figure 5.5b,c). In the CF55_CW_B experiment with bubble screen, the curvature-induced secondary flow is weakened (Figure 5.5b,c vs. Figure 5.6b,c) and an additional bubble-induced counter-rotating secondary flow exists near the outer bank (Figure 5.4 and Figure 5.5), with a transverse extent from about $n = -0.2$ m to about $n = 0.45$ m (position of the porous tube). The core of maximum vertical velocities impinging on the bed defines the limit of the two secondary flows. This core about coincides with the location of maximum scour, which indicates the important role it plays with respect to the development of bend scour. These vertical velocities impinging on the bed are due to the combined effect of the two counter-rotating secondary flows. Their amplitudes, however, are smaller than the ones observed near the outer bank in the reference CF63_LB_NB experiment, which could partially explain the observed reduction in the maximum scour depth.

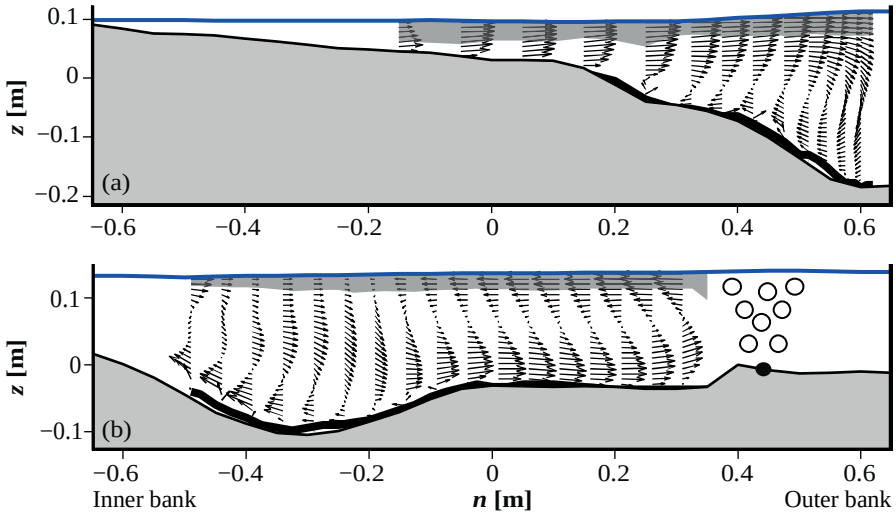

Figure 5.4: Patterns of normalized secondary flow $(v_n, v_z)/U$. Measurements performed in the cross-section at 70° in the bend (a) for the live-bed experiment without bubble screen (CF63_LB_NB) and (b) for the clear-water scour experiment with bubble screen (CF55_CW_B). Bed elevation estimated from ADVP measurements (thick black line) and from laser distometer measurements (thin black line). The shaded area near the water surface indicates extrapolated values. $U = Q/(BH)$ is the flume-averaged velocity. The transverse distance from the centerline is indicated by n, and the elevation over the flume-averaged bed level by z.

Secondary flow is known to be efficient in redistributing velocities (Blanckaert and de Vriend, 2003; Blanckaert and Graf, 2004). This is confirmed by the patterns of the streamwise velocity in both experiments. In the CF63_LB_NB experiment without bubble screen, the curvature-induced secondary flow (Figure 5.4a) advects high near-surface velocities in outward direction and towards the toe of the outer bank. As a result, the core of largest streamwise velocities v_s occurs near the toe of the outer bank (Figure 5.5a), where it promotes bend scour and enhances the flow attack on the bank. In the CF55_CW_B experiment with bubble screen, advective redistribution by both secondary flows causes the core of maximum streamwise velocities to occur at the junction between both secondary flows, where the maximum scour occurs (Figure 5.6a). Velocities near the bed in the core of maximum streamwise velocities are weaker in the experiment with bubble screen, which could partially explain the observed reduction in maximum scour depth.

5.4 DISCUSSION

The reported laboratory experiments convincingly demonstrate that the bubble-screen technique has the potential to become a useful tool for redistributing the flow patterns and the morphology in open-channel bends, and for mitigating bend scour. Its mechanism is schematically represented in Figure 5.7. The bubble screen generates a bubble-induced secondary flow with a sense of rotation opposite to the curvature-induced one. This additional secondary flow redistributes the velocity patterns and shifts the cores of maximum streamwise and downward velocities away from the outer bank, toward the junction between the two secondary flow cells. Consequently, the zone of maximal scouring is also shifted away from the outer bank toward the junction of the two secondary flow cells.

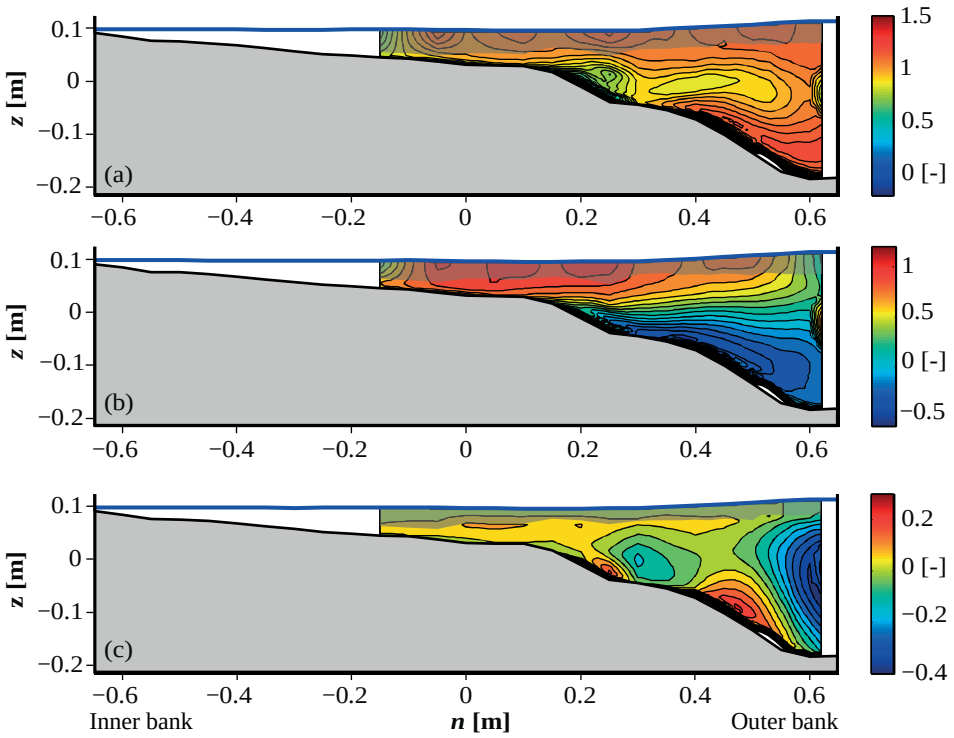

Figure 5.5: Patterns of normalized velocities measured in the cross-section at 70° in the bend in the CF63_LB_NB live-bed experiment without bubble screen. (a) Streamwise velocity v_s/U, (b) transverse velocity v_n/U, and (c) vertical velocity v_z/U. Bed elevation estimated from ADVP measurements (thick black line) and from laser distometer measurements (thin black line). The shaded area near the water surface indicates extrapolated values.

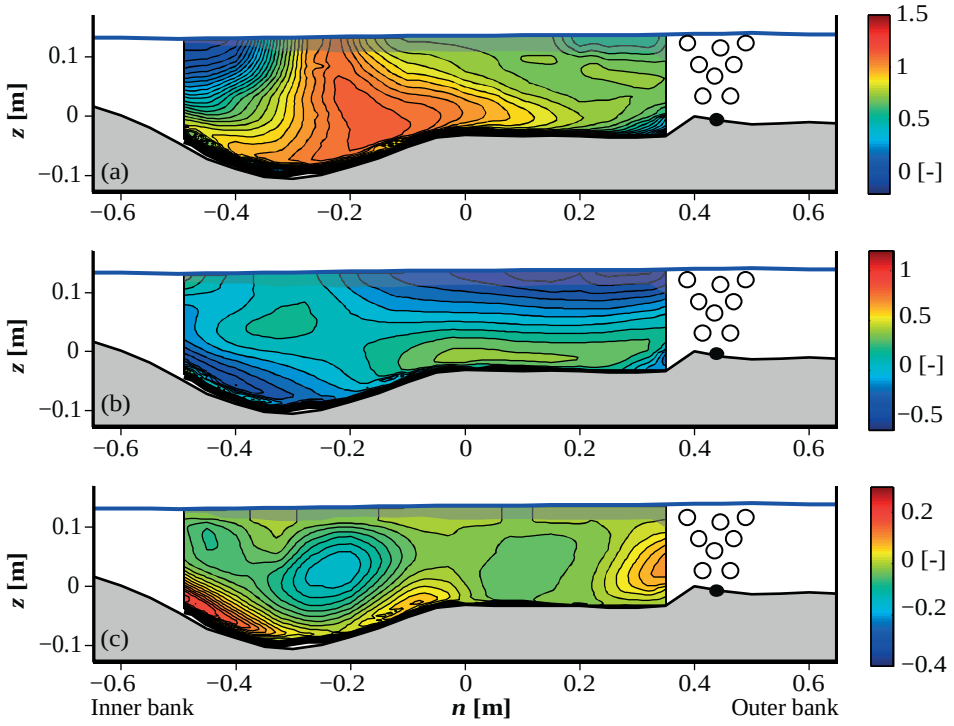

Figure 5.6: Patterns of normalized velocities measured in the cross-section at 70° in the bend in the CF55_CW_B clear-water scour experiment with bubble screen. (a) Streamwise velocity v_s/U, (b) transverse velocity v_n/U, and (c) vertical velocity v_z/U. Bed elevation estimated from ADVP measurements (thick black line) and from laser distometer measurements (thin black line). The shaded area near the water surface indicates extrapolated values.

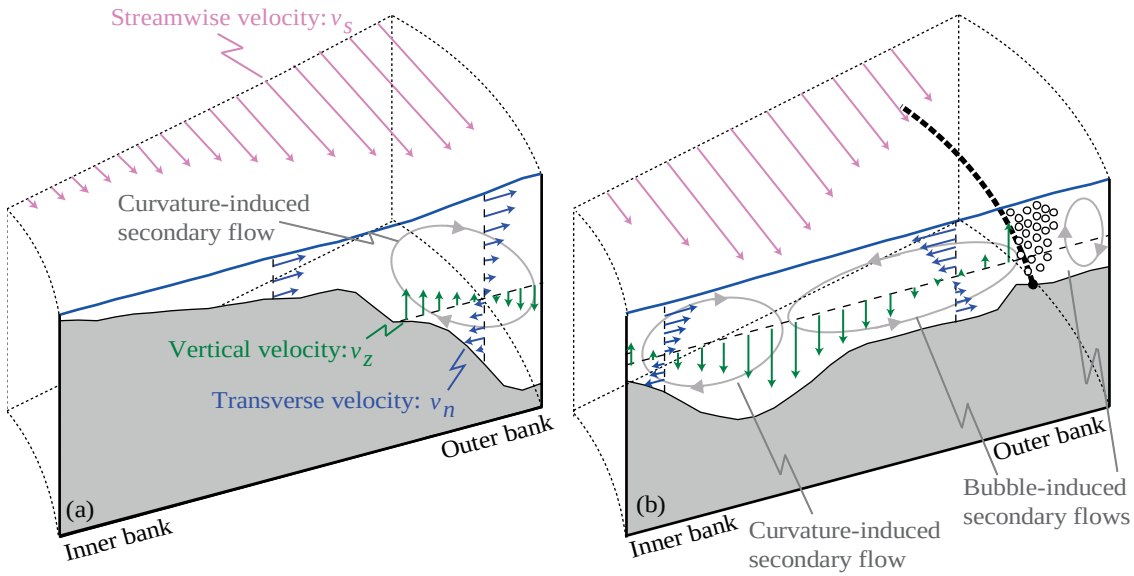

Figure 5.7: Mechanism of the bubble-screen technique deduced from the experimental results. Schematic representation of the flow and the morphology in a configuration (a) without bubble screen and (b) with bubble screen.

Hereafter, some further issues that need to be investigated in the process of developing the bubble-screen technique into a tool that is applicable in real world situations are discussed:

- The bubble-screen technique essentially consists in counteracting the curvature-induced secondary flow. Hence, its efficiency can be assumed to depend on the relative strengths of the bubble-induced and curvature-induced secondary flows. The strength of the bubble-induced secondary flow probably varies in a relatively narrow range. Comparison of experiments with the bubble screen in straight and curved flow configurations suggests that it is only weakly influenced by the degree of bend curvature (Blanckaert et al., 2008). Moreover, the rising velocity of air bubbles is known to be about constant at 0.24 m s^{-1} in the range of applied bubble sizes (Leifer et al., 2000). Therefore, the bubble screen can be assumed to induce comparable secondary-flow velocities in laboratory flumes and real world rivers. The curvature-induced secondary flow is known to depend on numerous parameters, including the river planform (degree of curvature and its streamwise evolution, river geometry and width), the flow characteristics (velocity of the mean flow, boundary roughness) and the scale of the river (flow depth). In first approximation, the curvature-induced secondary-flow velocities scale with the parameter *UH/R* (Rozovskii, 1957; Engelund, 1974). Based on this scaling argument, Blanckaert et al. (2008) has shown that the bubble-induced secondary-flow velocities are of comparable magnitude as the curvature-induced secondary-flow velocities in large natural rivers. The scaling argument further suggests that the bubble-screen technique's efficiency will decrease when the river's control parameter *UH/R* increases. Hence it can be assumed to be more efficient in mildly and moderately curved rivers, with gradual variations in curvature, and a flow characterized by a low Froude number ($Fr = U/(gH)^{1/2}$).
- The efficiency of the bubble-screen technique will also depend on the intensity of the flow-sediment interactions, which is determined by e.g., the sediment characteristics

(mean diameter and standard deviation), the sediment transport rate, and the occurrence of sediment transport in suspension. The here reported experiment with bubble screen was performed under conditions of clear-water scour, which is a mobile-bed configuration where sediment transport vanishes at equilibrium. Due to the highly nonlinear character of the flow-bed interactions, their influence is not straightforward to infer based on scaling arguments and the behavior under live-bed conditions cannot be anticipated.

- The efficiency of the bubble-screen technique will obviously also depend on the air flux and on the transverse position of the porous tube on the river bed.
- Potential adverse impacts of the bubble screen also need to be investigated. First, the bubble screen obviously modifies the flow field in the region between the bubble screen and the outer bank, where no measurements could be made in the here reported experiment. It is important to investigate the influence of the bubble screen on the flow forcing on the outer bank, as well as its dependence on the outer-bank configuration (slope and roughness of the bank). At present, application of the bubble-screen technique should be limited to applications with fixed banks. Second, the air bubbles in the water can decrease the density of the air-water mixture, and hence reduce the buoyancy of ships. It is important to quantify this buoyancy reduction in applications of the bubble-screen technique that aim at enlarging the navigable width of the river.

Additional experiments are required to quantify the influence of the dominant control parameters and of the sediment transport under live-bed conditions, to optimize the bubble-screen's air flux and positioning, and to investigate adverse impacts. These additional experiments will provide enhanced insight in the processes involved and allow for a more accurate delimitation of the application range of the bubble-screen technique.

Further research also needs to focus on the application of the bubble-screen technique in other river configurations. The bubble-screen technique may be particularly appropriate to reduce local scour around structures (bridge piers, abutments, etc). This local scour, provoked by vertical velocities impinging on the river bed, could be counteracted by the rising air bubbles.

5.5 CONCLUSION

Open-channel bends are characterized by a strong interplay between streamwise velocities, curvature-induced secondary flow, sediment transport and bed morphology. Maximum scour is typically found near the outer bank, and attributed to the maximum streamwise velocities that occur near the toe of the bank and the maximum vertical secondary-flow velocities that impinge on the bed near the toe of the bank.

The presence of a bubble screen near the outer bank, with its rising vertical velocities, generates an additional secondary flow located between the outer bank and the curvature-induced secondary flow, and with a sense of rotation opposite to the latter. The bubble screen shifts the cores of maximum streamwise velocities and maximum vertical velocities impinging on the bed away from the outer bank, to a distance where they do not endanger

bank stability anymore. Both these flow characteristics play an important role in the development of bend scour, as indicated by their coincidence with the location of maximum bend scour. This location further coincides with the junction of the curvature-induced and bubble-induced secondary flows, which indicates the dominant role played by the bubble-induced secondary flow in the modification of the morphology and flow patterns. The bubble screen causes a considerable attenuation of the morphological gradients. The maximum bend scour is reduced by about 50%, and the inner bank deposition bar has almost vanished, resulting in less shallow flow.

The reported results from laboratory experiments clearly demonstrate the potential of the bubble-screen technique to modify the morphology in open-channel bends. The paper discusses further steps that are required to develop this bubble-screen technique into a tool that is applicable in natural rivers.

Chapter 6

Influence of a bubble screen on bend morphodynamics under live-bed conditions

An air-bubble screen, generated by a porous tube, is installed in a sharply curved laboratory flume near the outer bank with the aim of reducing outer bend scour and sediment deposition near the inner bank. A reference experiment performed without the bubble screen is compared to an experiment performed with the bubble screen, under live-bed conditions. The efficiency of the bubble-screen technique is not uniform all around the bend. Three different zones are determined: A first zone in the upstream part of the bend where the strong outward transverse mass flux prevents the occurrence of the bubble-induced secondary flow cell, a second zone in the middle part of the bend where the bubble-induced secondary flow emerges, amplifies in downstream direction, and starts redistributing the downstream velocity, and a third zone in the downstream part of the bend where the redistributed velocities yield substantial morphological redistribution. The distribution of the transverse velocity at the water surface is found to be a good indicator on the efficiency of the bubble screen as the latter is directly related to the bubble-induced transverse flow at the water surface. Experiments performed with different positions of the porous tube respective to the outer bank show that the bubble screen is more efficient when placed the nearest from the outer bank. In addition to demonstrate the potential of the bubble-screen technique to reduce erosion, these experiments show that performing experiments under live-bed conditions is relevant to take into account all processes involved in the morphological development of a bend.

6.1 INTRODUCTION

Open-channel bends are characterized by interactions between the streamwise flow, the curvature-induced secondary flow and the bed morphology, resulting in the development of a typical bar-pool bend morphology (Rozovskii, 1957; Engelund, 1974; Odgaard, 1981; Struiksma et al., 1985; Whiting and Dietrich, 1993b; Blanckaert, 2010; Blanckaert and de Vriend, 2010). By advecting momentum, the curvature-induced secondary flow redistributes the streamwise velocity, leading to an outward shift of the core of maximum velocities and an increased erosive capacity of the flow in this region. Moreover, the curvature-induced secondary flow generates a transverse component of the bed shear stress which induces sediment transport from the outer to the inner part of the cross-section. Consequently, bend scour is observed near the outer bank whereas a bar develops near the inner bank (Figure 6.1a). This typical bend morphology can generate problems in the river: the bend scour at the outer bank may endanger the stability of structures (bridge abutments, bank protections) and the bar at the inner bank may reduce the navigable width due to insufficient flow depth.

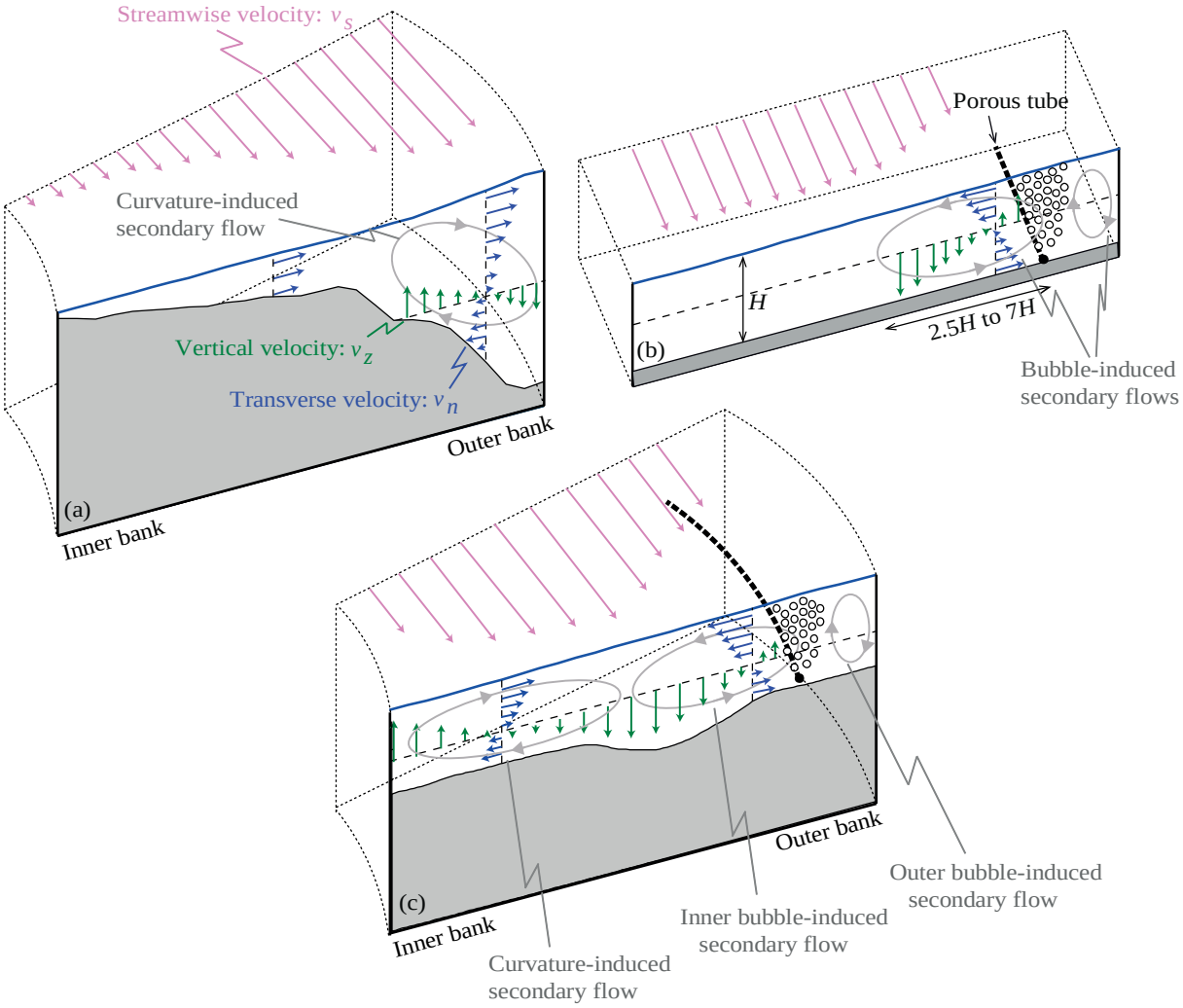

Figure 6.1: Conceptual sketches of flow and bed morphology in (a) a reference bend without bubble screen, (b) a straight flow with bubble screen and (c) a bend with bubble screen. *H* is the water depth.

Several techniques that aim at mitigating the development of the typical bend morphology have previously been studied and applied, such as bottom vanes (Odgaard and Spoljaric,

1986), a fixed outer bank layer (Roca et al., 2007) or submerged groynes (Przedwojski, 1995). However, these techniques imply fixed constructions in the river that may represent obstacles and a possible threat for shipping. An alternative technique consists in adding a momentum source that redistributes the flow patterns and consequently the boundary shear stresses, the sediment transport and the bed morphology. The present study investigates the use of an air-bubble screen as the momentum source. Advantages of bubble screens are that they can be used in a non-permanent way and be activated only under specific hydraulic conditions, do not alter the landscape and have reversible effects.

Bubble screens have previously been studied for large-scale applications: in lakes and reservoirs to prevent growth of algae or to avoid stratification (Schladow, 1992; Wüest et al., 1992), in ice-covered rivers to increase the dissolved oxygen level (Neto et al., 2007), in harbour entrances to prevent saltwater intrusion (Nakai and Arita, 2002), or in estuaries to stop the spread of invasive species (Sager et al., 1987; Welton et al., 2002). Under still-water conditions, a bubble screen generated from the channel bed is known to generate two cells of secondary flow symmetrically situated at either side of the bubble screen, with velocities that move perpendicularly away from the bubble screen in the upper part of the water column and towards the bubble screen in the lower part of the water column (Goossens, 1979; Fanneløp et al., 1991; Neto et al., 2008). The bubble-induced secondary flow cells are known to have a transverse size of about 2.5 to 7 times the water depth (Wen and Torrest, 1987; Fanneløp et al., 1991; Riess and Fanneløp, 1998).

The application of bubble screens in shallow open-channel flow with the purpose of modifying the flow and the morphology has only recently been investigated. Experiments presented in Chapter 4, in agreement with those from Blanckaert et al. (2008), have shown that a porous tube placed near the vertical bank in a shallow straight open-channel with still water or uniform baseflow generates a secondary flow cell with similar characteristics as in aforementioned large-scale configurations (Figure 6.1b). In Chapter 4, experiments have shown that interactions between the baseflow, the bubble-induced secondary flow, the sediment transport and the bed morphology enhanced the bubble-induced secondary flow. In an open-channel bend with a fixed flat bed, Blanckaert et al. (2008) found that a bubble screen placed near the outer bank generates a pattern of two counter-rotating secondary flow cells: a bubble-induced secondary flow cell exists between the curvature-induced secondary flow cell and the bubble screen in a region with a width of about 3 to 4 times the flow depth. A similar bi-cellular pattern of secondary flow cells was found in Chapter 5 in an open-channel bend with a morphology developed under clear-water scour conditions, which may be representative for low-mobility sediment transport conditions. The bubble-induced secondary flow cell causes a redistribution of the flow and the morphology (Figure 6.1c): the core of maximum streamwise velocities was found at the junction of both secondary flow cells and maximum bend scour occurred at that same location. Moreover, the morphological gradients were considerably attenuated.

The main objective of the bubble screen, however, is to modify the flow and the morphology under formative hydrological conditions, which are typically characterized by high-mobility sediment transport. Sediment transport conditions are expected to have an

important influence on the interaction between the base flow, the bubble-induced secondary flow, the sediment transport and the bed morphology. Therefore, the present chapter has the following specific aims:

- to extend the parameter space studied by Blanckaert et al. (2008), and in Chapter 4 and Chapter 5, by investigating the bubble-screen technique in an open-channel bend with live-bed sediment transport,
- to enhance insight in the interaction between baseflow, bubble-induced secondary flow, sediment transport and morphology in an open-channel bend,
- to provide detailed experimental data that will allow validation of numerical models.

It should be noted that the present investigation is limited to inbank flows in configurations with fixed banks.

6.2 EXPERIMENTS AND MEASUREMENTS

Experiments were performed in a sharply curved open-channel bend of constant width B = 1.3 m that consists of a 9 m long straight inflow reach, followed by a 193° bend with a constant centreline radius of curvature R = 1.7 m, and a 5 m long straight outflow reach which includes a 2 m long sediment deposition basin (Figure 6.2). The banks are vertical and made of smooth Plexiglas. This flume was designed in order to be representative of sharply curved natural open-channel bends (Blanckaert, 2011). A curvilinear reference system (s, n, z) is adopted where the s-axis represents the streamwise direction, the transverse n-axis points in the outward direction and the vertical z-axis in the upward direction. The flume bed was filled with a quasi-uniform quartz sand with a mean diameter d_m = 0.002 m. Sediment was continuously fed at the flume entrance at a constant rate (q_s = 0.025 kg m^{-1} s^{-1}), resulting in bed-load transport.

The bubble screen was generated by means of a porous tube (high-pressure tube of porous rubber, Multivis Waterbehandeling B. V.) placed on the channel bed parallel to the bank, and ballasted with a chain submerged in the sand to impede its movements. The tube was connected at both ends to a pressurized air system, thus generating a constant air pressure along its whole length. The air pressure was controlled by means of a manometer and the air discharge was measured by means of a rotameter.

A total of 6 experiments have been performed and their main experimental conditions are summarized in Table 6.1.

The two first experiments, CF75_LB_NB and CF75_LB_B, aimed at investigating the influence of the bubble screen on the flow and bed morphology and were performed under similar conditions of flow and sediment transport without and with bubble screen, respectively. Starting from an initially flat bed, dynamic equilibrium conditions developed in the flume, characterized by a stable macroscale bed topography overlaid by migrating mesoscale bedforms.

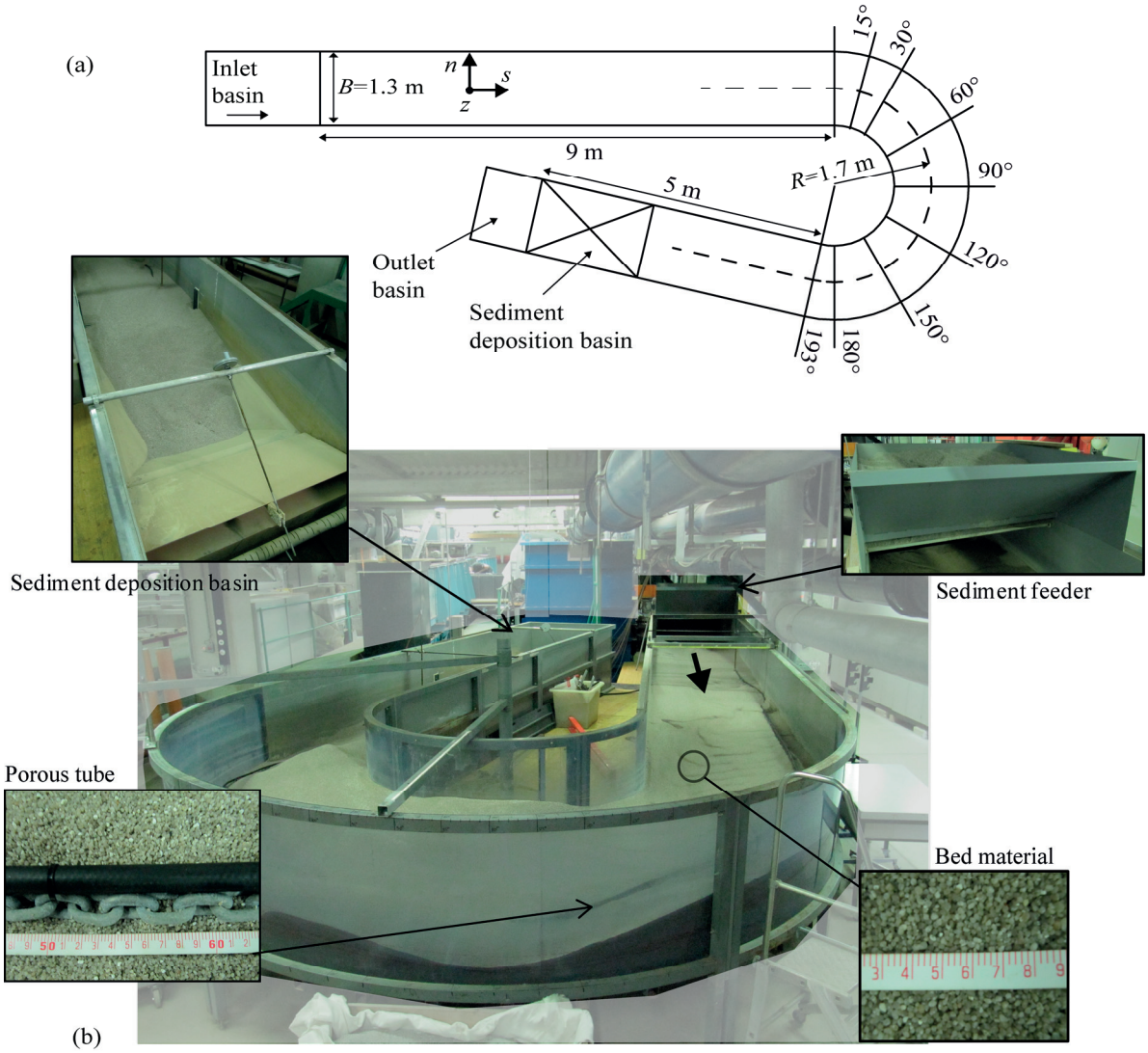

Figure 6.2: (a) Plan view of the curved channel with the porous tube and (b) pictures of the main components of the experimental setup: (top, left) sediment deposition basin , (top, right) sediment feeder, (bottom, left) porous tube ballasted with the chain, (bottom, right) quasi-uniform quartz sand.

Table 6.1: Experimental conditions at equilibrium.

Label*	Q $[m^3\ s^{-1}]$	H $[m]$	U $[m\ s^{-1}]$	Fr $[-]$	q_a $[dm^3\ s^{-1}\ m^{-1}]$	d $[m]$	R/B $[-]$	R/H $[-]$	B/H $[-]$
CF75_LB_NB	0.075	0.14	0.41	0.35	-	-	1.31	12.1	9.2
CF75_LB_B	0.075	0.14	0.41	0.35	0.24	0.2	1.31	12.1	9.2
CF63_LB_NB_{00}	0.063	0.11	0.46	0.45	-	-	1.31	16.2	12.3
CF63_LB_B_{10}	0.063	0.11	0.46	0.45	0.24	0.1	1.31	16.2	12.3
CF63_LB_B_{20}	0.063	0.11	0.46	0.45	0.24	0.2	1.31	16.2	12.3
CF63_LB_B_{30}	0.063	0.11	0.46	0.45	0.24	0.3	1.31	16.2	12.3

Q is the water discharge, H the flume-averaged water depth, $U = Q/(BH)$ the flume-averaged velocity, $Fr = U/\sqrt{gH}$ the flume-averaged Froude number, q_a the air discharge per unit length of porous tube and d the transverse distance between the porous tube and the outer bank. *The first part of the experiments' label refers to Curved Flow (CF) with the water discharge [l s^{-1}], the second part experiments performed under live-bed (LB) conditions, and the last part experiments without (NB) or with (B) the bubble screen. The subscript in the last four experiment gives the transverse distance between the porous tube and the outer bank [cm].

The other four experiments investigated the influence of the position of the porous tube and were stopped after 7h of run. Three different transverse positions of the porous tube from the outer bank were investigated and compared with a reference experiment without bubble screen CF63_LB_NB_{00}.

The transverse distance between the outer bank and the porous tube is given in Table 6.1. In CF63_LB_B_{20} experiments, the porous tube extended from 5 m upstream of the bend entry onto the flume exit, whereas in the other experiments involving the bubble screen, the porous tube only started at 0.1 m before the bend entry.

Velocity patterns were measured at equilibrium in the CF75_LB_NB and CF75_LB_B experiments, in the cross-sections at θ = [15, 30, 60, 90, 120, 150 and 180]° in the bend by means of an Acoustic Doppler Velocity Profiler (ADVP), developed at Ecole Polytechnique Fédérale Lausanne (EPFL). The ADVP is composed of a central emitter surrounded by four receivers and measures the quasi-instantaneous velocity vector along an entire profile, as well as the bed elevation. From these measurements, the time-averaged velocities in the three directions (v_s, v_n and v_z) are derived. More information on the ADVP process and accuracy estimations have been reported by (Lemmin and Rolland, 1997; Hurther and Lemmin, 1998; Blanckaert and de Vriend, 2004; Blanckaert and Lemmin, 2006). Data treatment procedures of ADVP measurements are described in detail in Blanckaert (2010). Vertical profiles of the three velocity components were measured in the investigated cross-sections every 0.05 m in the range n = –0.45 m to n = 0.45 m in the reference experiment without the bubble screen and in the range n = –0.45 m to n = 0.40 m when using the bubble screen. Velocity measurements were not possible with the ADVP near the bubble screen because of interferences between air bubbles and the acoustic signal. Sampling time for each profile was 100 s. Moreover, streamlines at the water surface were documented in both experiments by means of floating wool threads every 10° between cross-sections at 30° and 180° in the bend. ADVP measurements were performed under live-bed conditions, involving migrating bedforms. The bed elevation in the investigated cross-sections was measured with a point gauge before and after the ADVP measurements in order to verify that no important bed level variations occurred during the measurements, which took about one hour.

The water surface elevation was measured at equilibrium with a point gauge in the transverse positions n = [–0.6, –0.5, –0.3, –0.1, 0.1, 0.3, 0.5, 0.6] m in 70 cross-sections located between 4 m upstream of the bend entry and 2.2 m downstream of the bend exit.

The final bed morphology was measured in each experiments on a refined grid using a laser distometer with a transverse spacing of 0.05 m, from 4 m upstream of the bend to 2 m downstream of the bend, with a longitudinal spacing of 5° in the bend and of 0.2 m in the straight reaches.

6.3 RESULTS

6.3.1 Influence of the inner bubble-induced secondary flow on the bed morphology and flow patterns

The characteristics of the flow and the bed morphology, as well as their interactions, in the reference experiment without bubble screen are typical for sufficiently long single-bed configurations with mobile bed. Zeng et al. (2008) and Blanckaert (2010) reported a detailed description of these characteristics based on a live-bed experiment in the same experimental set-up, but with a higher discharge. Only the most important characteristics are briefly reviewed here, because they are important for understanding the influence of the bubble screen. They are illustrated in Figure 6.3 and Figure 6.4 for the CF75_LB_NB and CF75_LB_B experiments. Secondary flow (v_n, v_z) is defined in the present paper as the flow component perpendicular to the channel axis. According to Bradshaw (1987), it is composed of a translatory motion, $U_n = \langle v_n \rangle$ and a circulatory motion (v_n^*, v_z), where the brackets $\langle\ \rangle$ indicate depth-averaged values and an asterisk indicates the depth-varying part:

$$v_n = U_n + v_n^* \tag{6.1}$$

In order to simplify comparisons between the reference and the bubble-screen experiments, the secondary flows are visualized by means of the scalar pseudostreamfunction ψ_p (Batchelor, 1967; Blanckaert et al., 2008) in depth-averaged representations, which is computed from the circulatory part v_n^* of the transverse velocities as:

$$\psi_p = -(1 + n/R) \int_{z_b}^{z} v_n^* dz \tag{6.2}$$

where z_b represents the bed elevation.

In the reference experiment CF75_LB_NB, the secondary flow (v_n, v_z) (Figure 6.3, left column) starts to develop at the bend entry, grows to a maximum amplitude, that occurs near the cross-section at 60° in the present experiment, and subsequently decays in the second part of the bend. The circulatory part of the secondary flow is confined to the deepest part of the cross-section near the outer bank (Figure 6.4). The translatory part of the secondary flow U_n is mainly determined by the tendency of the flow to follow the thalweg. This tendency is commonly called topographic steering (Nelson, 1988; Blanckaert, 2010). Just downstream of the bend entry, the flow tends to follow a straight path, which leads to an important outward U_n. At about 60° in the bend, the flow collides with the outer bank at an oblique angle, causing pronounced vertical velocities that impinge on the channel bed and cause the maximum bend scour and the highest transverse bed slopes (Ferguson et al., 2003; Frothingham and Rhoads, 2003; Blanckaert, 2010). In the same region, the minimum flow depth occurs in the inner part of the cross-section, where a shallow point bar develops. Downstream of this region, between the cross-sections at 90° and 150°, the increasing flow depth in inner part of the cross-section and decreasing flow depths in the outer part of the cross-section cause U_n to be inward directed. At the bend exit, the sudden disappearance of the curvature leads to an acceleration of the flow in the outer part of the cross-section and a

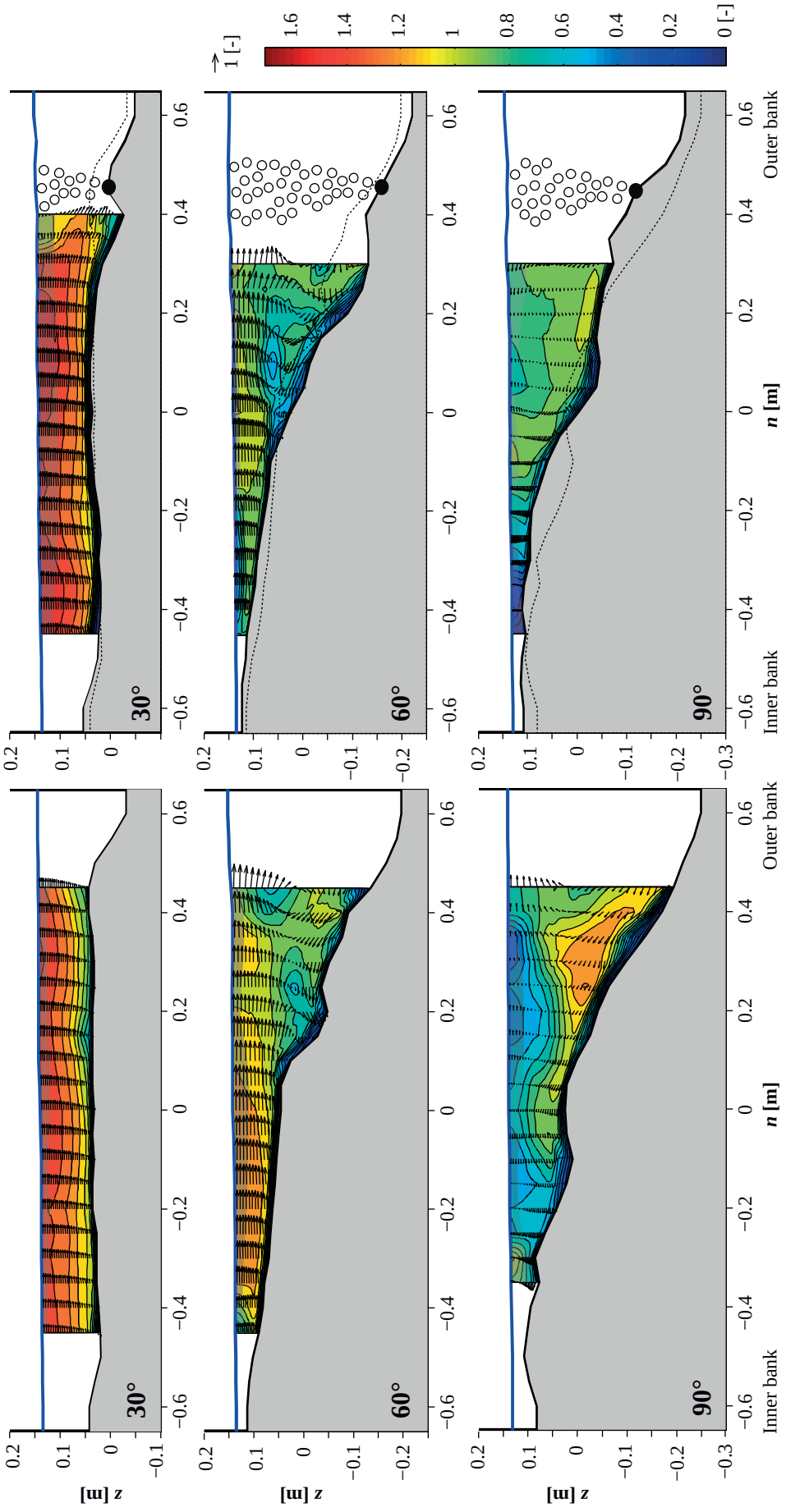

Figure 6.3: Normalized streamwise velocities v_s/U (contours) and normalized secondary flow (v_n, v_z)/U (vectors) in the cross-sections at 30°, 60°, 90°, 120°, 150° and 180° in the bend for CF75_LB_NB (left) and CF75_LB_B (right) experiments. The shaded area near the water surface indicates extrapolated values (Blanckaert, 2010). The same color and vector scales have been used to facilitate comparison. The reference level z = 0 m corresponds to the flume-averaged bed level. The dashed lines in CF75_LB_B cross-sections represent the bed elevation of CF75_LB_NB experiment.

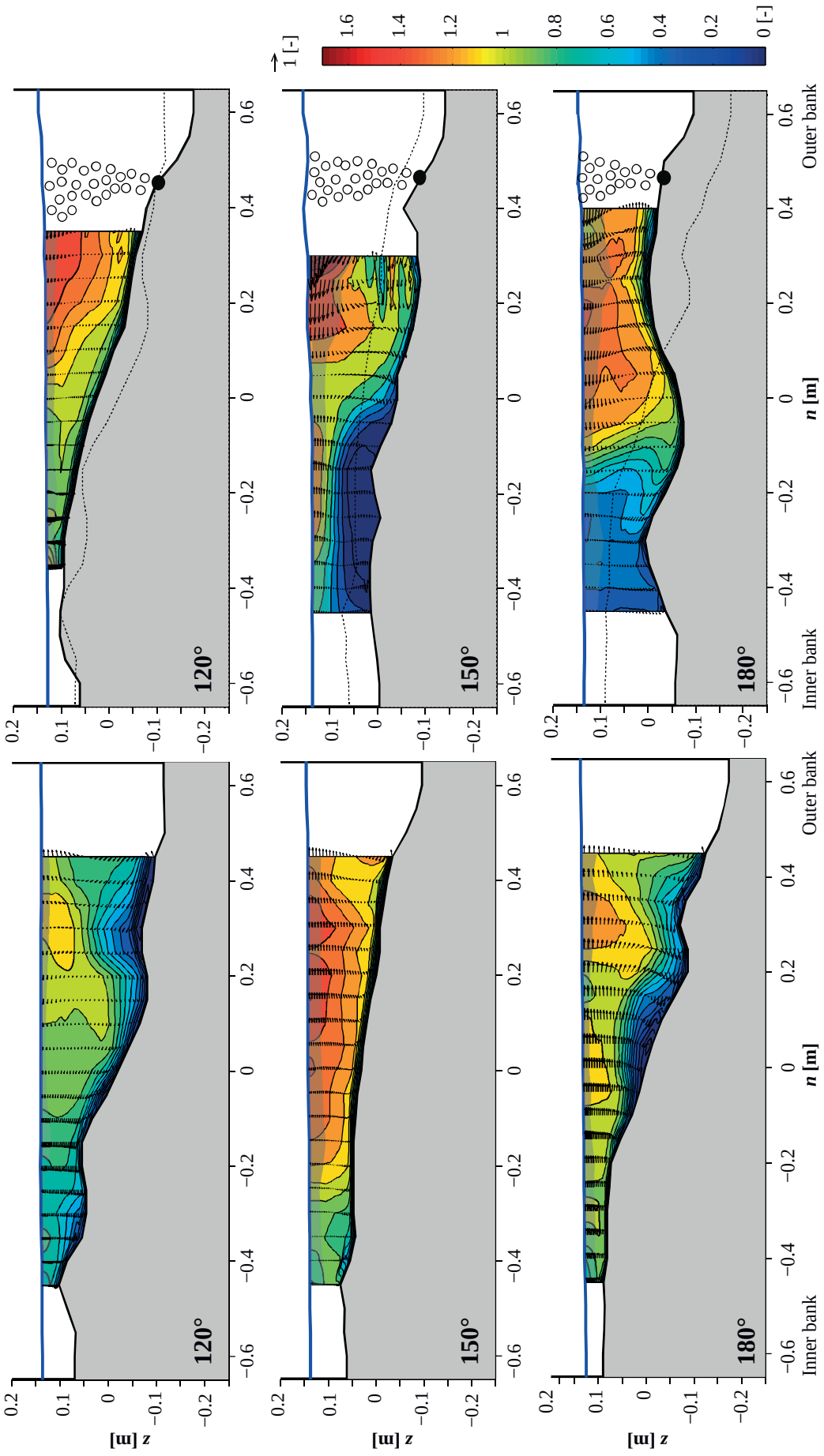

Figure 6.3: (continued)

deceleration in the inner part, which cause an increase in transverse bed slope and a zone of enhanced erosion at the outer bank. Due to mass conservation, this leads to outwards U_n. Advective momentum transport by the secondary flow redistributes the streamwise velocities around the bend (Figure 6.3). In the first part of the bend, the core of maximum v_s shifts in outward direction and reaches the outer bank near the cross-section at 60° (outside the measuring grid in Figure 6.3, but illustrated by Blanckaert, 2010), where the maximum bend scour occurs. It subsequently shifts inwards and is found in the centre of the cross-section at around 150°. Near the bend exit, it shifts again outwards.

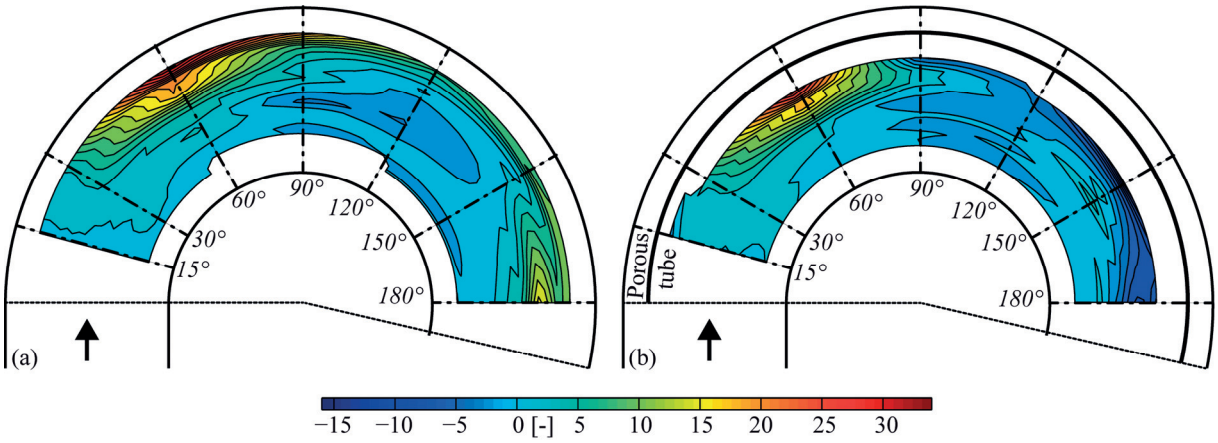

Figure 6.4: Isolines of normalized depth-averaged pseudostreamfunction $100\langle\psi_p\rangle/UH$ [-] in (a) CF75_LB_NB and (b) CF75_LB_B experiments. Patterns are based on high-resolution measurements in the indicated cross-sections.

The bubble screen causes significant modifications in flow patterns and bed morphology, as illustrated in Figure 6.3 and Figure 6.4. In the cross-sections at 30° and 60°, the flow patterns and the bed morphology are similar in the experiments with and without bubble screen. The flow is dominated by the pronounced outwards U_n, which avoid the formation of a bubble-induced secondary flow cell (Figure 6.3 and Figure 6.4). This is illustrated by the transverse velocities v_n which are outward oriented over the entire water column in the cross-sections at 30°. This means that the bubble screen is unable to prevent the incoming flow from following a straight path, colliding with the outer bank and causing maximum bend scour in the cross-section at 60°. The effect of the bubble screen is visible, however, in the inflexion in the upper part of the water column of the v_n-profile, which causes a reduction of the downstream velocity v_s in that region. From the cross-section at 90° on, a bubble-induced secondary flow cell occurs with a sense of rotation opposite to the curvature-induced cell, as illustrated by the reversed sign of v_n. This bubble-induced secondary flow cell widens and strengthens considerably in the downstream direction. The curvature-induced secondary flow is shifted in inward direction, and considerably weakened. Contrary to the curvature-induced secondary flow cell in the reference experiment without bubble screen which causes an outward redistribution of the downstream velocity v_s, the bubble-induced secondary flow causes an inward redistribution of v_s. As a result, differences between the flow patterns in the experiments without and with bubble screen gradually increase in downstream direction from the cross-section at 90° on. Due to inertia, differences in the bed morphology only emerge from the cross-section at around 150° on. The bubble screen is particularly efficient near the

bend exit, where the bubble-induced secondary flow cell extends well into the inner half of the cross-section. The transverse bed slope is considerably reduced, and the maximum scour does not occur anymore at the toe of the outer bank, but at the inner edge of the bubble-induced secondary flow cell.

The three distinct zones identified by means of these velocity patterns (Figure 6.3 and Figure 6.4) are indicated in the forthcoming figures: the first zone from the bend entry to about 90° where the strong outward transverse mass flux U_n prevents the occurrence of the bubble-induced secondary flow cell, the second zone from about 90° to about 150° where the bubble-induced secondary flow emerges, amplifies in downstream direction, and starts redistributing the downstream velocity v_s, and the third zone from about 150° to the flume exit where the redistributed velocities yield substantial morphological redistribution.

The results indicate that the transverse velocity at the water surface $v_{n,surf}$ is a good indicator of the efficiency of the bubble screen to modify the flow and morphology, which corroborates the findings of Fanneløp et al. (1991). Figure 6.5a and Figure 6.5b show the patterns of $v_{n,surf}$ in the experiments without and with bubble screen respectively, based on ADVP measurements in the cross-sections at 15°, 30°, 60°, 90°, 150° and 180° in the bend, and flow visualization by means of floating wool threads in cross-sections every 10° (Figure 6.5c). In the first zone between the bend entry and the cross-section at 90° in the bend, the flow at the water surface is similar in the two experiments and collides with the outer bank. No bubble-induced surface flow is observed. In the second zone from 90° to 150°, the emergence and amplification of the bubble-induced secondary flow cell is clearly discernible. In the third zone from the cross-section at 150°, the bubble-induced surface flow covers about half the width of the cross-section. The flow visualisation at the water surface further highlights a zone of horizontal flow recirculation over the point bar between the cross-section at 60° and 90°, which is similar to observations made by Blanckaert (2010). This recirculation is more pronounced in CF75_LB_B experiment, which may be due to small differences in the point bar morphology.

The morphological changes induced by the bubble screen are further illustrated in Figure 6.6, which shows the bed morphology in the experiments without (Figure 6.6a and Figure 6.6d) and with (Figure 6.6b and Figure 6.6e) bubble screen, as well as their difference (Figure 6.6c), based on measurements on a refined grid. In the reference experiment CF75_LB_NB, Figure 6.6a clearly illustrates the bar-pool bend topography that is typical of sharply curved bends (Odgaard, 1981; Dietrich and Smith, 1983; Struiksma et al., 1985; Olesen, 1987; Whiting and Dietrich, 1993a; Abad and Garcia, 2009a; Blanckaert, 2010) with the main scour hole between the cross-sections at 40° and 100°, the point bar which extends from near the bend entry onto until 2 m downstream of the bend exit, and the second scour hole at the bend exit with a comparable scour depth as the main scour hole. Mesoscale bedforms are migrating around the bend with maximal amplitude near the outer bank. They can be identified by the small scour holes near the outer bank (Figure 6.6a) and are illustrated by the picture in Figure 6.6d. In the experiment with bubble screen (Figure 6.6b and Figure 6.6d), the morphological gradients are considerably reduced in the zone ranging from about 150° in the bend to the flume exit. Near the bend exit, maximum scour is reduced from

z = –0.22 m to z = –0.08 m and shifted from near the outer bank towards the central part of the cross-section.

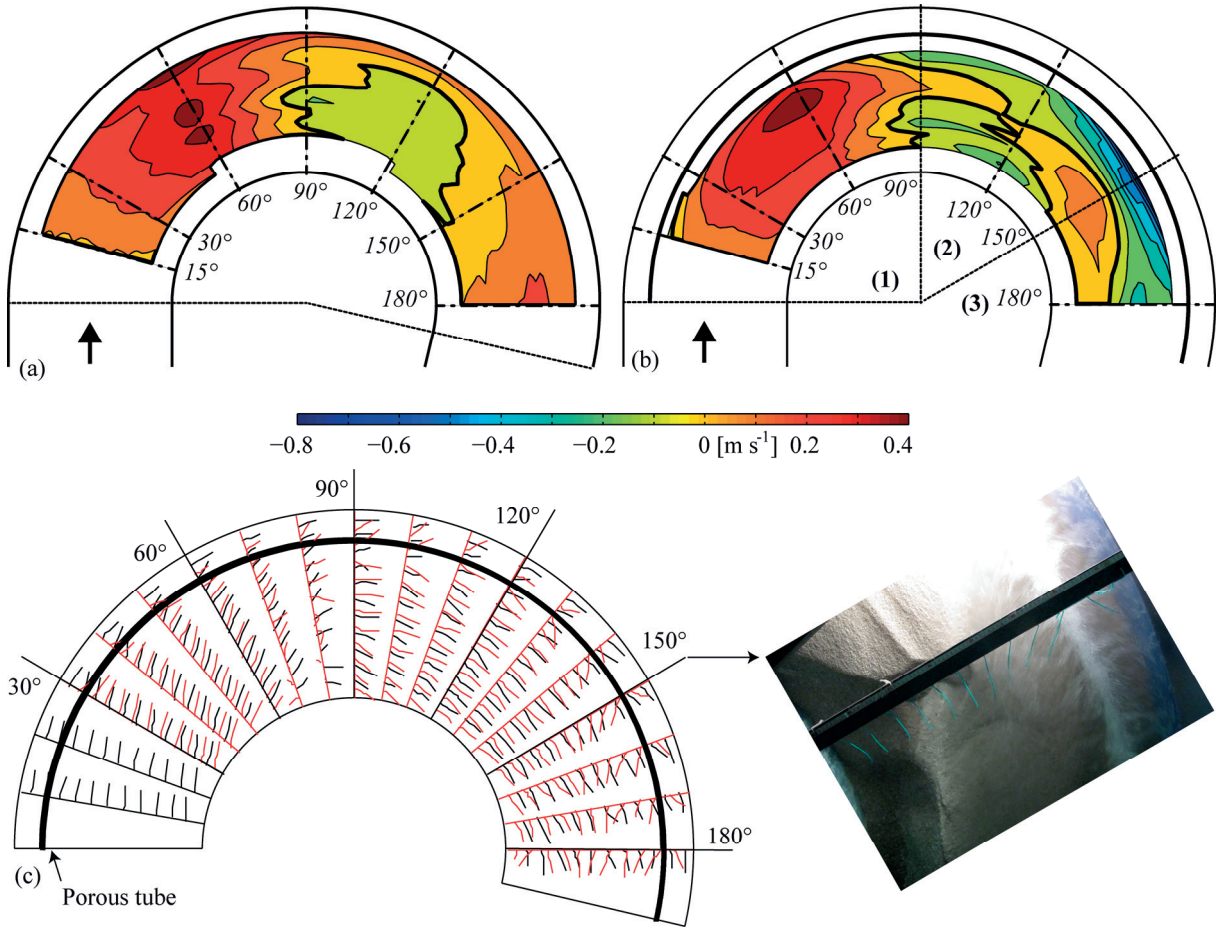

Figure 6.5: Transverse velocity at the water surface, $v_{n,surf}$, based on ADVP measurements in the indicated cross-sections in (a) CF75_LB_NB experiment and (b) CF75_LB_B experiment, and (c) based on flow visualization with floating wool threads. Results of CF75_LB_NB and CF75_LB_B experiments are represented in black and red, respectively. Three zones identified from the velocity patterns in Figure 6.3 are indicated: (1) no bubble-induced secondary flow cell; (2) bubble-induced secondary flow cell causing velocity redistribution; (3) bubble-induced secondary flow cell causing velocity and morphology redistributions. The bold lines in (a) and (b) represent $v_{n,surf}$ = 0 m s^{-1} contour.

The bubble screen also leads to a shortening of the point bar, which only extends from near the bend entry to about 150° in the bend. The lee face of the point bar is clearly visible in Figure 6.6e and its location explains the increased depth observed in the velocity measurements in the cross-section at 150° (Figure 6.3). Velocity measurements (Figure 6.3) reveal a zone of flow recirculation with return currents near the bottom in the wake of the point bar. It is noteworthy that the bubble screen modifies the pattern of the mesoscale bedforms. Whereas four mesoscale dunes with maximal amplitude of about z = 0.07 m migrate around the bend in the reference experiment (Figure 6.6a and Figure 6.6d), no mesoscale bedforms are observed in the experiment with bubble screen.

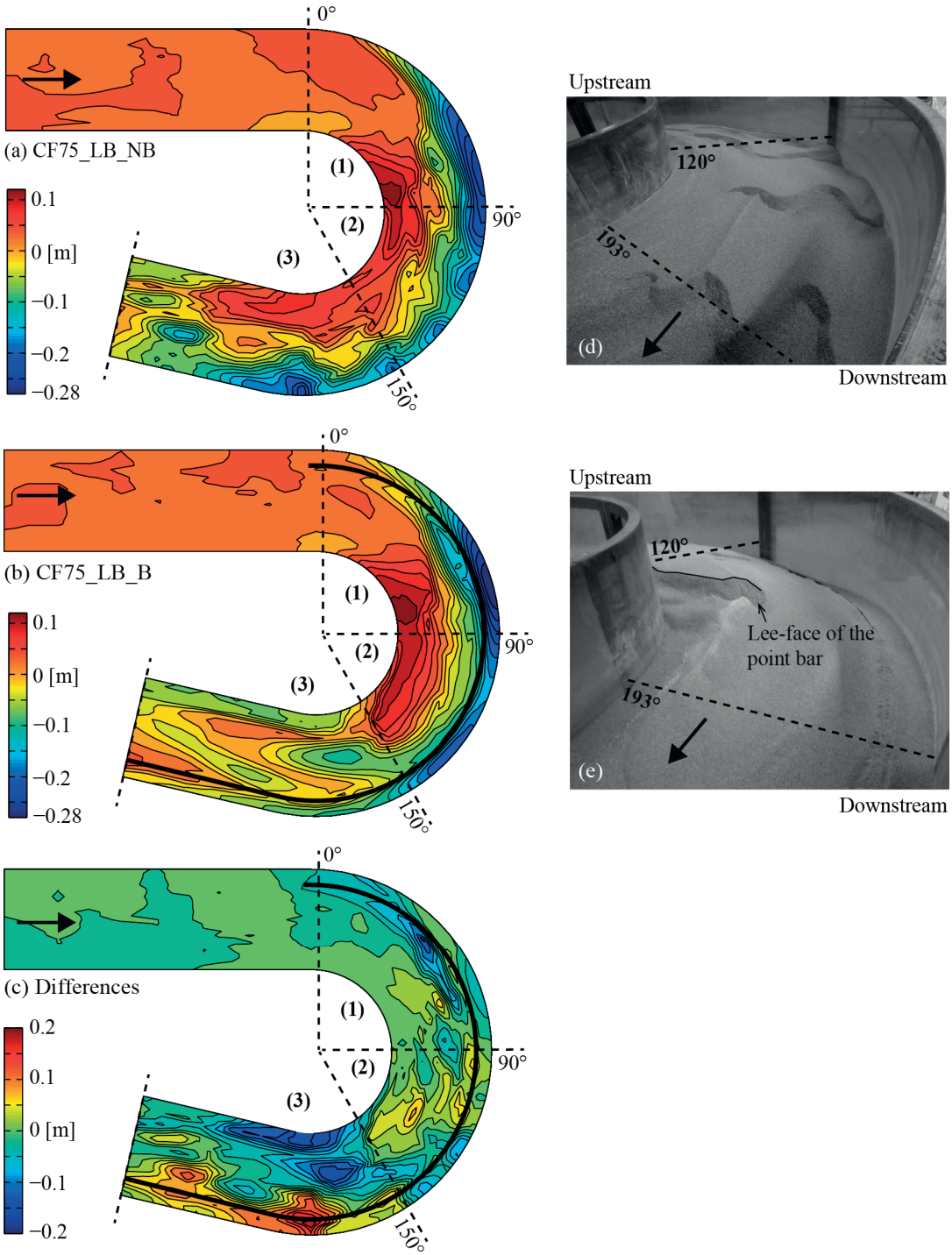

Figure 6.6: Equilibrium bed morphology derived from laser altimetry measurements for (a) CF75_LB_NB experiment, (b) CF75_LB_B experiment, and (c) their difference. Isolines are shown with an interval of 0.02 m. The same color scale has been used in (a) and (b) to facilitate comparison. Photography of the mesoscale bedforms in (d) CF75_LB_NB experiment and (e) CF75_LB_B experiment.

6.3.2 Influence of the outer bubble-induced secondary flow

Figure 6.6b and Figure 6.6c show that additional erosion occurs in the region between the porous tube and the outer bank, where no velocity measurements could be made. This erosion, with a maximal depth of $z = -0.17$ m, can be attributed to an additional bubble-induced secondary flow cell, which causes vertical velocities that impinge on the bed near the toe of

the bank. The flow visualisation also identifies this additional bubble-induced secondary flow cell situated between the bubble screen and the outer bank (Figure 6.5). At present, application of the bubble-screen technique should therefore be limited to configurations with fixed banks, in order to prevent any adverse effects on the bank stability.

The transverse location of the bubble screen is then assumed to have an important role on this additional scour and was investigated by means of short live-bed experiments (Table 6.1). Figure 6.7 provides the detailed bed topography for the four short-term experiments measured after 7h of run. In the three bubble-screen experiments, the first scour hole located between 60° and 90° still exists but its spatial extent and its maximal depth have been reduced whereas the second pool located at the exit of the bend does not appear anymore.

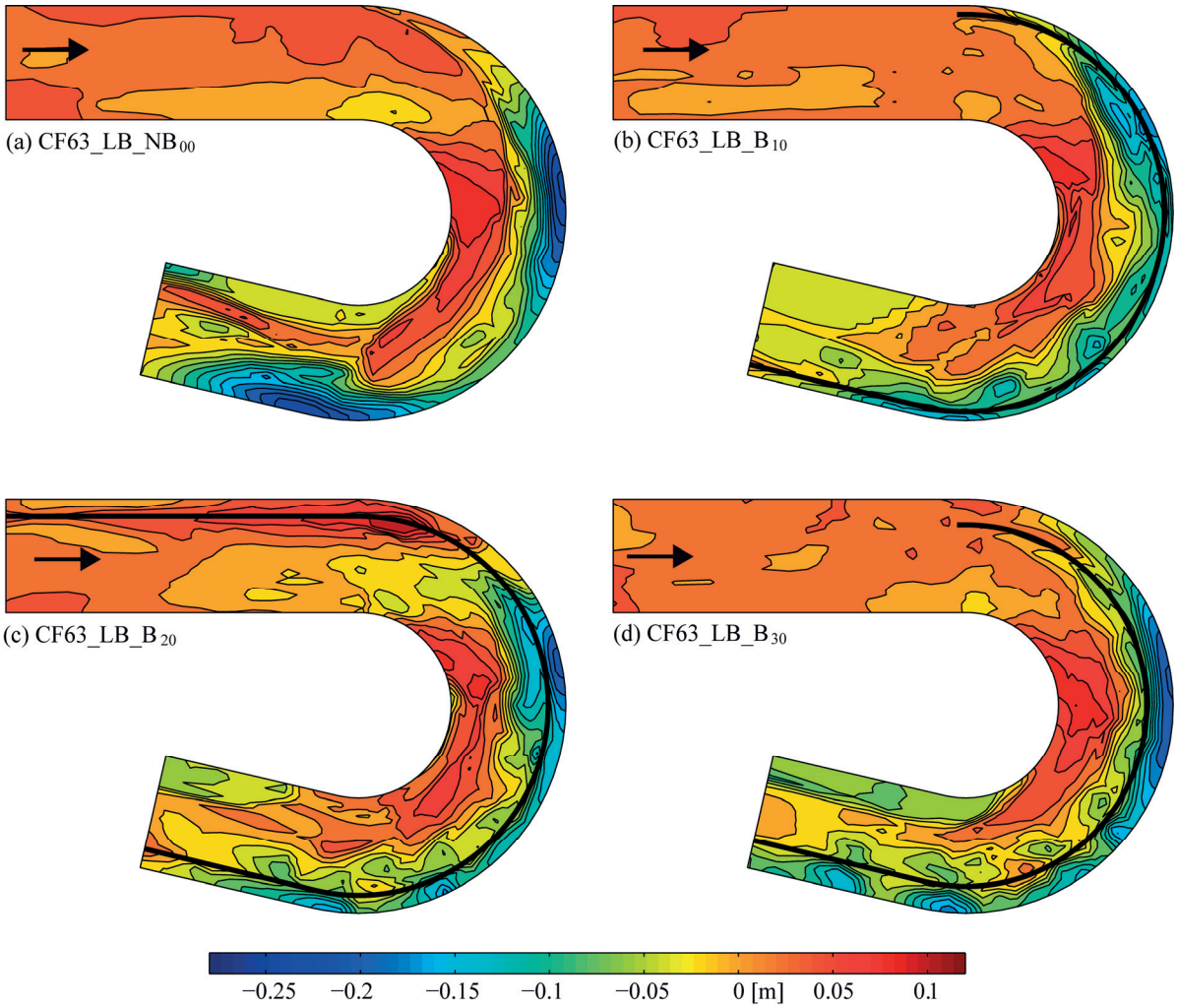

Figure 6.7: Isolines of the bed elevation with an interval of 0.02 m derived from laser altimetry measurements for (a) CF63_LB_NB_{00}, (b) CF63_LB_B_{10}, (c) CF63_LB_B_{20} and (d) CF63_LB_B_{30} experiments. The same color scale as Figure 6.6a is used to simplify comparison.

In the CF63_LB_B_{10} and CF63_LB_B_{20} experiments (Figure 6.7b and Figure 6.7c), the area covered by the first scour hole is reduced and the maximal depth is decreased by 0.08 and 0.05 m, respectively, as compared to the CF63_LB_NB_{00} experiment (Figure 6.7a). In the CF63_LB_B_{30} experiment, the area covered by the first scour hole is not modified by the bubble screen. The point bar's spatial extent has decreased when using the bubble screen

especially when the porous tube is located at 0.1 m (Figure 6.7b) or 0.2 m (Figure 6.7c) from the outer bank.

These results suggest that positioning the porous tube and the bubble screen closer to the outer bank can reduce this additional erosion. However, this point deserves further attention and is discussed in the following section.

6.4 DISCUSSION

The results indicate that the bubble-screen technique is only efficient over the entire length of the bend if the bubble-induced secondary flow cell exists all around the bend. The most critical zones are regions of strong curvature increase, which are characterized by pronounced outward flow U_n which is opposed to the generation of a bubble-induced secondary flow cell.

The experiments reported here and the straight-flow experiments reported in Chapter 4 revealed that the efficiency of the bubble screen amplifies in downstream direction due to interactions between the baseflow, the bubble-induced secondary flow and the morphology. This indicates that the bubble screen should be generated upstream of the bend entry, in order to attain a well-developed bubble-induced secondary flow in the region of strong curvature increase just downstream of the bend entry.

The feasibility of the bubble-screen technique can be estimated based on the transverse velocities occurring at the water surface. In first approximation, if the maximum transverse velocity that can be produced by the bubble screen, $v_{n,surf,bub}$, is higher than the maximum transverse velocity induced by the curvature, $v_{n,surf,ref}$, the bubble-induced secondary flow may be able to develop: $\max(v_{n,surf,bub}) > \max(v_{n,surf,ref})$. The maximum value of $v_{n,surf,ref}$ can be obtained from measurements or numerical modeling. Based on this criterion, the minimum air discharge $q_{a,min}$ required to counteract the maximal value of $v_{n,surf,ref}$ in a given bend can be determined, as $v_{n,surf,bub}$ is known to increase with the air discharge (Brevik, 1977; Wen and Torrest, 1987; Brevik and Kristiansen, 2002). The operating cost of the bubble-screen technique can then be derived from $q_{a,min}$.

The results obtained under live-bed conditions are significantly different from those under clear-water scour conditions (Chapter 5) and on a fixed horizontal bed (Blanckaert et al., 2008). Consequently, the efficiency of the bubble-screen technique depends on the sediment mobility conditions and on the flow-sediment interactions.

The transverse position of the bubble screen respective to the outer bank merits further attention, as mentioned in Section 6.3.2. The shape, inclination and roughness of the outer bank are supposed to have an influence on the outer bubble-induced secondary flow and this interaction should be further investigated. Countermeasures may be required to avoid the bank erosion generated by the bubble-induced surface flow.

Finally, the development length of the bubble-induced secondary flow is not found to be a dominant parameter with respect to the development of the bend morphology. In CF63_LB_B_{20} experiment (Figure 6.7c), the porous tube originates 5 m upstream of the bend entry and affects the morphological development in the straight reach, as noticed in Chapter 4, with deposition on top of the porous tube. However, similar morphological features are

observed in the upstream part of the bend in each bubble screen experiment irrespective of the origin of the porous tube. These observations indicate that the longitudinal position of the origin of the porous tube is not the dominant parameter in the design of a bubble-screen application. In open-channel bend applications, these observations indicate that placing the origin of the bubble screen at the bend entry is appropriate.

6.5 CONCLUSIONS

In open-channel bends, the coupled interaction between the streamwise flow, the curvature-induced secondary flow and the bed morphology leads to the development of a typical bar-pool bed topography. The latter is characterized by a shallow point bar at the inner bend and by local scour near the outer bank.

In the reported laboratory experiments, a bubble screen is used as a countermeasure to reduce morphological gradients in a sharply curved flume, such as outer bank erosion and sediment deposition near the inner bank. Two experiments performed without and with the bubble screen under live-bed conditions revealed that the bubble-screen efficiency is not uniform all around the bend. In the upstream part of the bend, the bubble-induced secondary flow is not able to counteract the cross-flow generated by the strong increase in curvature. However, in the downstream part of the bend, the bubble screen is able to generate a bubble-induced secondary flow that is efficient in redistributing the flow patterns as well as the bed morphology. The second local scour due to the decrease in curvature is shifted at the center of the flume and considerably reduced. Moreover, experiments performed with different position of the bubble screen respecting to the outer bank, show that the latter is more efficient when placed the nearest to the outer bank.

The bubble screen is efficient only if the bubble-induced secondary flow exists all around the bend and is strong enough to counteract the curvature-induced secondary flow. A first assessment of the efficiency of the bubble-screen technique can be performed based on the knowledge of the transverse velocities at the water surface that have to be counteracted and of the maximal velocities at the water surface that can be produced by a bubble screen under a specific air discharge.

These experiments also revealed that sediment transport should not be neglected when evaluating the efficiency of the bubble-screen technique. Interaction between the bubble-induced secondary flow cell located between the bubble screen and the outer bank and the sediment transport leads to additional erosion near the outer bank. This adverse effect can be reduced by placing the bubble screen the nearest to the outer bank. At present, however, application of the bubble-screen technique should be limited to configurations with fixed banks.

In addition of demonstrating the potential of the bubble-screen technique, detailed data on the 3D flow field and bed topography in open-channel bends are provided, which can be used for the validation of numerical models.

Chapter 7

Application range of a bubble screen for reducing scour in open-channel bends

The typical bar-pool bend topography which develops in open-channel bends due to complex interaction between streamwise flow, curvature-induced secondary flow, sediment transport and bed morphology leads to adverse impacts such as outer bank erosion and sediment deposition near the inner bank which can reduced the navigable width of the river. Previous chapters have shown that a bubble screen placed near the outer bank can produce a bubble-induced secondary flow that is able to redistribute the base flow pattern and consequently the bed morphology. The feasibility of the so-called bubble-screen technique is investigated in a sharply curved laboratory flume under different conditions of bed and sediment transport. Results of experiments performed on a fixed horizontal bed and on a mobile bed under both clear-water scour and live-bed conditions are compared. They show that the bubble-screen technique is more efficient under low-mobility conditions. The bubble screen is found to be efficient if the maximum inward transverse velocities at the water surface produced by the bubble screen are higher than the maximal outward transverse velocities induced by the bend curvature. Moreover, this condition has to be satisfied all around the bend. Based on this criteria, a straightforward method to evaluate the efficiency of a bubble screen to redistribute the flow patterns and the morphology is proposed, and illustrated by means of two application cases. The minimum air discharges required to counteract the maximal transverse velocities induced by the curvature are relatively low as compared to other types of environmental applications of the bubble screens.

7.1 INTRODUCTION

In the past decades, river engineering projects have shown a tendency towards more sustainable techniques. Preserving river ecomorphology and biodiversity while maintaining its principal economical functions calls for engineering techniques that intelligibly influence the fluvial system rather than forcing it.

This chapter describes an innovative technique that consists in indirectly manipulating river morphology by provoking changes in the flow patterns. A bubble screen, originating from a porous tube located on the river bed, can generate a secondary flow perpendicular to the bubble-screen axis, called bubble-induced secondary flow, which is able to redistribute the velocities and consequently to modify the bed morphology. The main advantages of this technique, contrary to "hard" engineering techniques such as submerged groynes, riprap or bottom vanes, are that it does not imply a fixed construction on the river bed that can represents a threat for shipping, it has no visual impact, it is also reversible and can be used in a non-permanent way, for example only during high discharge events that may provoke scour.

Simmons (1967) performed a literature survey about different hypothetical applications of the so-called "bubble-screen technique". He suggested to use it to avoid saltwater intrusion in estuaries, to reduce shoaling of navigation channels and harbour with the aim of reducing dredging requirements or to improve flushing characteristics. Nowadays, bubble screens or curtains are already applied in a wide range of environmental applications, such as aeration and destratification of lakes and reservoirs (Schladow, 1992; Wüest et al., 1992; Lemckert and Imberger, 1993; Sahoo and Luketina, 2006; Boegman and Sleep, 2012), to reduce saltwater intrusion in harbour entrances (Nakai and Arita, 2002) or as fish barriers to stop the spread of invasive species in estuaries (Sager et al., 1987; Welton et al., 2002).

Application of the bubble-screen technique in river morphodynamics has been investigated only recently (Blanckaert et al., 2008). It has been tested in a sharply curved flume with the aim of reducing outer bank erosion, sediment deposition near the inner bank and the strong morphological gradients resulting from complex interactions between the streamwise flow, the curvature-induced secondary flow and the bed morphology (Odgaard, 1981; Olesen, 1987; Whiting and Dietrich, 1993a; Roca et al., 2007; Blanckaert, 2010). Indeed, in open-channel bends, the curvature-induced secondary flow redistributes the streamwise velocity and causes it to decrease/increase in the inner/outer part of the bend, respectively. In addition, the curvature-induced secondary flow induces sediment transport from the outer to the inner part of the bend. Consequently, sedimentation/erosion occurs at the inner/outer bank and thereby creates the typical bar-pool bed topography (Figure 7.1a). The bubble-screen technique can be used to generate a secondary flow that counteracts the curvature-induced secondary flow and thus decreases its effect on the morphological evolution of the bend (Figure 7.1b).

Fixed horizontal bed experiments have shown that the bubble-induced secondary flow reduces the strength and extent of the curvature-induced secondary flow (Blanckaert et al., 2008). Streamwise velocity and bed shear stress patterns were redistributed, which would have provoked morphological changes if the bed has been mobile.

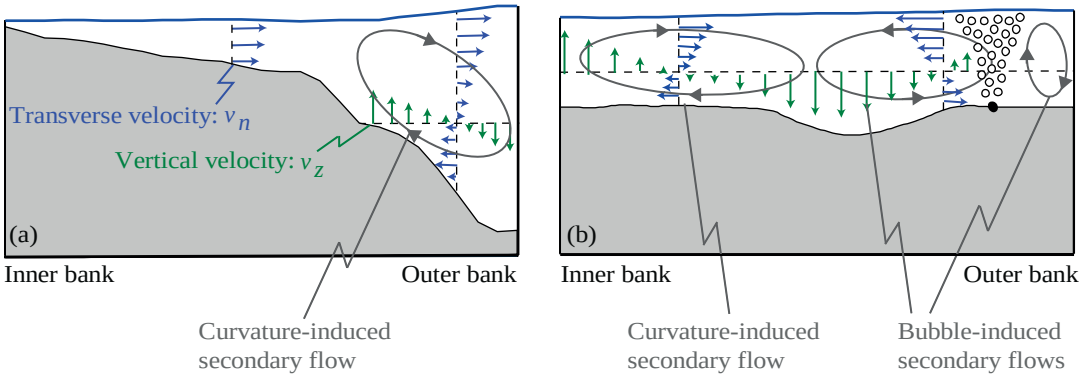

Figure 7.1: Conceptual sketch of (a) a reference case in an open-channel bend and (b) a case using the bubble-screen technique (downstream view).

Experiments were then performed on a mobile bed under both clear-water scour and live-bed conditions (Chapter 5 and Chapter 6). Under clear-water scour conditions, the local bend scour, observed at the bend entry was reduced by 50% and shifted from the outer bank to the central part of the flume. However, under live-bed conditions, the efficiency of the bubble-screen technique to redistribute bend morphology was found to be non-uniform around the bend (Chapter 6), its efficiency was clearly higher at the downstream part of the bend than in its upstream part.

The present chapter analyzes knowledge available from literature, the fixed horizontal bed experiments by Blanckaert et al. (2008) and the mobile-bed experiments under clear-water scour conditions (Chapter 5) and under live-bed conditions (Chapter 6), with the aim to investigate the application range of the bubble-screen technique in morphodynamical applications. The investigation is limited to inbank flow in open-channel bends with fixed banks.

7.2 EXPERIMENTS AND MEASUREMENTS

7.2.1 Experimental set-up

Laboratory experiments were performed in a sharply curved flume of constant width B = 1.3 m with smooth vertical banks (Figure 7.2). The flume is composed of a 9 m long upstream straight reach, followed by a 193° bend with a constant centerline radius of curvature R = 1.7 m, and ended by a 5 m long downstream straight reach which includes a 2 m long sediment deposition basin.

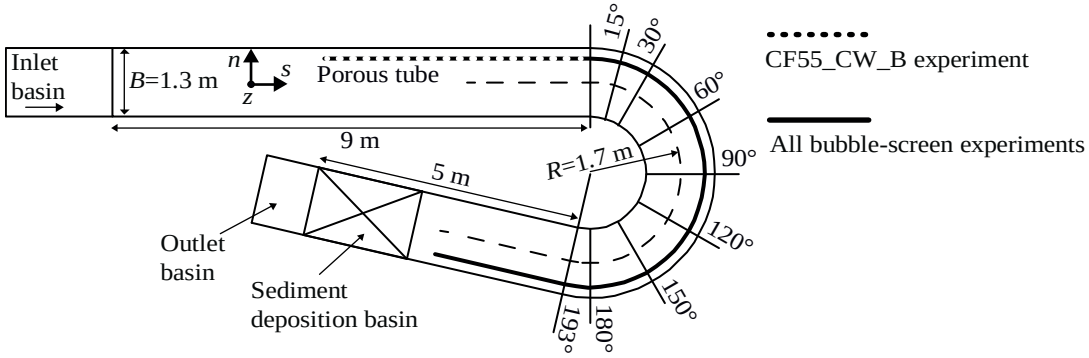

Figure 7.2: Plan view of the experimental set-up

A curvilinear reference system (*s*, *n*, *z*) is adopted where the *s*-axis represents the streamwise direction, the transverse *n*-axis points in the outward direction and the vertical *z*-axis in the upward direction.

The sediment used as bed material was a quasi-uniform quartz sand with a mean diameter d_m = 0.002 m. When conducting experiments under live-bed conditions, sediment was continuously fed into the flume near the entrance by means of a back-and-forth moving scraper which controlled the sediment discharge. At the end of the flume, a sediment basin allowed for the deposition of the transported sediment.

The bubble screen was generated by means of a porous rubber tube (high-pressure tube of porous rubber, Multivis Waterbehandeling B. V.) with an inner diameter of 0.01 m, connected at both ends to a pressurized-air system to guarantee a quasi-constant air pressure on the entire length of the tube. Microscopic holes in the tube were located on opposite sides of the diameter with a longitudinal spacing of 0.003 m. The porous tube was ballasted on its whole length to avoid large-amplitude movements due to buoyancy effects, and was located at 0.2 m from the outer bank. During each experiment, the air pressure in the porous tube was controlled by means of a manometer and the air discharge measured by means of a rotameter.

7.2.2 Experimental conditions and measurements

Three types of experiments were performed with different bed and sediment transport conditions: Fixed Horizontal bed (FH), mobile bed under Clear-Water scour conditions (CW), mobile bed under Live-Bed conditions (LB). Experimental conditions are summarized in Table 7.1.

Table 7.1: Experimental conditions at equilibrium.

Label	Q $[m^3\ s^{-1}]$	q_s $[kg\ m^{-1}\ s^{-1}]$	H $[m]$	U $[m\ s^{-1}]$	Fr $[-]$	q_a $[dm^3\ s^{-1}\ m^{-1}]$	R/H $[-]$	B/H $[-]$
CF89_FH_NB	0.089	-	0.16	0.43	0.34	-	10.7	8.2
CF89_FH_B	0.089	-	0.16	0.43	0.34	0.16	10.7	8.2
CF57_CW_NB	0.057	-	0.14	0.31	0.26	-	11.9	9.1
CF55_CW_B	0.055	-	0.14	0.31	0.26	0.21	12.2	9.3
CF75_LB_NB	0.075	0.025	0.14	0.41	0.35	-	12.1	9.2
CF75_LB_B	0.075	0.025	0.14	0.41	0.35	0.24	12.1	9.2

Q is the water discharge, q_s the sediment discharge per unit width, H the flume-averaged water depth, $U = Q/(BH)$ the flume-averaged velocity, $Fr = U/\sqrt{gH}$ the flume-averaged Froude number, q_a the air discharge per unit length of porous tube. The first part of the experiments' labels refers to Curved Flow (CF) with the water discharge in [l s^{-1}], the second part fixed horizontal bed (FH), live-bed (LB) or clear-water scour (CW) conditions, and the last part experiments without (NB) or with (B) bubble screen.

In the fixed horizontal bed experiments, sediments were glued on the bed. A downstream bed slope of 0.22% was installed in the straight inflow reach, and the bed was horizontal in the rest of the flume.

In experiments performed under clear-water scour and live-bed conditions, the bed was mobile and initially horizontal. Under clear-water scour conditions, no sediment was fed at the flume entry, whereas a constant sediment feeding (q_s = 0.025 kg m^{-1} s^{-1}) was introduced in the live-bed experiments. Both experiments were performed until morphological equilibrium was reached. Under live-bed conditions, this implied a stable morphology with migrating mesoscale bedforms. Under clear-water scour conditions, experiments were performed until all sediment transport vanished.

In CF89_FH_B and CF75_LB_B experiments, the porous tube started from 0.1 m before the entry and finished in the sediment deposition basin. In CF55_CW_B experiment, the porous tube extended from 5 m upstream of the bend entry to 2.5 m downstream of the bend exit (cf. Figure 7.2).

At morphologic equilibrium, velocity patterns were measured in several cross-sections around the bend by means of an Acoustic Doppler Velocity Profiled (ADVP) (Lemmin and Rolland, 1997; Hurther and Lemmin, 1998; Blanckaert and Lemmin, 2006; Blanckaert, 2010). From these measurements, the time-averaged velocities in the three-directions (v_s, v_n and v_z), as well as the bed elevations were derived. Data treatment procedures of ADVP measurements and near-surface extrapolations are described in detail in Blanckaert (2010). Vertical velocity profiles were measured in the investigated cross-sections every 0.05 m in the range n = –0.45 m to n = 0.40 m. ADVP measurements were not possible in the vicinity of the bubble screen because of interferences between air bubbles and the acoustic signal.

At the end of the experiments, water surface elevation was measured by means of a point gauge and final bed elevation measurements were performed in the mobile-bed experiments on a refined grid by means of a laser distometer every 5° in the bend and with a transverse spacing of 0.05 m.

7.3 RESULTS

7.3.1 Impact of the bubble-induced secondary flow on the bend morphology

Figure 7.3 shows the final bed morphology in the experiments under clear-water scour and live-bed conditions without (Figure 7.3a and Figure 7.3b) and with (Figure 7.3c and Figure 7.3d) the bubble screen, as well as their differences (Figure 7.3e and Figure 7.3f).

In the two reference experiments (Figure 7.3a and Figure 7.3b), the typical bar-pool bed topography is observed with a shallow point bar near the inner bank (Odgaard, 1981; Dietrich and Smith, 1983; Struiksma et al., 1985; Olesen, 1987; Whiting and Dietrich, 1993a; Abad and Garcia, 2009a; Blanckaert, 2010; Kashyap et al., 2012). Two main scour holes are observed: the first one near the bend entry between the cross-sections at 40 and 100°, and the second one near the bend exit around the cross-section at 180°.

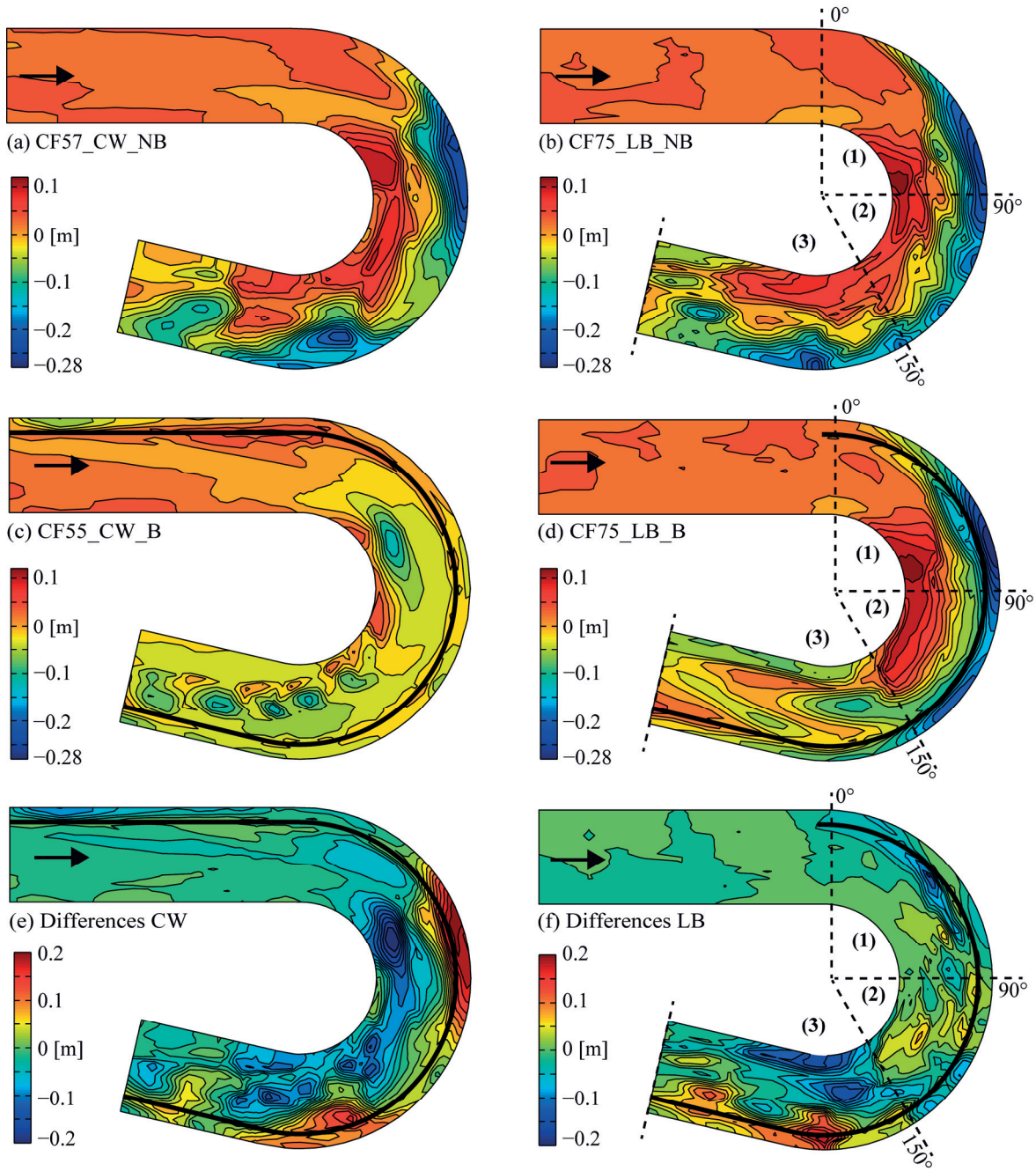

Figure 7.3: Equilibrium bed morphology from laser altimetry measurements for the reference experiments without bubble screen (a) CF57_CW_NB and (b) CF75_LB_NB, the bubble-screen experiments (c) CF55_CW_B and (d) CF75_LB_B and, in (e) and (f), the difference between morphologies with and without bubble screens (e), (f). Isolines are shown with an interval of 0.02 m. The same color scale has been used in (a), (b), (c) and (d) to simplify comparison. Three zones in the live-bed experiments refer to Chapter 6: (1) no bubble-induced secondary flow cell; (2) bubble-induced secondary flow cell causing velocity redistribution; (3) bubble-induced secondary flow cell causing velocity and morphology redistributions.

The bed morphologies in reference tests with and without sediment feeding are not significantly different. In the clear-water scour experiment (Figure 7.3a), no sediment comes from upstream. Consequently, the morphology only develops due to bend effects. The curvature-induced secondary flow redistributes the streamwise velocity pattern and cause it to be higher than the critical bed shear stress in some parts of the bend. At the end of the experiment, sediment transport totally vanishes. This leads to the development of a point bar

at the inner bend and to erosion near the outer bank, a morphology that is similar to the reference experiment under live-bed conditions CF75_LB_NB (Figure 7.3b). The only difference comes from the migration of mobile bedforms under live-bed conditions, which can be identified by the small scour holes near the outer bank. However, they do not affect the large-scale bar-pool bed topography.

Under clear-water scour conditions, the bubble screen dramatically modifies the bed morphology all around the bend (Figure 7.3c). The maximum scour hole between the cross-sections at 40° and 100° is shifted from the outer bank towards the center of the flume and its depth has been reduced by about 50%. The bed level is in general much flatter than in the reference experiment and the second scour hole at the bend exit does not develop.

Under live-bed conditions (Figure 7.3d), the bubble-screen technique has a favourable influence only in the second part of the bend. Indeed, the second scour hole is considerably reduced and shifted from the outer bank to the middle of the cross-section. However, in the upstream part of the bend, the first scour hole and the point bar are still observed.

The different efficiencies of the bubble screen in the upstream part of the bend between clear-water scour and live-bed experiments should not be related to the different origins of the bubble screen; 5 m and 0.1 m before the bend entry in CF55_CW_B, and CF75_LB_B, respectively. Indeed, in Chapter 6, experiments performed with similar hydraulic and sediment conditions, but with different origin of the porous tube, have shown similar bed morphologies in the upstream part of the bend.

The bubble-induced secondary flow is generated by the transverse velocities at the water surface induced by the deflection of the upward bubble-screen flow at the water surface (Fanneløp et al., 1991; Friedl and Fanneløp, 2000). Consequently, the distribution of the transverse velocities at the water surface is a good indicator of the occurrence and size of the bubble-induced secondary flow (Figure 7.4). In the fixed horizontal bed experiment (Figure 7.4b), the bubble-induced secondary flow is observed all around the bend and its size increases in downstream direction, similar to observations in straight flow experiments (Chapter 4). The bubble-induced secondary flow cell extents from $n = 0.1$ m to $n = 0.45$ m in the cross-section at 60°, and from $n = -0.1$ m to $n = 0.45$ m to half the cross-section at 180° in the bend.

In CF75_LB_NB experiment (Figure 7.4c), the bed topography leaves a strong footprint on the distribution of $v_{n,surf}$. Strong outward velocities are observed on the cross-sections where the two scour holes are observed. With the bubble screen (Figure 7.4d), strong outward velocities are still observed at the bend entry. However, the bubble-induced secondary flow is observed in the downstream part of the bend where the bubble screen was efficient in influencing the bed morphology. In the cross-sections at 180°, the bubble-induced secondary flow size is similar in CF89_FH_B and CF75_LB_B experiments.

7.3.2 Efficiency of the bubble screen in the upstream part of the bend

The influence of the bubble screen on the bed morphology and on the transverse velocity at the water surface differs between the two mobile bed experiments, especially in the upstream

part of the bend. The interplay between the flow characteristics and the sediment conditions is supposed to explain the difference in efficiency of the bubble-screen technique. This is illustrated by means of the three-dimensional velocity measurements (normalized streamwise velocity v_s/U and secondary flow (v_n, v_z)) performed in the cross-section at 60° in CF89_FH_B and CF75_LB_B experiments and in the cross-section at 70° in CF55_CW_B experiment where the maximum scour depth is observed (Figure 7.5). Furthermore, the transverse velocities at the water surface in the same cross-sections are provided in Figure 7.6.

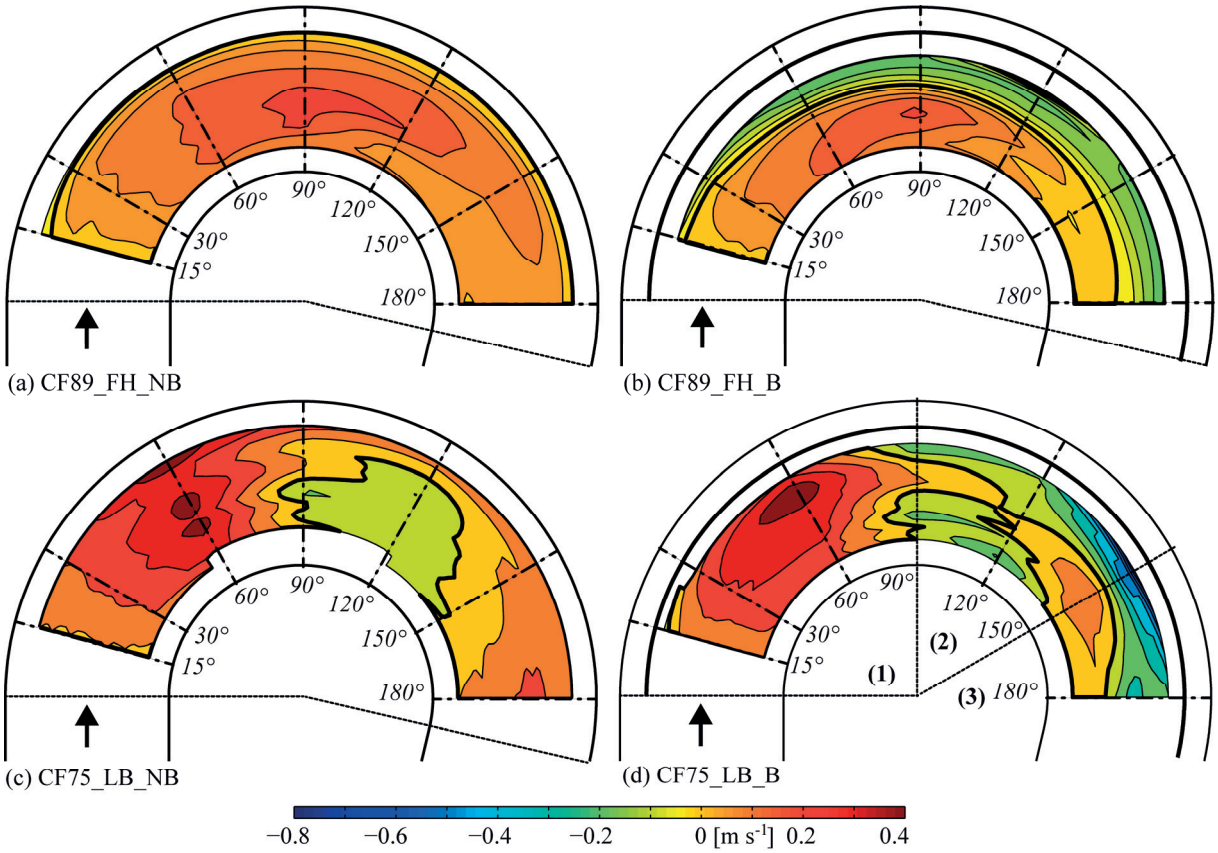

Figure 7.4: Transverse velocity at the water surface, $v_{n,surf}$, based on ADVP measurements in the indicated cross-sections in (a) CF89_FH_NB, (b) CF89_FH_B, (c) CF75_LB_NB and (d) CF75_LB_B experiments. The same color scale has been used to simplify comparison.

In the following sections, the secondary flow (v_n, v_z) is defined as the flow component perpendicular to the channel axis and is decomposed into two contributions (Bradshaw, 1987); a cross-flow $U_n = \langle v_n \rangle$ and a circulatory motion (v_n^*, v_z), where the brackets $\langle\ \rangle$ indicate depth-averaged values and an asterisk indicates the depth-varying part:

$$v_n = U_n + v_n^* \tag{7.1}$$

Each experiment is performed on an initially flat bed. Consequently, the initial flow distribution is close to the one measured in CF89_FH_B experiment (Figure 7.5a). The core of maximum streamwise velocities is observed at the inner bank. The junction of the bubble-induced and curvature-induced secondary flow cells occurs at n = 0.05 m. The transverse velocities at the water surface induced by the curvature reach a maximum value of 0.17 m s^{-1} in the inner part of the cross-section (Figure 7.6).

On a mobile bed (Figure 7.5b and Figure 7.5c), two final bed topographies are observed depending on the interaction between the baseflow, the bubble-induced flow and the sediment transport.

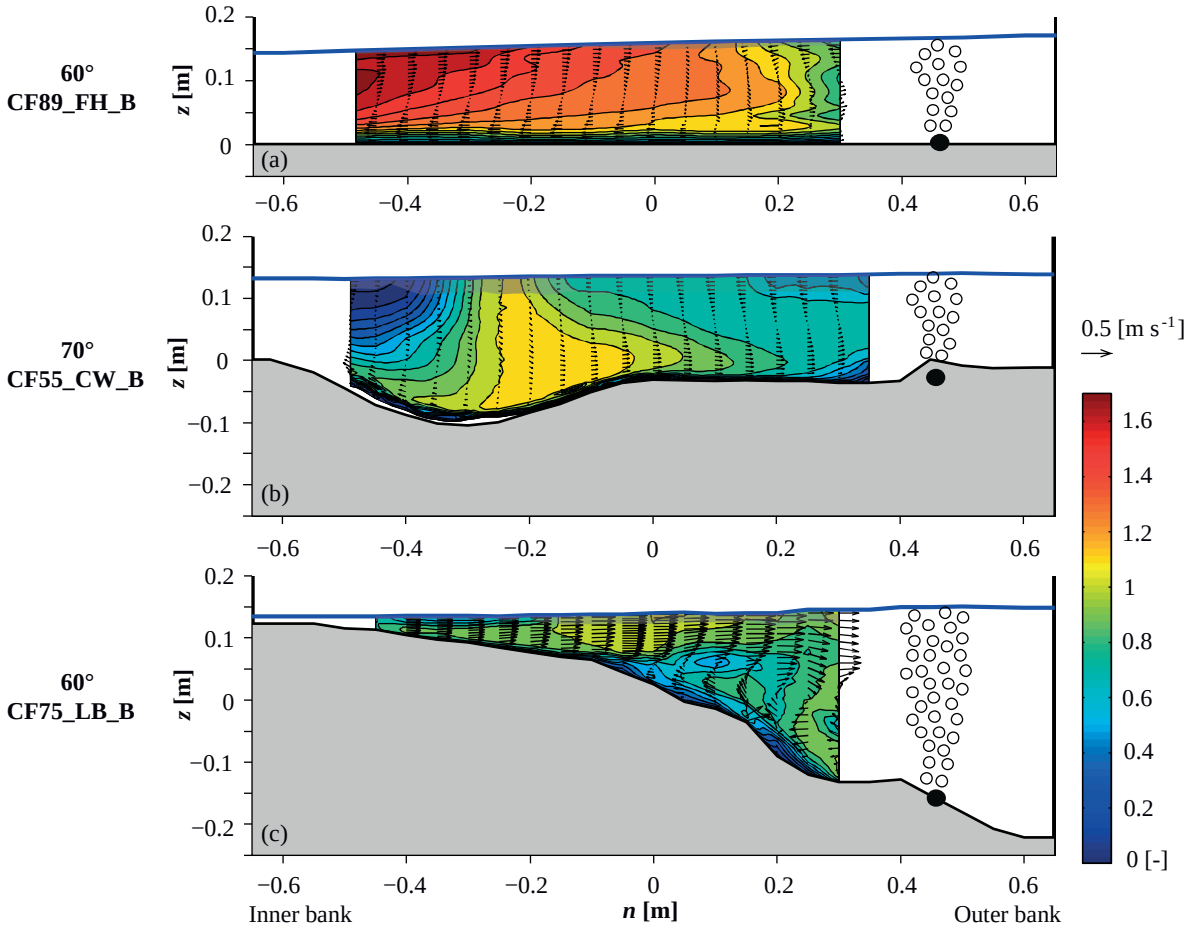

Figure 7.5: Mean normalized streamwise velocities v_s/U (contours) and normalized secondary flow (v_n, v_z) (vectors) (a) in the cross-section at 60° in the bend for CF89_FH_B experiment, (b) at 70° in the bend for CF55_CW_B experiment and (c) at 60° in the bend for CF75_LB_B experiment. The shaded area near the water surface indicates extrapolated values.

Under clear-water scour conditions (Figure 7.5b), the bubble screen is efficient to redistribute the flow patterns and bed morphology. From an initial flow distribution similar to the one observed in CF89_FH_B experiment, sediment transport starts to occur only at the junction of the curvature-induced and the bubble-induced secondary flow cells where the core of maximum downward velocities is observed. At the same location (n = –0.3 m), erosion starts to develop that shifts the core of maximum streamwise velocities from the inner bank, enhances the bubble-induced secondary flow and stabilizes its position. A positive feedback occurs between the morphology and the bubble-induced secondary flow, as observed in the straight flow experiments (Chapter 4). Indeed, the bubble-induced secondary flow size is higher in the CF55_CW_B (n = –0.1 m to n = 0.45 m) than in the CF89_FH_B (n = 0.1 m to n = 0.45 m). The point bar at the inner bank starts to develop with the sediment eroded in the inner part at the bend entry (Blanckaert, 2010) but its maximal height is limited by the small amount of sediment that is transported.

Under live-bed conditions (Figure 7.5c), the bubble screen is inefficient to redistribute neither the flow pattern neither bed morphology. Only the curvature-induced secondary flow is observed and the typical morphology of open-channel bend, with a high transverse slope, develops. Similar transverse velocities at the water surface than in the reference experiment are observed with a mean value of about 0.39 m s^{-1} (Figure 7.6), which is about twice more than those observed in the CF89_FH_B experiment.

In CF75_LB_B experiment, the initial situation is rather similar than in CF55_CW_B experiment, except that sediment transport occurs over the entire width. Erosion starts at the junction of the two secondary flow cells. Sediments coming from the upstream part of the bend in addition to those eroded at the bend entry deposits near the inner bank and starts to form the point bar. As the latter is growing due to a constant input of sediment, topographic steering appears and further enhances the flow tendency to follow a straight path and collides with the outer bank (Nelson, 1988; Blanckaert, 2010). Consequently, U_n increases as well. The transverse velocities at the water surface induced by the curvature, $v_{n,surf,ref}$, are then considerably higher on a developed bed morphology than on a fixed horizontal bed (Figure 7.6). When $v_{n,surf,ref}$ is higher than the transverse velocities at the water surface induced by the bubble screen, $v_{n,surf,bub}$, the bubble-induced secondary flow is no longer able to develop and to counteract the curvature-induced secondary flow. A similar bed morphology is then observed in the experiments without and with the bubble screen.

The amount of sediment that forms the point bar is considerably higher under live-bed conditions than under clear-water scour conditions. Consequently, the topographic steering is much higher under live-bed conditions. This result indicates that clear-water scour experiments are not representative of natural alluvial rivers and that the sediment mobility is an important control parameter.

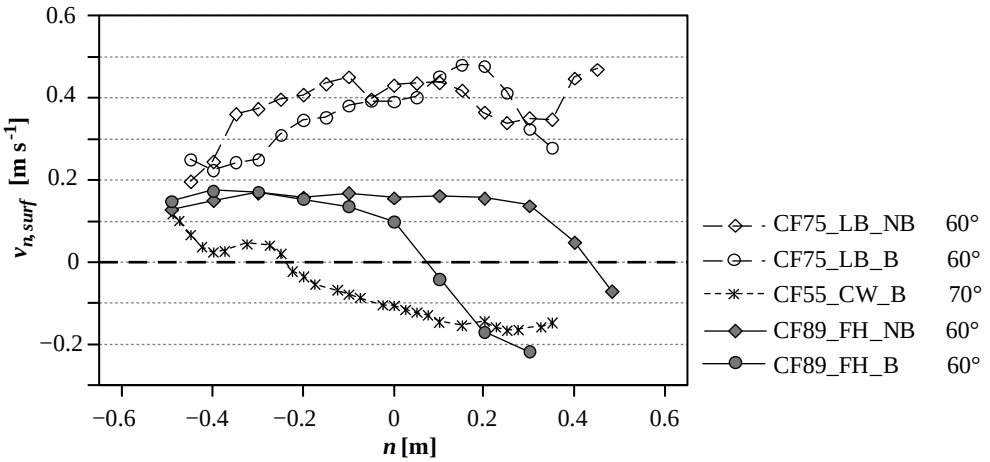

Figure 7.6: Transverse velocity at the water surface, $v_{n,surf}$, in the cross-sections at 60° in the bend for CF75_LB_NB, CF75_LB_B, CF89_FH_NB and CF89_FH_B experiments, and in the cross-section at 70° in the bend for the clear-water scour experiment CF55_CW_B.

The efficiency of the bubble-screen technique to redistribute the bed morphology can be directly deduced from the knowledge of the transverse velocities at the water surface (Figure 7.6). In CF89_FH_NB experiment, low outward velocities are observed on the major part of the cross-section with a constant value of about 0.17 m s^{-1}. $v_{n,surf}$ decreases from n = 0.3 m to

the outer bank due to the outer-bank cell of secondary flow ((Blanckaert and de Vriend, 2004). In CF89_FH_B experiment, the junction between the two secondary flow cells correspond to $v_{n,surf} = 0$ m s^{-1} which occurs at about $n = 0.05$ m.

In CF55_CW_B experiment, the size of the bubble-induced secondary flow is enhanced and extends from $n = -0.25$ m to the bubble screen. The location of the maximal erosion, which coincides with the junction of the two secondary flow cells is found where $v_{n,surf} = 0$ m s^{-1}. The curvature-induced secondary flow is almost not observed which confirm the ability of the bubble screen to redistribute the velocity patterns as well as the bed morphology in this experiment.

In CF75_LB_NB and CF75_LB_B experiments, the outward velocities induced by the curvature are too high to be counteracted by the bubble-induced secondary flow ($v_{n,surf,ref,max} = 0.47$ m s^{-1}). The inward transverse velocities induced by the bubble screen are not observed which indicates that the bubble screen is inefficient to redistribute either velocity pattern or bed morphology.

7.4 FEASIBILITY OF THE BUBBLE-SCREEN TECHNIQUE

7.4.1 Application range of the bubble-screen technique

The reported laboratory experiments indicate that the bubble-screen technique is able to modify the flow patterns and the morphological development of the bend only if the bubble-induced secondary flow cell exists from the bend entry on (Figure 7.3 and Figure 7.4). In first approximation, this condition is satisfied if the bubble-induced transverse inwards velocities at the water surface, $v_{n,surf,bub}$, are strong enough to counteract the curvature-induced transverse outward velocities at the water surface in the reference situation without bubble screen, $v_{n,surf,ref}$.

$$\max\left(-v_{n,surf,bub}\right) > \max\left(v_{n,surf,ref}\right) \tag{7.2}$$

In order to validate this hypothesis, the maximal values of $v_{n,surf,ref}$ measured in the reference experiments CF89_FH_NB and CF75_LB_NB are compared to the maximal transverse velocities at the water surface that can be produced by the bubble screen in the reported laboratory experiments.

Maximal value of $v_{n,surf,bub}$ can be either estimated from a semi-theoretical formula or from measurements performed in the straight open-channel under still water and straight flow conditions (Chapter 4). Different analytical models gives estimation of the maximal value of $v_{n,surf,bub}$, based on the flow depth, air discharge and several empirical parameters under still water conditions (Milgram, 1983; Wen and Torrest, 1987; Fanneløp et al., 1991; Riess and Fanneløp, 1998; Brevik and Kristiansen, 2002). Maximum transverse surface velocities produced by a bubble screen, under still-water conditions, can be straightforwardly determined based on Brevik's formula which does not include empirical parameters (Brevik, 1977; Brevik and Kristiansen, 2002). His assumption is that the upward flow velocity in the centreline of the bubble screen at the water surface is equal to the maximum transverse velocity which occurs at $0.6H$ from the bubble screen, independently of the air discharge. His

observation agrees well with Wen and Torrest (1987) experiments performed with a similar water depth than in the reported experiments.

According to his assumption, the maximum transverse velocity in a plane plume is mainly dependent of the air discharge q_a and the water depth H and is given by:

$$v_{n,surf,bub,\max} = 1.7\left(gq_a\right)^{1/3}\left(1+\frac{H}{H_a}\right)^{-1/3} \tag{7.3}$$

where H_a is the atmospheric pressure head [m]. The atmospheric pressure is expressed as the equivalent of 10 m high water column.

Measurements of the transverse velocities induced by the bubble screen under still water and straight flow conditions (Chapter 4) are compared with the theoretical estimation in order to validate Brevik's formula (Figure 7.7). The same air discharge (q_a = 0.24 dm^3 s^{-1} m^{-1}) was used for all the investigated tests. In the range of investigated flow depth (H from 0.11 m to 0.21 m), the water depth is found to have no influence on $v_{n,surf,bub,max}$. Moreover, under straight flow conditions, the bubble-induced flow structures were not influenced by the base flow velocity. Brevik's model give a value of $v_{n,surf,bub,max}$ = 0.23 m s^{-1} which is lower than the measured velocities at the same distance from the bubble screen $v_{n,surf,bub,max}$ = 0.33 m s^{-1}. This suggests that Brevik's model provides a conservative estimate of $v_{n,surf,bub,max}$.

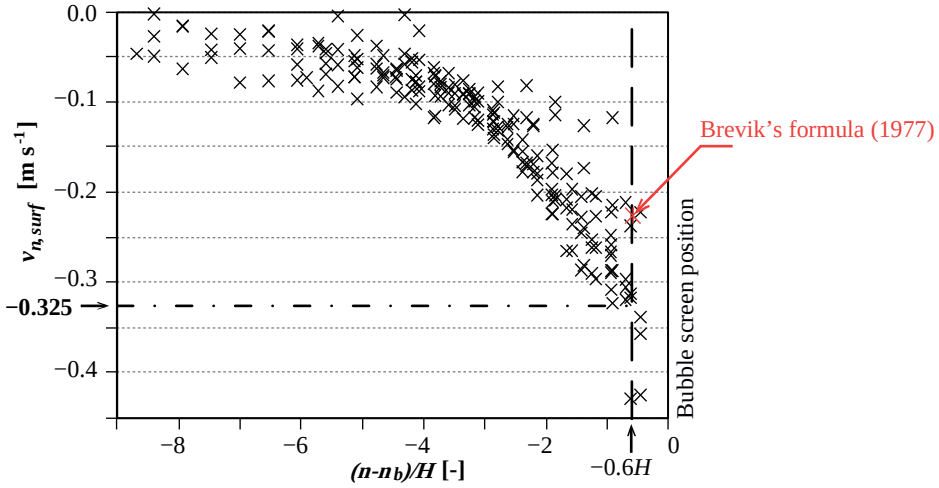

Figure 7.7: Transverse evolution of $v_{n,surf,bub}$ based on measurements in still water and straight flow conditions (Chapter 4). n_b is the location of the porous tube. Measurements were performed with H = 0.11; 0.16 and 0.21 m and q_a = 0.24 dm^3 s^{-1} m^{-1}. Comparison with the value computed with Brevik's formula (1977).

The maximal values of $v_{n,surf,ref}$ measured in the two reference experiments under live-bed conditions and on a fixed horizontal bed (Blanckaert et al., 2008) are compared with $v_{n,surf,bub,max}$ in Figure 7.8. On a developed morphology, $v_{n,surf,ref}$ oscillates along the bend with a maximal value $v_{n,surf,ref}$ = 0.47 m s^{-1} in the cross-section at 60°. Values are higher than on a flat bed because of the strong outward U_n, resulting from the topographic steering that occurs at the entry of the bend.

In CF89_FH_NB experiment, the maximal values of $v_{n,surf,ref}$ are lower than the two estimated values of $max(-v_{n,surf,bub})$. The bubble-induced secondary flow was observed all

around the bed. This first result validates the condition in Eq. (7.2), on an horizontal bed. On a developed morphology, in the upstream part of the bend (30° to 90°), $max(v_{n,surf,ref}) > max(-v_{n,surf,bub})$, and the bubble screen was found to be non efficient in this part. However, in the downstream part of the bend, (90° to 193°), the condition is satisfied and the bubble screen was found to be efficient to redistribute the flow field (Regions 2 and 3) which agree with the hypothesis.

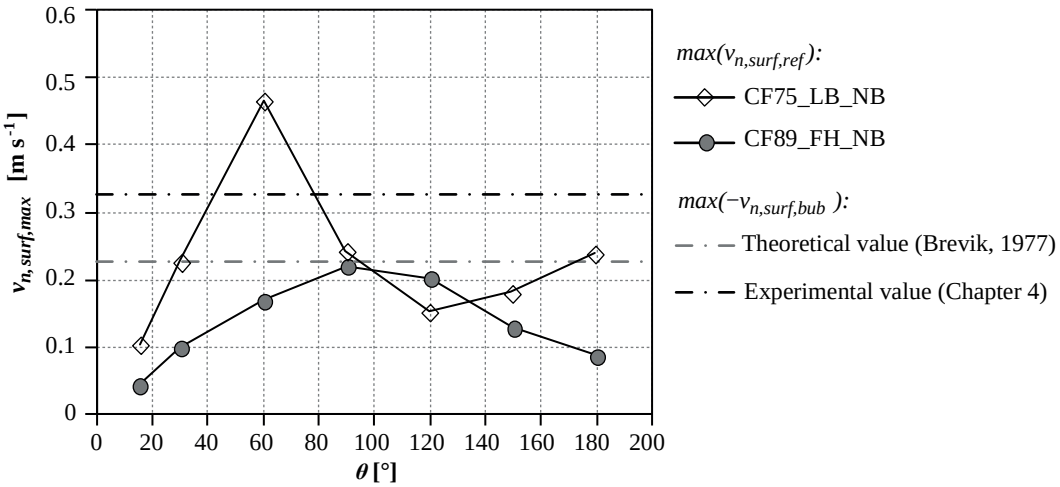

Figure 7.8: Streamwise evolution of the maximal value of $v_{n,surf,ref}$ in the live-bed CF75_LB_NB and in the fixed horizontal bed CF89_FH_NB experiments. Comparison with the maximal value of $v_{n,surf,bub}$ based on the theoretical (Brevik, 1977) and experimental estimation (Chapter 4).

The limit fixed by the theoretical value of Brevik is more conservative than the experimental one and is conserved in the following sections. According to Eq. (7.2), the minimum $v_{n,surf,bub}$ required to counteract the transverse velocity at the water surface induced by the curvature of the flume can be estimated if flow properties in a given bend are known.

7.4.2 Estimation of $v_{n,surf,ref}$

With the considerable increased number of field studies over the last decades, in addition to the improvement in measuring equipment, $v_{n,surf,ref}$ can be estimated by direct measures of the 3-D flow patterns in the concerned river (Frothingham and Rhoads, 2003; Blanckaert et al., 2009; Nanson, 2010; Engel and Rhoads, 2012; Sukhodolov, 2012). However, field measurements are mostly not feasible during high-flow conditions which are mainly responsible for the river morphological development.

Modeling of three-dimensional flow field in a curved channel can be performed by means of large-eddy simulation (LES) (van Balen et al., 2009; van Balen et al., 2010a; van Balen et al., 2010b) or Reynolds-averaged numerical simulations (RANS) (Zeng et al., 2008; van Balen et al., 2010b). However, these models require a detailed information of the bathymetry and are often time-consuming and computationally too expensive when applied to real river configurations (Rüther and Olsen, 2007; Fischer-Antze et al., 2008).

A straightforward first assessment of the transverse velocities at the water surface can be performed using a reduced-order nonlinear hydrodynamic model (Blanckaert and de Vriend, 2003; 2010). This model is derived from the three-dimensional momentum equations,

and accounts for curvature-induced secondary flow, topographic steering and inertia. This model successfully simulated the flow redistribution and the secondary flow in various laboratory or field experimental studies (Ottevanger et al., 2012).

In the model, the velocity field is described by four parameters : U_w the cross-sectional averaged velocity, α_s the normalized transverse velocity gradient, defined in Eq. (7.4), U_n the cross-flow and the intensity of the curvature-induced secondary flow.

$$\frac{\alpha_s}{R} = \frac{1}{U_s}\frac{\partial U_s}{\partial n} \tag{7.4}$$

The bed topography is described either by means of the scour factor *A/R*, derived from the transverse bed slope (Eq. (7.5)) or computed as part of the model solution.

$$\frac{A}{R} = -\frac{1}{H_w}\frac{\partial z_b}{\partial n} \tag{7.5}$$

where H_w is the cross-sectional averaged velocity and $\partial z_b/\partial n$ is the transverse bed slope.

As mentioned in Eq. (7.1), the secondary flow can be decomposed in a translatory component U_n and a circulatory motion v_n^*. Commonly used depth-integrated models (Rozovskii, 1957; de Vriend, 1977; Blanckaert and de Vriend, 2003) predict the equilibrium profile of the transverse velocity to increase proportionally with the curvature ratio *H/R* as:

$$v_n^* = \frac{U_w H_w}{R} f_{n,0}(C) \tag{7.6}$$

where C is the Chézy friction coefficient and $f_{n,0}$ is a function from linear model that represents the form of the vertical profiles of v_n^* (de Vriend, 1977).

At the water surface, Eq. (7.6) leads to:

$$v_{n,surf,ref}^* = \frac{U_w H_w}{R} f_{n,0,\max}(C) \tag{7.7}$$

Blanckaert et de Vriend (2003; 2010) have shown that the linear-formulation overestimates the strength of the curvature-induced secondary flow. Indeed, a non-linear feedback exists between the streamwise and secondary flows which induces a self-saturation of the secondary flow (de Vriend, 1981; Yeh and Kennedy, 1993). This non-linear feedback is integrated in the non-linear model of Blanckaert and de Vriend (2010) which also provides the value for U_n:

$$v_{n,surf,ref}^* = U_w H_w \left(\frac{\sqrt{f_n^2}}{R}\right)\frac{1}{\sqrt{f_{n,0}^2}} f_{n,0,\max} \tag{7.8}$$

where f_n is the function from the non-linear model that includes saturation of the curvature-induced secondary flow.

Finally, the non-linear model allows to estimate $v_{n,surf,ref}$ according to Eq. (7.9):

$$v_{n,surf,ref} = U_n + U_w H_w \left(\frac{\sqrt{f_n^2}}{R} \right) \frac{1}{\sqrt{f_{n,0}^2}} f_{n,0,\max}(C) \tag{7.9}$$

Subsequently, with this approach, computation of $v_{n,surf,ref}$ in a given bend only requires few parameters of the river geometry, sediment and flow characteristics:

$$v_{n,surf,ref} = f\left(C, \frac{A}{R}, Q, B \right) \tag{7.10}$$

Blanckaert and de Vriend's model (2010) has been applied to CF89_FH_NB and CF75_LB_NB experiments. In the mobile-bed experiment, *A/R* has been derived from the detailed topographic measurements.

Table 7.2 summarizes the solutions for $v_{n,surf,ref,max}$ resulting from the non-linear modeling of CF89_FH_NB and CF75_LB_NB experiments. Comparing to the experimental results, the non-linear model underestimates $v_{n,surf,ref,max}$ by 27% and by 4 % in CF89_FH_NB and CF75_LB_NB experiments, respectively. The simulations give a good estimation of $v_{n,surf,ref,max}$ with only few required parameters, especially in the case of a mobile bed.

Table 7.2: Comparison of linear-model and non-linear model results with experimental data.

Label				Experiments	Non-linear model
	Q	H/R	$1/\sqrt{C_{f0}}$	$v_{n,surf,ref,max}$	$v_{n,surf,ref,max}$
	$[m^3\ s^{-1}]$	[-]	[-]	$[m\ s^{-1}]$	$[m\ s^{-1}]$
CF89_FH_NB	0.089	0.093	11.7	0.22	0.16
CF75_LB_NB	0.075	0.083	11.4	0.47	0.45

C_{f0} (the subscript 0 refers to straight uniform flow) is the friction factor which relates to the Chézy friction coefficient C via $C_f = g/C^2$

7.4.3 Estimation of the minimum required air discharge $q_{a,min}$

As the energy expended by an air compressor depends on the air discharge, the relative operating cost of a compressor is directly related to the air discharge (Sahoo and Luketina, 2006). Consequently, the cost of the bubble-screen technique will be the lowest if the air discharge is minimized.

Based on the values of $v_{n,surf,ref}$ determined by numerical modeling, the required (or minimum) air discharge to counteract the curvature-induced secondary flow can be estimated, based on the hypothesis in Eq. (7.2), and on Brevik's theoretical model in Eq. (7.3). The minimum required air discharge can be then computed as:

$$q_{a,\min} = \left(\frac{1}{1.7} \max\left(v_{n,surf,ref} \right) \right)^3 \frac{1}{g} \left(1 + \frac{H}{H_a} \right) \tag{7.11}$$

This result allows to evaluated the minimum cost of the required installation and determined if the solution is economically feasible.

7.5 APPLICATION CASES

In order to have an idea on the range of transverse velocities encountered at the water surface $v_{n,surf,ref}$ in field configurations, two sharply curved bends will be considered in the present section. The first case considers a bend of the Ledra river (Italy) which was investigated by Blanckaert et al. (2009). Places at the outer bank that are vulnerable to erosion were protected by riprap. Flow patterns in six cross-sections and bed topography in the whole reach were documented. The second case concerns a bend of the East Nishnabotna river (USA) which was investigated by Odgaard and Mosconi (1987). The purpose of their study was to design bottom vanes in order to eliminate the secondary flow component along the bank and reduce the bend migration (6-9 m/year). It is quite common that the most vulnerable places for bank erosion are protected, even in natural rivers. Main reach-averaged characteristics of these two meanders are summarized in Table 7.3.

Table 7.3: Estimation of geometrical parameters in some natural meandering rivers. *[1]* Data from Odgaard and Mosconi (1987), *[2]* Data from Blanckaert et al. (2009).

Label	Q $[m^3\ s^{-1}]$	B $[m]$	H $[m]$	U $[m\ s^{-1}]$	R $[m]$	C $[m^{1/2}\ s^{-1}]$	R/B $[-]$	R/H $[-]$	B/H $[-]$
East Nishnabotna river (USA) *[1]*	116	50	2.0	1.25	238	35.4	4.8	119	25
Ledra river (Italy) *[2]*	18	15	1.5	0.8	45	22.8	3	30	10

The bed topography for the Ledra river was available, and the scour factor A/R is directly derived from the transverse bed slope measurements. Model results are illustrated in Figure 7.9 where the sections with maximal $v_{n,surf,ref}$ have been indicated. Three sections with high transverse velocities at the water surface were found with a maximum value of 0.14 m s^{-1}. The predicted $v_{n,surf,ref}$ agrees reasonably well with the field measurements which were within the range between –0.11 and –0.20 m s^{-1} around the section 2.

Section	$v_{n,surf,ref}$ $[m\ s^{-1}]$
①	0.11
②	−0.13
③	0.14

Figure 7.9: Bend on the Ledra River (Italy, Image: Google Earth) and maximal $v_{n,surf,ref}$ computed with Blanckaert and de Vriend's model (2010). The dashed lines indicate the extent of the numerical simulation. The white arrows indicate the location of the maximum values of $v_{n,surf,ref}$.

In the Nishnabotna modeling, the bed topography has not been measured on a refined grid. Determination of *A/R* was based on Odgaard's theory (1981):

$$\frac{\partial z_b}{\partial n} = K \frac{H}{R} \tag{7.12}$$

The factor of proportionality, K = 5.6, was estimated from 21 cross-sectional measurements performed under different flow conditions on the East Nishnabotna river (Odgaard and Mosconi, 1987). Model results for the East Nishnabotna river are summarized in Figure 7.10. Five cross-sections characterized by high $v_{n,surf,ref}$ were determined with a maximal value of 0.24 m s^{-1}. Unfortunately, field measurements of $v_{n,surf,ref}$ in the Nishnabotna East river are not available for comparison.

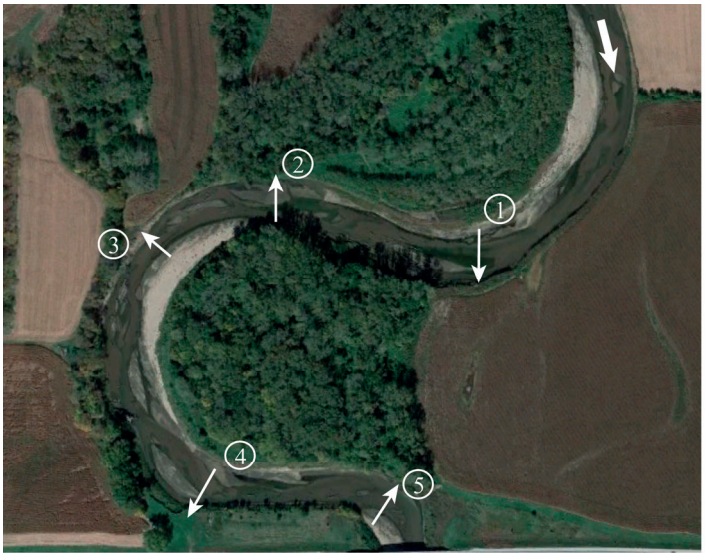

Section	$v_{n,surf,ref}$ [m s^{-1}]
①	0.12
②	−0.12
③	−0.10
④	−0.15
⑤	0.24

Figure 7.10: Bend on the Nishnabotna East river (USA, Image: Google Earth) and maximal $v_{n,surf,ref}$ computed with Blanckaert and de Vriend's model (2010). The white arrows indicate the location of the maximum values of $v_{n,surf,ref}$.

From the simulation results, the minimum air discharges required to counteract the curvature-induced secondary flow for the investigated water discharges are computed with Eq. (7.11). Results for the two investigated bends are summarized in Table 7.4.

Table 7.4: Estimation of required air discharges for the two investigated sharp bends.

Label	$max(v_{n,surf,ref})$ [m s^{-1}]	q_a [dm^3 s^{-1} m^{-1}]	L [m]	Qa [m^3 s^{-1}]
East Nishnabotna river (USA)	0.24	0.34	951	0.33
Ledra river (Italy)	0.14	0.07	671	0.04

L is the length of the required air-line source and Q_a the required air discharge.

The required air discharges in the two meanders are not so high comparing to other environmental application. For example, lakes destratification are using air discharges ranging from 0.01 to 1.2 m^3 s^{-1} (Wüest et al., 1992; Schladow, 1993; Sahoo and Luketina, 2006; Boegman and Sleep, 2012) and Neto et al. (2007) who applied a bubble screen to increased the dissolved oxygen level in an ice-covered river used an oxygen flow rate of 0.87 m^3 s^{-1} on a

air-line source length of 52 m. Consequently, the bubble-screen technique can represent a good alternative to influence the flow field and the bed morphology in rivers with a non-prohibitive cost as compared to other environmental applications.

7.6 DISCUSSION

Although the two mentioned application cases are natural rivers, the bubble-screen technique is intended to be applied in open-channel bends with fixed or protected banks. Consequently, bank erosion should not be considered. The bubble screen is an additional technique to attenuate bed morphology gradients and to shift bed erosion away from the outer bank without affecting the bank.

A special feature of meanders with straight flood plain banks is the reversal of the sense of rotation of the curvature-induced secondary flow between inbank and overbank flows (Shiono and Muto, 1998; Wormleaton et al., 2005). The primary velocity within the main channel below the bankfull level tends to follow the channel axis, whereas above the bankfull level it tends to follow the valley direction. Interaction between flows coming from the floodplain and the main channel generates an additional secondary flow cell near the bank.

The effect of the bubble screen in configurations with overbank flow has not been investigated yet. A conservative operational approach would consist in turning of the bubble generation in conditions of overbank flow to avoid any potential adverse effect.

7.7 CONCLUSIONS

A bubble screen, placed near the outer bank in a sharply curved flume, can produce a bubble-induced secondary flow that is able to redistribute the flow pattern, the bed shear stress distribution and consequently the bend morphology.

Three types of experiments performed under different conditions of bed and sediment transport have shown that the bubble screen is more efficient to redistribute velocity pattern and bed morphology under clear-water scour conditions than under live-bed conditions, especially in the upstream part of the bend. Indeed, the development of the point bar, which is higher with sediment feeding, enhances topographic steering which increases the transverse outward velocities that the bubble screen has to counteract.

The bubble screen is found to be efficient if the maximum inward transverse velocities at the water surface produced by the bubble screen are higher than the maximal outward transverse velocities induced by the bend curvature. Moreover, this condition has to be satisfied over the whole length of the bend.

Based on this criteria, a straightforward method to evaluate the efficiency of a bubble screen to redistribute the flow patterns and the morphology has been proposed, and illustrated by means of two application cases. The minimum air discharges required to counteract the maximal transverse velocities induced by the curvature are relatively low as compared to other types of environmental applications of the bubble screens.

The bubble-screen technique has the potential to be applied as a countermeasure for reducing bend scour and inner bank sediment deposition in low-gradient rivers.

Chapter 8

Conclusions

Rivers shape our landscapes, provide us with food and water, constitute routes for navigation. Since centuries, Humans' desire to control its natural force leads to strong modification of the river ecosystem. Construction of dams modifies the sedimentary balance and are obstacles for fish migration. River training works can damage the natural morphology of the river and can lead to a lack of biodiversity in river ecosystem. At the end of the 20^{th} century, river engineering tends to be more respectful of river environments. River restoration tries to give more freedom to the river system while maintaining its economical, social and safety aspects.

The present research project introduces an innovative technique to influence river morphodynamics without acting directly on the river morphology but on the flow field. A bubble screen or curtain, generated by a porous tube linked to an air compressor generates a secondary flow that can be used to redistribute the base flow patterns and consequently the bed morphology. This technique, already applied in a sustainable way for destratification in lakes and reservoirs, has never been investigated in shallow free-surface flow. The bubble-screen technique could be used to reduce local scour at structures in rivers as bridge piers and abutments or, as it has been investigated in the present research, to reduce local scour near the outer bank in open-channel bends or meanders.

The application of the bubble-screen technique in several laboratory configurations has shown promising results which are summarized in the following.

8.1 SYNTHESIS

Measurements of the three-dimensional flow field and the bed morphology in several experiments performed with and without the use of the bubble screen have shown that the bubble-screen technique has the potential to redistribute the flow pattern and the bed morphology in sharply curved open-channel bends. At present, application of the bubble-screen technique should, however, be limited to configurations with fixed banks. Main results of the different investigated laboratory configurations are summarized below.

Influencing flow patterns and bed morphology in straight open-channels by means of a bubble screen

Experiments performed under still and straight flow conditions show that the bubble screen generates a bubble-induced secondary flow which size and strength are found to increase proportionally with the water depth. These results are in line with the literature for higher water depths. Experiments performed without sediment transport under straight flow conditions show that the base flow does not modify the bubble-induced flow structures but only advects them in the downstream direction. However, the streamwise velocity pattern is modified under the action of the bubble-induced secondary flow. In the vicinity of the porous tube, the maximum streamwise velocities are found at about mid-depth which increase the bed shear stress. Under mobile-bed conditions, this leads to the development of a scour hole which develops at the end of the bubble-induced secondary flow where the maximal downward velocities are observed. Moreover, a strengthening process is observed between the base flow, the bubble screen, the bubble-induced secondary flow and the morphology which leads to an increase of the bubble-induced flow structures in the downstream direction.

Reduction of bend scour under clear-water scour conditions with a bubble screen

Under clear-water scour conditions, a bubble screen, located near the outer bank on the whole length of a sharply curved bend, generates a bubble-induced secondary flow with a sense of rotation opposite to the curvature-induced secondary flow. Both secondary flows redistribute the streamwise velocity patterns. The cores of maximum streamwise and downward velocities are no longer near the outer bank but at the junction between the bubble-induced and the curvature-induced secondary flow cells, in the central part of the cross-section. Consequently, maximal bend scour is observed in the same location where it does not endanger the outer bank stability anymore. Moreover, morphological gradients are reduced as the point bar does not develop.

Influence of a bubble screen on bend morphodynamics under live-bed conditions

Under live-bed conditions, the efficiency of the bubble screen is found to be lower than under clear-water scour conditions. In the upstream part of the bend, the transverse velocities at the water surface induced by the bubble screen are not high enough to counteract both the circulatory motion and the cross-flow that develops with topographic steering. Consequently, bend scour occurs in the same location than in a similar experiment without the bubble screen. However, in the downstream part of the bend, the bubble screen is efficient to redistribute the velocity patterns and the bed morphology as the second scour hole is not observed at the outer

bank but in the central part of the cross-section. Experiments performed with several position of the bubble screen respective to the outer banks show that the latter is more efficient to influence the morphological development when placed the nearest to the outer bank

Application range of a bubble screen for reducing scour in open-channel bends

Objectives of this research are not only to describe and explain the flow and morphological features induced by the bubble screen but also to provide preliminary guidelines for river engineering. A methodology based on the evaluation of the curvature-induced transverse velocities at the water surface and the maximal transverse velocities at the water surface that can produce a bubble screen is introduced. This method is successfully applied in two sharply curved meanders in the Nishnabotna East river (USA) and the Ledra river (Italy). This methodology can be used either to determine if a given bubble screen will be efficient in a specific case of application or to determine the minimum air discharge required to counteract the base flow, and consequently the corresponding cost of the bubble-screen technique. The required air discharges for the two application cases are not so high as compared to other environmental applications of bubble screens.

8.2 OUTLOOK

8.2.1 Application of the bubble-screen technique in open-channel bends

Knowledge on the efficiency and applicability of the bubble-screen technique in open-channel bends may be further increased by combining laboratory experiments, numerical simulations, and field investigations.

Further laboratory investigations

Laboratory experiments are simplified configurations that allow to investigate the effect of a single parameter under controlled conditions. Several parameters have already been investigated in the present research project. However, the investigated parameter space could largely be broaden for example by investigating:

- effect of sediment characteristics (mean diameter and standard deviation).
  Very fine sediment should be maintained in suspension by the bubble-induced secondary flow. In the case of very coarse gravel, the bubble screen may not be sufficient to influence sediment transport;
- effect of shape, inclination and roughness of the outer bank.
  As observed in the present research, additional erosion was observed between the bubble screen and the outer bank. Better knowledge is required to limit this adverse effect;
- effect of bend geometry (curvature ratio H/R and aspect ratio B/H).
  The strength of the curvature-induced secondary flow is directly dependent of the river geometry. Consequently, the efficiency of the bubble-screen technique is also directly related to the river planform.

These further experiments would provide additional data for the validation of numerical morphodynamic codes that can account for the effects of the bubble screen.

Further numerical simulations

Numerical modeling can extend the parameter space, which is inevitably limited to a relatively small number of experiments.

In this research project, the efficiency of the bubble-screen technique is straightforwardly estimated by means of a reduced-order model. Better insights on the generated flow structures and interplay with the bed morphology can be provided using three-dimensional models that are already used in open-channel bend morphodynamics, as well as for modeling air-bubble plumes.

Implementation of the bubble screen effect in a 3D morphodynamic model can provide a tool that can be used to optimize and design the bubble-screen technique in prototype configurations.

Prototype installation

Finally, the feasibility of applying the bubble-screen technique in natural rivers should be directly investigated on the field. The results could guarantee an optimal feedback and transfer of the research results to the engineering practice, as the scale effect are supposed to have their importance. It could for example include measurements of the bed morphology and the flow field in a reference situation without the bubble screen and during operation of the bubble screen.

Comparison of laboratory experiments with prototype scale will also give some insights on scale effects.

8.2.2 Extension to a wider range of configurations

The bubble-screen technique may be applied in a wide range of configurations. As shown in this report, it could be an interesting technique to prevent local scour due to pronounced downward velocities impinging on the bed, such as bridge pier or abutment scour.

Preliminary experimental research has been performed on the application of the bubble-screen technique to reduce local scour around abridge pier (Appendix E). A bubble screen placed on a collar at the upstream side of the bridge pier was used to reduced the downward velocity. Efficiency of the bubble-screen technique was strongly related to water and air discharges but was found to slightly reduce the maximal scouring depth. Further research is required to investigate how the flow field is redistributed by the bubble screen.

Other potential applications of the bubble-screen technique in river morphodynamics could be to reduce scour near bridge abutments or to prevent sediment deposition in harbours or reservoirs.

Moreover, the bubble-screen technique can be considered using a multidisciplinary approach, for example:

- to influence the river morphological development during high-flow conditions and to increase the dissolved oxygen level in the river during low-flows, by using the same oxygen-bubble screen,
- to avoid sediment deposition in navigation channel and be used meanwhile as breakwaters in order to reduce the amplitude of ship waves against erodible banks,
- during river training works to avoid sediment deposition while reducing the acoustic waves induced by works to protect the aquatic life.

Both the promising results of this research and the wide range of possible applications show that the bubble-screen technique has the potential for practical applications in hydraulic engineering.

References

Abad J. D., and Garcia M. H. (2009a). Experiments in a high-amplitude Kinoshita meandering channel: 2. Implications of bend orientation on bed morphodynamics, *Water Resources Research*, 45, W02402, doi:10.1029/2008WR007017.

Abad J. D., and Garcia M. H. (2009b). Experiments in a high-amplitude Kinoshita meandering channel: 1. Implications of bend orientation on mean and turbulent flow structure, *Water Resources Research*, 45, W02401, doi:10.1029/2008WR007016.

Batchelor G. K. (1967). *An introduction to fluid dynamics*, 615 pp., Cambridge University Press, Cambridge, England.

Bathurst J. C., Thorne C. R., and Hey R. D. (1979). Secondary flow and shear-stress at river bends, *Journal of the Hydraulics Division-Asce*, 105(10), 1277-1295.

Blanckaert K. (2002). Flow and turbulence in sharp open-channel bends, Thesis 2545, Ecole Polytechnique Fédérale de Lausanne, Lausanne, Switzerland.

Blanckaert K. (2010). Topographic steering, flow recirculation, velocity redistribution, and bed topography in sharp meander bends, *Water Resources Research*, 46, W09506, doi:10.1029/2009WR008303.

Blanckaert K. (2011). Hydrodynamic processes in sharp meander bends and their morphological implications, *Journal of Geophysical Research-Earth Surface*, 116, F01003, doi:10.1029/2010JF001806.

Blanckaert K., and Graf W. H. (2001). Mean flow and turbulence in open-channel bend, *Journal of Hydraulic Engineering-Asce*, 127(10), 835-847.

Blanckaert K., and de Vriend H. J. (2003). Nonlinear modeling of mean flow redistribution in curved open channels, *Water Resources Research*, 39(12), 1375-1381.

Blanckaert K., and de Vriend H. J. (2004). Secondary flow in sharp open-channel bends, *Journal of Fluid Mechanics*, 498(1), 353-380.

Blanckaert K., and Graf W. H. (2004). Momentum transport in sharp open-channel bends, *Journal of Hydraulic Engineering-Asce*, 130(3), 186-198.

Blanckaert K., and Lemmin U. (2006). Means of noise reduction in acoustic turbulence measurements, *Journal of Hydraulic Research*, 44(1), 3-17.

Blanckaert K., and de Vriend H. J. (2010). Meander dynamics: A nonlinear model without curvature restrictions for flow in open-channel bends, *Journal of Geophysical Research-Earth Surface*, 115, F04011, doi:10.1029/2009JF001301.

Blanckaert K., Duarte A., and Schleiss A. J. (2010). Influence of shallowness, bank inclination and bank roughness on the variability of flow patterns and boundary shear stress due to secondary currents in straight open-channels, *Advances in Water Resources*, 33(9), 1062-1074.

Blanckaert K., Buschman F. A., Schielen R., and Wijbenga J. H. A. (2008). Redistribution of velocity and bed-shear stress in straight and curved open channels by means of a bubble screen: Laboratory experiments, *Journal of Hydraulic Engineering-Asce*, 134(2), 184-195.

Blanckaert K., Schnauder I., Sukhodolov A., van Balen W., and Uijttewaal W. S. J. (2009). Meandering: field experiments, laboratory experiments and numerical modeling, *Proc. of the 6th IAHR Symposium on River, Coastal and Estuarine Morphodynamics*, Santa Fe, Argentina.

Boegman L., and Sleep S. (2012). Feasibility of bubble plume destratification of central lake Erie, *Journal of Hydraulic Engineering-Asce*, 138(11), 985-989.

Bombardelli F. A., Buscaglia G. C., Rehmann C. R., Rincón L. E., and García M. H. (2007). Modeling and scaling of aeration bubble plumes: A two-phase flow analysis, *Journal of Hydraulic Research*, 45(5), 617-630.

Bradshaw P. (1987). Turbulent secondary flows, *Annual Review of Fluid Mechanics*, 19, 53-74.

Brevik I. (1977). Two-dimensional air-bubble plume, *Journal of the Waterway Port Coastal and Ocean Division-Asce*, 103(1), 101-115.

Brevik I., and Kristiansen O. (2002). The flow in and around air-bubble plumes, *International Journal of Multiphase Flow*, 28(4), 617-634.

Bulson P. S. (1963). Large scale bubble breakwater experiments, *Dock and Harbour Authority, London, England*, XI(516), 191-197.

Bulson P. S. (1968). The theory and design of bubble breakwaters, *Proc. of the 11th Conference of Coastal Engineering*, 2, 995-1015.

Chèvre P., and Schleiss A. J. (2005). Influence of the macro-roughness of a bank protection by rip-rap on bed load transport and local scouring in river bends, *Proc. of the XXXI IAHR Congress*, 1356-1365, Seoul, Korea.

Church M. (2007). 1 Multiple scales in rivers, *Developments in Earth Surface Processes, Gravel-Bed Rivers IV: From process understanding to river restoration*, 11, 3-28.

de Vriend H. J. (1977). Mathematical-model of steady flow in curved shallow channels, *Journal of Hydraulic Research*, 15(1), 37-54.

de Vriend H. J. (1981). Velocity redistribution in curved rectangular channels, *Journal of Fluid Mechanics*, 107(JUN), 423-439.

DeMoyer C. D., Schierholz E. L., Gulliver J. S., and Wilhelms S. C. (2003). Impact of bubble and free surface oxygen transfer on diffused aeration systems, *Water Research*, 37(8), 1890-1904.

Dietrich W. E., and Smith J. D. (1983). Influence of the Point-Bar on Flow through Curved Channel, *Water Resources Research*, 19(5), 1173-1192.

Ditmars J. D., and Cederwall K. (1974). Analysis of air-bubble plumes, *Proc. of the 14th Conference on Coastal Engineering*, 2209-2226, Copenhagen.

Duarte A. (2008). An experimental study on main flow, secondary flow and turbulence in open-channel bends with emphasis on their interaction with the outer-bank geometry, Thesis 4227, Ecole Polytechnique Fédérale de Lausanne, Switzerland, Lausanne.

Dugué V., Blanckaert K., and Schleiss A. J. (2011). Influencing bend morphodynamics by means of an air-bubble screen - Topography and velocity field., *Proc. of the 7th IAHR Symposium on River, Coastal and Estuarine Morphodynamics*, 2239-2247, Beijing, China.

Eidnes G. (2004). Bubble curtain to prevent freezing, *Proc. of the 14th International Offshore and Polar Engineering Conference*, 905-909, International Society Offshore & Polar Engineers, Toulon, France.

Engel F. L., and Rhoads B. L. (2012). Interaction among mean flow, turbulence, bed morphology, bank failures and channel planform in an evolving compound meander loop, *Geomorphology*, 163, 70-83.

Engelund F. (1974). Flow and bed topography in channel bends, *Journal of the Hydraulics Division-Asce*, 100(NHY11), 1631-1648.

Fanneløp T. K. (1994). *Fluid mechanics for Industrial Safety and Environmental Protection*, Industrial Safety series, 3, Elsevier, Amsterdam.

Fanneløp T. K., Hirschberg S., and Küffer J. (1991). Surface current and recirculating cells generated by bubble curtains and jets, *Journal of Fluid Mechanics*, 229, 629-657.

Fazli M., Ghodsian M., and Neyshabouri S. (2008). Scour and flow field around a spur dike in a 90 degrees bend, *International Journal of Sediment Research*, 23(1), 56-68.

Ferguson R. I., Parsons D. R., Lane S. N., and Hardy R. J. (2003). Flow in meander bends with recirculation at the inner bank, *Water Resources Research*, 39(11).

Fischer-Antze T., Olsen N. R. B., and Gutknecht D. (2008). Three-dimensional CFD modeling of morphological bed changes in the Danube River, *Water Resources Research*, 44(9).

Friedl M. J., and Fanneløp T. K. (2000). Bubble plumes and their interaction with the water surface, *Applied Ocean Research*, 22(2), 119-128.

Frothingham K. M., and Rhoads B. L. (2003). Three-dimensional flow structure and channel change in an asymmetrical compound meander loop, Embarras River, Illinois, *Earth Surface Processes and Landforms*, 28(6), 625-644.

Goossens L. (1979). Reservoir destratification with bubble columns, PhD-thesis, Delft University press, Delft, The Netherlands.

Hersberger D. S. (2002). Wall roughness effects on flow and scouring in curved channels with gravel bed, Thesis 2632, Ecole Polytechnique Fédérale de Lausanne, Lausanne, Switzerland.

Hurther D., and Lemmin U. (1998). A constant-beam-width transducer for 3D acoustic Doppler profile measurements in open-channel flows, *Measurement Science & Technology*, 9(10), 1706-1714.

Jirka G. H., and Harleman D. R. F. (1979). Stability and mixing of a vertical plane buoyant jet in confined depth, *Journal of Fluid Mechanics*, 94(SEP), 275-304.

Johannesson H., and Parker G. (1989). Velocity redistribution in meadering rivers, *Journal of Hydraulic Engineering-Asce*, 115(8), 1019-1039.

Kashyap S., Constantinescu G., Rennie C. D., Post G., and Townsend R. (2012). Infuence of channel aspect ratio and curvature on flow, secondary circulation, and bed shear stress in a rectangular channel bend, *Journal of Hydraulic Engineering-Asce*, 138(12), 1045-1059.

Kobus H. E. (1968). Analysis of the flow induced by air-bubble systems, *Proc. of the 11th Conference on Coastal Engineering*, II, 1016-1031, London.

Kubasch J. H. (2001). Bubble Hydrodynamics in Large Pools, PhD-thesis, ETH, Zürich, Switzerland.

Leifer I., Patro R. K., and Bowyer P. (2000). A study on the temperature variation of rise velocity for large clean bubbles, *Journal of Atmospheric and Oceanic Technology*, 17(10), 1392-1402.

Lemckert C. J., and Imberger J. (1993). Energetic bubble plumes in arbitrary stratification, *Journal of Hydraulic Engineering-Asce*, 119(6), 680-703.

Lemmin U., and Rolland T. (1997). Acoustic velocity profiler for laboratory and field studies, *Journal of Hydraulic Engineering-Asce*, 123(12), 1089-1098.

Martin-Vide J. P., Roca M., and Alvarado-Ancieta C. A. (2010). Bend scour protection using riprap, *Proc. of the Institution of Civil Engineers-Water Management*, 163(10), 489-497.

Masjedi A., Bejestan M. S., and Esfandi A. (2010). Experimental study on local scour around single oblong pier fitted with a collar in a 180 degree flume bend, *International Journal of Sediment Research*, 25(3), 304-312.

McDougall T. J. (1978). Bubble Plumes in Stratified Environments, *Journal of Fluid Mechanics*, 85(4), 655-672.

Milgram J. H. (1983). Mean flow in round bubble plumes, *Journal of Fluid Mechanics*, 133(AUG), 345-376.

Nakai M., and Arita M. (2002). An experimental study on prevention of saline wedge intrusion by an air curtain in rivers, *Journal of Hydraulic Research*, 40(3), 333-339.

Nanson R. A. (2010). Flow fields in tightly curving meander bends of low width-depth ratio, *Earth Surface Processes and Landforms*, 35(2), 119-135.

Nelson J. E. (1988). Mechanics of flow and sediment transport over non-uniform erodible beds, University of Washington, Seattle.

Neto I. E. L., Zhu D. Z., and Rajaratnam N. (2008). Effect of tank size and geometry on the flow induced by circular bubble plumes and water jets, *Journal of Hydraulic Engineering-Asce*, 134(6), 833-842.

Neto I. E. L., Zhu D. Z., Rajaratnam N., Yu T., Spafford M., and McEachern P. (2007). Dissolved oxygen downstream of an effluent outfall in an ice-covered river: Natural and artificial aeration, *Journal of Environmental Engineering-Asce*, 133(11), 1051-1060.

Nikora V. (2007). 3 Hydrodynamics of gravel-bed rivers: scale issues, *Developments in Earth Surface Processes, Gravel-Bed Rivers IV: From process understanding to river restoration*, 11, 61-81.

Odgaard A. J. (1981). Transverse bed slope in alluvial channel bends, *Journal of the Hydraulics Division-Asce*, 107(12), 1677-1694.

Odgaard A. J., and Spoljaric A. (1986). Sediment control by submerged vanes, *Journal of Hydraulic Engineering-Asce*, 112(12), 1164-1181.

Odgaard A. J., and Mosconi C. E. (1987). Streambank protection by submerged vanes, *Journal of Hydraulic Engineering-Asce*, 113(4), 520-536.

Odgaard A. J., and Bergs M. A. (1988). Flow processes in a curved alluvial channel, *Water Resources Research*, 24(1), 45-56.

Odgaard A. J., and Wang Y. (1991). Sediment management with submerged vanes .1. Theory, *Journal of Hydraulic Engineering-Asce*, 117(3), 267-283.

Olesen K. W. (1987). Bed topography in shallow river bends, Delft University of Technology, Delft, The Netherlands.

Ottevanger W., Blanckaert K., and Uijttewaal W. S. J. (2012). Processes governing the flow redistribution in sharp river bends, *Geomorphology*, 163, 45-55.

Przedwojski B. (1995). Bed topography and local scour in rivers with banks protected by groynes, *Journal of Hydraulic Research*, 33(2), 257-273.

Riess I. R., and Fanneløp T. K. (1995). On deflecting drifting icebergs, *Proc. of the 14th International Conference on Offshore Mechanics and Artic Engineering*, Copenhagen.

Riess I. R., and Fanneløp T. K. (1998). Recirculating flow generated by line-source bubble plumes, *Journal of Hydraulic Engineering-Asce*, 124(9), 932-940.

Roca M., Martin-Vide J. P., and Blanckaert K. (2007). Reduction of bend scour by an outer bank footing: Footing design and bed topography, *Journal of Hydraulic Engineering-Asce*, 133(2), 139-147.

Rozovskii I. L. (1957). *Flow of water in bends of open channels*, Academy of Sciences of the Ukrainian SSR, Kiev 1957; Israel program for Scientific Translations, Jerusalem, 1961.

Rüther N., and Olsen N. R. B. (2007). Modelling free-forming meander evolution in a laboratory channel using three-dimensional computational fluid dynamics, *Geomorphology*, 89(3-4), 308-319.

Sager D. R., Hocutt C. H., and Stauffer J. R. (1987). Estuarine fish responses to strobe light, bubble curtains and strobe light bubble-curtain combinations as influenced by water-flow rate and flash frequencies, *Fisheries Research*, 5(4), 383-399.

Sahoo G. B., and Luketina D. (2006). Response of a tropical reservoir to bubbler destratification, *Journal of Environmental Engineering-Asce*, 132(7), 736-746.

Schladow S. G. (1992). Bubble plume dynamics in a stratified medium and the implications for water quality amelioration in lakes, *Water Resources Research*, 28(2), 313-321.

Schladow S. G. (1993). Lake destratification by bubble-plume systems - design methodology, *Journal of Hydraulic Engineering-Asce*, 119(3), 350-368.

Shiono K., and Muto Y. (1998). Complex flow mechanisms in compound meandering channels with overbank flow, *Journal of Fluid Mechanics*, 376, 221-261.

Simmons H. B. (1967). Potential Benefits of Pneumatic Barriers in Estuaries, *Journal of the Hydraulics Division*, 93(3), 1-16.

Sloff C. J., Mosselman E., and Sieben J. (2006). Effective use of non-erodible layers for improving navigability, *Proc. of the River Flow 2006*, Taylor & Francis Ltd, Porto, Portugal, 2006.

Smith B. L. (1998). On the modelling of bubble plumes in a liquid pool, *Applied Mathematical Modelling*, 22(10), 773-797.

Struiksma N., Olesen K. W., Flokstra C., and De Vriend H. J. (1985). Bed deformation in curved alluvial channels, *Journal of Hydraulic Research*, 23(1), 57-79.

Sukhodolov A. N. (2012). Structure of turbulent flow in a meander bend of a lowland river, *Water Resources Research*, 48, W01516, doi: 01510.01029/02011WR10765.

Sukhodolov A. N., Uijttewaal W. S. J., and Engelhardt C. (2002). On the correspondence between morphological and hydrodynamical patterns of groyne fields, *Earth Surface Processes and Landforms*, 27(3), 289-305.

Taylor G. I. (1955). The action of a surface current used as a breakwater, *Proc. of the Royal Society*, Series A 231, 466-478, London.

Teraguchi H., Nakagawa H., Kawaike K., Baba Y., and Zhang H. (2011). Effects of hydraulic structures on river morphological processes, *International Journal of Sediment Research*, 26(3), 283-303.

van Balen W. (2007). A feasibility study on the numerical modelling of air-bubble screens in flowing water, *Internal report Rep.*, Delft University of Technology, Deldt, The Netherlands.

van Balen W., Uijttewaal W. S. J., and Blanckaert K. (2009). Large-eddy simulation of a mildly curved open-channel flow, *Journal of Fluid Mechanics*, 630, 413-442.

van Balen W., Blanckaert K., and Uijttewaal W. S. J. (2010a). Analysis of the role of turbulence in curved open-channel flow at different water depths by means of experiments, LES and RANS, *Journal of Turbulence*, 11(12), 1-34.

van Balen W., Uijttewaal W. S. J., and Blanckaert K. (2010b). Large-eddy simulation of a curved open-channel flow over topography, *Physics of Fluids*, 22, 075108(7).

Voisin A., and Townsend R. D. (2002). Model testing of submerged vanes in strongly curved narrow channel bends, *Canadian Journal of Civil Engineering*, 29(1), 37-49.

Welton J. S., Beaumont W. R. C., and Clarke R. T. (2002). The efficacy of air, sound and acoustic bubble screens in deflecting Atlantic salmon, Salmo salar L., smolts in the River Frome, UK, *Fisheries Management and Ecology*, 9(1), 11-18.

Wen J., and Torrest R. S. (1987). Aeration-induced circulation from line sources .1. Channel flows, *Journal of Environmental Engineering-Asce*, 113(1), 82-98.

Whiting P. J., and Dietrich W. E. (1993a). Experimental studies of bed topography and flow patterns in large-amplitude meanders.1. Observations, *Water Resources Research*, 29(11), 3605-3614.

Whiting P. J., and Dietrich W. E. (1993b). Experimental studies of bed topography and flow patterns in large-amplitude meanders. 2. Mechanisms, *Water Resources Research*, 29(11), 3615-3622.

Wormleaton P. R., Hey R. D., Sellin R. H. J., Bryant T., Loveless J., and Catmur S. E. (2005). Behavior of meandering overbank channels with graded sand beds, *Journal of Hydraulic Engineering-Asce*, 131(8), 665-681.

Wüest A., Brooks N. H., and Imboden D. M. (1992). Bubble plume modeling for lake restoration, *Water Resources Research*, 28(12), 3235-3250.

Yeh K. C., and Kennedy J. F. (1993). Moment model of nonuniform channel-bend flow.1 . Fixed beds, *Journal of Hydraulic Engineering-Asce*, 119(7), 776-795.

Zeng J., Constantinescu G., Blanckaert K., and Weber L. (2008). Flow and bathymetry in sharp open-channel bends: Experiments and predictions, *Water Resources Research*, 44, W09401, doi:10.1029/2007WR006303(9).

Appendixes

A. STILL WATER EXPERIMENTS

In Appendix A cross-sectional velocity patterns of bubble-induced secondary flow under still water conditions using two different air pressures are compared. Experimental hydraulic and air conditions are summarized in Table A.1.

Measurements are performed in the upstream straight reach of the flume, 2 m before the bend entry. Detailed information about still water experiments can be found in Section 3.3.1.

Table A.1: List of the Appendixes A and experimental conditions

Appendix	Label	Q $[m^3\ s^{-1}]$	H $[m]$	U $[m\ s^{-1}]$	Fr $[-]$	P_a $[kPa]$	B/H $[-]$
A.1	SW_11	-	0.11	-	-	400, 600	12.1
A.2	SW_16	-	0.16	-	-	400, 600	8.3
A.3	SW_21	-	0.21	-	-	400, 600	6.1

Information contained in each Appendix is summarized in Table A.2:

Table A.2: List of figures included in each Appendix

Legend	Experiment
Isolines of the measured pattern of the **mean transverse velocity v_n** with an interval of 0.02 m s^{-1}	SW_H_p4
	SW_H_p6
Isolines of the measured pattern of the **mean vertical velocity v_z** with an interval of 0.005 m s^{-1}	SW_H_p4
	SW_H_p6
Measured pattern of the **streamfunction ψ** (color isolines with an interval of 0.001 $m^2\ s^{-1}$) and **secondary flow (v_n, v_z)** (quiver)	SW_H_p4
	SW_H_p6

In each figure, the shaded area near the water surface indicates extrapolated values.

A.1 Still water experiments SW_11_p4 and SW_11_p6

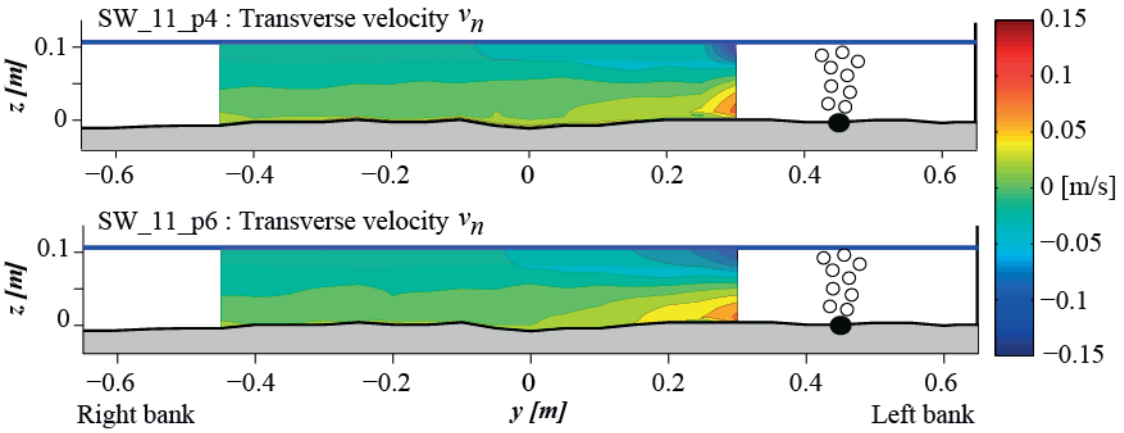

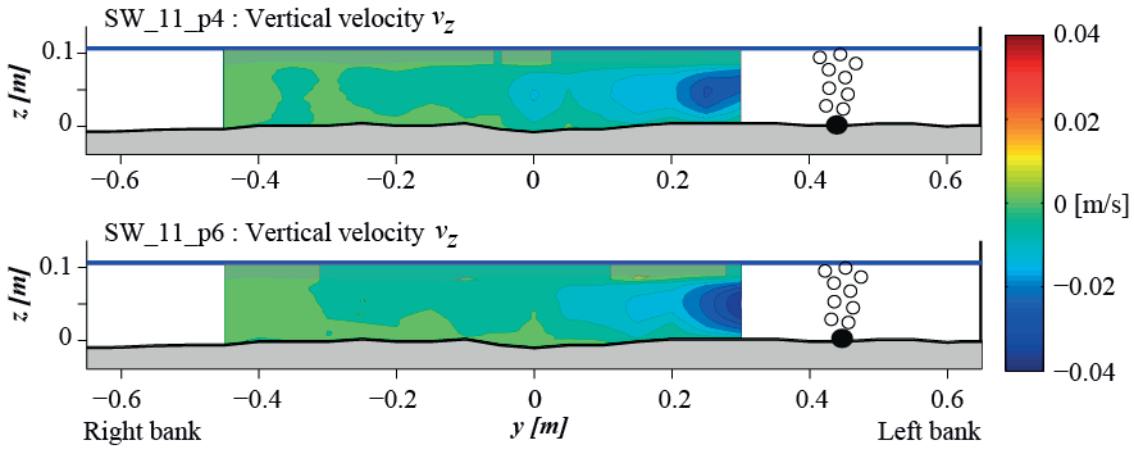

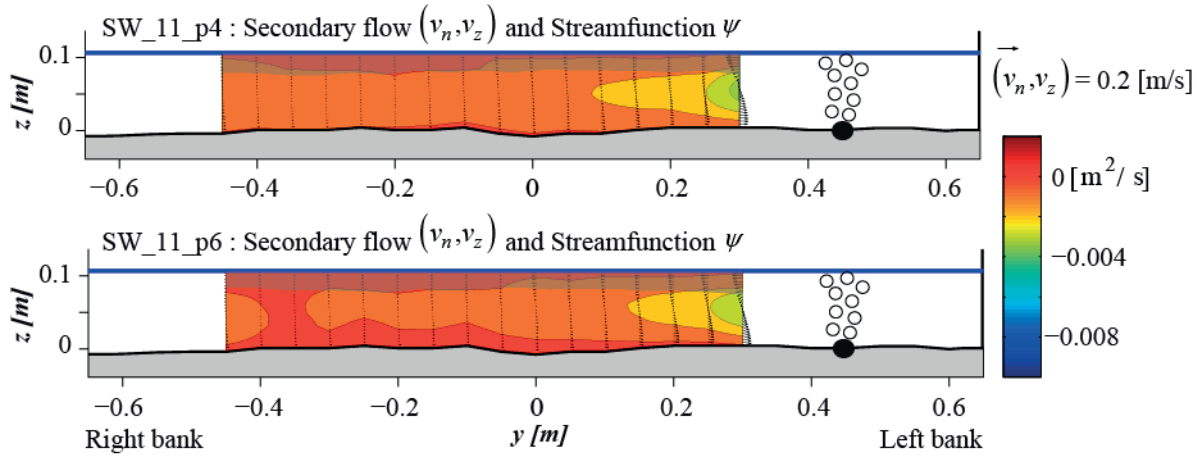

A.2 Still water experiments SW_16_p4 and SW_16_p6

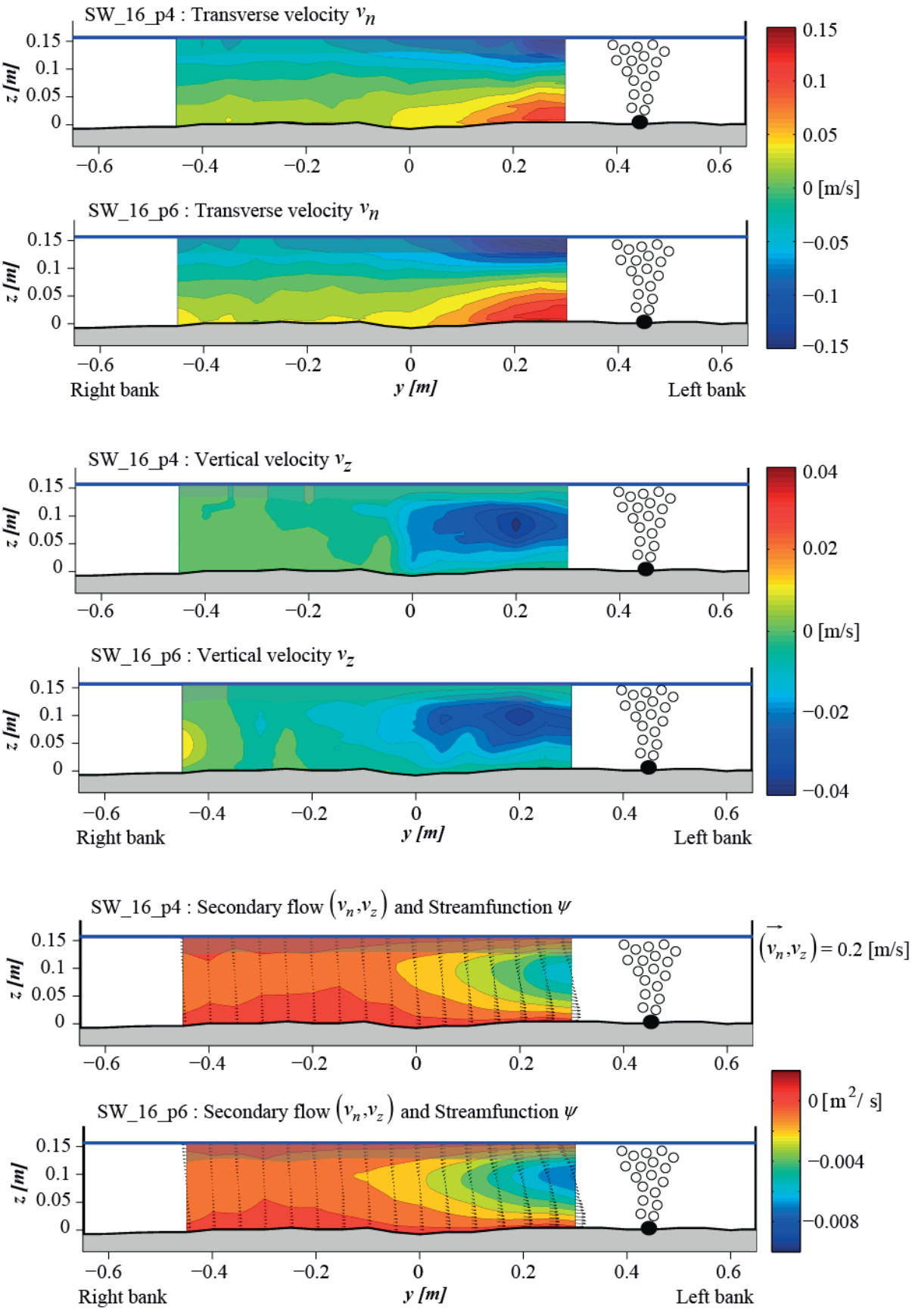

A.3 Still water experiments SW_21_p4 and SW_21_p6

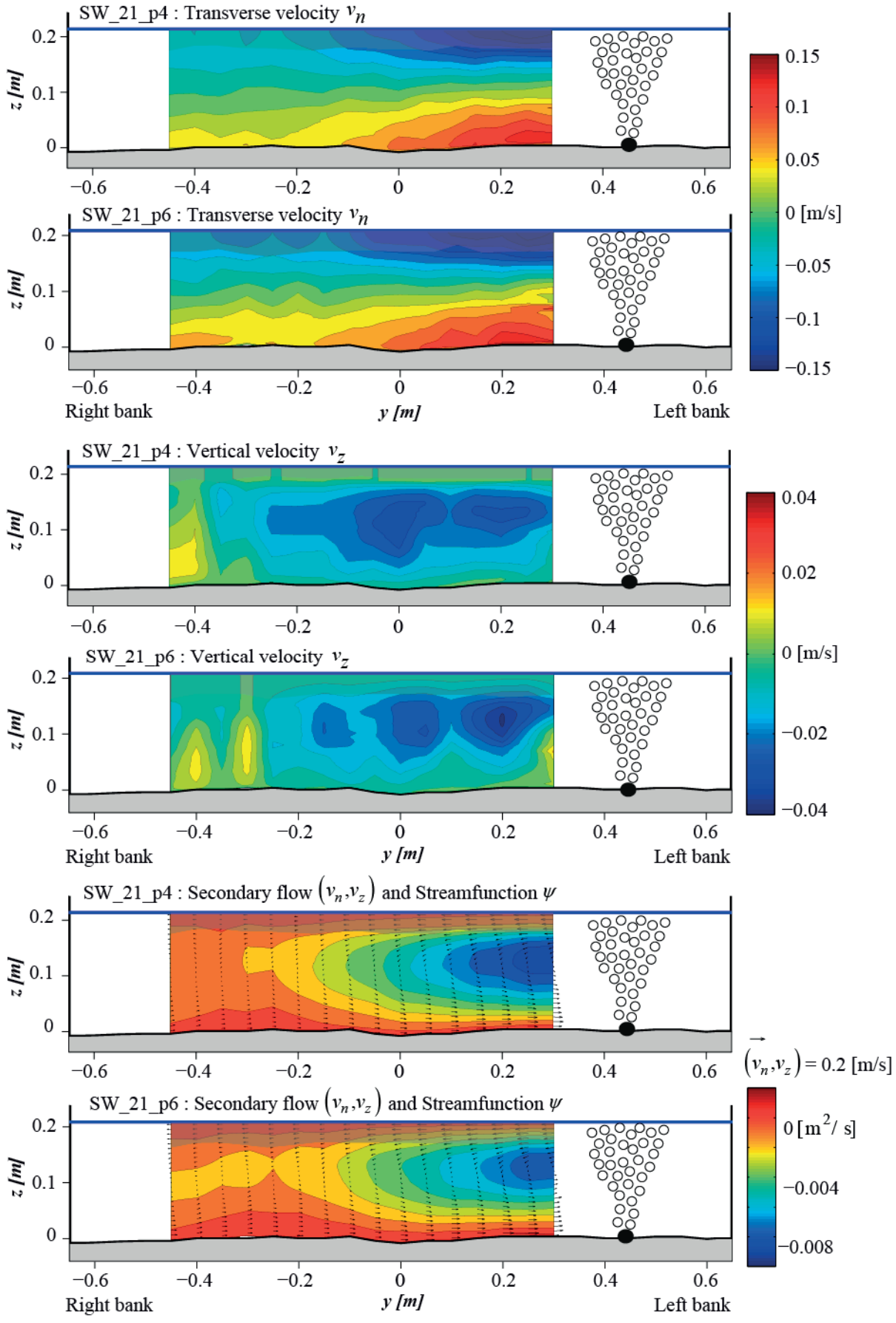

B. STRAIGHT FLOW EXPERIMENTS ON AN IMMOBILE BED

In appendix B, cross-sectional velocity patterns of the flow patterns obtained in the straight flow experiments performed on an immobile bed are compared. Experimental hydraulic and air conditions are summarized in Table B.1

Measurements are performed in the cross-section at x = 3 m downstream from the origin of the porous tube in the upstream straight reach of the flume. Detailed information about the experiments can be found in Section 3.3.2.

Table B.1: List of the Appendixes B and experimental conditions

Appendix	Label	Q $[m^3\ s^{-1}]$	H $[m]$	U $[m\ s^{-1}]$	Fr $[-]$	P_a $[kPa]$	B/H $[-]$
B.1	SF_11_1	0.013	0.11	0.09	0.09	600	12.1
	SF_16_1	0.019	0.16	0.09	0.08	600	8.2
	SF_21_1	0.026	0.21	0.10	0.07	600	6.3
B.2	SF_11_2	0.026	0.11	0.19	0.18	600	12.1
	SF_16_2	0.039	0.16	0.19	0.15	600	8.2
	SF_21_2	0.052	0.21	0.19	0.13	600	6.3
B.3	SF_11_3	0.039	0.11	0.28	0.27	600	12.1
	SF_16_3	0.058	0.16	0.28	0.23	600	8.2
	SF_21_3	0.078	0.21	0.29	0.20	600	6.3

Information contained in each Appendix is summarized in Table B.2:

Table B.2: List of figures included in each Appendix

Legend
Isolines of the measured pattern of the **normalized mean streamwise velocity v_s/U** with an interval of 0.1
Measured pattern of the **streamfunction ψ** (color isolines with an interval of 0.001 $m^2\ s^{-1}$) and **secondary flow (v_n, v_z)** (quiver)
Isolines of the measured pattern of the **mean transverse velocity v_n** with an interval of 0.02 m s^{-1}
Isolines of the measured pattern of the **mean vertical velocity v_z** with an interval of 0.005 m s^{-1}

In each figure, the shaded area near the water surface indicates extrapolated values.

In Appendix B.4, patterns of turbulent kinetic energy (*tke*) in the straight flow experiments are compared.

B.1 Straight flow experiments SF_11_1, SF_16_1, SF_21_1

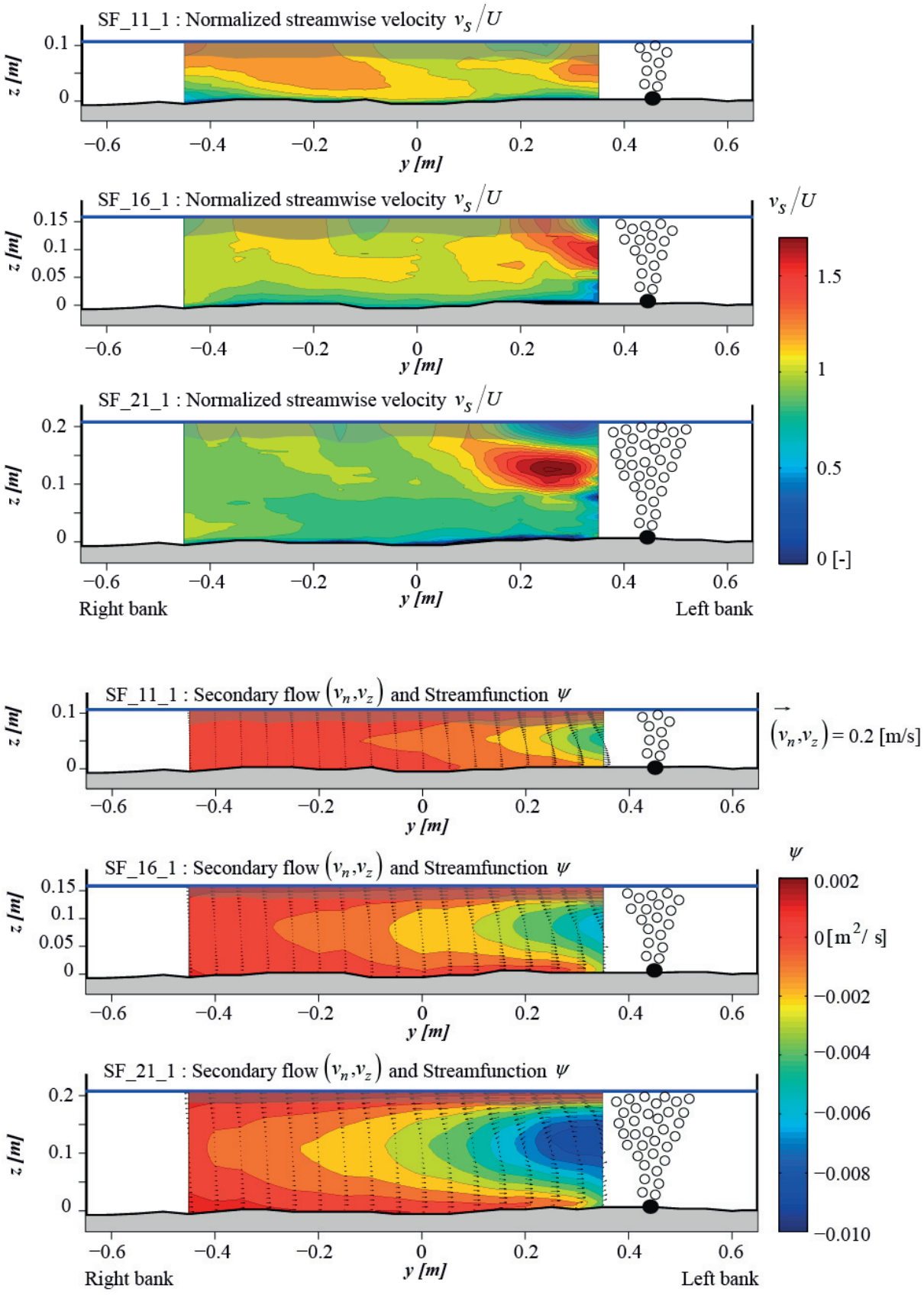

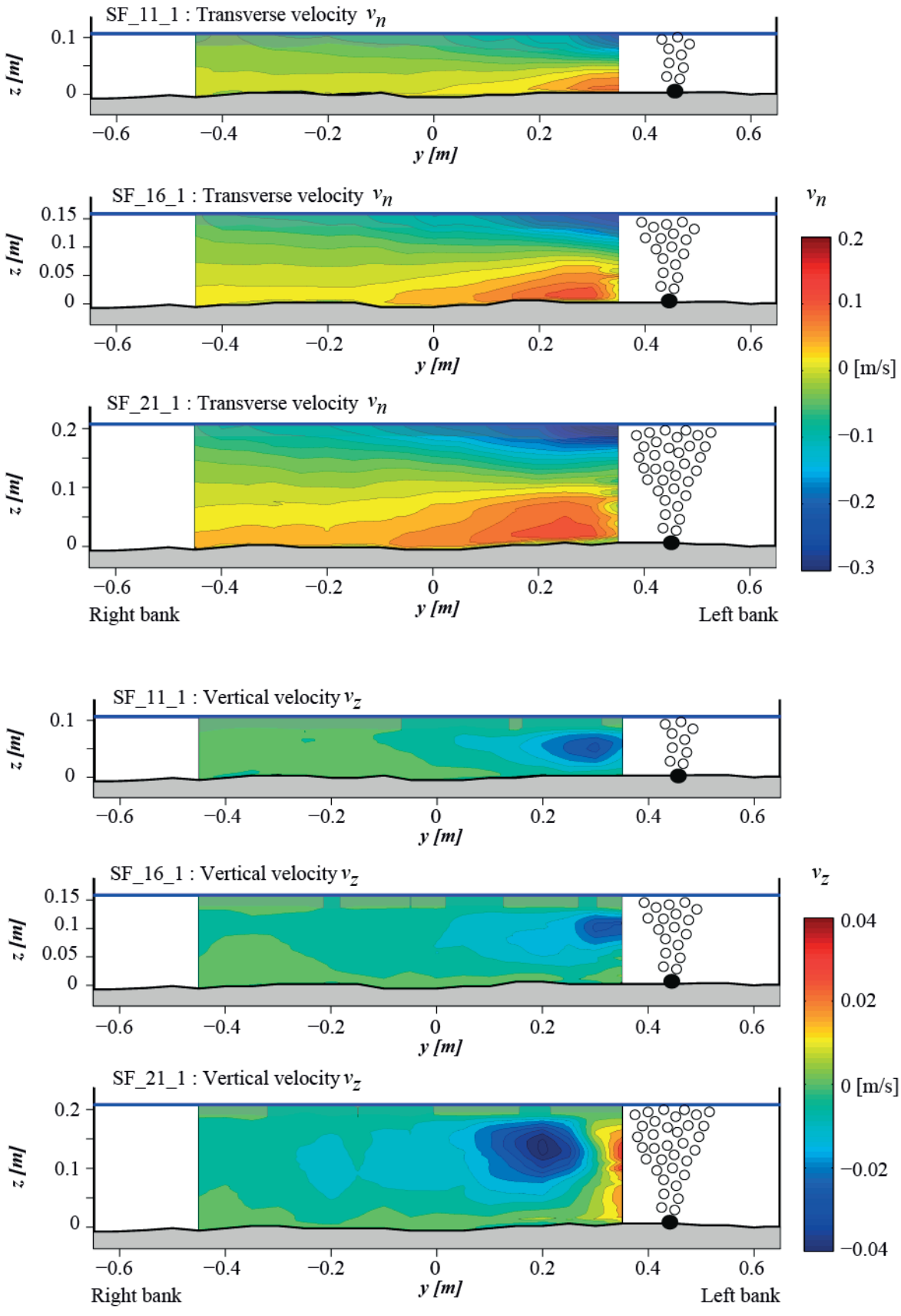
SF_11_1 : Transverse velocity v_n
SF_16_1 : Transverse velocity v_n
SF_21_1 : Transverse velocity v_n
v_n
0.2
0.1
0 [m/s]
−0.1
−0.2
−0.3
SF_11_1 : Vertical velocity v_z
SF_16_1 : Vertical velocity v_z
SF_21_1 : Vertical velocity v_z
v_z
0.04
0.02
0 [m/s]
−0.02
−0.04
z [m]
y [m]
Right bank
Left bank

B.2 Straight flow experiments SF_11_2, SF_16_2, SF_21_2

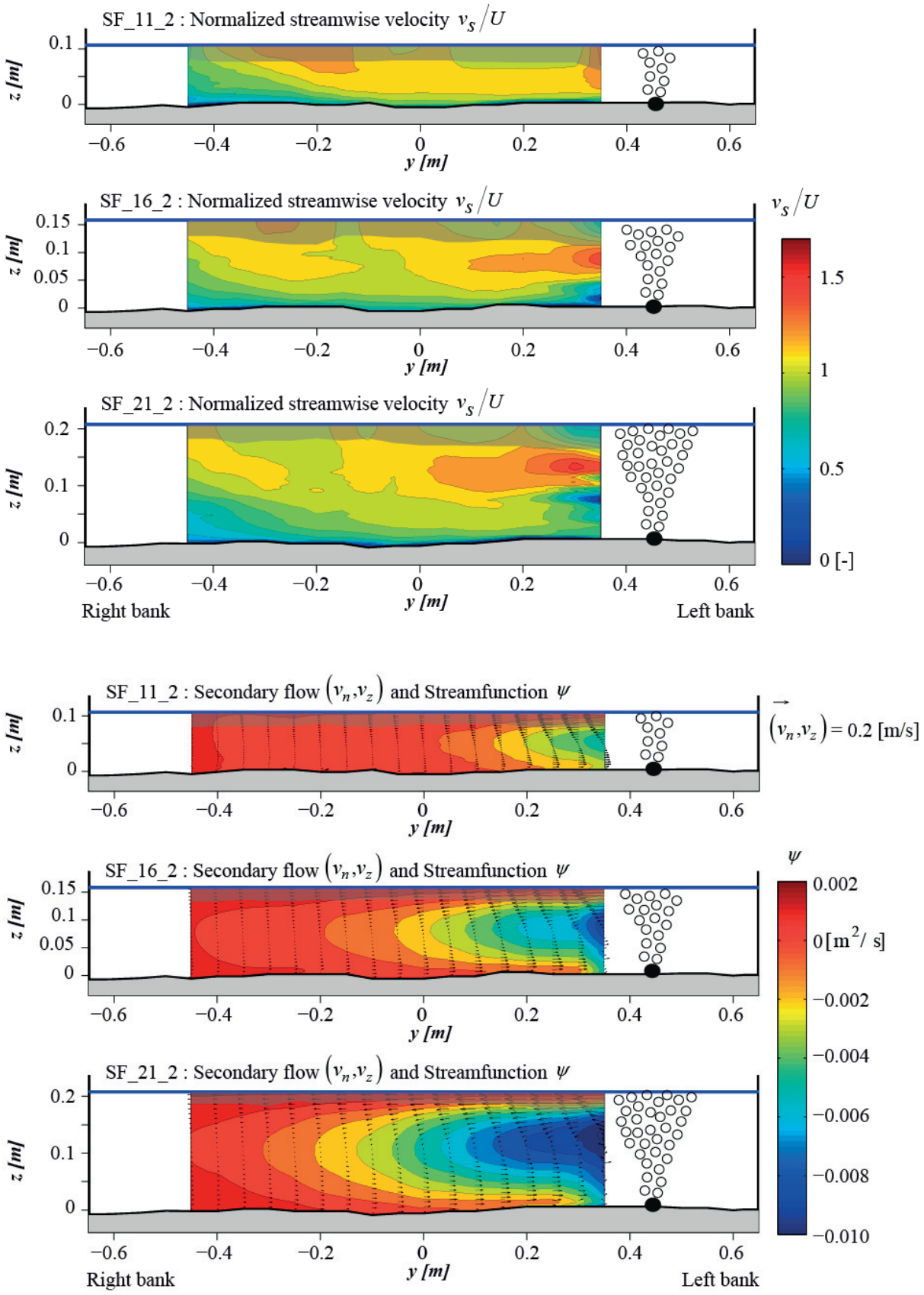

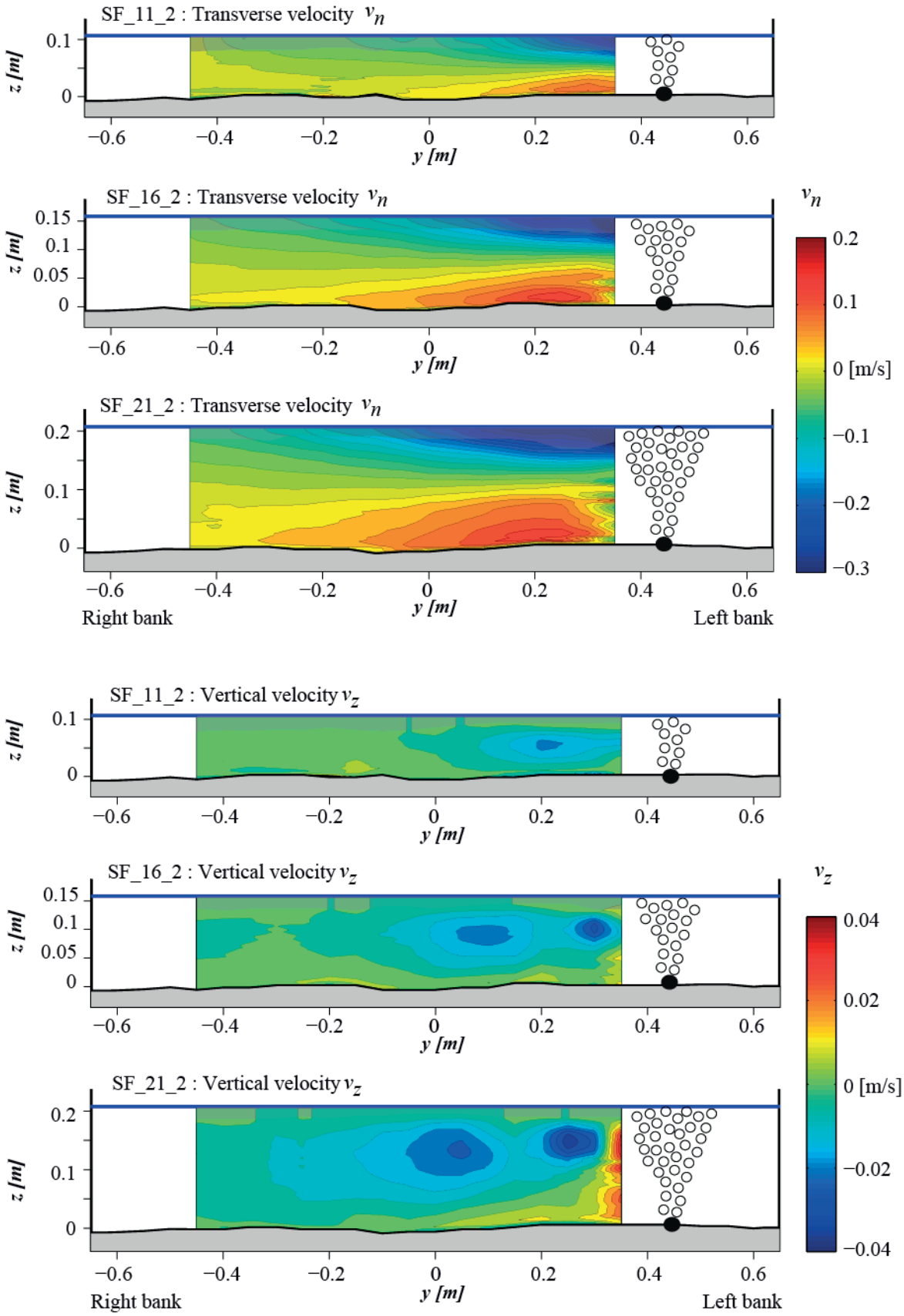
SF_11_2 : Transverse velocity v_n
SF_16_2 : Transverse velocity v_n
SF_21_2 : Transverse velocity v_n
v_n
0.2
0.1
0 [m/s]
−0.1
−0.2
−0.3
z [m]
y [m]
Right bank
Left bank
SF_11_2 : Vertical velocity v_z
SF_16_2 : Vertical velocity v_z
SF_21_2 : Vertical velocity v_z
v_z
0.04
0.02
0 [m/s]
−0.02
−0.04

B.3 Straight flow experiments SF_11_3, SF_16_3, SF_21_3

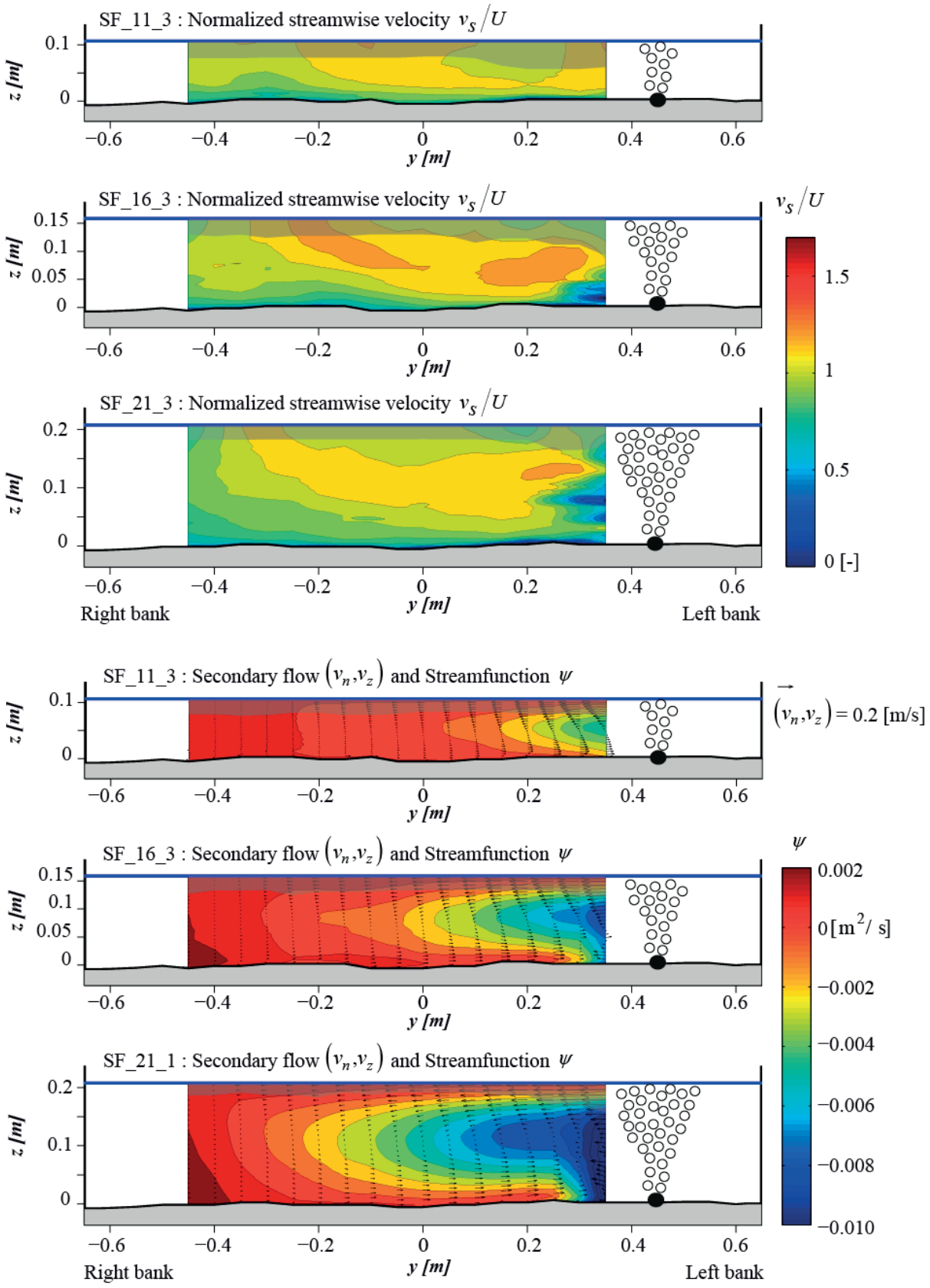

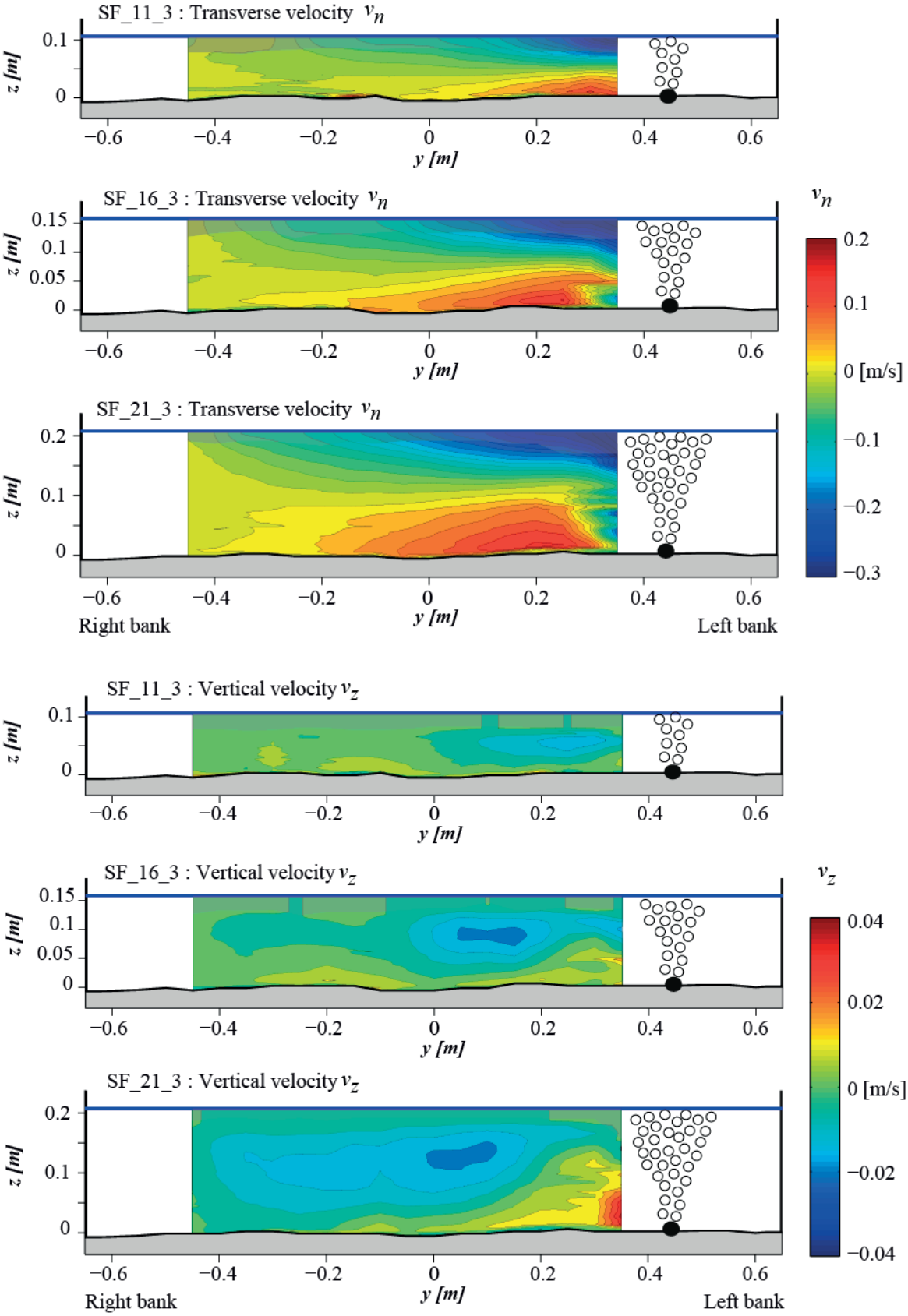
SF_11_3 : Transverse velocity v_n
SF_16_3 : Transverse velocity v_n
SF_21_3 : Transverse velocity v_n
v_n
0.2
0.1
0 [m/s]
−0.1
−0.2
−0.3
SF_11_3 : Vertical velocity v_z
SF_16_3 : Vertical velocity v_z
SF_21_3 : Vertical velocity v_z
v_z
0.04
0.02
0 [m/s]
−0.02
−0.04
z [m]
y [m]
Right bank
Left bank

B.4 Straight flow experiments: Turbulent kinetic energy

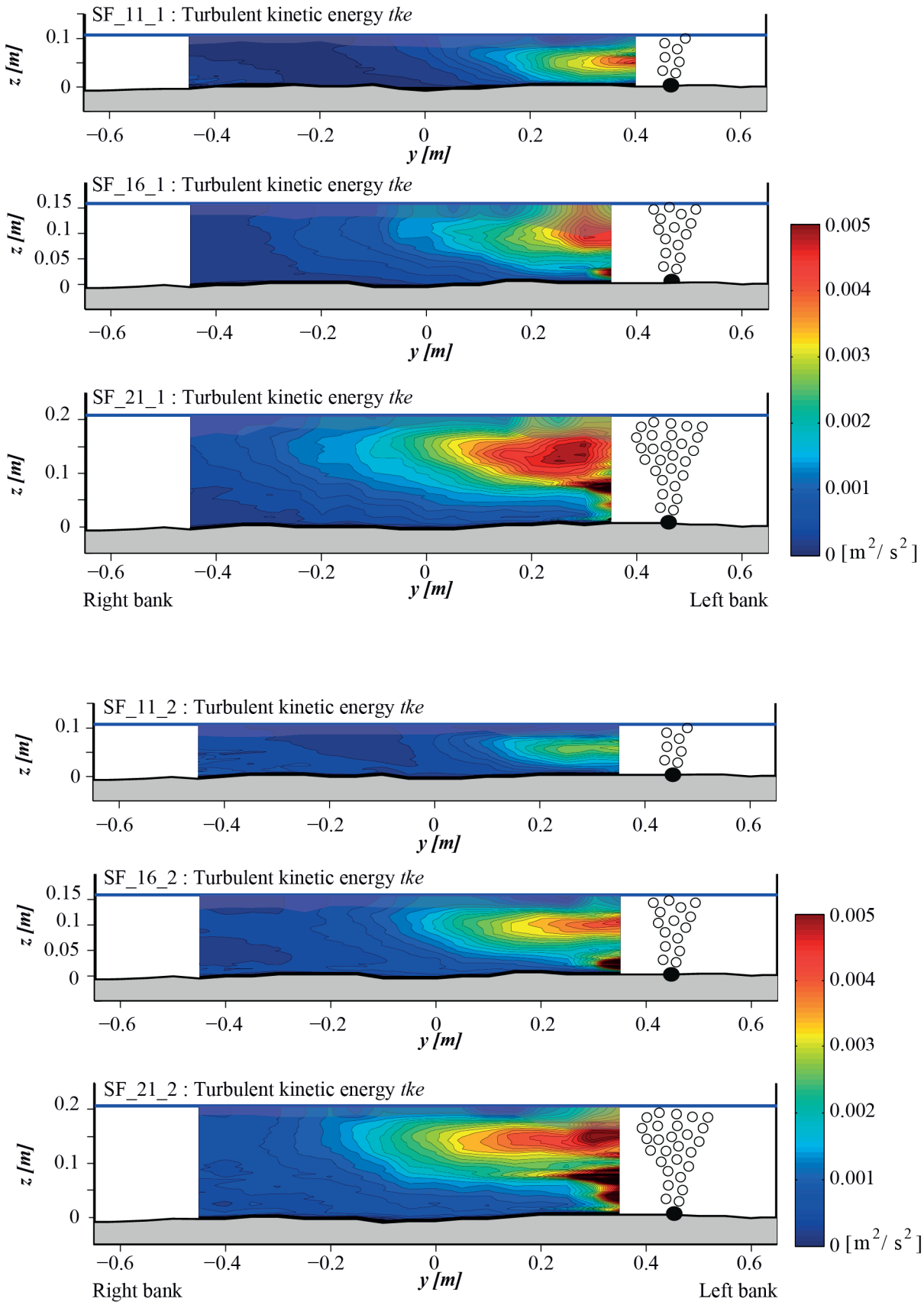

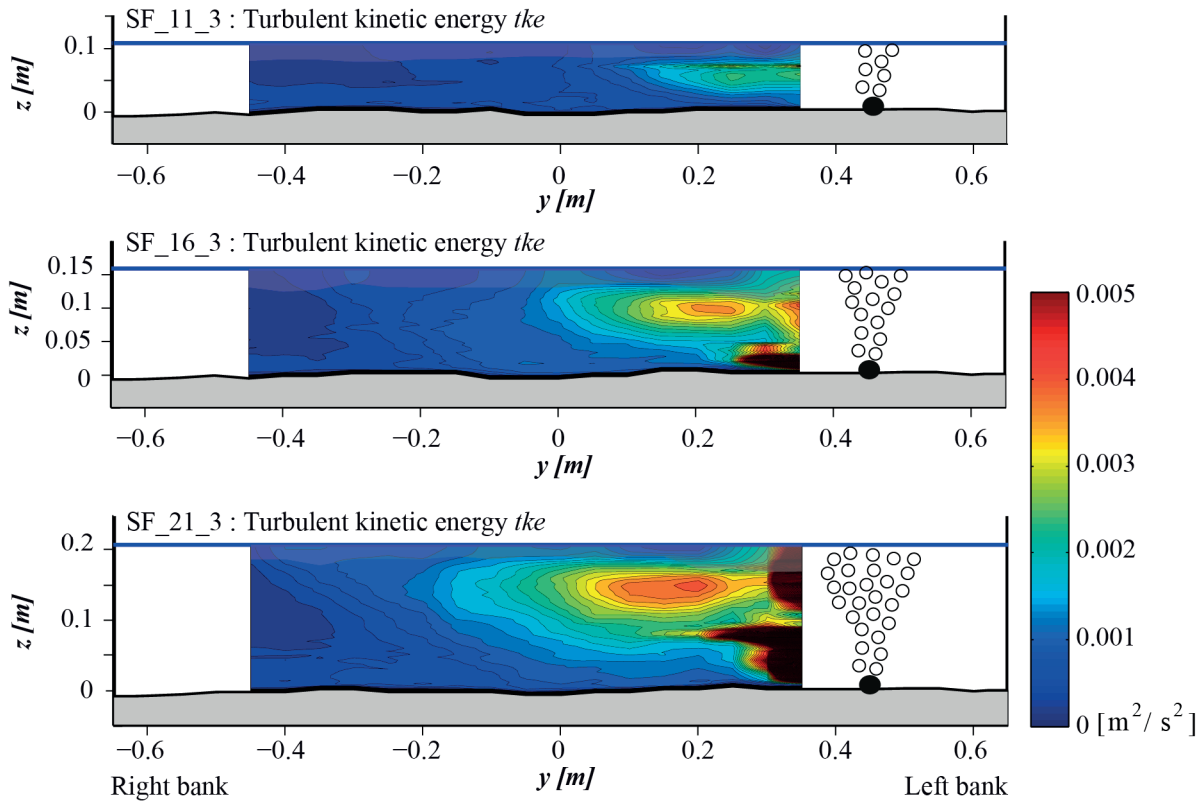
SF_11_3 : Turbulent kinetic energy tke
SF_16_3 : Turbulent kinetic energy tke
SF_21_3 : Turbulent kinetic energy tke
z [m]
y [m]
0.1
0
0.15
0.05
0.2
−0.6
−0.4
−0.2
0.2
0.4
0.6
0.005
0.004
0.003
0.002
0.001
0 [m²/ s²]
Right bank
Left bank

C. STRAIGHT FLOW EXPERIMENTS UNDER LIVE-BED CONDITIONS

In Appendix C, velocity patterns measured in several cross-sections in the straight flow experiments performed under live-bed conditions are compared. Experimental hydraulic and air conditions are summarized in Table C.1

Measurements are performed in the cross-section at x = 2 m (Appendix C.1), x = 2.5 m (Appendix C.2), x = 3.0 m (Appendix C.3), x = 3.5 m (Appendix C.4), x = 4.0 m (Appendix C.5) and x = 4.5 m (Appendix C.6) downstream from the origin of the porous tube in the upstream straight reach of the flume. Detailed information about the experiment can be found in Section 3.3.3.

Table C.1: Experimental conditions of the straight flow experiments under live-bed conditions

Label	Q $[m^3\ s^{-1}]$	q_s $[kg\ m^{-1}\ s^{-1}]$	H $[m]$	U $[m\ s^{-1}]$	Fr $[-]$	P_a $[kPa]$	B/H $[-]$
SF_LB_B	0.075	0.025	0.12	0.47	0.42	600	10.5

Information contained in each Appendix is summarized in Table C.2:

Table C.2: List of figures included in each Appendix

Legend
Isolines of the measured pattern of the **normalized mean streamwise velocity v_s/U**
Isolines of the measured pattern of the **mean transverse velocity v_n**
Isolines of the measured pattern of the **mean vertical velocity v_z**
Measured pattern of the **streamfunction ψ** (color isolines with an interval of 0.001 $m^2\ s^{-1}$) and **secondary flow (v_n, v_z)** (quiver)
Isolines of the measured pattern of turbulent kinetic energy *tke*

In each figure, the shaded area near the water surface indicates extrapolated values.

C.1 Cross-section at x = 2 m in the upstream straight reach

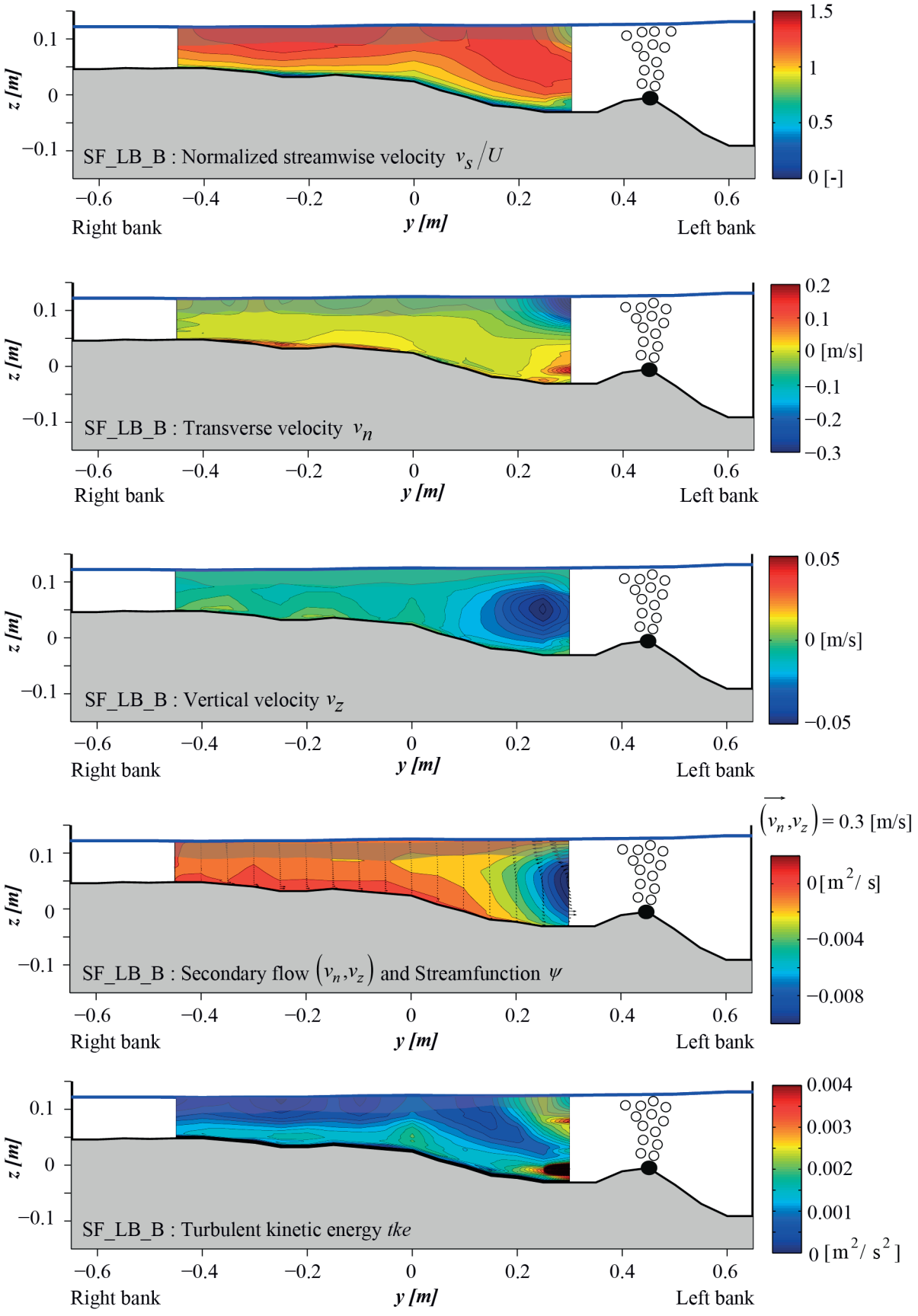

C.2 Cross-section at x = 2.5 m in the upstream straight reach

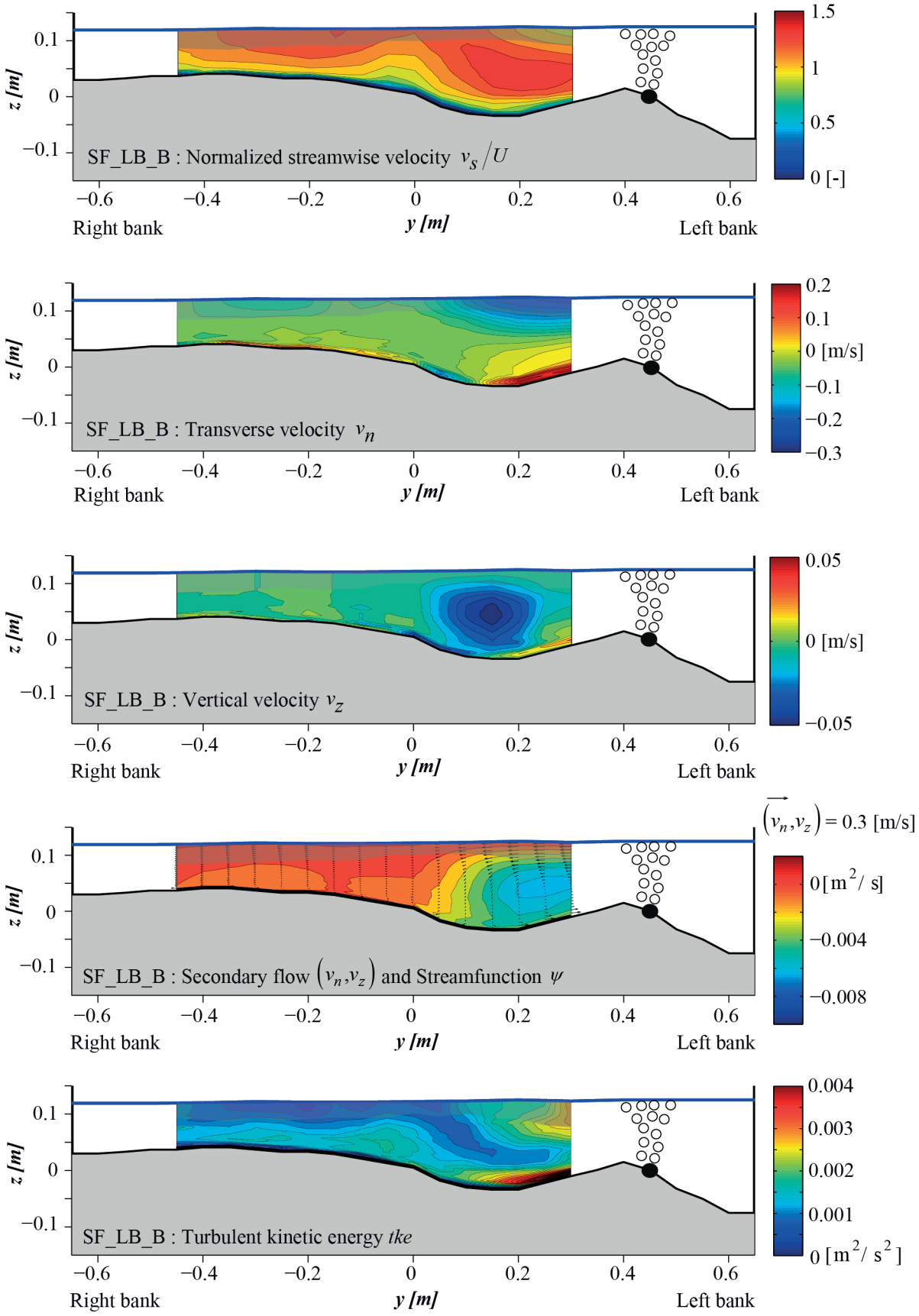

C.3 Cross-section at x = 3 m in the upstream straight reach

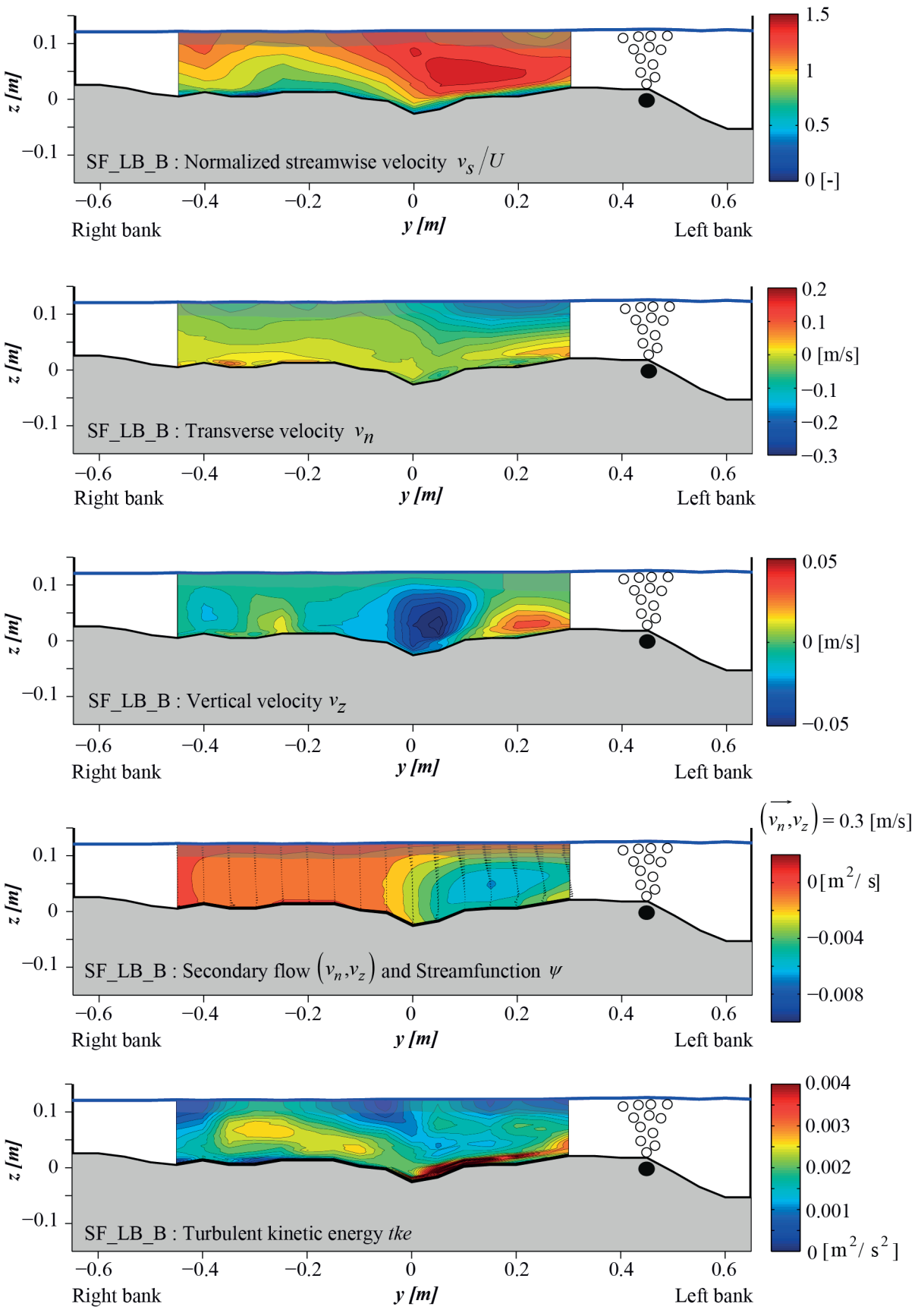

C.4 Cross-section at x = 3.5 m in the upstream straight reach

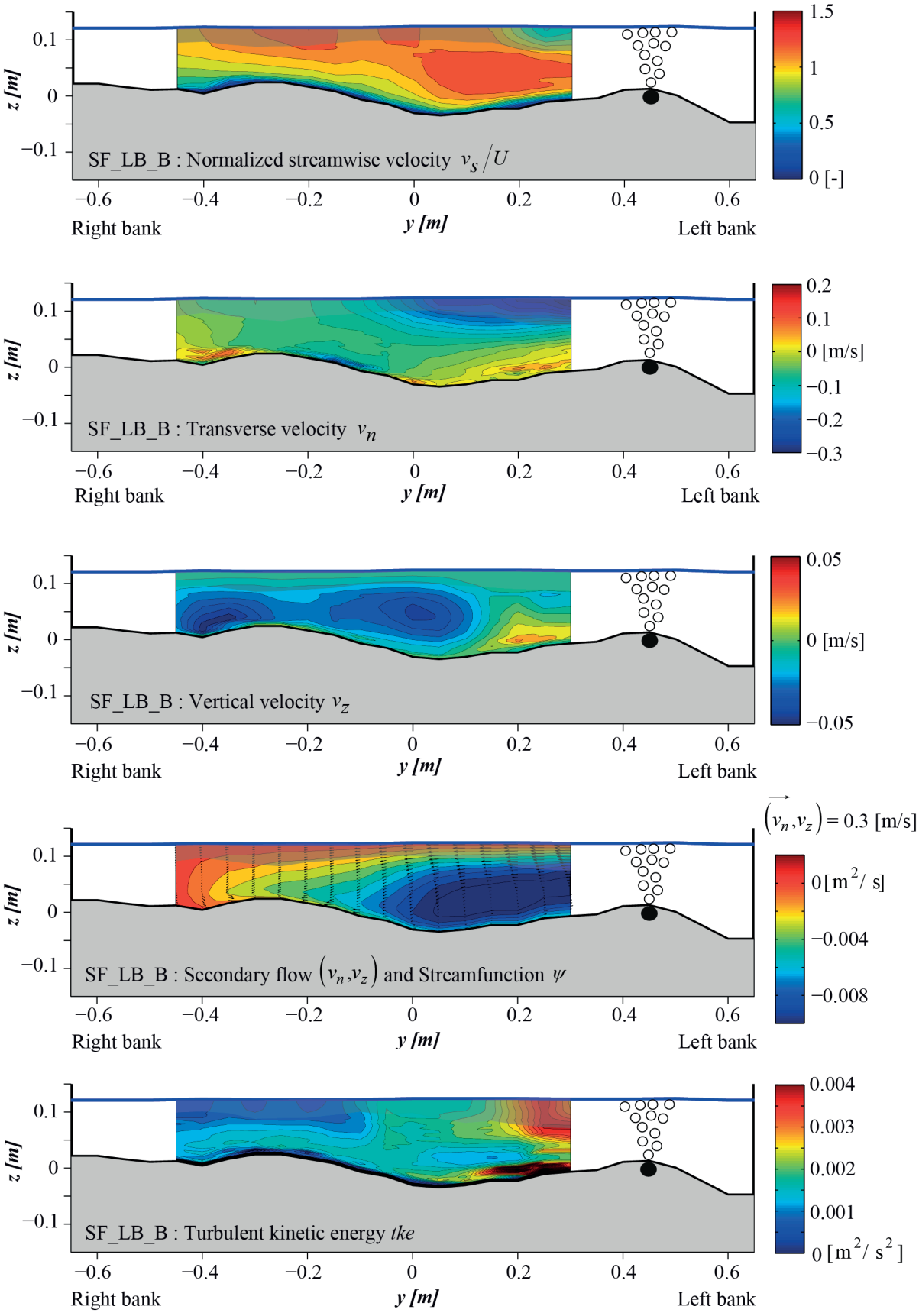

C.5 Cross-section at x = 4 m in the upstream straight reach

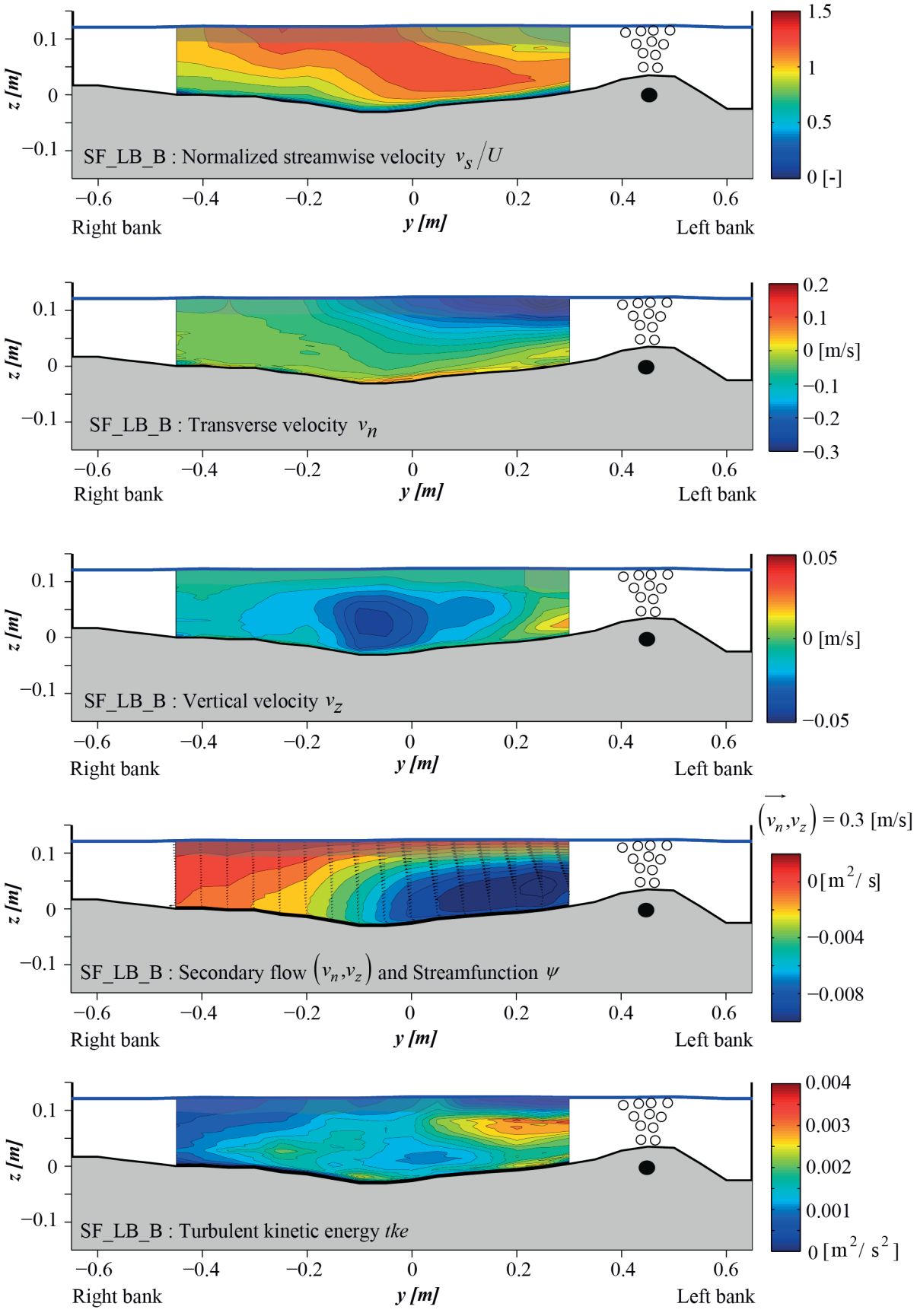

C.6 Cross-section at x = 4.5 m in the upstream straight reach

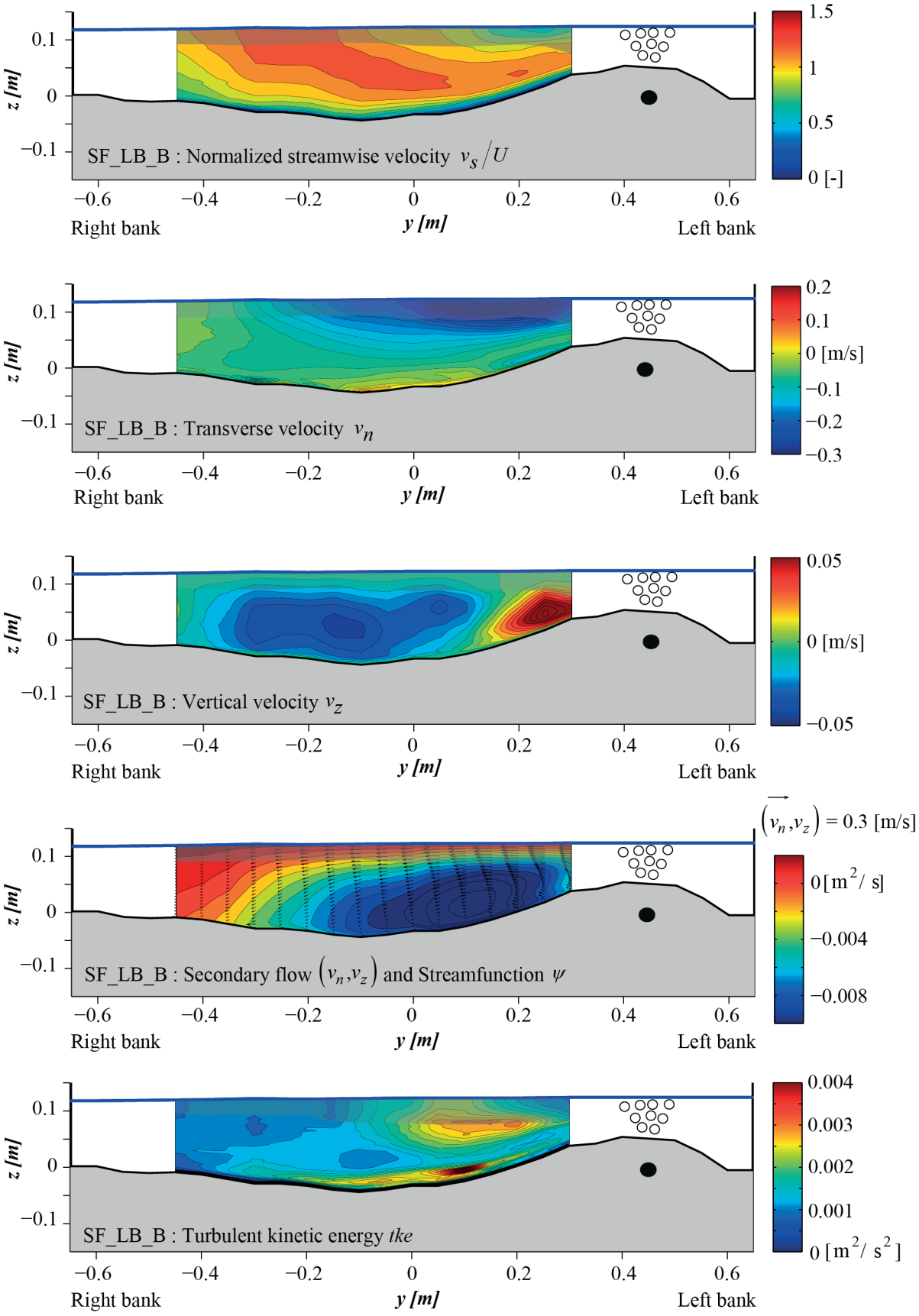

D. CURVED FLOW EXPERIMENTS UNDER LIVE-BED CONDITIONS

In Appendix D, cross-sectional velocity patterns measured in the curved flow experiments under live-bed conditions performed with and without the bubble screen are compared. Experimental hydraulic and air conditions of the two experiments are summarized in Table D.1

Measurements are performed in the cross-sections at 15° (Appendix D.1), 30° (Appendix D.2), 60° (Appendix D.3), 90° (Appendix D.4), 120° (Appendix D.5), 150° (Appendix D6) and 180° (Appendix D.7) in the bend. Detailed information about the experiments and the measurements can be found in Section 3.3.5.

Table D.1: Experimental conditions

Label	Q $[m^3\ s^{-1}]$	q_s $[kg\ m^{-1}s^{-1}]$	P_a $[kPa]$	H $[m]$	U $[m\ s^{-1}]$	R/B $[-]$	R/H $[-]$	B/H $[-]$
CF75_LB_NB	0.075	0.025	-	0.14	0.41	1.31	12.1	9.2
CF75_LB_B	0.075	0.025	600	0.14	0.41	1.31	12.1	9.2

Information contained in Appendixes D.1 to D.7 is summarized in Table D.2:

Table D.2: List of the figures included in each Appendix

Legend	Experiment
Isolines of the measured pattern of the **normalized mean streamwise velocity v_s/U**	CF75_LB_NB
	CF75_LB_B
Patterns of **normalized cross-stream circulation** $\left(v_n^*, v_z\right)/U$	CF75_LB_NB
	CF75_LB_B
Isolines of the measured pattern of the **normalized mean transverse velocity v_n/U**	CF75_LB_NB
	CF75_LB_B
Isolines of the measured pattern of the **normalized mean vertical velocity v_z/U**	CF75_LB_NB
	CF75_LB_B

In each figure, the shaded area near the water surface indicates extrapolated values.

In Appendix D.8, patterns of turbulent kinetic energy (*tke*) without and with bubble screen in each investigated cross-sections around the bend are compared.

D.1 Cross-section at 15° in the bend

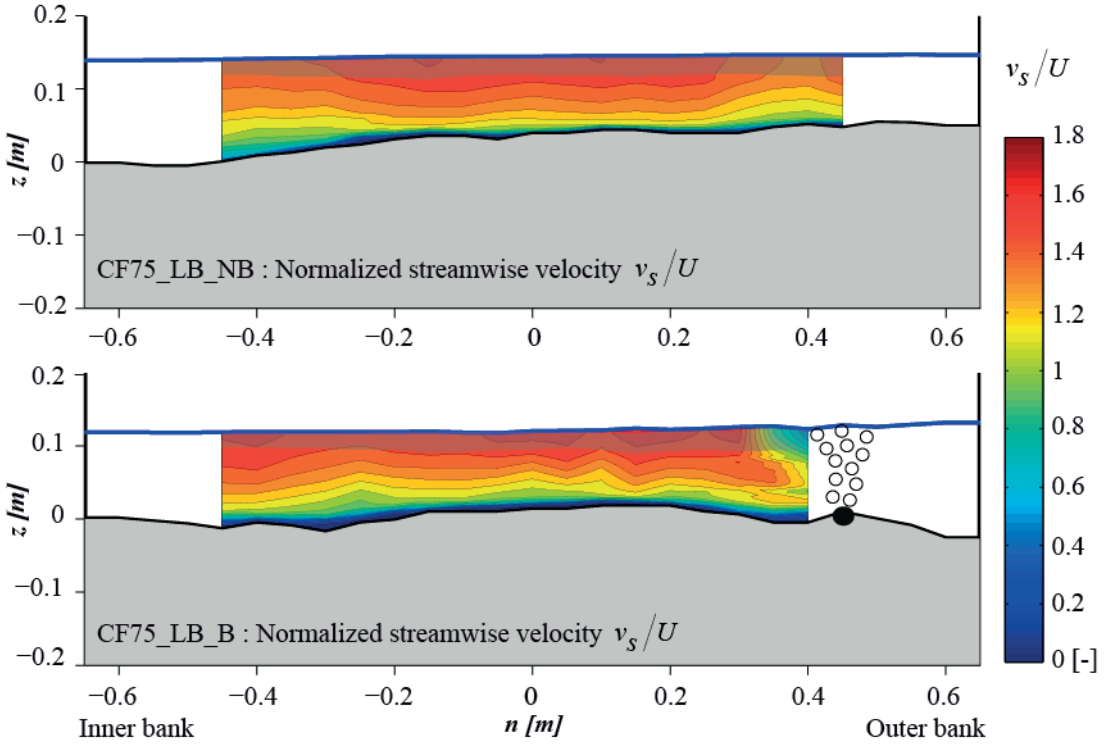

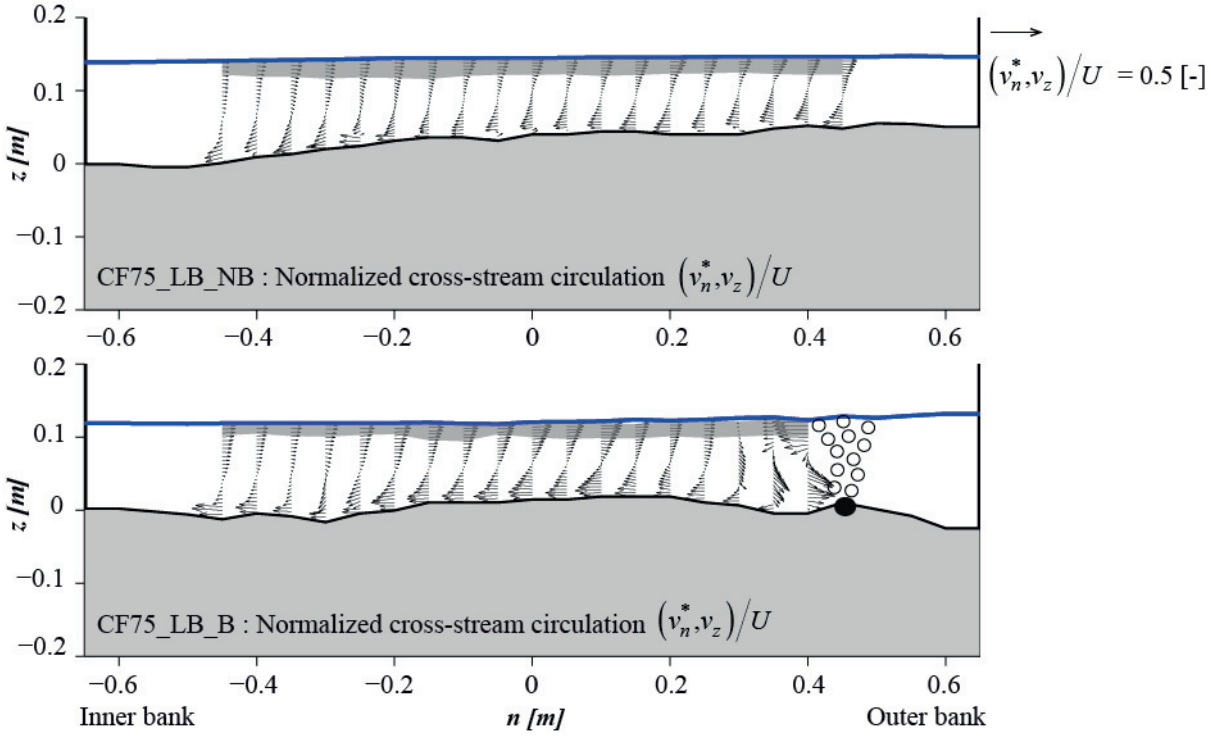

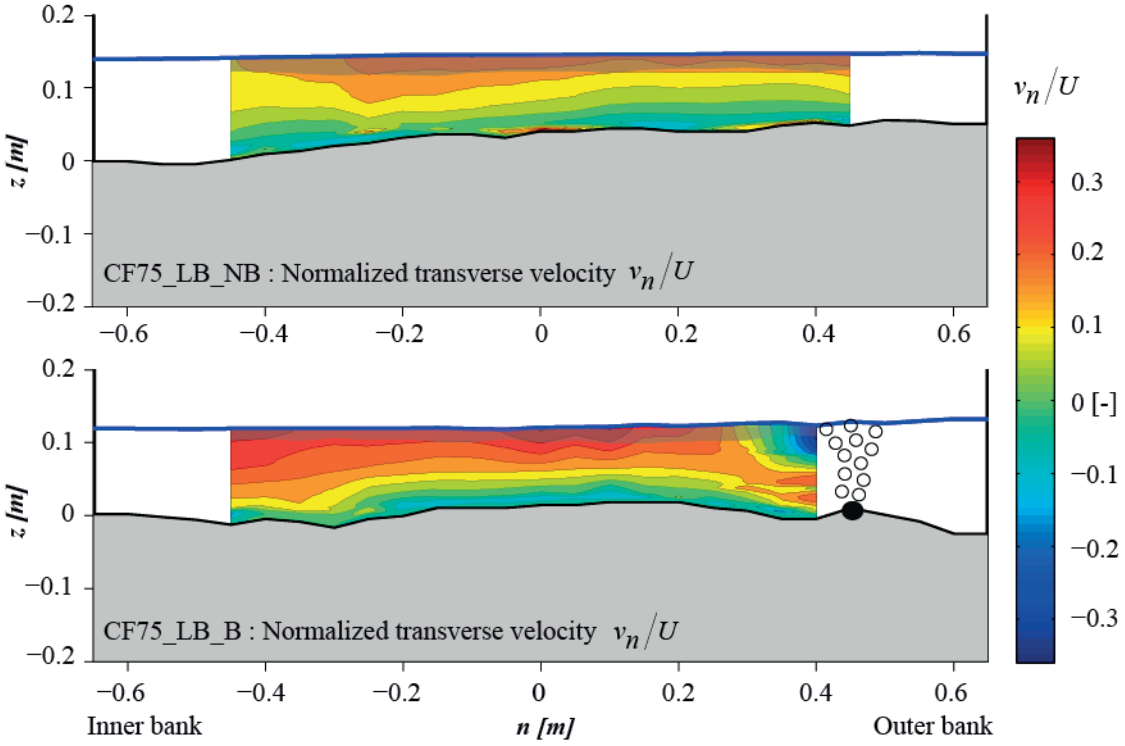
CF75_LB_NB : Normalized transverse velocity v_n/U
CF75_LB_B : Normalized transverse velocity v_n/U
v_n/U
0.3
0.2
0.1
0 [-]
−0.1
−0.2
−0.3
z [m]
n [m]
Inner bank
Outer bank

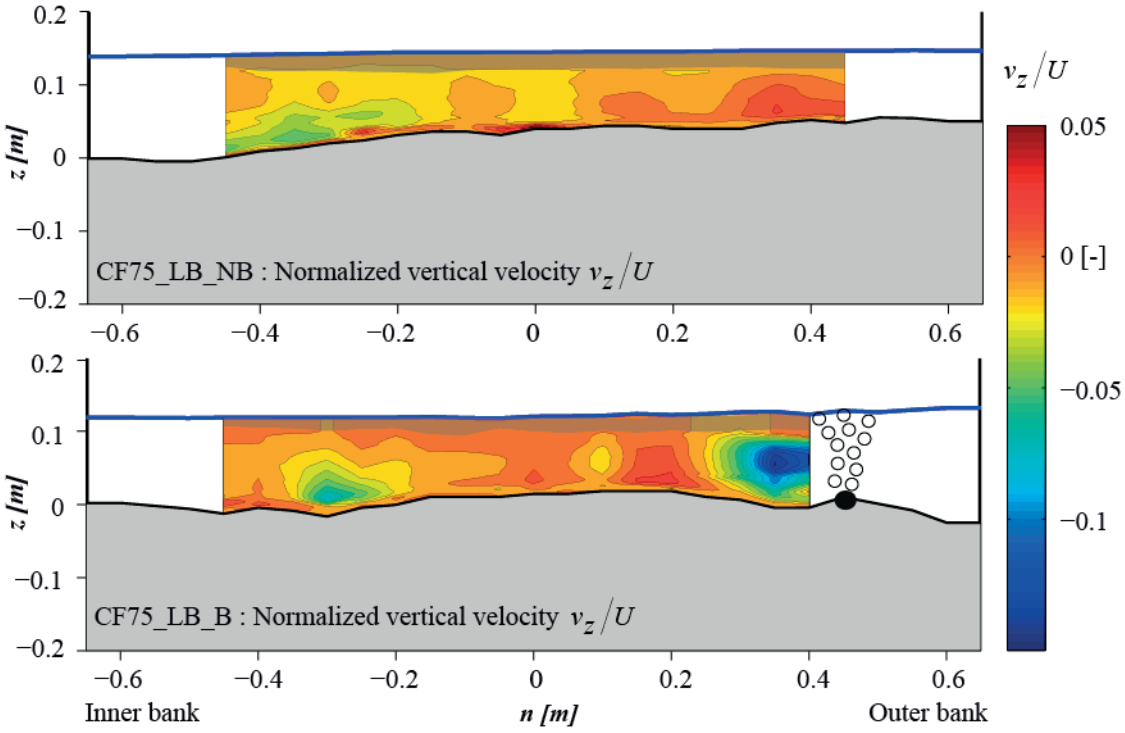
CF75_LB_NB : Normalized vertical velocity v_z/U
CF75_LB_B : Normalized vertical velocity v_z/U
v_z/U
0.05
0 [-]
−0.05
−0.1
z [m]
n [m]
Inner bank
Outer bank

D.2 Cross-section at 30° in the bend

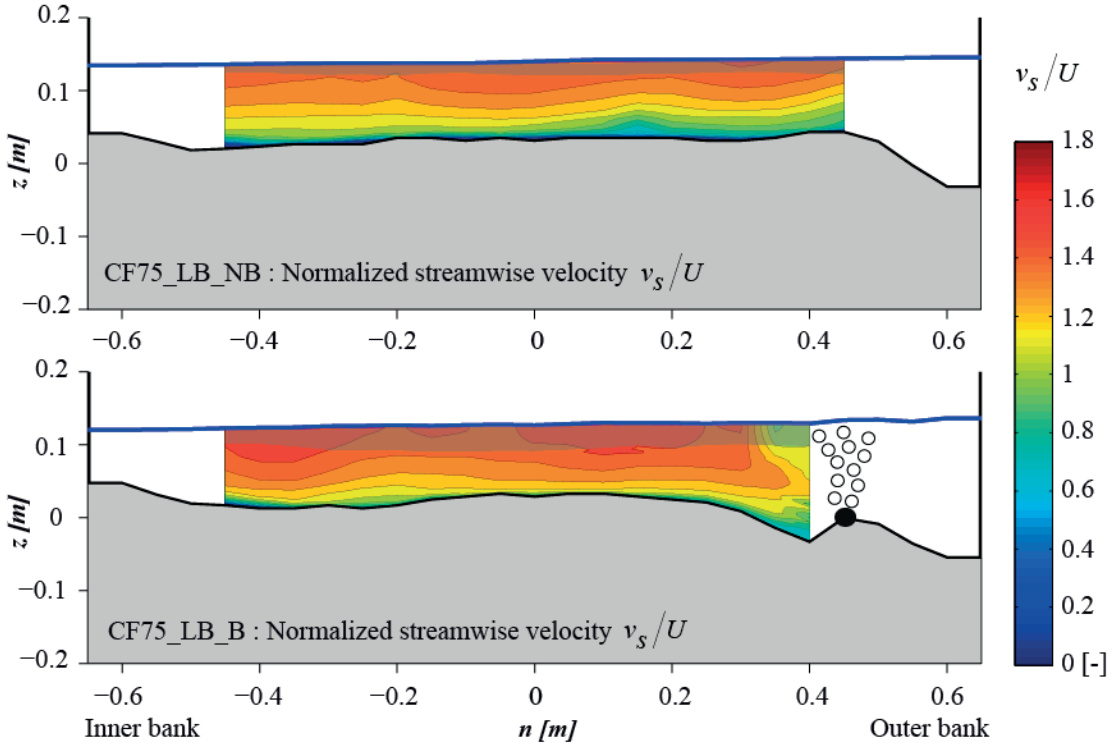

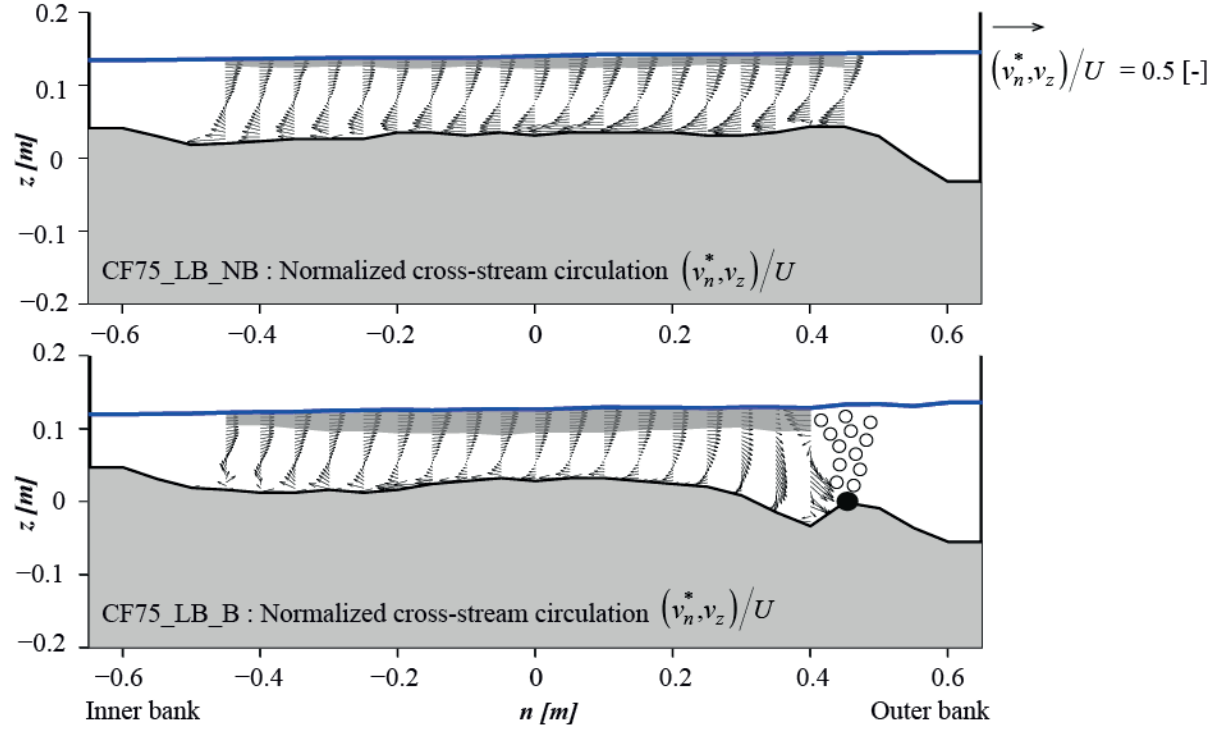

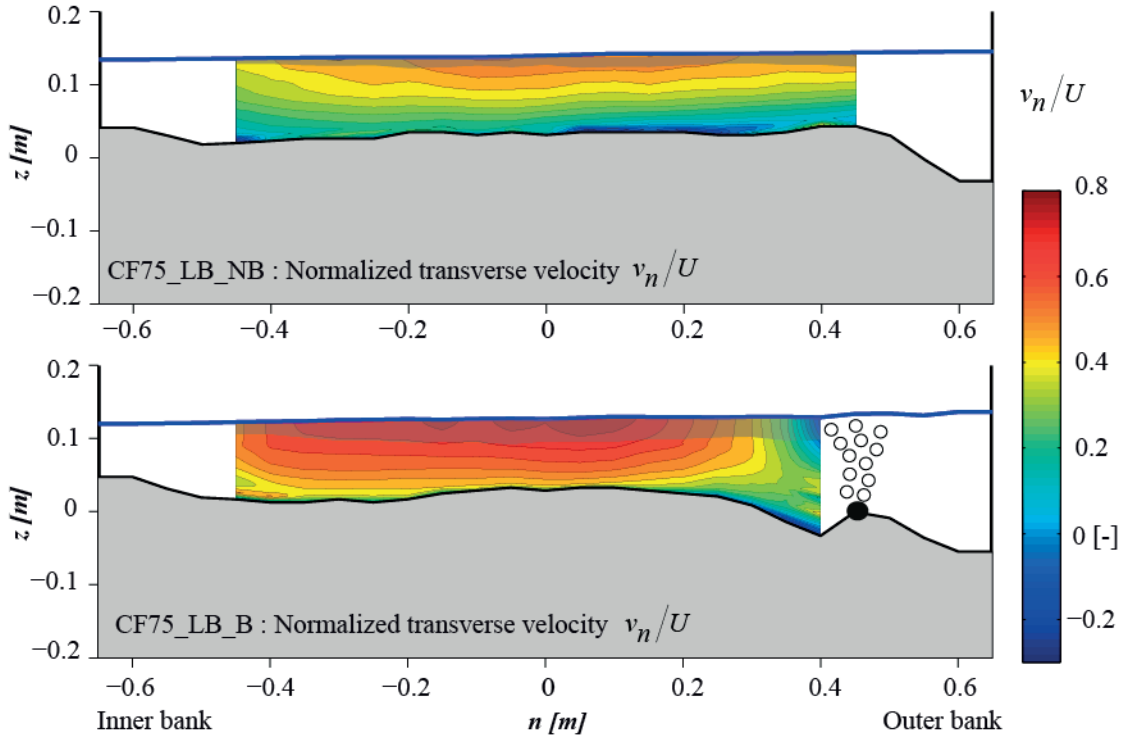
CF75_LB_NB : Normalized transverse velocity v_n/U
CF75_LB_B : Normalized transverse velocity v_n/U
v_n/U
0.8
0.6
0.4
0.2
0 [-]
−0.2
z [m]
n [m]
Inner bank
Outer bank

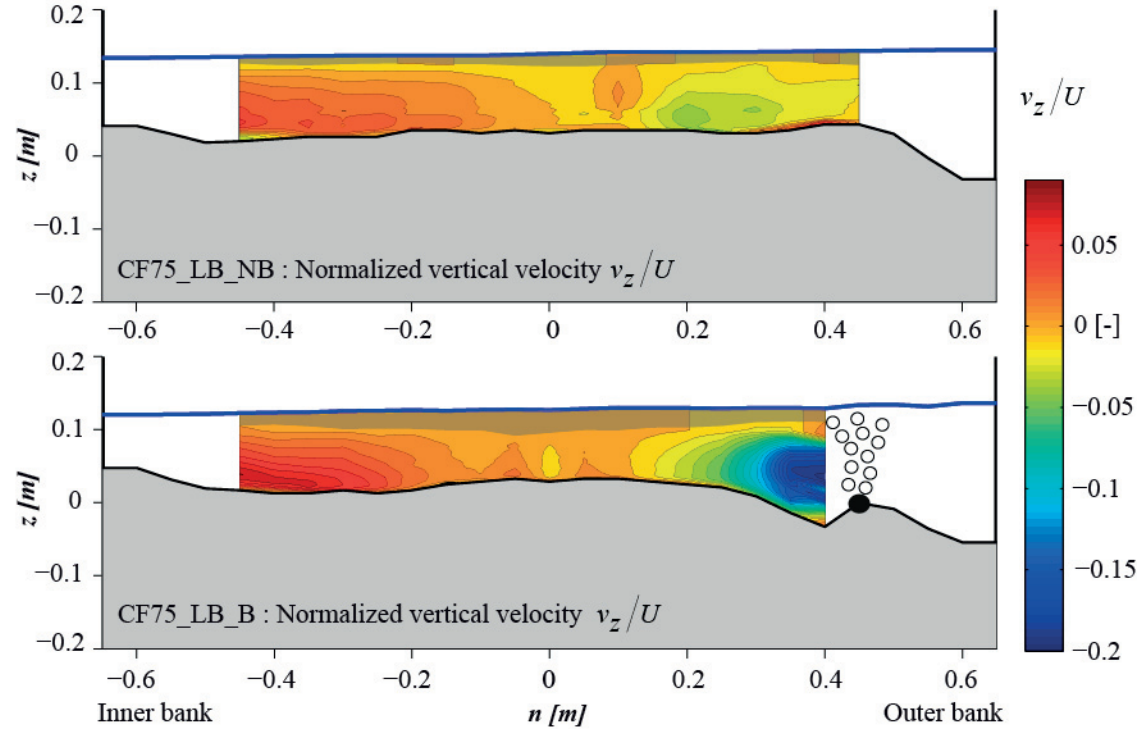
CF75_LB_NB : Normalized vertical velocity v_z/U
CF75_LB_B : Normalized vertical velocity v_z/U
v_z/U
0.05
0 [-]
−0.05
−0.1
−0.15
−0.2
z [m]
n [m]
Inner bank
Outer bank

D.3 Cross-section at 60° in the bend

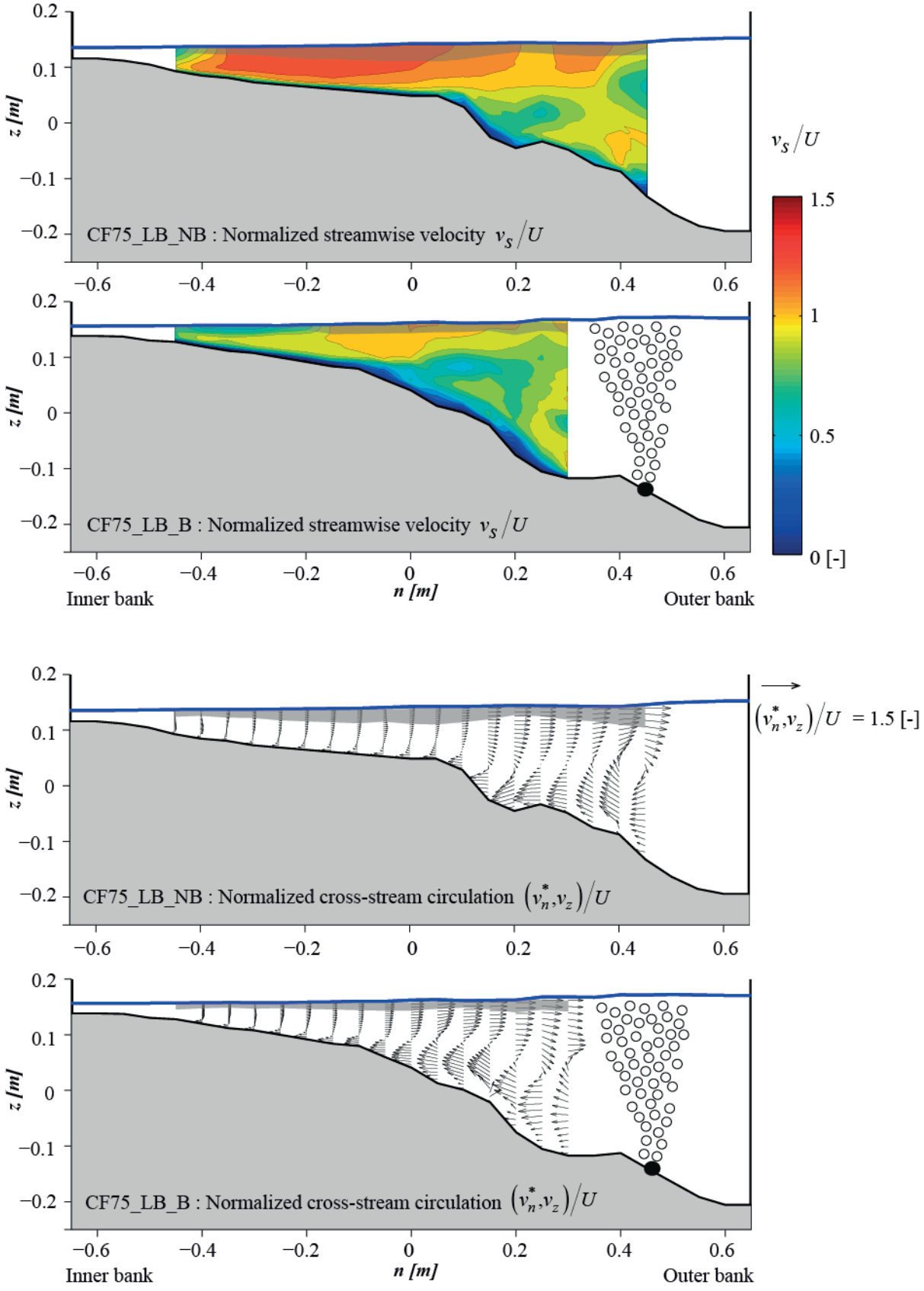

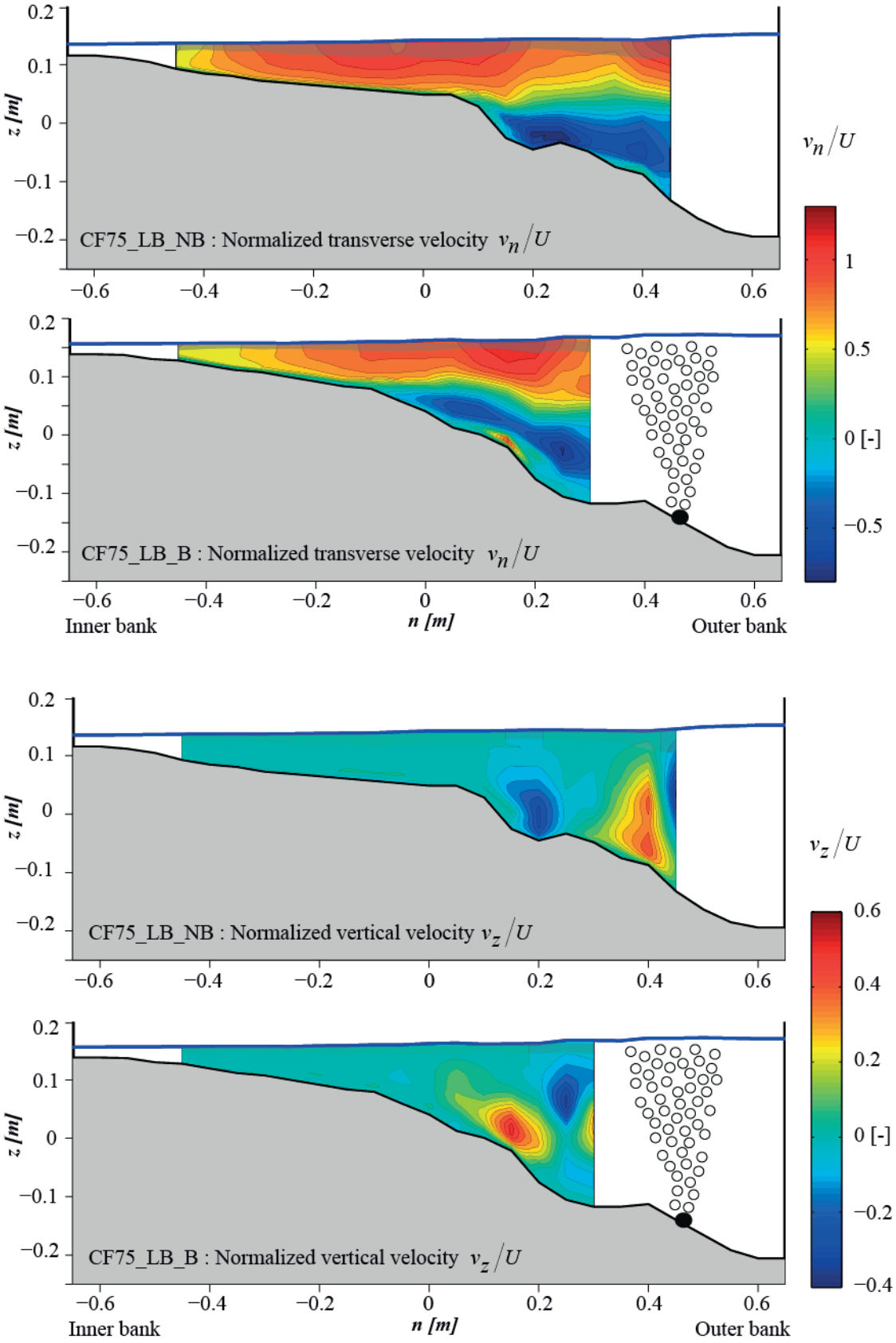
CF75_LB_NB : Normalized transverse velocity v_n/U
CF75_LB_B : Normalized transverse velocity v_n/U
v_n/U
1
0.5
0 [-]
−0.5
CF75_LB_NB : Normalized vertical velocity v_z/U
CF75_LB_B : Normalized vertical velocity v_z/U
v_z/U
0.6
0.4
0.2
0 [-]
−0.2
−0.4
z [m]
n [m]
Inner bank
Outer bank

D.4 Cross-section at 90° in the bend

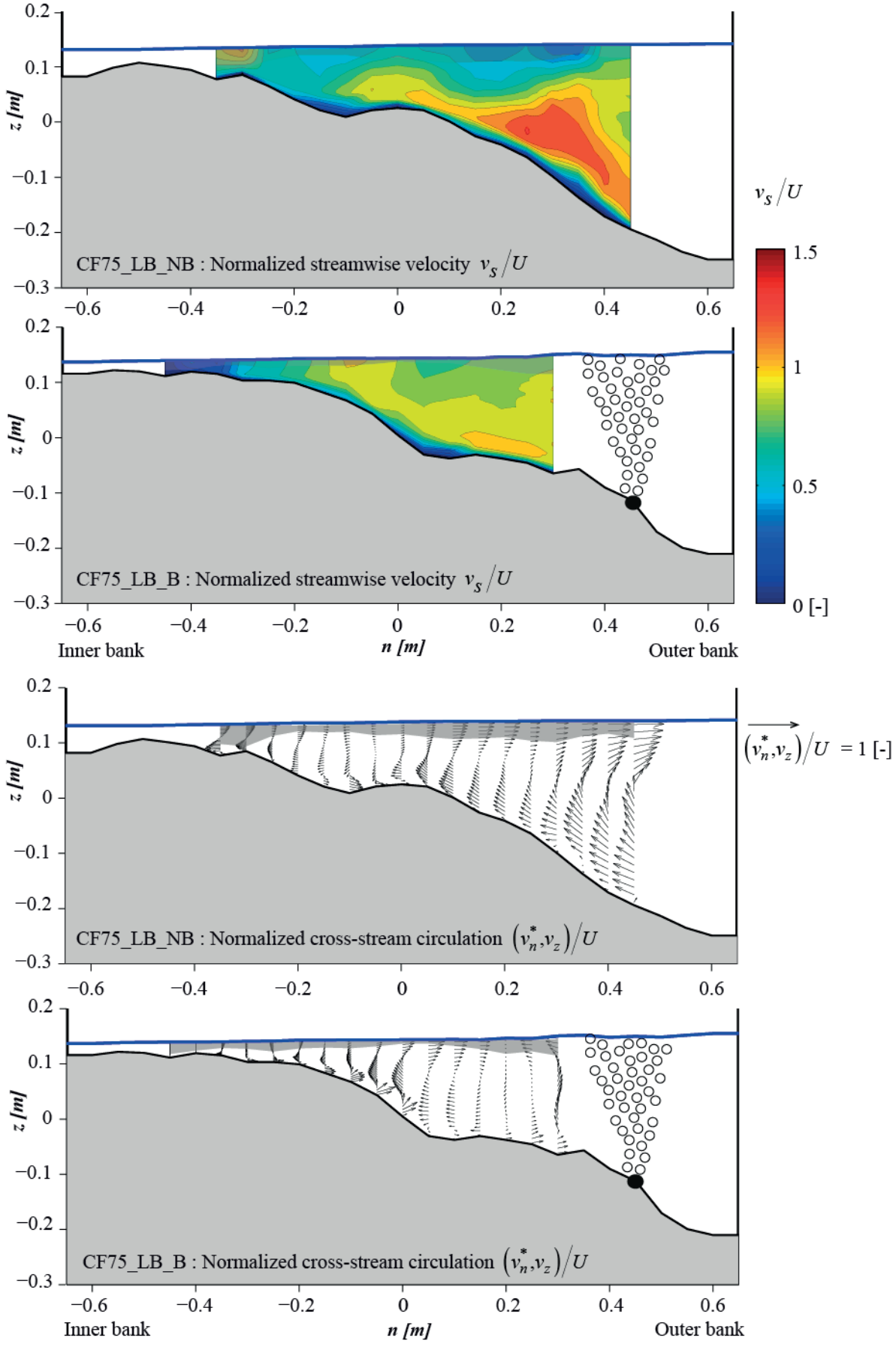

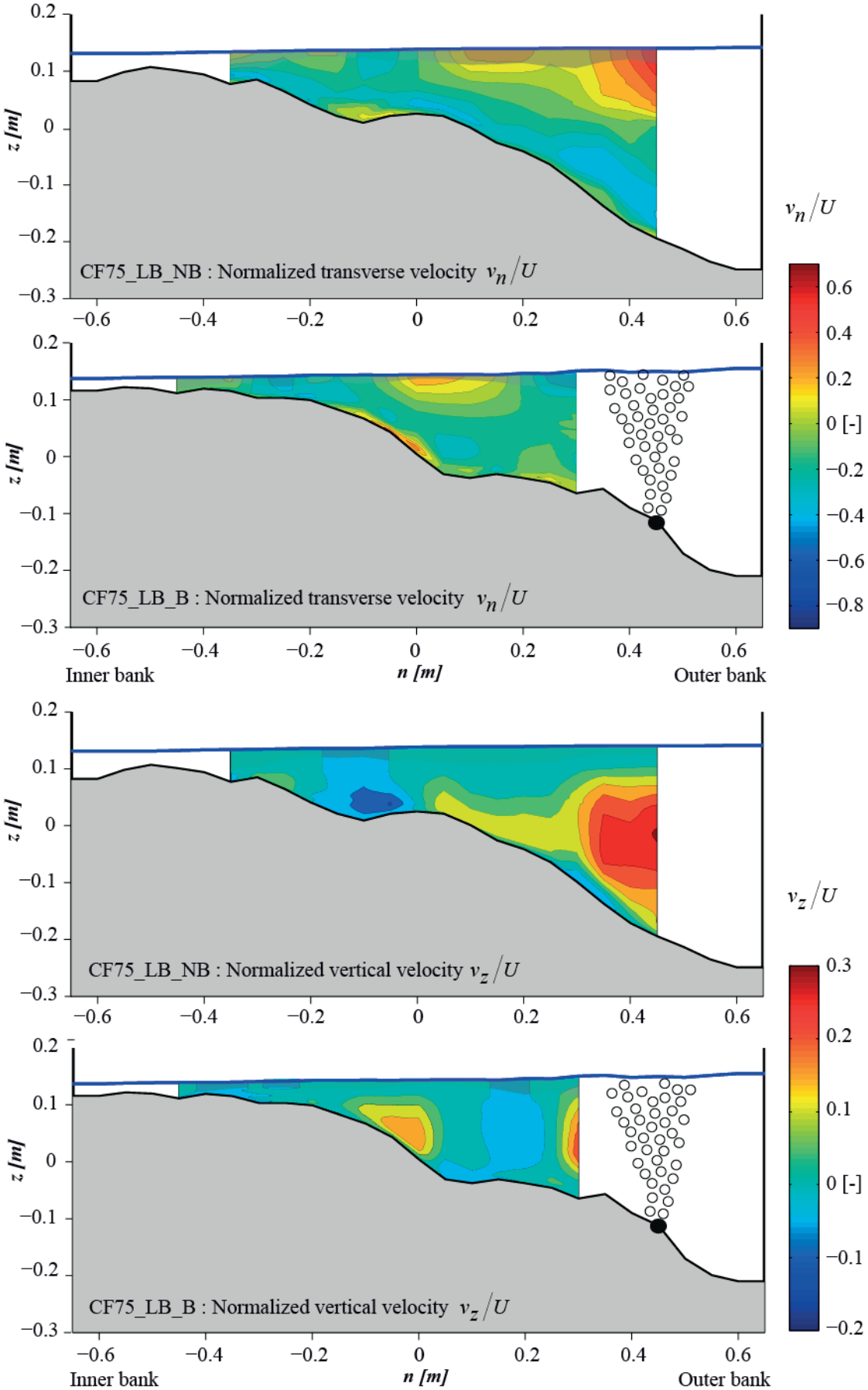
CF75_LB_NB : Normalized transverse velocity v_n/U
CF75_LB_B : Normalized transverse velocity v_n/U
v_n/U
CF75_LB_NB : Normalized vertical velocity v_z/U
CF75_LB_B : Normalized vertical velocity v_z/U
v_z/U
z [m]
n [m]
Inner bank
Outer bank

D.5 Cross-section at 120° in the bend

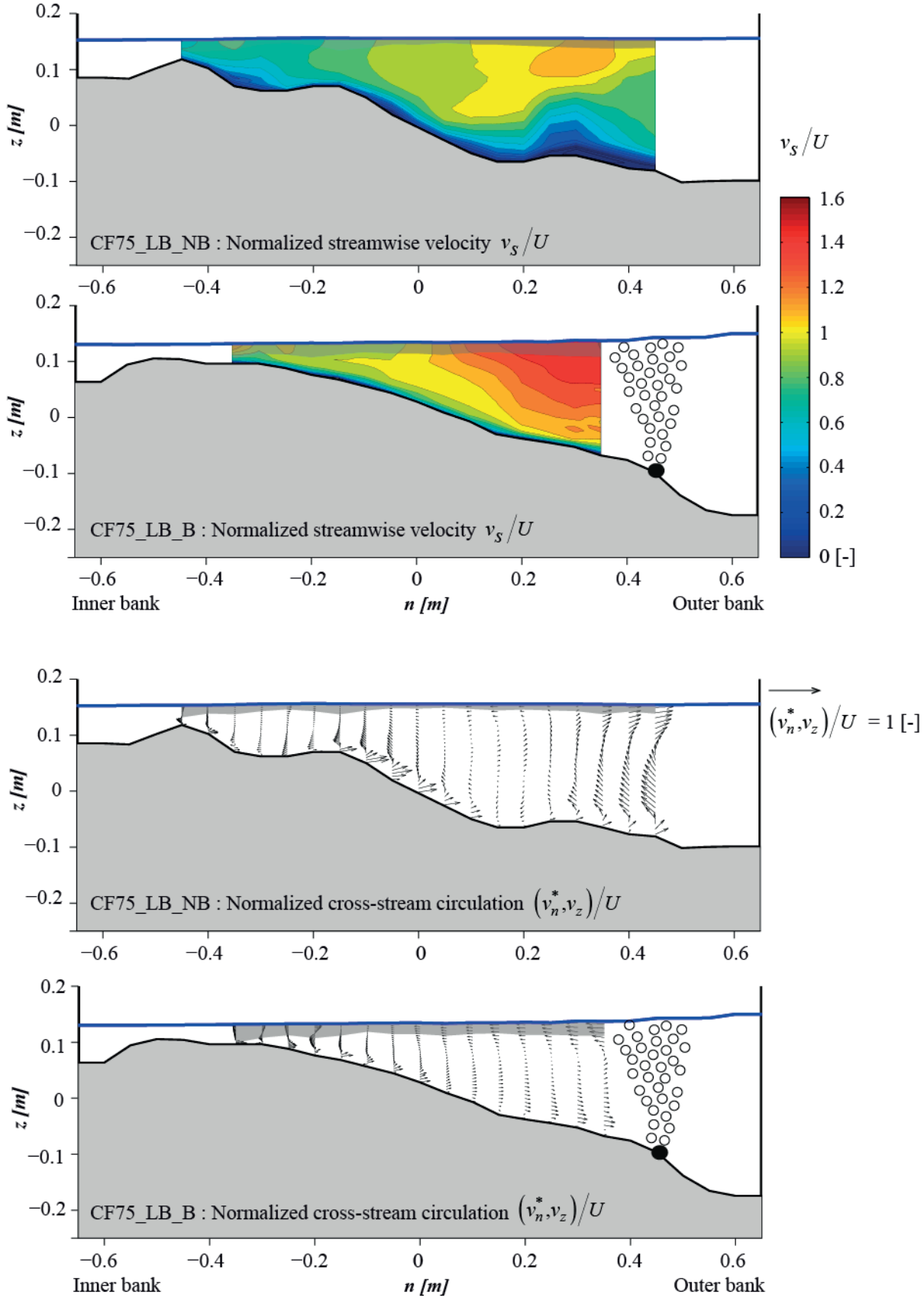

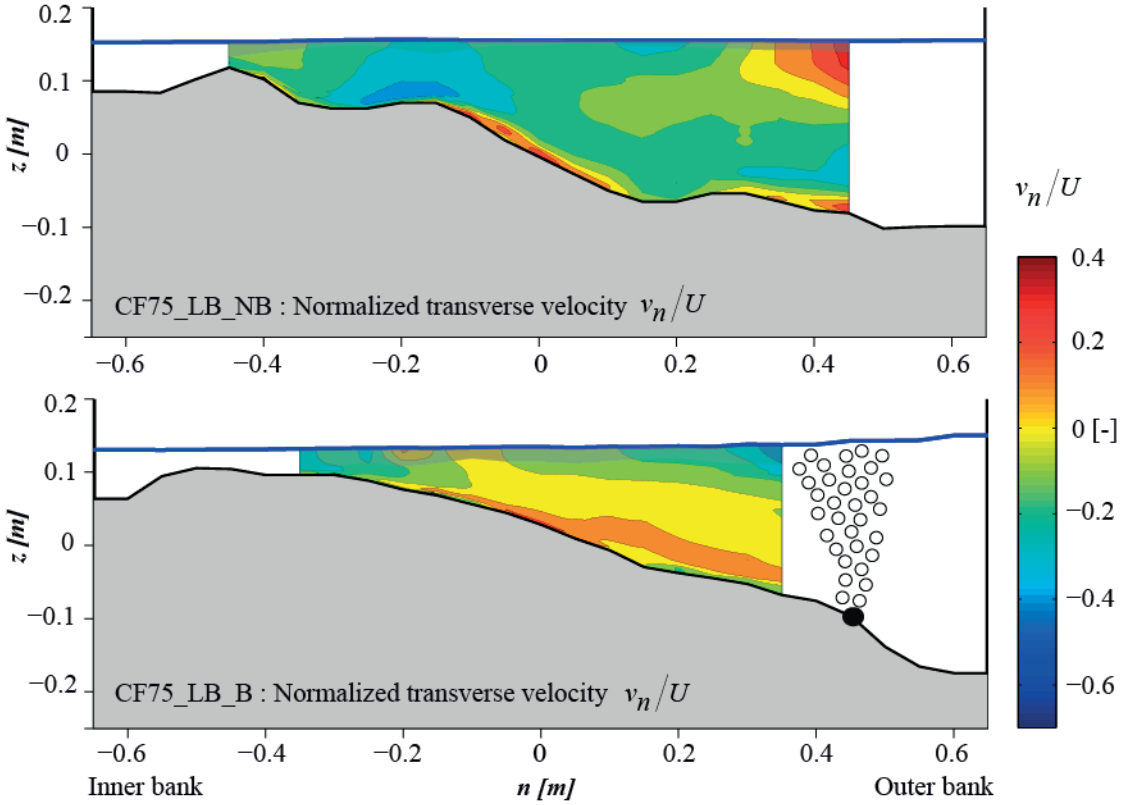
CF75_LB_NB : Normalized transverse velocity v_n/U
CF75_LB_B : Normalized transverse velocity v_n/U
z [m]
n [m]
Inner bank
Outer bank
v_n/U
0.4
0.2
0 [-]
−0.2
−0.4
−0.6

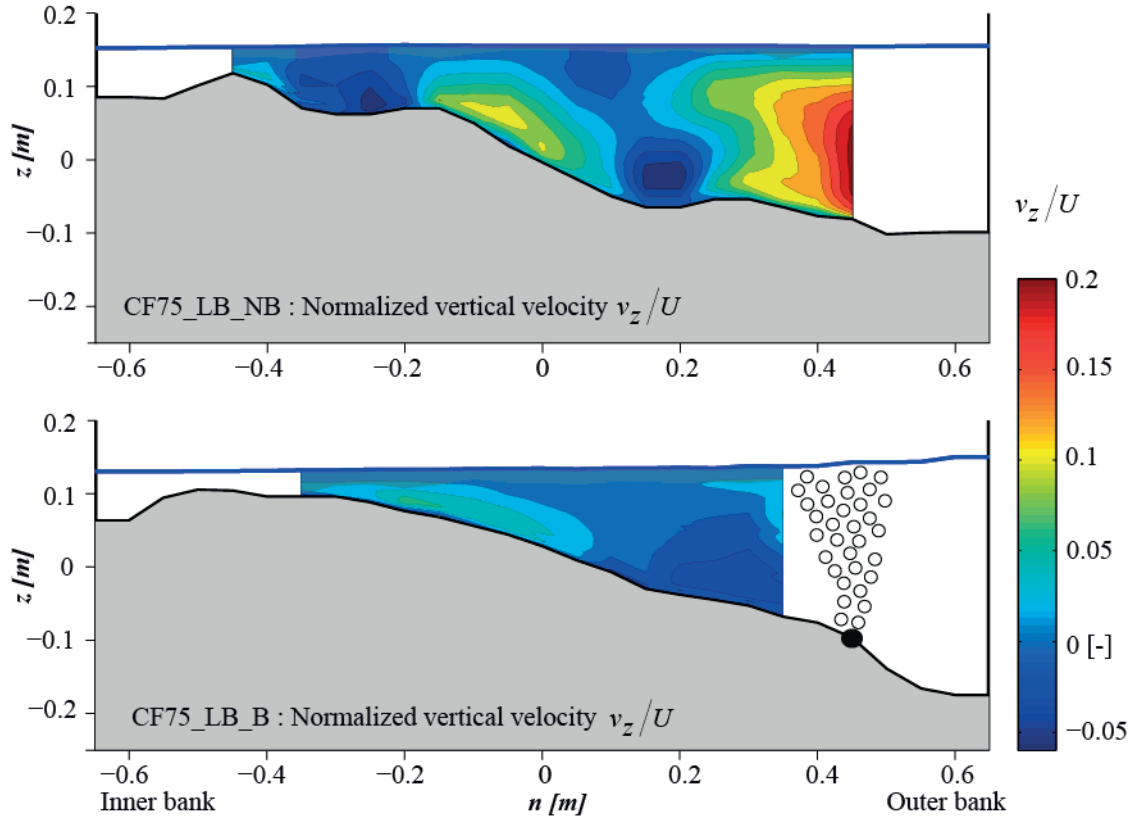
CF75_LB_NB : Normalized vertical velocity v_z/U
CF75_LB_B : Normalized vertical velocity v_z/U
z [m]
n [m]
Inner bank
Outer bank
v_z/U
0.2
0.15
0.1
0.05
0 [-]
−0.05

D.6 Cross-section at 150° in the bend

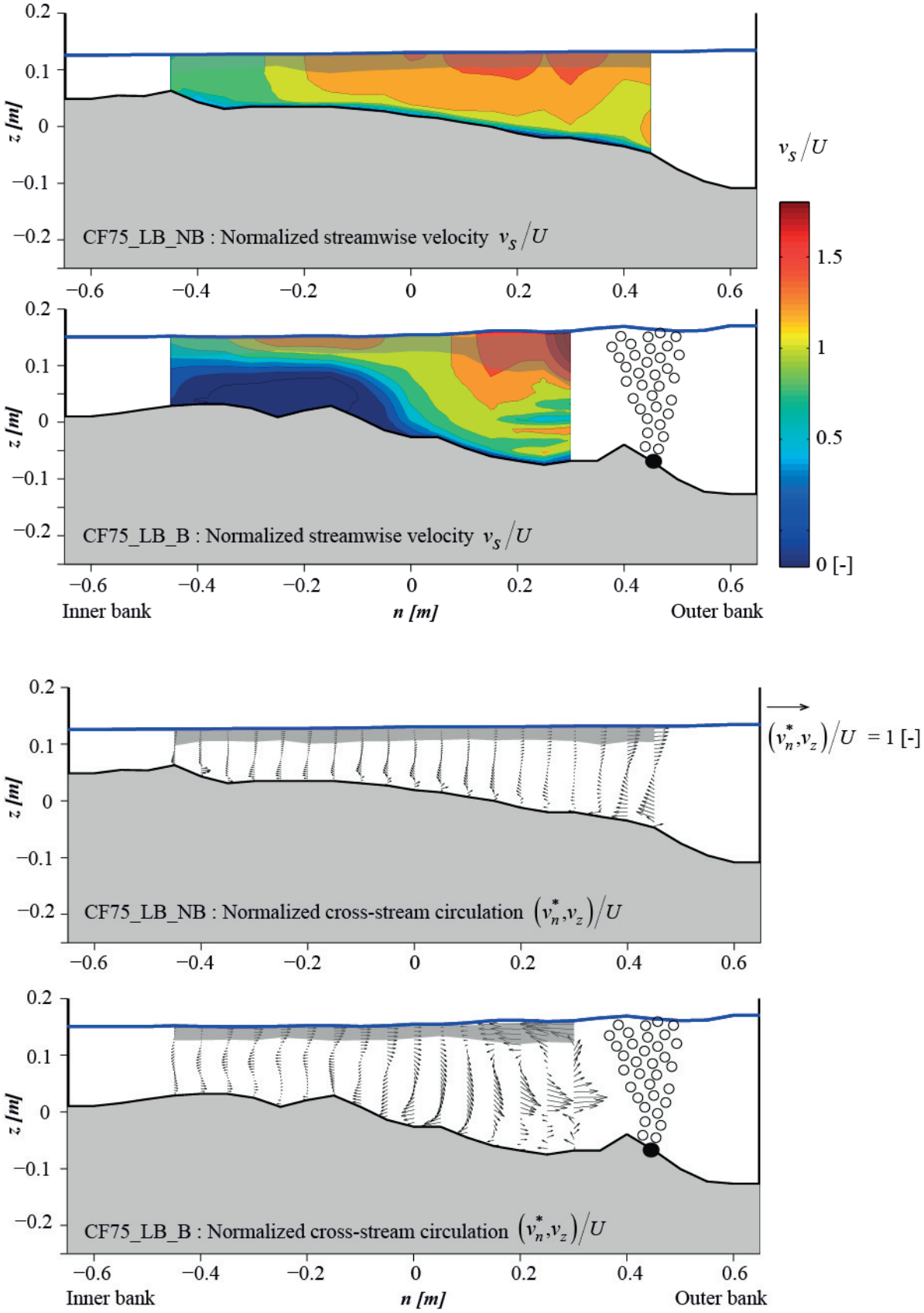

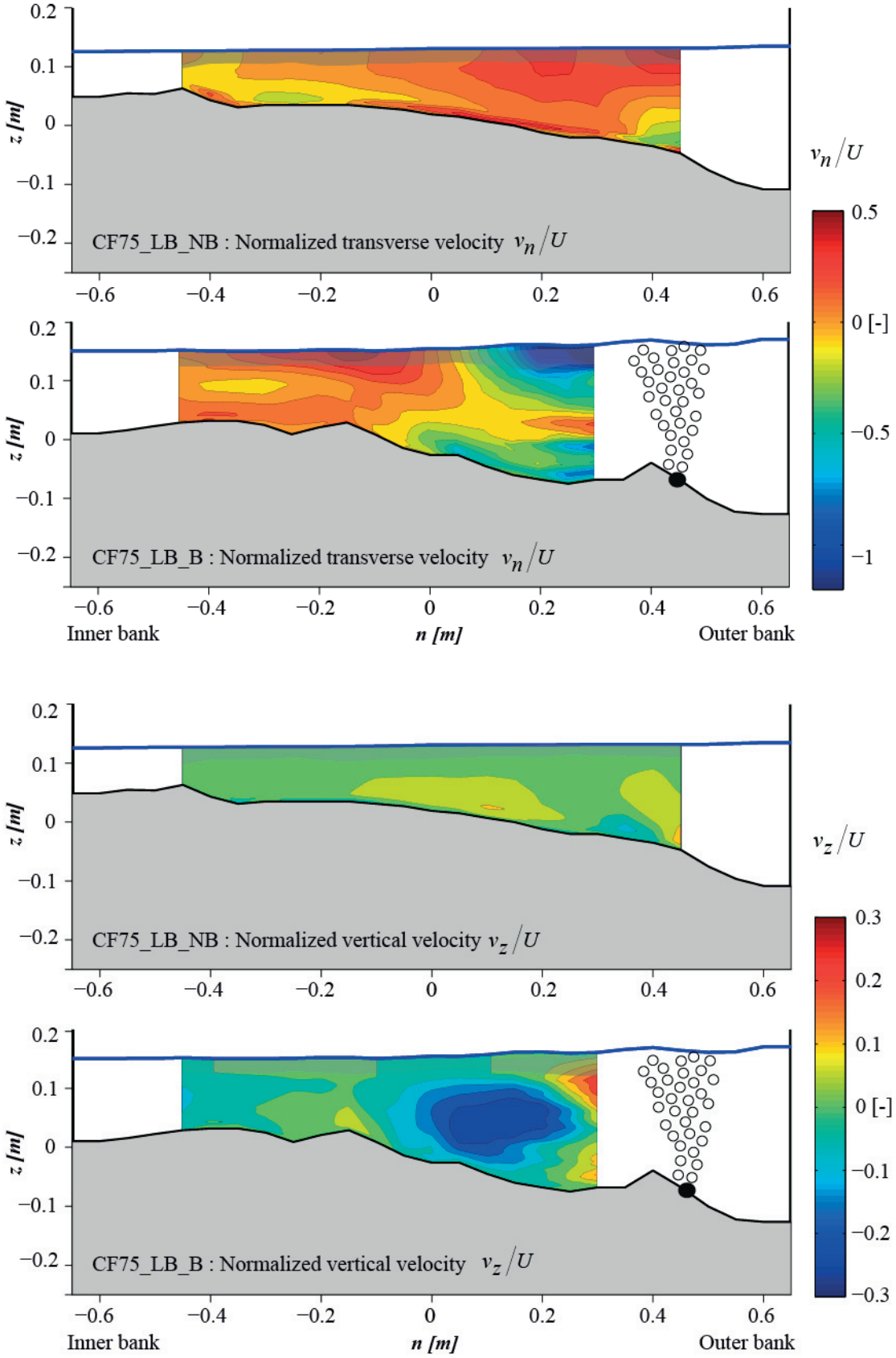
CF75_LB_NB : Normalized transverse velocity v_n/U
CF75_LB_B : Normalized transverse velocity v_n/U
v_n/U
0.5
0 [-]
−0.5
−1
CF75_LB_NB : Normalized vertical velocity v_z/U
CF75_LB_B : Normalized vertical velocity v_z/U
v_z/U
0.3
0.2
0.1
0 [-]
−0.1
−0.2
−0.3
z [m]
n [m]
Inner bank
Outer bank
0.2
0.1
0
−0.1
−0.2
−0.6
−0.4
−0.2
0
0.2
0.4
0.6

D.7 Cross-section at 180° in the bend

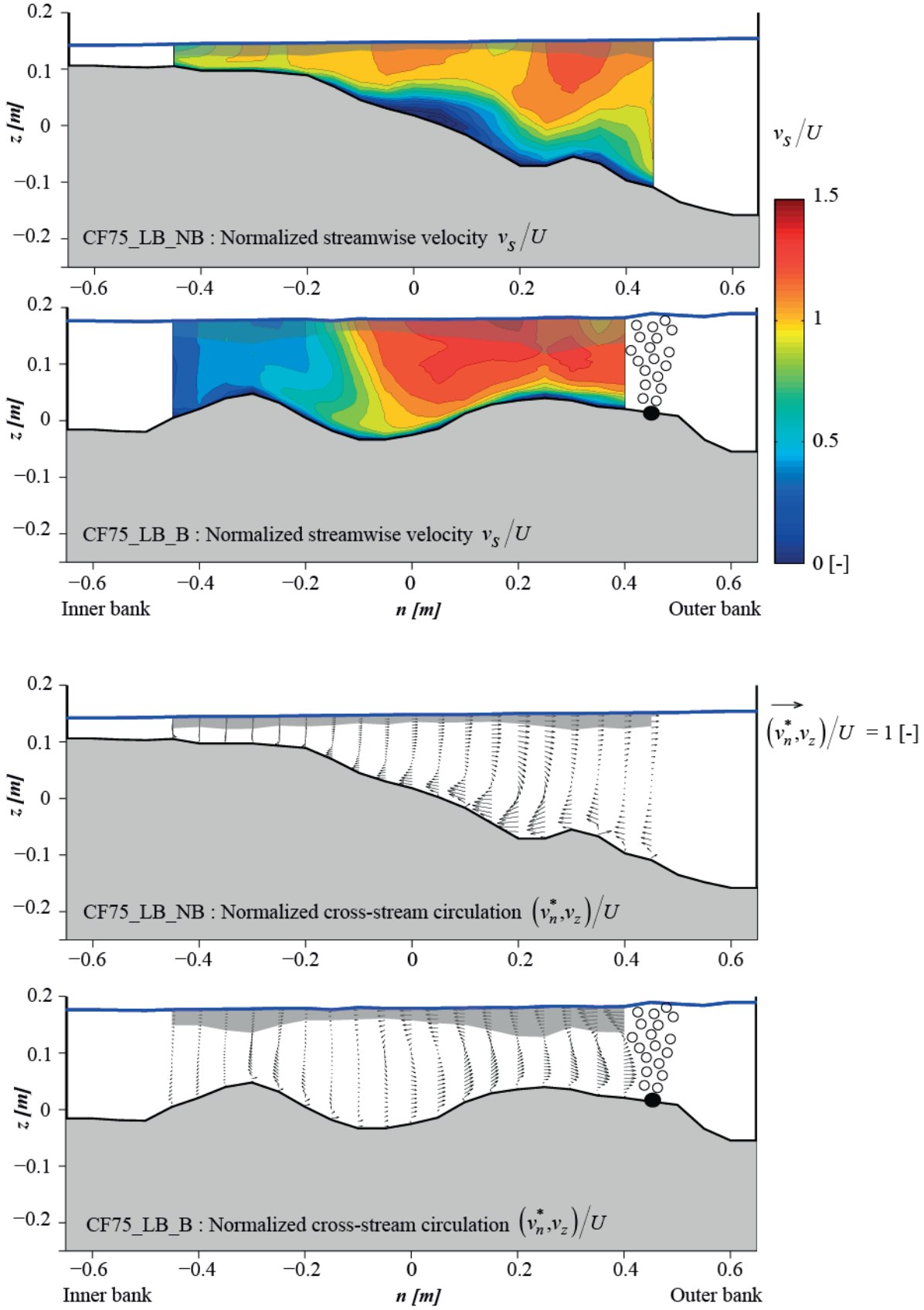

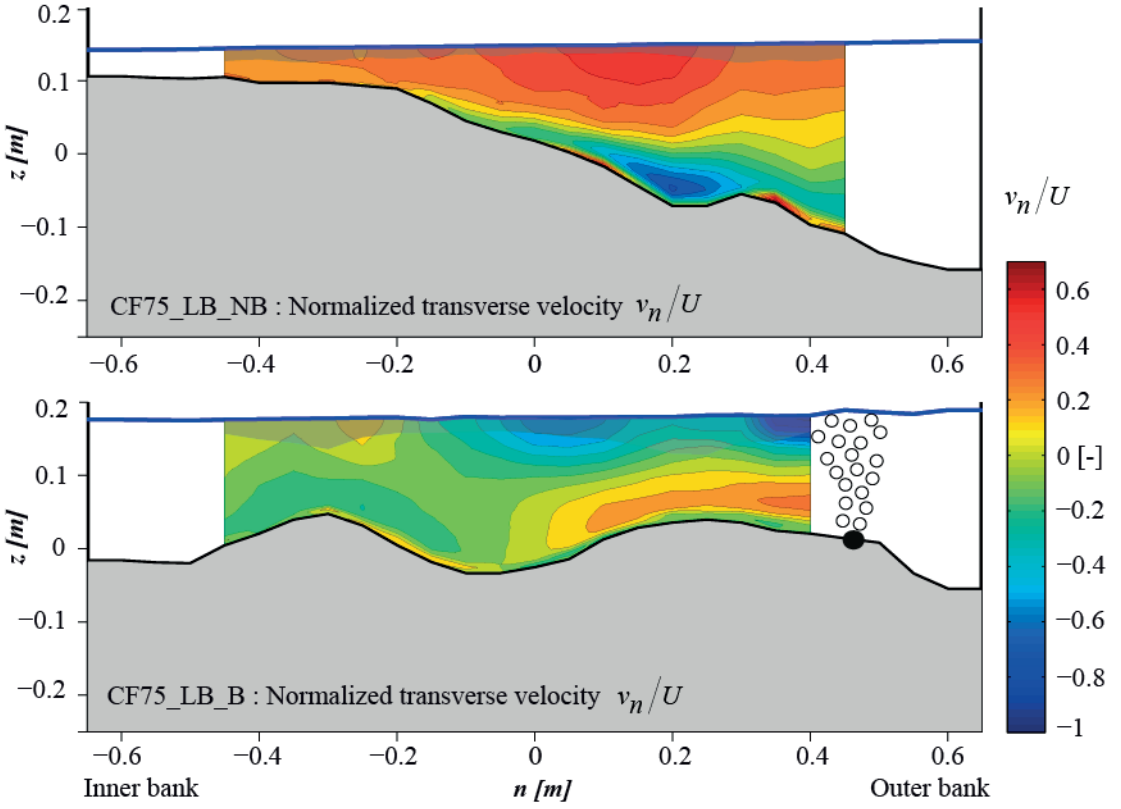
CF75_LB_NB : Normalized transverse velocity v_n/U
CF75_LB_B : Normalized transverse velocity v_n/U
v_n/U
z [m]
n [m]
Inner bank
Outer bank

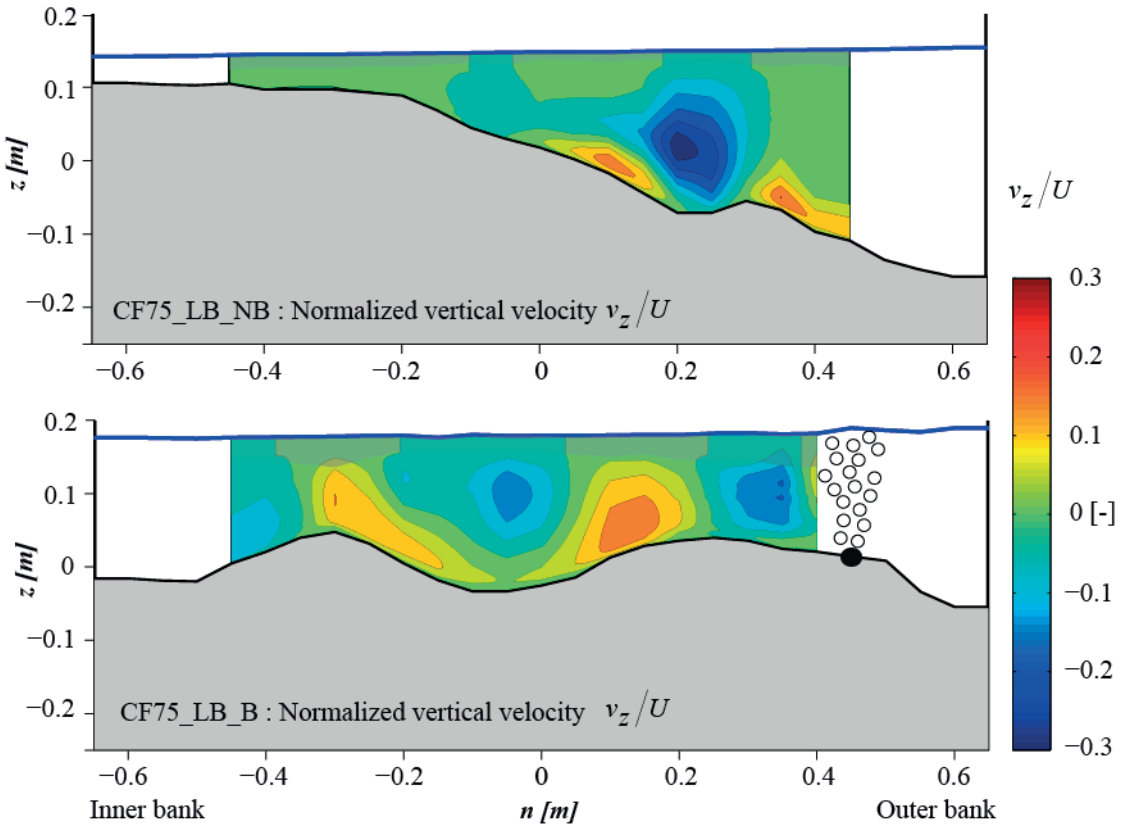
CF75_LB_NB : Normalized vertical velocity v_z/U
CF75_LB_B : Normalized vertical velocity v_z/U
v_z/U
z [m]
n [m]
Inner bank
Outer bank

D.8 Turbulent kinetic energy

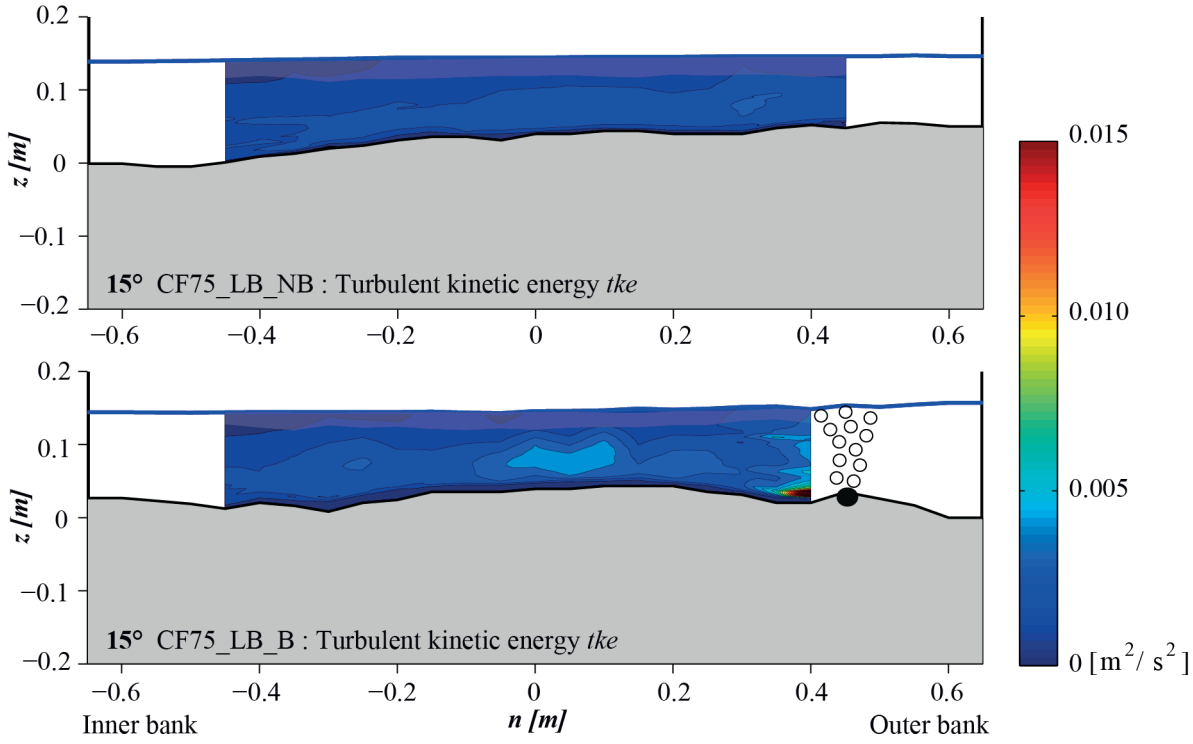

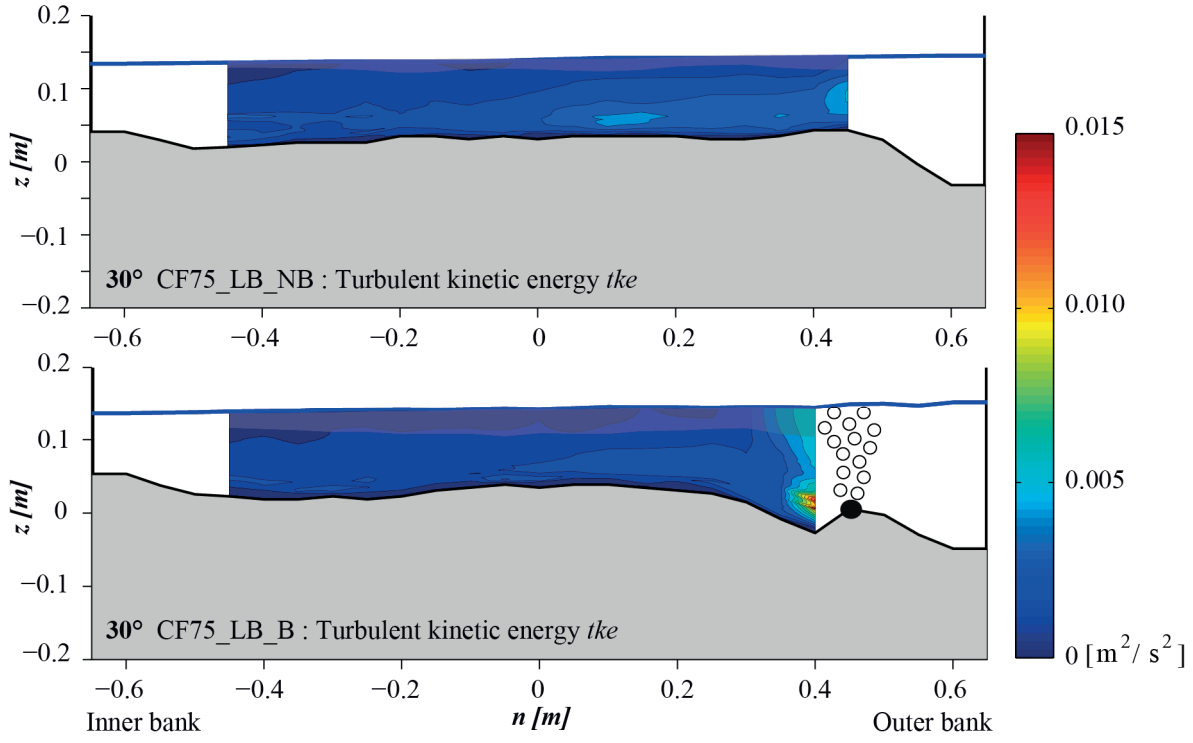

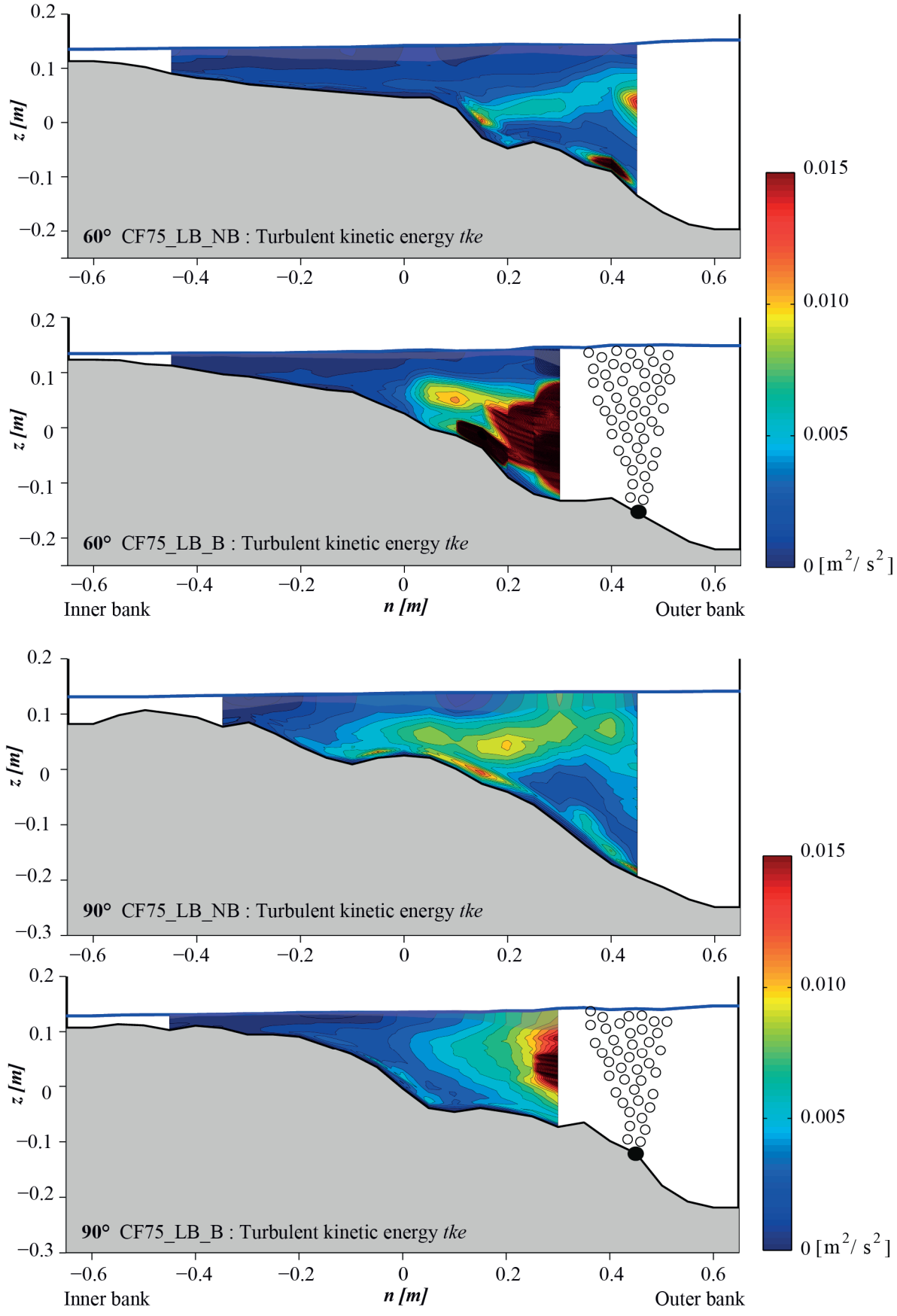
60° CF75_LB_NB : Turbulent kinetic energy tke
60° CF75_LB_B : Turbulent kinetic energy tke
90° CF75_LB_NB : Turbulent kinetic energy tke
90° CF75_LB_B : Turbulent kinetic energy tke
z [m]
n [m]
Inner bank
Outer bank
0.015
0.010
0.005
0 [m²/ s²]

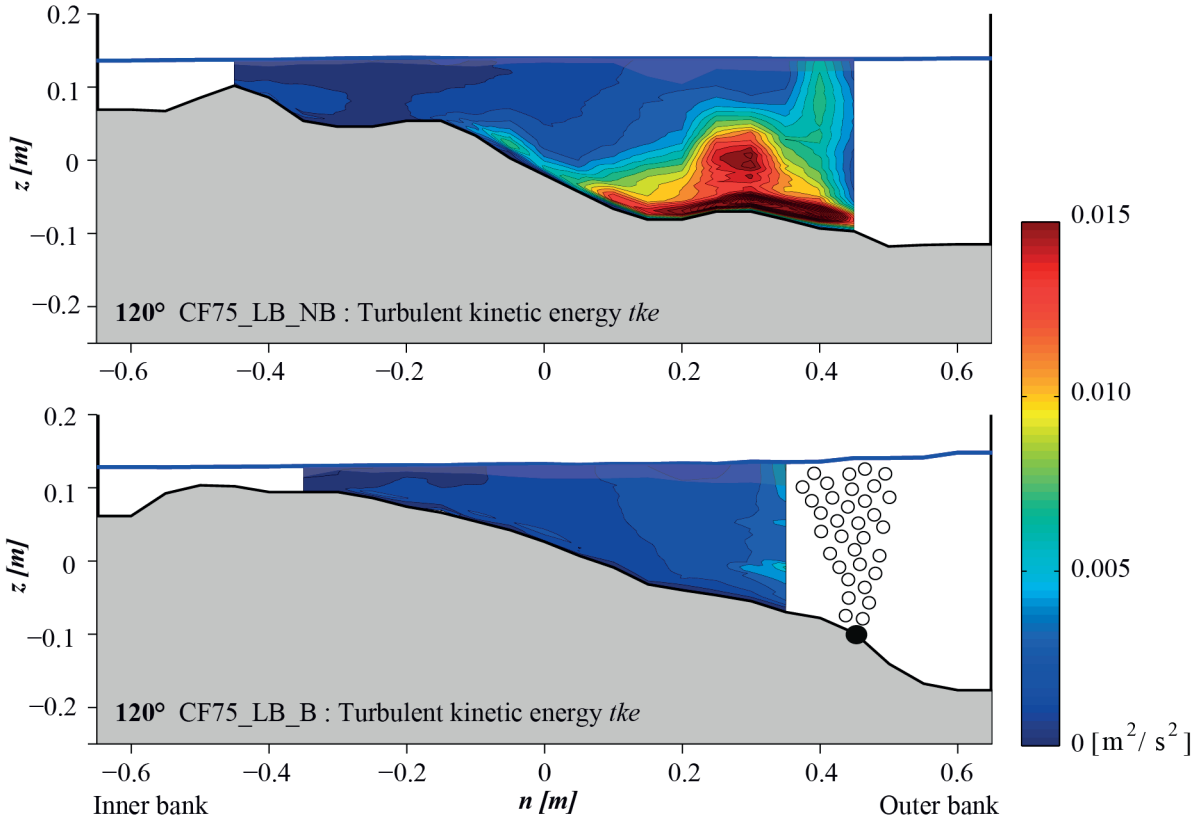
0.2
0.1
0
−0.1
−0.2
z [m]
120° CF75_LB_NB : Turbulent kinetic energy tke
120° CF75_LB_B : Turbulent kinetic energy tke
−0.6
−0.4
−0.2
0
0.2
0.4
0.6
Inner bank
n [m]
Outer bank
0.015
0.010
0.005
0 [m²/ s²]

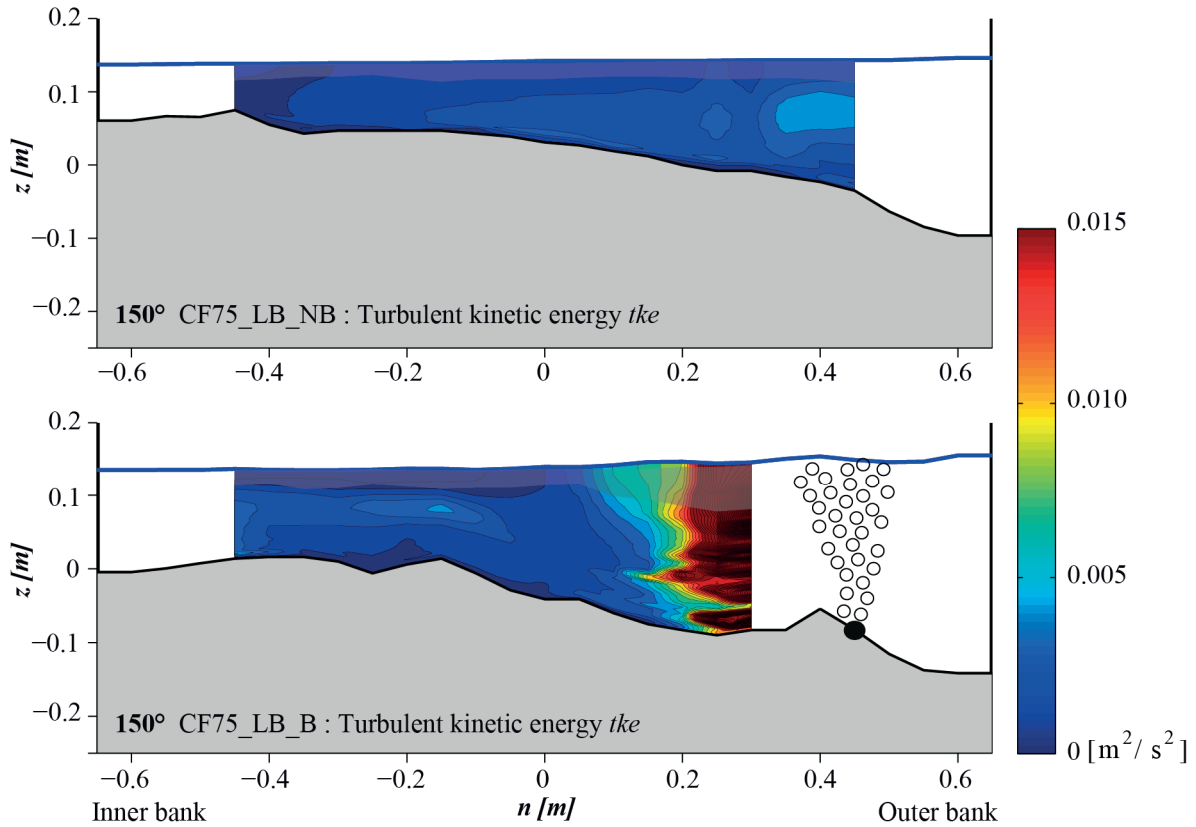
0.2
0.1
0
−0.1
−0.2
z [m]
150° CF75_LB_NB : Turbulent kinetic energy tke
150° CF75_LB_B : Turbulent kinetic energy tke
−0.6
−0.4
−0.2
0
0.2
0.4
0.6
Inner bank
n [m]
Outer bank
0.015
0.010
0.005
0 [m²/ s²]

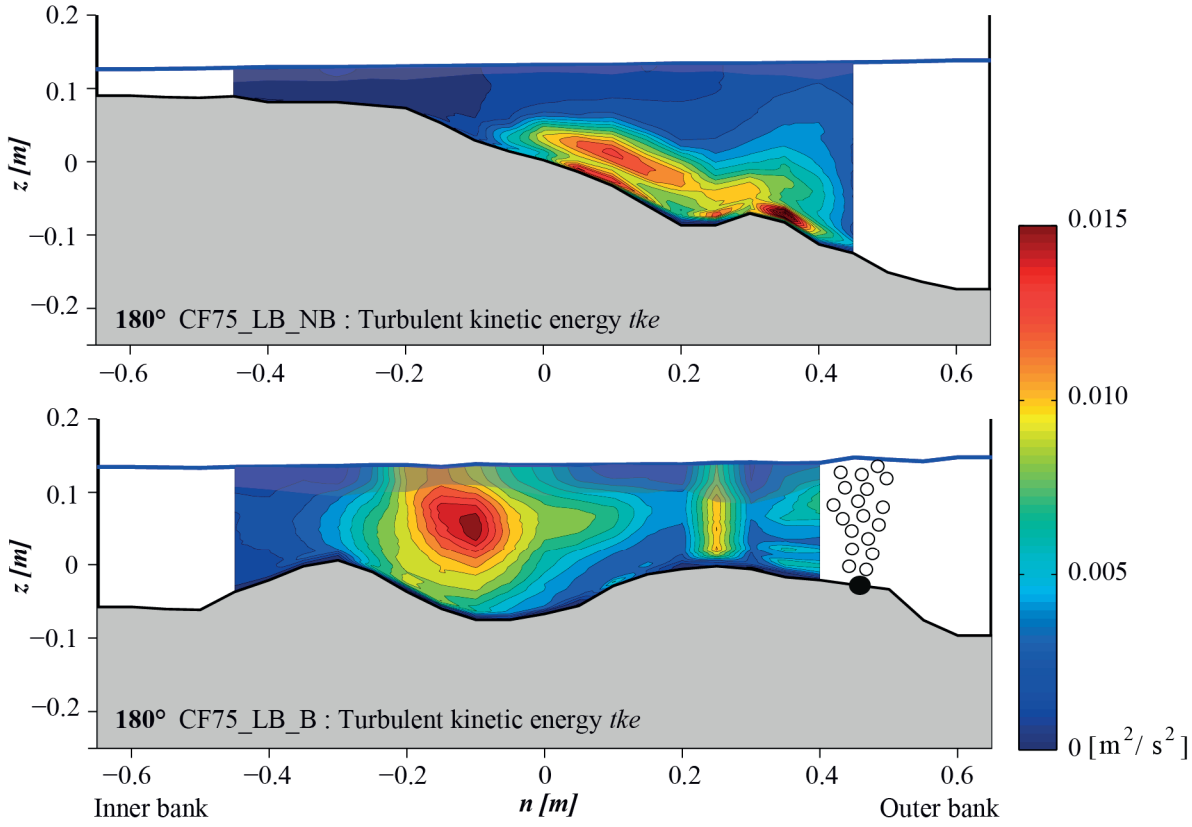
0.2
0.1
0
−0.1
−0.2
z [m]
180° CF75_LB_NB : Turbulent kinetic energy tke
−0.6
−0.4
−0.2
0
0.2
0.4
0.6
180° CF75_LB_B : Turbulent kinetic energy tke
Inner bank
n [m]
Outer bank
0.015
0.010
0.005
0 [m²/ s²]

E. PRELIMINARY STUDY ON THE INFLUENCE OF AN AIR-BUBBLE SCREEN ON LOCAL SCOUR AROUND A BRIDGE PIER

(by V. Dugué, E. Izadinia, S. Rigaud and A. J. Schleiss, *proc. of the 2nd IAHR Europe Congress*, Munich, Germany)

Abstract

Flow interactions with a bridge pier and movable river bed result in local scour which can endanger bridge pier foundations. This scour is initiated by the downward flow and amplified by the so-called horseshoe vortex. A new method to reduce scouring around bridge piers has been assessed with preliminary tests. A bubble screen located upstream of the pier may counteract the downward flow and avoid the initiation of scour.

Laboratory experiments have been performed in a shallow flume with a physical scale model of a bridge pier under clear-water scour conditions. The bubble screen is generated by means of a collar linked to the pier and connected to a pressurized air system. Different water and air discharges have been tested. Vertical and horizontal location of the bubble screen have also been investigated. For each experiment, the final bed topography has been measured and compared to a reference experiment without the bubble screen.

The long-term experiments (approximately 56 hours) have revealed that a well-designed bubble screen may reduce the local scour around the bridge pier.

Introduction

Interactions amongst a bridge pier, the approach flow and the erodible bed result in local scouring which can endanger the stability of the foundations. The presence of the pier generates a three-dimensional turbulent flow, characterized by downward velocities that impinge on the bed and generate the scour, and the so-called horseshoe vortex which amplify the scouring effect (Melville & Raudkivi, 1977, Breuser & Raudkivi, 1991, Graf & Yulistiyanto, 1998, Graf & Istiarto, 2002).

According to previous studies, local pier scour is directly related to the magnitude of vertical flow (discharge and velocity) parallel to the pier face. Therefore, it should be possible to reduce the scour depth by reducing the magnitude of the vertical flow at the upstream pier face. It could be also blocked by using a barrier placed perpendicular to the pier face.

The two major controlling measures employed for preventing or minimizing local scour at bridge piers reported in literature are (i) bed armoring countermeasures (Lagasse et al., 2001, Lauchlan & Melville, 2001) and (ii) flow-altering countermeasures such as circular collars around piers (Zarrati et al., 2006, Heidarpour et al., 2010), or cables wrapped spirally on the pile (Dey et al., 2006). However, they generally imply substantial constructive work.

The objective of the present preliminary study performed in the framework of a Master thesis is to have a first idea on the potential of a new technique that consists in counteracting the vertical velocities impinging on the bed by means of upward velocities induced by air bubbles rising from a pressurized half collar situated near the bed.

This principle was successfully used to attenuate local scour in open-channel bends (Blanckaert et al., 2008, Dugué et al., 2011).

With respect to "hard" engineering techniques, bubble screens have the advantages of being controllable, ecological (oxygenation), reversible and non-permanent. Bubble plumes or screens have already been successfully applied in several hydraulic fields at large and small scales such as lakes destratification (Schladow, 1993), as a pneumatic barrier against saltwater intrusion (Nakai & Arita, 2002) or to prevent shoaling in navigation channels (Chapman & Scott-Douglas, 2002).

Experiments with mobile-bed morphology under clear-water scour conditions have been performed in a shallow flume with a circular bridge pier in its center. Morphologic comparisons are provided in this paper with the aim to answer the following questions:

- Can a bubble screen reduce local scour near a bridge pier?
- What is the influence of the base flow on the bubble screen behaviour?

This paper first describes the experimental device and the bubble generation technique, then provides topographic comparisons between a reference experiment and several other ones with the bubble screen and finally presents visualization of the flow with the bubble screen near the bridge pier.

Experimental Set-up and Measurements

Experiments were performed in a 29 m long and 2.5 m wide rectangular erodible-bed channel at the Ecole Polytechnique Fédérale de Lausanne (EPFL) in Switzerland. This flume is described in Figure 1a. The same flume was used by Graf & Istiarto (2002) to investigate the flow patterns and turbulence around a cylinder in a scoured channel bed.

The sediment used for the experiments is uniform sand having a mean diameter of d_{50} = 2.1 mm and a distribution ratio of σ = 1.3. All experiments are performed under clear-water scour conditions.

The bridge pier, located 10 m after the entry of the channel has a diameter of D = 0.162 m. The bubble screen is generated by half a collar linked to the upstream side of the pier (Figure 1b). This collar is just a structural device required to generate the bubble screen but not intended to fix the bed in the entire zone covered by the local scour. Indeed, this collar was 4 cm wide, which is less than typical values for regular collar of 2 to 3 times the pier width (Zarrati et al., 2006).

The bubble screen can be generated by three different rows of 9 holes with an inner diameter of 4 mm (Figure 1b). The rows are located at three different positions from the upstream side of the pier (0.01, 0.02 and 0.03 m). To facilitate the generation of the bubble screen, the pier and the collar are entirely pressurized and connected to the pressurized air-system of the laboratory. Three different horizontal positions of the bubble screen have been previously investigated and the farthest from the pier (0.03 m) was found to be the most efficient and has been retained for all the presented tests.

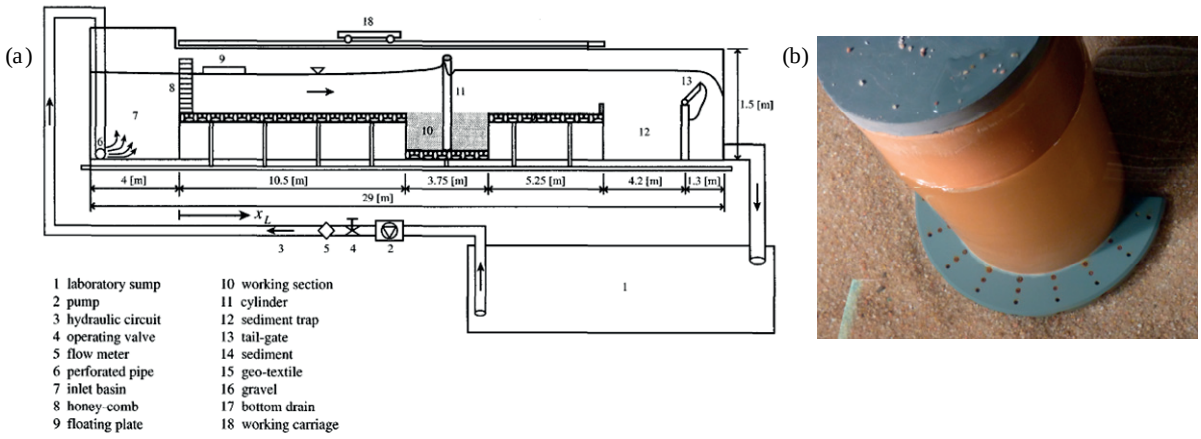

Figure 1: (left) General view of the channel (from Istiarto, 2001), (right) Photography of the pier with the collar and the bubble-screen generation system

Two different vertical positions for the collar and the bubble screen have been investigated. First, the collar was installed at the initial bed level (z = 0 m). In a second step, the collar was buried 5 cm below the mean bed level.

Water surface elevation was measured by means of a point gauge and final bed elevation measurements were performed on a refined grid with a Mini Echo Sounder. Bubble-screen behaviour was documented by means of photographs. The air pressure was regulated with a manometer and the air discharge measured with a rotameter.

Experiments have been performed continuously during 56 hours to obtain a morphology close to the equilibrium and to determine the maximal scouring depth under different configurations, with and without the bubble screen, but with similar air and water conditions. Configurations, main hydraulic and air parameters of these experiments are summarized in Table 1. For all tests, the initial condition was a flat bed.

Hydraulic conditions were chosen based on Istiarto & Graf (2002) experiments in which scour evolution was found to be asymptotic and 95 % of the maximal scouring depth was obtained before 56 hours of run. Based on these results, the tests were stopped after 56 hours of run to perform the bottom elevation measurements.

In addition, visualization of the influence of the base flow on the bubble screen has been performed for different air and water discharges, before the scour initiation.

Table 1: Experimental conditions of the long-term experiments

Label	Q_w $[m^3/s]$	H_w $[m]$	U_w $[m/s]$	Fr_w $[-]$	Collar $[-]$	Collar elevation $[m]$	Bubble screen $[-]$	Q_a $[10^{-3}\ m^3/s]$
1 : Reference	0.2	0.24	0.34	0.22	-	-	-	-
2 : Collar	0.2	0.24	0.34	0.22	✓	0	✓	-
3 : Collar + Bubble	0.2	0.24	0.34	0.22	✓	0	✓	2.25
4 : Buried collar	0.2	0.24	0.34	0.22	✓	-0.05	-	-
5 : Buried collar + Bubble	0.2	0.24	0.34	0.22	✓	-0.05	✓	2.25

Q_w is the water discharge, H_w is the flume-averaged water depth, U_w is the flume-averaged streamwise velocity, Fr_w is the water Froude number and Q_a is the air discharge.

Influence of the different configurations tested on the local scour morphology

Figure 2 illustrates patterns of the bed topography for the five long-term experiments and compares the reference situation of a non-protected pier with the four different configurations (Table 1, tests 2 to 5). For each experiment, the bed reference (z=0 m) coincides with the initial bed level in the flume. As the topography is symmetrical on each side of the bridge pier, only the right side of the topography is represented in the figures.

In all experiments, the scour hole development starts at the sides of the pier and propagates rapidly around the upstream part of the pier to finally reach the centerline.

The reference case, without collar and bubble screen is presented in Figure 2a. A scour hole develops all around the pier with a maximal depth located upstream of the pier on the centerline axis, as observed in the literature (Breuser & Raudkivi, 1991). The upstream part of the scour hole has a streamwise slope close to the angle of repose of the sediment. The maximal scour depth measured was 15.5 cm under the initial bed level.

With the collar (Figure 2c), scouring still occurs but its spatial extent has decreased, especially downstream of the pier. The maximal scour depth has been decreased by 2 cm in comparison with the reference situation, which represents a reduction of 10%.

With the bubble screen added to the collar (Figure 2d), this spatial extent as well as the maximal scour depth is even more reduced, extending to 25 cm upstream from the pier and 20 cm downstream from the pier. However, the maximal scouring depth has not been modified by the bubble generation.

As found in literature (Zarrati et al., 2004), lowering the collar below the initial bed level increases the extension of the scour around the pier as well as the maximal scouring depth compared to a collar placed at the initial bed level (Figures 2c, e). The extension is especially increased downstream of the pier. In both cases, scour develops underneath the collar. However, when the bubble screen is used in addition to the buried collar (Figure 2f), the spatial extent of the scour hole is considerably reduced downstream of the pier. Moreover, the maximal scour depth reached 9.5 cm which represents a reduction of 39 % in comparison with the reference situation of a non-protected pier.

The streamwise evolution of the bed elevation at the centerline of the flume in the five experiments is represented in Figure 2b. The maximal scouring depth could not be measured very near the pile, except for the reference situation, because of the protrusion of the collar. In each experiment, scouring occurs near and upstream of the bridge pier but its maximal depth is evolving with the different configurations. Compared to a non-protected pier, the maximal scour depth is reduced when using the four different investigated configurations. In both bubble-screen cases, the maximal scour depth has decreased in comparison to the reference case. It shows that the bubble screen does not have a negative impact on the erosion.

The minimal scour depth was obtained when using the bubble screen in addition to a buried collar. However, the maximal spatial extent was obtained for the buried collar without the bubble screen. This would imply a continuous use of the bubble screen and the non-permanent advantage of this countermeasure would be lost.

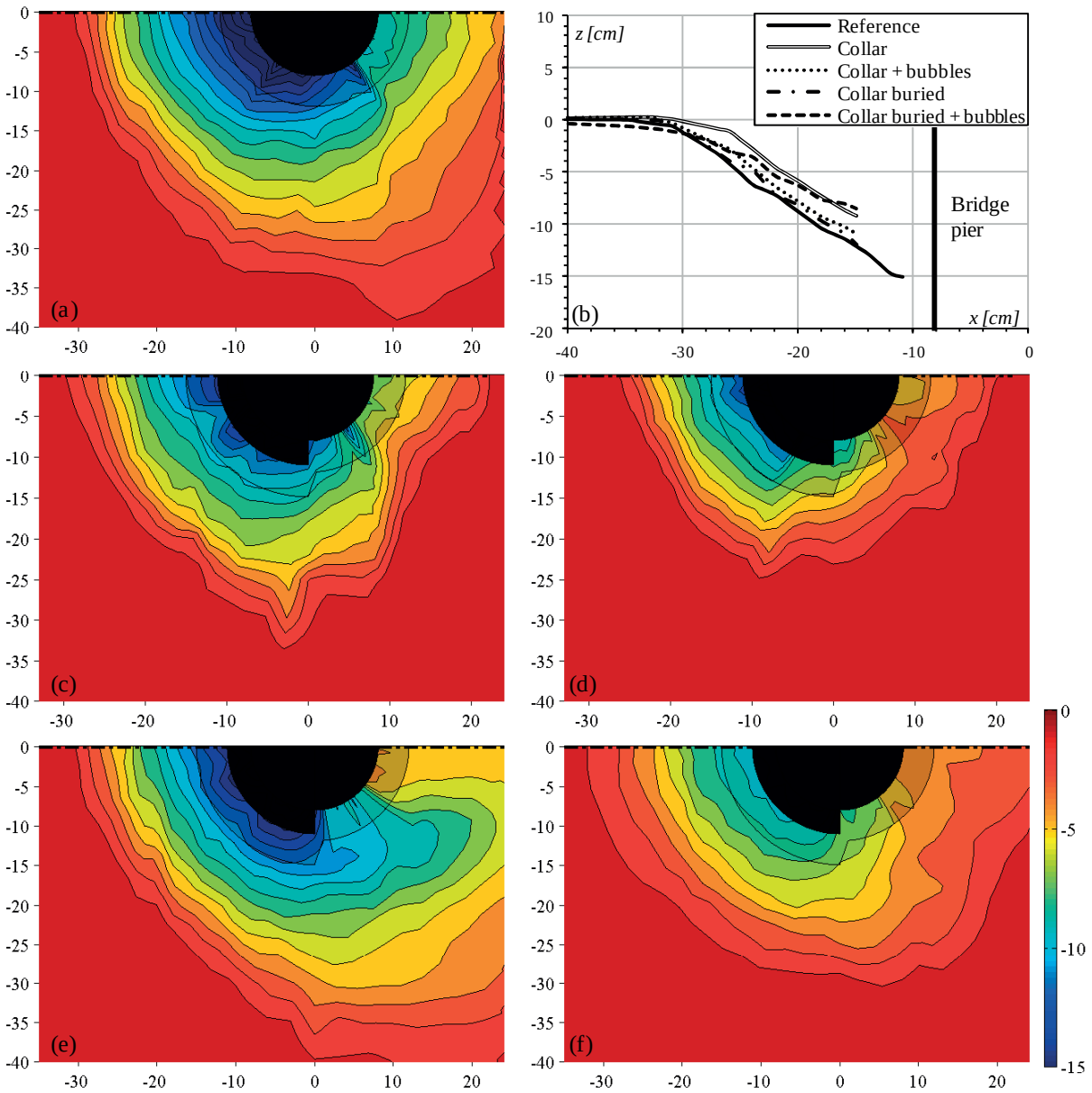

Figure 2: Isolines of the bed level with an interval of 0.01 cm derived from Mini Echo Sounder measurements for the reference (a), collar (c), collar + bubble screen (d), buried collar (e) and buried collar + bubble screen (f) experiments. The same color scale has been used to simplify comparison. The dashed area near the bridge pier indicates the area bridged by means of extrapolations. (b) Streamwise evolution of the bed slope at the center line of the flume

Finally, the optimal configuration would be the bubble screen used in addition of a collar with a small width (Configuration 3). The maximal scouring depth has only been decreased of 13% but the spatial extent of the scour is considerably reduced. Moreover, this configuration has the advantages to induce less fixed and permanent constructions in the river.

Consequently, the Configuration 3 has been chosen to perform the visualization of the bubble screen involving different air and water discharges.

Influence of air and hydraulic conditions on the bubble-screen behaviour

The present section will investigate the impact of both air and river discharges on the bubble-screen behaviour and determines the different flow type induced. For these tests, Configuration 3, with the bubble screen used in addition to the collar installed on the bed reference level, was chosen.

In order to have a better visualization of the phenomenon involved, photographs have been taken before the scour initiation for different hydraulic and air conditions to illustrate the existence of the different flow types observed (Figure 3).

In a similar procedure, Nakai and Arita (2002) experimentally investigated the flow mechanism of a saline wedge intrusion in the presence of a transverse bubble screen. They classified interactions between the bubble screen and the river base flow into two types which have also been observed in the reported experiments.

First, flow behaviour is controlled by the buoyancy flux of the bubble screen (Figure 3, sketch 1). Bubbles rise to the water surface and surface flow can be observed in either upstream or downstream direction. Moreover, a weak secondary flow can be observed in the upstream side of the bubble screen. This bubble-induced secondary flow can be visualized on Figures 3a and 3b where surface current exits upstream of the pier.

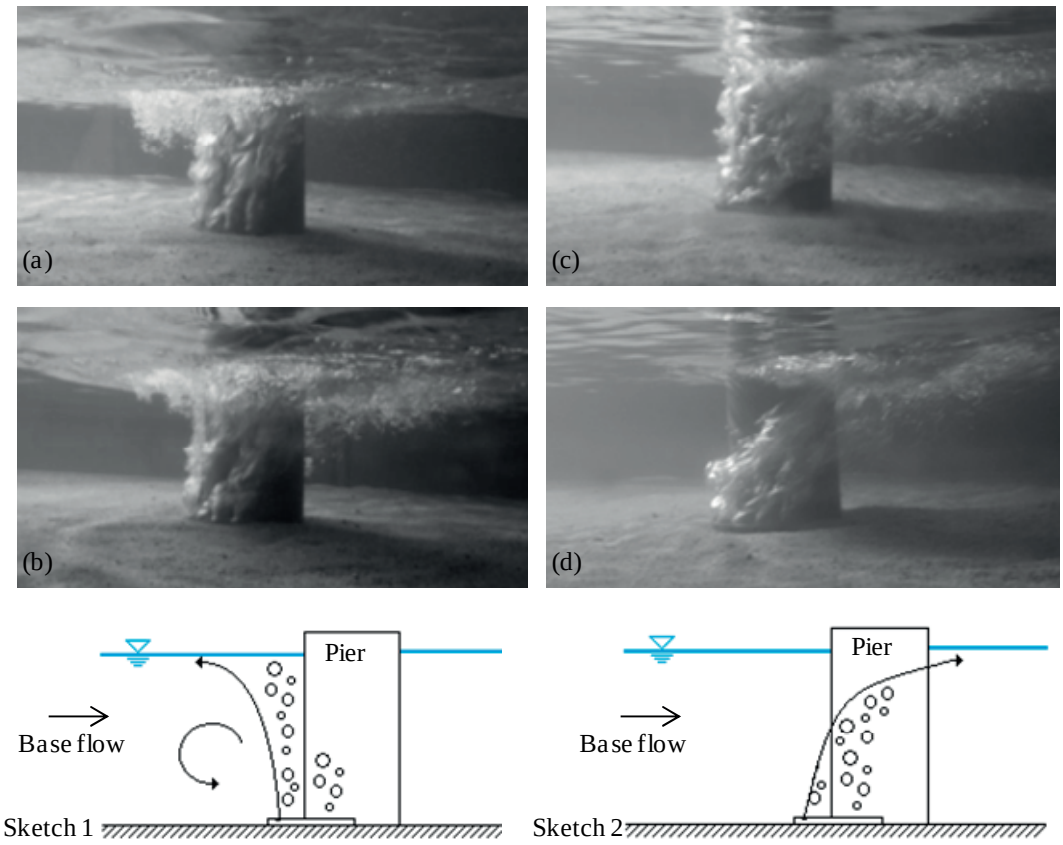

Figure 3 : (Top) Examples of different behaviour of the air-bubble screen regarding the air and water discharges: (a) Q_w = 0.1 m^3/s and Q_a=2.25 10^{-3} m^3/s, (b) Q_w = 0.15 m^3/s and Q_a=2.25 10^{-3} m^3/s, (c) Q_w = 0.2 m^3/s and Q_a = 3 10^{-3} m^3/s, (d) Q_w=0.18 m^3/s and Q_a=1.7 10^{-3} m^3/s. (Bottom) Schemes of the two different types of flow. Dominant effect of the bubble screen (Sketch 1), Dominant effect of the base flow (Sketch 2).

Second, flow behaviour is controlled by the inertial force of the river base flow (Figure 3, sketch 2). The surface flow induced by the bubble screen only exists in the downstream direction (Figure 3c). The upstream bubble-induced secondary flow is no longer observed. In extreme conditions (Figure 3d), the bubbles are no longer able to reach the water surface upstream of the pier. However, vertical upwards velocities can still be observed near the bed upstream of the pier. This indicates that the bubble screen may be efficient for a large range of river discharges.

However, morphologic investigations have to be performed in order to conclude on the long-term occurrence of these observations.

Conclusion

In the reported study, morphodynamics around a bridge pier was experimentally investigated introducing a new technique to counteract erosion: a bubble screen. The concluding remarks obtained are as follows:

If the bubble screen is optimally located (distance from the pier, vertical elevation) and if the air discharge is carefully chosen, the local scour may be reduced. The maximal scouring depth obtained with the bubble screen buried 5 cm below the bed level was reduced by 40% in comparison to a non-protected pile.

Bubble screen and river discharges were found to be relevant to optimize the efficiency of this countermeasure. Indeed, two different types of flow behaviour have been observed. When the buoyancy effect are dominant, the bubbles rise in front of the pier and surface flow spreads on both side generating a secondary flow in the upstream side of the pier. The efficiency of the bubble screen would then be optimal.

If the inertial force of the river base flow is dominant, bubbles are transported by the streamwise flow and the upstream bubble-induced secondary flow does not exist anymore. Only near bed upwards velocity still occurs.

In this report, several parameters, such as the horizontal and vertical location of the bubble screen, have been investigated in different configurations. However, interactions with other parameters, such as the bed material characteristics, the pier geometry and the mean water depth have to be investigated in order to clearly define the efficiency of the bubble screen to protect bridge pier against erosion.

Moreover, a better understanding of the redistribution of the velocity field induced by the bubble screen is relevant and is under investigation.

References

Blanckaert, K., Buschman, F. A., Schielen, R. &Wijbenga, J. H. A. (2008). Redistribution of velocity and bed shear stress in straight and curved open-channels by means of a bubble screen: Laboratory experiments. Journal of Hydraulic Engineering-ASCE ,134(2): 184-195.

Breuser, H. N. C., & Raudkivi, A. J. (1991). Scouring. International Association for Hydraulic Research, ed., Bakelma, Rotterdam, The Netherlands.

Chapman, J. E. & Scott-Douglass, L. (2002). Evaluation of a berth sedimentation control technology in the Kill Van Kull. The AirGuard pneumatic barrier system. Proc. of the third Specialty Conference on Dredging and dredged material disposal, Orlando, USA.

Dey, A., Sumer, B. M. & Fredsøe J. (2006). Control of scour at vertical circular piles under waves and current. Journal of Hydraulic Engineering, 132(3), 270-279.

Dugué, V., Blanckaert, K. & Schleiss, A. J. (2011). Influencing bend morphodynamics by means of an air-bubble screen - Topography and velocity field. Proceedings of the 7th IAHR Symposium on River, Coastal and Estuarine Morphodynamics, Beijing, China.

Graf, W. H., & Yulistiyanto, B. (1998). Experiments on flow around a cylinder; the velocity and vorticity fields. Journal of Hydraulic Research, 36(4), 637-653.

Graf, W. H. & Istiarto, I. (2002). Flow pattern in the scour hole around a cylinder. Journal of hydraulic research, 40(1), 13-20.

Heidarpour, M., Afzalimehr, H. & Izadinia, E. (2010). Reduction of local scour around bridge pier groups using collars. International Journal of Sediment Research, 25(4), 411-422.

Istiarto, I. (2001). Flow around a cylinder in a scoured channel bed. PhD-thesis Nr 2368, Ecole Polytechnique Fédérale de Lausanne, Switzerland.

Lagasse, P. F., Zevenbergen, L. W., Schall, J. D., and Clopper, P. E. (2001). Bridge scour and stream instability countermeasures. HEC23 FHWA NHI 01-003. Federal Highway Administration, U.S. Dept. of Transportation, Washington, D.C.

Lauchlan, C. S. & Melville, B. W. (2001). Riprap protection at bridge piers. Journal of Hydraulic Engineering-ASCE, 127(5), 412-418.

Melville, B. W. & Raudkivi, A. J. (1977). Flow characteristics in local scour at bridge piers. Journal of Hydraulic Research, 15(4), 373-380.

Nakai, M., & Arita, M. (2002). An experimental study on prevention of saline wedge intrusion by an air curtain in rivers. Journal of Hydraulic Research, 40(3), 333-339.

Schladow, S. G. (1993). Lake destratification by bubble-plume systems - design methodology. journal of Hydraulic Engineering-ASCE, 119(3), 350-368.

Zarrati, A. R., Nazariha, M. & Mashahir, M. B. (2004). Application of collar to control scouring around rectangular bridge piers. Journal of Hydraulic Research, 42(1), 97-103.

Zarrati, A. R., Nazariha, M. & Mashahir, M. B. (2006). Reduction of local scour in the vicinity of bridge pier groups using collars and riprap. Journal of Hydraulic Engineering, 132(2), 154-162

Curriculum Vitae

Violaine DUGUÉ

Engineer in Hydraulic and Fluid Mechanics

French
Born March 22, 1987
violaine.dugue@gmail.com

EDUCATION

2009-2013 **PhD. student and research assistant**

Laboratory of Hydraulic Constructions, Ecole Polytechnique Fédérale de Lausanne (EPFL), Switzerland

Research project : "Influencing river morphodynamics by means of bubble screens - Fundamental and application to open-channel bends"

2008-2009 **Master degree in Hydrology, Hydrochemistry, Ground and Environment**

Paul Sabatier University, Toulouse, France

2006-2009 **Master degree in Hydraulic and Fluid Mechanics Engineering with specialization in Water and Environment Sciences**

National Engineering School of Electrotechnics, Electronics, Computer Science, Hydraulics and Telecommunications, Toulouse, France

EXPERIENCE

2009-2013 **Research assistant at the Laboratory of Hydraulic Constructions (LCH), EPFL**

Hydraulic physical modeling of an auxiliary spillway for Gage II Dam, France

(Client: Electricité de France)

Assistance for undergraduate students in river ecomorphology, design of small hydropower plants and hydraulic constructions courses.

2009 (6 months) **Trainee at CEMAGREF (National Research Institute of Science and Technology for Environment and Agriculture), Lyon, France**

Influence of floods and dam flushes on a mountain river morphodynamic

2008 (3 months) **Trainee at the Environmental Hydraulics Laboratory (LHE), EPFL**

Experimental laboratory work and simulation of granular avalanches

LANGUAGE SKILLS

French	Mother tongue
English	Fluent
German	Basic knowledge

COMPUTER SKILLS

Modeling	Fluent, HEC-RAS, Telemac 2D
Drawing	AutoCAD, Adobe Illustrator
Data analysis	Matlab
Others	Latex, Microsoft Office

LIST OF PUBLICATIONS

Dugué, V., Blanckaert, K., Chen, Q. and Schleiss, A.J. (2012). Influencing flow patterns and bed morphology in rivers by means of an air-bubble screen. ***River Research and Applications*** (submitted for publication).

Dugué, V., Pfister, M., Hachem, F., Boillat, J.-l., Nagel, V. and Laugier, F. (2012). Etude sur modèle physique du nouvel évacuateur d crue du barrage de Gage II. ***La Houille Blanche*** (accepted for publication)

Dugué, V., Blanckaert, K., Chen, Q. and Schleiss, A.J. (2013). Reduction of bend scour with an air-bubble screen - Morphology and Flow patterns. ***International Journal of Sediment Research*** (accepted for publication).

Dugué, V., Blanckaert, K. and Schleiss, A.J. (2012). Flow patterns induced by a bubble screen in a sharply curved flume based on Acoustic Doppler Velocity Profiler measurements. *Proceedings of the eight International Symposium on Ultrasonic Doppler Methods for Fluid Mechanics and Fluid Engineering, 8th ISUD*, September 19-21, 2012, Dresden, Germany, pp.29-32.

Dugué, V., Schleiss, A. J. and Blanckaert, K. (2012). Bend scour reduction induced by an air-bubble screen under live-bed conditions. *Proceedings of the International Conference on Fluvial Hydraulics. River Flow 2012*, Costa Rica, pp. 609-615.

Dugué, V., Blanckaert, K. and Schleiss, A.J. (2012). An air-bubble screen used as a countermeasure to reduce erosion in open-channel bends. *Proceedings of the 6th International Conference on Scour and Erosion*, Paris, France.

Dugué, V., Izadinia, E., Rigaud, S. and Schleiss, A. J. (2012). Preliminary study on the influence of an air-bubble screen on local scour around a bridge pier. *Proceedings of the 2nd IAHR Europe Congress*, Munich, Germany.

Dugué, V., Blanckaert, K. and Schleiss, A.J. (2011). Influencing bend morphodynamics by means of an air-bubble screen - Topography and velocity field. *Proceedings of the 7th IAHR Symposium on River, Coastal and Estuarine Morphodynamics*, Beijing, China.

Dugué, V., Hachem, F., Boillat, J.-L., Nagel, V., Roca, J.-P. and Laugier, F. (2011). PKWeir and flap gate spillway for the Gage II Dam. *Proceedings of International Conference on Labyrinth and Piano Key Weirs*, Liège, Belgium.

Blanckaert, K., van Balen, W., Duarte, A., **Dugué, V.**, Garcia X.-F., Ottevanger, W., Pusch, M., Ricardo, A., Schnauder, I., Sukhodolov, A., Uijttewaal, W.S.J. and Wilkes, R. (2010). Research on eco-hydro-morphological river processes by combining field investigations, physical modeling and numerical simulations. *Proceedings of the International Symposium on Hydraulic Physical Modeling and Field Investigation*, Nanjing, China.

Camenen, B., **Dugué V.**, Proust, S., Le Coz, J. and Paquier, A. (2009). Formation of standing waves in a mountain river and its consequences on gravel bar morphodynamics. *Proceedings of the 6th IAHR Symposium on River, Coastal and Estuarine Morphodynamics*, Santa Fe, Argentina.